Non-local Hydrodynamic Transport in Dirac Liquids

Zur Erlangung des akademischen Grades eines

Doktors der Naturwissenschaften

von der KIT-Fakultät für Physik
des Karlsruher Instituts für Technologie (KIT)

genehmigte

Dissertation

von

Egor Kiselev, M. Sc.

Tag der mündlichen Prüfung: 08.05.2020

Referent: Prof. Dr. Jörg Schmalian
Korreferent: Prof. Dr. Alexander D. Mirlin

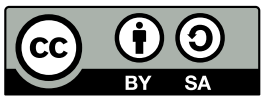

Introduction

The study of transport phenomena in solids has shaped condensed matter physics since its beginnings. Arguably, the Wiedemann-Franz law, based on work by Wiedemann and Franz [1], and developed by Lorenz [2, 3], can be seen as one of the foundations of the field. Together with the discovery of the electron by Thomson [4], it led to the first microscopic theory of transport – the Drude theory [5, 6]. Here, the electrons were treated as an ideal gas that scatters off the positive ions of the crystal lattice. While the latter assumption is wrong, as is known since the work of Bloch [7], the idea to treat the electrons as an ideal gas was fruitful. It was put on a sound basis by Sommerfeld by treating the electrons as a Fermi gas and explains some important properties of solids, such as the low temperature heat capacity [8].

However, treating the electrons as an ideal gas, one is bound to miss phenomena that are due to interaction effects. Here, a useful analogy is that of a liquid. Gurzhi showed first, that electrons in extremely clean materials can behave similar to a viscous liquid [9, 10]. He theoretically investigated the conductivity of wires of a small diameter d. If the material has sufficiently small impurity and defect concentrations, he found, and the temperature is low enough, such that electron-phonon scattering is unimportant, furthermore, if the mean free path between electron-electron collisions l_{ee} is much smaller than d, then the electrons move within the sample in a Brownian motion due to collisions with other electrons. In a given period of time Δt they travel a distance $\sqrt{l_{\mathrm{ee}} v_F \Delta t}$, where v_F is the Fermi velocity. Electron-electron collisions conserve momentum, such that, if all above conditions hold, the only channel of momentum loss is boundary scattering. On averge, the time passing between two collisions of an electron with the boundaries will be $\tau_b = d^2 / \left(l_{ee} v_F\right)$. Following Drude-Sommerfeld, the conductivity σ will scale as $\sigma \propto \tau_b$. It is interesting, that stronger electron-electron interactions, i.e. smaller scattering lengths l_{ee}, enhance the conductivity of the sample. The electrons act collectively and shield each other from boundary collisions. This becomes particularely clear if the temperature dependence of the conductivity is considered. According to Landau's Fermi liquid theory, the lifetime of electron quasiparticles τ_{ee}, and therefore the electron-electron scattering length $l_{\mathrm{ee}} = \tau_{\mathrm{ee}} v_F$ is proportional to the inverse square of the Temperature: $l_{\mathrm{ee}} \sim T_F / T^2$, where T_F is the Fermi temperature [11–13]. In the above described regime the resistance of the sample, therefore, drops according to a $1/T^2$ law. This was Gurzhi's original prediction, which is illustrated in Fig. 1. The same behavior follows, if the electrons are treated as a viscous liquid, and the problem is solved by means of the Navier-Stokes equation [9]. The flow is then completely analogous to the well known Poiseuille flow of classical hydrodynamics [14].

Gurzhi's discovery, often called *Gurzhi effect* or Gurzhi scaling, stands at the biginning of electron hydrodynamics. At the same time, it outlines many challanges that have to be tackled, in order to observe the viscous flow of electrons experimentally. The most fundamental difficulty is finding a sample that is sufficiently clean, such that the scattering length of impurity scattering is much larger than l_{ee}. Since in all materials l_{ee} grows with decreasing temperatures, whereas the distance between impurities is constant, this condition sets a lower bound on temperatures at which hydrodynamic behavior can be observed. The upper temperature bound is set by electron-phonon interactions, which become increasingly important at high temperatures [15]. If the two regimes dominated by impurity and phonon scattering do not overlap, a regime where the electrons behave hydrodynamically lies inbetween.

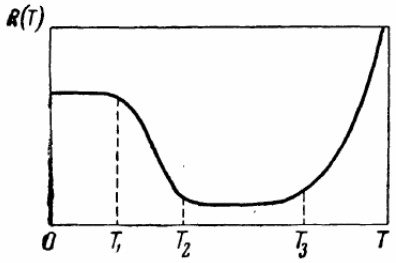

Figure 1: An illustration of the Gurzhi effect if shown. The resistance $R\left(T\right)$ of a thin wire as a function of the temperature T is shown. As the temperature rises above T_1, the scattering length of momentum conserving electron-electron collisions $l_{\mathrm{ee}} \sim T_F/T^2$ becomes shorter than the diameter of the wire, electrons begin to screen each other from collisions with the sample boundaries. As these momentum dissipating collisions become less probable, the resistance drops according to $R\left(t\right) \propto T_F/T^2$. The collective motion of electrons through the wire is more efficient than the motion of single electrons. This behavior continues until the temperature T_2 is reached, where the resistance takes a minimal value set by the impurity concentration of the sample. At T_3 momentum non-conserving electron-phonon scattering sets in, and the resistance raises. The figure is copied from Gurzhi's originial work [9].

The experimental realization of this regime is very challenging. Several attempts were made [16–18], however, the first fully accepted experimental observation of the Gurzhi effect was reported by de Jong and Molenkamp more than thirty years after the theoretical prediction [19]. The experiments were carried out with a two dimensional electron gas confined in GaAs heterostructures. The boundaries of the two dimensional wires were imposed electrostatically.

Recently, electron hydrodynamics has started to attract the interest of an increasing number of experimentalists and theoreticians. To a large extent, this is because more and more materials are becoming available, in which the hydrodynamic regime can be reached. Here, the most important example is *graphene*. Graphene crystals are exceedingly pure [20], and the electron-phonon interaction in this material is suppressed by the high lattice stiffness, as well as by strong phase-space constraints [21, 22]. Another interesting experimental plattform for electron hydrodynamics are ultrapure *delafossite metals*, which have extremely low residual resistances [23]. The de Jong-Molenkamp experiment has been repeated for the delafossite $PdCoO_2$ with some success [24]. Similar behavior has been observed in the Weyl material WP_2 [25]. Many recent works are concerned with different methods for the detection of hydrodynamic flows. Direct measurements of the Gurzhi effect are difficult, because the materials have to have extremely low impurity concentrations, such that the effect can be measured over a wide range of ratios w/l_{ee}, where w is the width of the mostly two dimensional samples. A different approach to the detection of the hydrodynamic regime is the measurement of negative non-local resitances caused by viscous vorices [26, 27]. This effect, however, can also appear in the ballistic regime [28]. Other detection methods rely on the measurement of current profiles through the samples [29–31]. Here, the problem is that impurity and boundary scattering can produce very similar profiles to those expected for hydrodynamic flow [32]. Very recent progress was, however, achieved by Sulpizio et. al. [30]. Here, parabolic Poiseuille profiles of electric currents in graphene in the Fermi liquid regime were observed [30].

From a theoretical point of view, electron hydrodynamics is intriguing because of its universality. Hydrodynamic equations can be derived from simple symmetry principles and conservation laws, whithout

much knowledge of the microscopic properties of the system [33]. This, in return, means that they are applicable in strongly interacting systems where no clear theoretical picture of the underlying microscopics is available [34, 35]. Another interesting point is, that the collective behavior of electrons in the hydrodynamic regime can greatly enhance the transport properties of a material. This effect can be anticipated from what was said about the Gurzhi effect. There, the coherent motion of electrons as a liquid led to an enhanced conductivity at intermediate temperatures. A striking effect that is related to Gurzhi's result appears in quantum point contacts. A quantum point contact is a constriction which confines electrons in the coordinate transverse to their flow direction. This leads to a quantization of the electron states in the constriction. This, in its turn, results in the fact, that the conductance of currents through the constriction is given by $G = 2Ne^2/h$, where N is an integer number corresponding to the number of states in the constriction that carry the current [36]. This conductance quantization is a purely ballistic effect, which can be seen clearest at very low temperatures. It was shown theoretically [37] and observed experimentally [38], that when the temperature is raised, such that the system enters the hydrodynamic regime, the conductivity at each step N improves as compared to the ballistic value.

The majority of works on electron hydrodynamics focuses on graphene [22, 39]. This has several reasons. First, high quality graphene is nowadays a widely available material [40, 41]. Second, graphene is a two dimensional material and hence can be investigated by means of scanning techniques, such as the scanning single-electron transistor technique, which allows to measure the current and voltage profiles along a graphene sample [29]. Furthermore, due to its unique band structure [42], electrons in graphene behave as massless Dirac particles with a linear spectrum [41] and a constant group velocity v_0. Thus, relativistic quantum physics [43], for example the Klein tunneling [44, 45] can be observed.

The charge density of graphene can be widely tuned by applying a gate voltage [46]. In this way, two very different regimes can be accessed: the *Fermi liquid* regime at large charge densities, and the *Dirac liquid* regime [47] at vanishing charge densities [22, 48]. The collective behavior of electrons in the two regimes is very different. The Fermi liquid is characterized by a large chemical potential $\mu \gg k_B T$, where k_B is the Boltzmann constant. The lifetime of quasiparticles follows the well known scaling $\tau_{\text{ee}} \sim \hbar\mu/\left(k_B T\right)^2$[11–13]. In the Dirac liquid regime, the chemical potential vanishes, i.e. it is tuned right to the so called *Dirac point* which separates the electron and hole bands. The only remaining relevant energy scale is the thermal energy $k_B T$. Therefore the quasiparticle lifetime must be proportional to the inverse thermal energy of the quasiparticle $\tau_{\text{ee}} \sim \hbar/\left(k_B T\right)$ [49]. Although the energy and the inverse lifetime of the quasiparticle are of the same order, the quasiparticles are sharply defined. This has the following reason: The interaction strength is determined by the fine structure constant $\alpha_0 = e^2/\left(\epsilon v_0 \hbar\right)$, where ϵ is the dielectric constant of the substrate. If the excited quasiparticles are confined to a small region $k_B T$ around the Dirac point, the fine structure constant is renormalized to small values $\alpha_0 \to \alpha \ll 1$ [47]. Interactions between quasiparticles are then governed by the small α, allowing for a perturbative approach. To leading order in α, the lifetime then is $\tau_{\text{ee}} \sim \hbar/\left(\alpha^2 k_B T\right)$, leading to pronounced quasiparticle behavior.

The Dirac liquid has a unique transport behavior. At the Dirac point, graphene exhibits a strong violation of the Wiedemann-Franz law [50]. While the transport of heat in graphene is ballistic – because of the linear spectrum, the energy current is proportional to the density of momentum – electric currents can decay due to electron-electron interactions [49, 51, 52]. The latter phenomenon is caused by the fact that graphene at the charge neutrality point is particle-hole symmetric. Oppositely charged electrons and holes contribute equally to the electric current, but flow in opposite directions. The electric current therefore does not carry any momentum and is not protected by momentum conservation. The violation of the Wiedemann-Franz law, i.e. the divergence of the ratio of thermal and electrical conductivities,

is a unique feature of graphene hydrodynamics. The interaction induced resistivity is a phenomenon known from the theory of quantum critical systems [53]. In graphene, it was studiend in the two works of Fritz et. al. and Kashuba [49, 54]. A very recent experiment by Gallagher et. al. [55] confirmed the predictions of Refs. [49, 54].

An important general point is that the behavior in the hydrodynamic regime intrinsically depends on the nature of electron-electron interactions in a system. For example, in two dimensional Fermi liquids, a fundamental difference exists between the relaxation times of excitations which are even and odd in momentum space. While the even modes relax according to the usual T_F/T^2 law, the odd modes relax by a factor of $\left(T_F/T\right)^2$ slower. This law, originally due to Gurzhi and collaborators [56, 57], was recently rediscovered [58]. Experiments on focussed electron beams confirmed the theoretical predictions [59]. It was shown, that the effect has a direct influence on the current profiles in the hydrodynamic regime [60]. This results motivated a part of the original work presented here.

In this thesis several aspects of electron hydrodynamics will be addressed with an emphasis on graphene at the charge neutrality point. The first three chapters provide a brief introduction to the physics of the Dirac liquid (***chapter 1***), electron hydrodynamics (***chapter 2***) and the theory of anomalous diffusion (***chapter 3***).

The topic of ***chapter 4*** directly relates to the discussion of the Gurzhi effect, with which this introduction began. This discussion showed the fundamental role of momentum dissipating electron-boundary scattering, in the abscense of other mechanisms of momentum relaxation. To gain a more quantitative picture of the Gurzhi effect, as well as of viscous electron flow in more complicated geometries, boundary scattering has to be treated more seriously. Following the general strategy of Refs. [61–63], boundary conditions for the kinetic distribution function of electrons will be derived. To this purpose, the boundary will be treated as a rough surface reflecting the impinging electrons. With this microscopic picture in mind, boundary conditions for the electronic Navier-Stokes equations will be derived. The central quantity here will be the so called slip length ζ, which relates the flow velocity at the bondary to its gradient. ζ measures how strongly the liquid is slowed down by the boundary and is determined by two aspects: how much momentum gets lost during electron-boundary collisions, and how efficient the viscous transport of momentum towards the boundary is. A large slip length corresponds to a weak slowdown of the liquid at the boundary. It will be shown, that the slip length is large for smooth boundaries (due to the small momentum loss in single scattering events) and at low temperatures (due to the inefficiency of viscous momentum transport). The results will be shown to agree with experiments on the Gurzhi effect in graphene [27, 30] and $PdCoO_2$ [24]. In general, it will become clear, that the Gurzhi effect only has significant impact on the electron flow, if the slip length is much smaller than the sample size, which is achived in most recent experiments [30]. At the same time, interesting physics can be observed in the regime of large slip lengths. This will be demonstrated by solving the Navier-Stokes equation of graphene at the charge neutrality point for the flow past an impenetrable obstacle in a long graphene strip. For a large slip length, the pressure differences along the strip arise due to viscous forces alone, providing a method to measure the viscosity of a Dirac liquid. Furthermore, the so-called Stokes paradox can be observed: there exists no regime, in which the response to an applied pressure gradient is linear.

In ***chapter 5***, non-local transport in a Dirac liquid will be studied. The non-local conductivities, wavenumber dependent quantities that govern the transport in spatially modulated fields or confined geometries, will be derived. It will be shown that constitutive relations involving non-local conductivities are closely connected to hydrodynamic equations, and can be used to calculate the current profiles

of hydrodynamic flows. To derive the non-local transport coefficients, the electron-electron scattering in a Dirac liquid must be considered in detail. Building upon the quantum Boltzmann equation for the Dirac liquid derived in the Refs. [49, 51], the full set of relaxation times $\tau_{c/\epsilon,m}$ of excitations in different angular harmonic channels m will be calculated. Here, the subscripts c/ε stand for excitations in the charge and energy channels, respectively. It will be shown, that the scattering rates $\tau^{-1}_{c/\epsilon,m}$ increase linearly with growing m for large m: $\tau^{-1}_{c/\epsilon,m} \sim |m|$. This peculiar behavior will enable an exact solution of the Boltzmann equation. Using this solution, the transport coefficients will be calculated. Furthermore, the collective modes of a Dirac liquid will be studied. It will be shown, that the propagation of thermal excitations in a Dirac liquid is goverend by a wave equation, rather than by a diffusion equation [52]. This phenomenon is called second sound, and is the analogue of a plasmon mode in Galilean invariant system. Since in a Dirac liquid, thermal transport is ballistic, but electric transport is diffusive, the two modes switch places. Besides these known excitations, an infinite set of strongly damped collective modes corresponding to exotic excitations in higher angular harmonic channels will be found.

Finally, in ***chapter 6*** the phase space dynamics of a Dirac liquid will be studied. It well be demonstrated, that due to the non-analytic behavior of the scattering rates $\tau^{-1}_{c/\epsilon,m} \sim |m|$, graphene electrons perform Lévy flights in phase space. Lévy flights are random walks with unusual statistical properties and will be introduced in chapter 3. While many interacting plasmas and gases can be described by ordinary Fokker-Planck equations [64–70], the behavior of the Dirac liquid is governed by a fractional Fokker-Planck equation, and the phase space motion of graphene electrons is superdiffusive. This has important consequences for the relaxational behavior of non-equilibrium states. As an example, the decay of an injected focussed current beam will be considered. It will be shown, that the Lévy flight behavior results in a superdiffusive heating of the Dirac liquid. The resulting heating rates are much larger than in an ordinary gas or plasma, where the phase space dynamics is governed by normal diffusion.

Contents

1 Chapter 1

Fundamentals: Graphene

Graphene is a two dimensional crystal consisting of carbon atoms that are bound in a honeycomb lattice. It was the first perfectly two dimensional material and opened the gateway to many exciting experiments and applications [41]. For a long time it was believed that two dimensional crystals are intrinsically unstable due to large thermal fluctuations and therefore cannot be found in nature or synthesized [71]. This belief was based on ideas of Landau and Peierls that were further substantiated by Mermin [72]. However, the experimental succes of Geim and Novoselov that brought us graphene, showed that such materials indeed do exist [46]. The first graphene samples were mounted to a solid substrate, but soon suspended samples followed [73]. It became clear under the electron microscope, that suspended samples are not perfectly flat, but are crumpled on a nanometer scale, which, together with a large lattice stiffness, stabilizes the graphene sheets[73]. The experimental success motivated an enormous amount of works on graphene. However, even before the first samples were available, the electronic structure of graphene aroused interest on the theoretical side. Notable examples are the band structure calculations of Wallace [42], and the renormalization group study of electron interactions by Gonzaleza et. al. [74] anticipating the concept of the Dirac liquid.

In electron hydrodynamics, graphene is the by far most studied material [22, 39]. As will be explained in chapter 2, the hydrodynamic description of an electronic system is feasible, when the electron-electron scattering length is the shortest length scale in the system. Other scattering mechanisms, such as electron-impurity or electron-phonon scattering are therefore the natural enemies of hydrodynamics. Graphene, however, is a system with remarkably low defect concentrations and impurity mean free paths on the ten micrometer scale [20]. The electron-phonon scattering is small due to kinematic constraints [21], and due to the fact that only a small fraction of the acoustic phonon states is thermally occupied because of the high Debye temperature of the order of $10^3\,\mathrm{K}$, which can be traced back to the high lattice stiffness of graphene.

Graphene electrons are massless, Coulomb interacting Dirac fermions with a linear dispersion relation $\varepsilon_{\mathbf{k},\lambda} = \lambda v k$. Here, $\lambda = \pm 1$ is the band index labeling the electron ($\lambda = +1$) and hole ($\lambda = -1$) bands, v is the group velocity, and k the particles' wavenumber. Pristine graphene is a semimetal with a fully filled hole band and an empty electron band. Thus, the chemical potential lies at the so-called Dirac point – the touching point of the two bands. At finite temperatures the region around the Dirac point is populated by thermally excited electrons and holes. These excitations form the so called Dirac liquid. By doping or gating, the chemical potential can be raised or lowered, such that the system eventually turns into an electron- or hole-doped Fermi liquid, when the condition $\left|\mu\right| \gg k_B T$ is fulfilled. This is illustrated in Fig. 1.1. In this thesis, mostly the Dirac liquid will be of interest. It will be shown

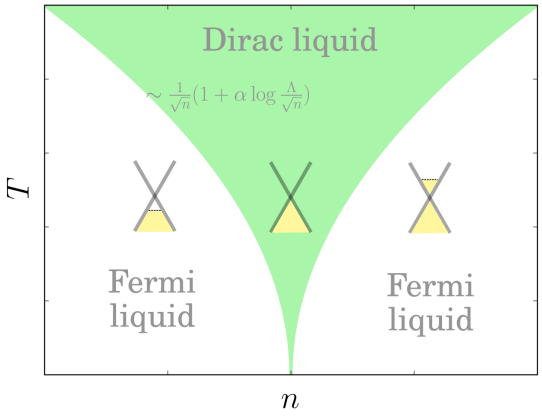

Figure 1.1: The figure shows the Fermi liquid and Dirac liquid regimes of graphene in the colors of the season. There is no sharp boundary between the regimes. The crossover is determined by $k_B T \approx \mu$, where μ is the chemical potential. Up to logarithmic corrections due to Coulomb interactions (see section 1.2), it is $\mu \sim \sqrt{n}$, where n is the charge density. If the chemical potential is below the Dirac point, the system is in the hole doped Fermi liquid regime. For a positive chemical potential, the system is an electron doped Fermi liquid.

in section 1.2, that the excitations of the Dirac liquid are clearly pronounced quasiparticles, whose transport properties can be studied using a quantum Boltzmann equation.

1.1 Graphene: band structure

In this section, the nearest neighbor, tight binding band structure of graphene will be derived. A section of the Graphene lattice is shown in Fig 1.2. The lattice separates into two sublattices A (white atoms in Fig. 1.2) and B (blue atoms in Fig. 1.2). The primitive lattice vectors $\mathbf{a}_1$ and $\mathbf{a}_2$ can be chosen as

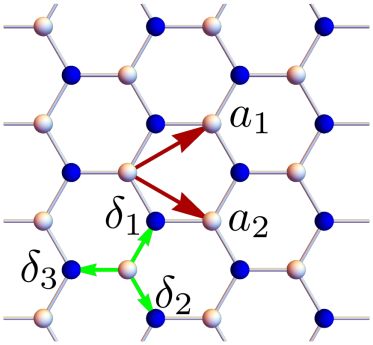

Figure 1.2: The honeycomb lattice of graphene. The A(B) sublattice is represented by white(blue) spheres.

$$\begin{aligned}\mathbf{a}_1 &= \frac{a}{2}\left(3,\sqrt{3}\right)^T,\\ \mathbf{a}_1 &= \frac{a}{2}\left(3,-\sqrt{3}\right)^T.\end{aligned}$$

Here $a \approx 1.42 \cdot 10^{-10} m$ is the nearest neighbor spacing. The reciprocal basis can be found using the condition $\mathbf{a}_i \cdot \mathbf{b}_j = 2\pi\delta_{ij}$:

$$\begin{aligned}\mathbf{b}_1 &= \frac{2\pi}{3a}\left(1,\sqrt{3}\right)^T,\\ \mathbf{b}_1 &= \frac{2\pi}{3a}\left(1,-\sqrt{3}\right)^T.\end{aligned}$$

The nearest neighbor vectors on the A sublattice are given by

$$\begin{aligned}\boldsymbol{\delta}_1 &= \frac{a}{2}\left(1,\sqrt{3}\right)^T,\\ \boldsymbol{\delta}_2 &= \frac{a}{2}\left(1,-\sqrt{3}\right)^T,\\ \boldsymbol{\delta}_3 &= a\left(-1,0\right)^T.\end{aligned}$$

The nearest neighbor tight binding Hamiltonian for this configuration can be written in the form

$$H_{tb} = -t\sum_{\langle i,j\rangle}\left(a_i^\dagger b_j + b_j^\dagger a_i\right),$$

where $a_i^\dagger = \sum_{\mathbf{k}} a_{\mathbf{k}}^\dagger e^{-i\mathbf{k}\cdot\mathbf{r}_i}$, $b_j = \sum_{\mathbf{k}} b_{\mathbf{k}} e^{i\mathbf{k}\cdot\mathbf{r}_j}$, etc. are creation and annihilation operators at lattice points i, j. Spin quantum numbers were suppressed. In the Fourier representation, the above Hamiltonian reads

$$H_{tb} = \sum_{\mathbf{k}}\left(\xi_{\mathbf{k}} a_{\mathbf{k}}^\dagger b_{\mathbf{k}} + \xi_{\mathbf{k}}^* b_{\mathbf{k}}^\dagger a_{\mathbf{k}}\right)$$

with $\xi_{\mathbf{k}} = -t\sum_j e^{i\mathbf{k}\cdot\boldsymbol{\delta}_j}$. Introducing the spinor $\psi_{\mathbf{k}}^\dagger = \left(a_{\mathbf{k}}^\dagger, b_{\mathbf{k}}^\dagger\right)$ the Hamiltonian becomes

$$H_{tb} = \sum \psi_{\mathbf{k}}^\dagger \begin{bmatrix} 0 & \xi_{\mathbf{k}} \\ \xi_{\mathbf{k}}^* & 0 \end{bmatrix} \psi_{\mathbf{k}}.$$

It is

$$\xi_{\mathbf{k}} = -te^{-ik_x a}\left(1 + 2\exp\left(\frac{i3k_x}{2}a\right)\cos\left(\frac{\sqrt{3}k_y}{2}a\right)\right),$$

and the energy eigenvalues are

$$\varepsilon_{\mathbf{k}} = \pm\left|\xi_{\mathbf{k}}\right|.$$

$\xi_{\mathbf{k}}$ and $\varepsilon_{\mathbf{k}}$ vanish at the points $\mathbf{k} = \frac{2\pi}{3a}\left(\pm 1, \pm\frac{1}{\sqrt{3}}\right)$. The low energy physics of graphene electrons will therefore be governed by the behavior of $\varepsilon_{\mathbf{k}}$ around these points, two of which lie in the Brillouin zone:

$$\begin{aligned}\mathbf{K} &= \frac{2\pi}{3a}\left(1,\frac{1}{\sqrt{3}}\right),\\ \mathbf{K}' &= \frac{2\pi}{3a}\left(1,-\frac{1}{\sqrt{3}}\right).\end{aligned}$$

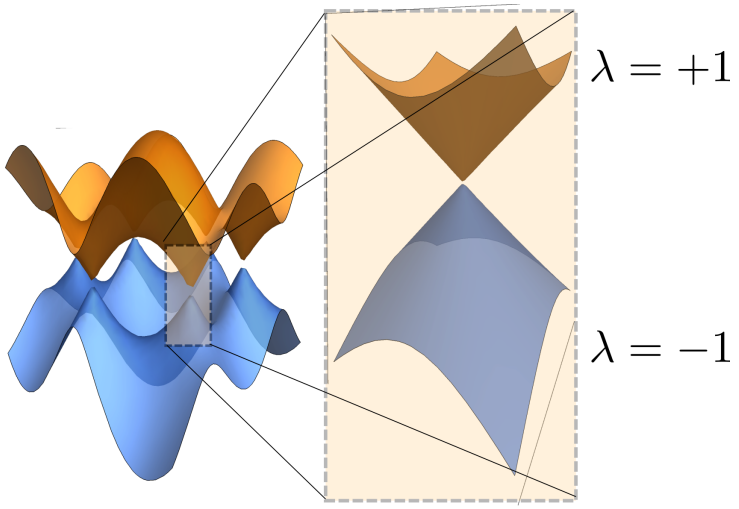

Figure 1.3: The tight-binding band strucure of graphene. The Dirac point with the two Dirac cones is highlited.

Expanding $\xi_{\mathbf{k}}$ around $\mathbf{K}$ and $\mathbf{K}'$ we find

$$\begin{aligned} \xi_{\mathbf{K}+\mathbf{k}} &= v\left(k_y - ik_x\right)e^{-iK_x a}, \\ \xi_{\mathbf{K}'+\mathbf{k}} &= -v\left(k_y + ik_x\right)e^{-iK_x a}, \end{aligned}$$

with the group velocity of electrons $v = 3ta/2 \approx 10^6 m/s$. Neglecting the constant phase factor, the low energy physics around the Dirac point $\mathbf{K}$ is described by the effective Hamiltonian

$$H_0 = v\sum_{\mathbf{k}} \psi^{\dagger}_{\mathbf{k}} \left(\boldsymbol{\sigma}\cdot\mathbf{k}\right)\psi_{\mathbf{k}}.$$

This is the Hamiltonian of massless Dirac particles. The regions around the two Dirac points $\mathbf{K}$, $\mathbf{K}'$ are called Dirac valleys. The degeneracy of the Hamilonian is fourfold: 2×2 for spin$\times$number of valleys. The eigenvalues of the Dirac Hamiltonian are

$$\varepsilon_{\mathbf{k}} = \lambda v k,$$

where $\lambda = \pm 1$ labels the lower and upper Dirac cones (see Fig. 1.3). For details on the single particle physics of graphene see Ref. [41], which was followed throughout this section.

1.2 Graphene: Coulomb interactions

The question whether the Coulomb interaction plays a crucial role in the physics of graphene is not trivial. On the one hand the fine structure constant of free standing graphene is of the order of unity: $\alpha_0 = e^2/\left(\epsilon v_0 \hbar\right) \approx 2.2$. Such a large value (compared to e.g. the fine structure constant of QED $\alpha_{\mathrm{QED}} = 1/137$) indicates that interaction effects in graphene should be very important. On the other hand many experimental results can be understood using the non-interacting massless Dirac model.

Some examples are the minimum conductivity of disordered samples [75], as well as the observations of Klein tunneling [45] and the quantum hall effect [76, 77].

Monte-Carlo simulations showed that at $\alpha \sim 1$, graphene can be expected to exhibit a semimetal-insulator transition due to chiral symmetry breaking [78]. Here the electrons acquire a finite mass - a gap opens around the Dirac point. For small values of α, however, Coulomb interactions are marginally irrelevant. The critical point corresponding to the semimetal-insulator transition is repulsive. A crucial question therefore is, on which side of the semimetal-insulator transition graphene lies. Both, experimentally [79] and theoretically [80], free standing graphene was shown to lie on the semimetal side of the critical point. It follows that at low temperatures, α will be renormalized to lower values, and that the physics of graphene will be governed by small α physics (see Fig. 1.4). Below the renormalization group (RG) analysis of graphene will be performed to first order in α.

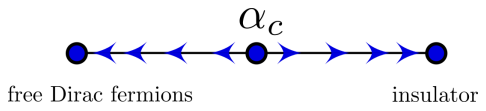

Figure 1.4: RG flux around the critical point of the Dirac semimetal - insulator transition. Graphene lies to the left of the critical point of the semimetal-insulator transition α_c, and is thus flows to small values under the RG procedure. At low temperatures, a perturbative analysis, where α is a small parameter, is justified.

There exits a number of studies concerned with the RG analysis of graphene [47]. The Coulomb interaction between graphene electrons at charge neturality was shown to be marginally irrelevant [47]. At experimental temperatures the fine structure constant α is renormalized to small values. This justifies a quasiparticle interpretation of the electronic Dirac liquid and explains why in a wide range of regimes Coulomb interactions can be treated as a perturbation. Ultimately this behavior opens the door to a description of transport properties of graphene in terms of a quantum kinetic equation - the essential tool for the remainder of this thesis.

The following analysis closely follows Ref. [47], for technical details concerining the renormalization group analysis see Ref. [81]. The action for the electron fields $\psi^\dagger_{\mathbf{k}}$, $\psi_{\mathbf{k}}$ in the Matsubara representation reads

$$\begin{aligned} S &= S_0 + S_{int} \\ S_0 &= \int_{k,n} \psi^\dagger_{\mathbf{k}}(\omega_n)\left(-i\omega_n + v_0 \mathbf{k}\cdot\boldsymbol{\sigma}\right)\psi_{\mathbf{k},n}(\omega_n) \\ S_{int} &= \frac{1}{2}\int_{k_1,n}\int_{k_2,m}\int_{q,l} \psi^\dagger_{\mathbf{k}_1+\mathbf{q}}(\omega_n-\omega_l)\,\psi^\dagger_{\mathbf{k}_2-\mathbf{q}}(\omega_m+\omega_l)\,V\left(|\mathbf{q}|\right)\psi_{\mathbf{k}_1}(\omega_n)\,\psi_{\mathbf{k}_2}(\omega_m)\,. \end{aligned} \tag{1.1}$$

Here and in the following the abbreviation

$$\int_{k,n} = T\sum_n \int \frac{d^2k}{(2\pi)^2}$$

is used. The summation over pseudo-spin is implicitely assumed, as is the summation over the degenerate spin and valley indices. The Coulomb potential of electrons on a 2D graphene sheet is given by

$$V\left(|\mathbf{q}|\right) = \frac{2\pi e^2}{\epsilon\,|\mathbf{q}|}.$$

Performing the RG, it should be kept in mind that, as usual in condensed matter physics, the system has a natural momentum cut-off Λ which is set by coarse-graining nature of the solid lattice. The physically relevant scale in the case of graphene Dirac electrons of is given by energies around 1eV, above which the dispersion relation deviates from the linear Dirac spectrum.

1.2.1 Preliminary scaling analysis

A preliminary scaling analysis shows that Coulomb interactions in graphene are marginal. Ultimately, the behavior at large length scales and small momenta will be of interest. Thermally excited electrons will populate a small portion of the Dirac cone around the neutrality point. Their momenta will occupy a range $|k| \leq \Lambda/b$ with $b \gg 1$. At this point, it is useful to separate the field operators into so called slow and fast modes

$$\psi_{\mathbf{k}} = \begin{cases} \psi^{>}_{\mathbf{k}} & \Lambda/b < |\mathbf{k}| \leq \Lambda \\ \psi^{<}_{\mathbf{k}} & |\mathbf{k}| \leq \Lambda/b \end{cases}$$

The fast modes can be "integrated out", i.e. the functional integration of e^{-S} over field variables $\psi^{\dagger>}_{\mathbf{k}}$, $\psi^{>}_{\mathbf{k}}$ with $\Lambda/b < |\mathbf{k}| \leq \Lambda$ is carried out, leaving us with an effective distribution $e^{-S_{\text{eff}}}$ characterized by an effective action. This procedure will be presented in more detail in the next section. It is followed by a rescaling of the variable $\mathbf{k} \to b\mathbf{k}$, such that the range of fluctuations of the remaining fields again matches the original length scales (see Fig. 1.5). The hole transformation can be thought of as selecting a small window in momentum space and zooming into it, or zooming out into a larger window in real space thereby roughening the image.

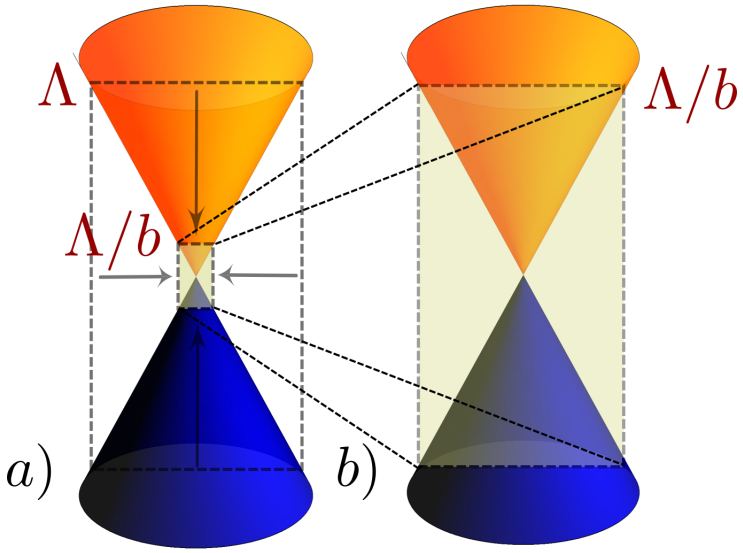

Figure 1.5: Illustration of coarse graining in the RG procedure. Small wavelengths (high momentum) physics is integrated out (a), followed by a rescailing of the wavelengths. This corresponds to a zooming into smaller values in momentum space (b).

In this section, the discussion will be limited to an RG transformation at zeroth order in the coupling constant. The contributions stemming from integrating out the high momentum fields $\psi^{\dagger>}_{\mathbf{k}}$, $\psi^{>}_{\mathbf{k}}$ of the

interaction part of the action will be ignored. The functional integration over the fields $\psi^{\dagger>}_{\mathbf{k}}$, $\psi^{>}_{\mathbf{k}}$ in the free part of the action just gives an overall factor, which is not important. The resulting effective action is just the S of Eq. (1.1), where the momentum integrals are limited by Λ/b. For the rescaling, a new set of variables is introduced:

$$\begin{aligned} \mathbf{k}' &= b\mathbf{k} \\ \omega'_n &= b\omega_n. \end{aligned} \tag{1.2}$$

The rescaling of the frequencies is chosen such that the free electron propagator propagator

$$G_{\mathbf{k}'}\left(i\omega'_n\right) = \left(-i\omega'_n + v\mathbf{k}'\cdot\boldsymbol{\sigma}\right)^{-1}$$

scales in a consistent manner. It will change, once the interaction terms are considered. In general, the frequency is rescaled according to $\omega'_n = b^z\omega_n$, with z depending on the power of $\mathbf{k}$ in the free electron dispersion. Since the Matsubara frequencies are given by $\omega_n = (2n+1)\,\pi T$, the temperature scales according to

$$T' = bT. \tag{1.3}$$

The scaling behavior of the field variables can be chosen freely. To compare how the free and interactiong parts of the action scale under the RG transformation, the rescaled field operators are defined as $\psi^{<\prime}_{\mathbf{k}} = b^{-2}\psi^{<}_{\mathbf{k}}$, such that the free part of the action is invariant, i.e. such that the factors of b cancel in the free part. It turns out that the interaction part is invariant, too. At zeroth order, Coulomb interactions are marginal. Higher orders will decide, that the effective interactions of Dirac electrons near the charge neutrality point tend to decrease at small temperatures.

1.2.2 Renormalization at the one loop level

Since the scaling analysis of the last section did not provide insights into how interactions enter the effective action of low energy Dirac electrons, a renormalization analysis to first order in the coupling constant has to be performed. The field operators are subdivided according to $\psi_{\mathbf{k}} = \psi^{<}_{\mathbf{k}}\Theta\left(\Lambda/b - \left|\mathbf{k}\right|\right) + \psi^{>}_{\mathbf{k}}\Theta\left(\left|\mathbf{k}\right| - \Lambda/b\right)\Theta\left(\Lambda - \left|\mathbf{k}\right|\right)$. Schematically, the action subdivided into slow and fast modes can be written as

$$S = S^{<} + S^{>} + S^{><},$$

where the first two terms are the just the original action where the field operators are replaced by their fast or slow parts. Anticipating the functional integration over fast modes, we dropped all terms that contain uneven powers of field operators. $S^{><}_{int}$ consists of four non-vanishing contributions:

$$\begin{aligned} S^{><} = &\frac{1}{2}\int_{k_1,n}\int_{k_2,m}\int_{q,l}\psi^{\dagger<}_{\mathbf{k}_1+\mathbf{q}}\left(\omega_n-\omega_l\right)\psi^{\dagger>}_{\mathbf{k}_2-\mathbf{q}}\left(\omega_m+\omega_l\right)V\left(\left|\mathbf{q}\right|\right)\psi^{>}_{\mathbf{k}_1}\left(\omega_n\right)\psi^{<}_{\mathbf{k}_2}\left(\omega_m\right) \\ &+\frac{1}{2}\int_{k_1,n}\int_{k_2,m}\int_{q,l}\psi^{\dagger>}_{\mathbf{k}_1+\mathbf{q}}\left(\omega_n-\omega_l\right)\psi^{\dagger<}_{\mathbf{k}_2-\mathbf{q}}\left(\omega_m+\omega_l\right)V\left(\left|\mathbf{q}\right|\right)\psi^{<}_{\mathbf{k}_1}\left(\omega_n\right)\psi^{>}_{\mathbf{k}_2}\left(\omega_m\right) \\ &+\frac{1}{2}\int_{k_1,n}\int_{k_2,m}\int_{q,l}\psi^{\dagger<}_{\mathbf{k}_1+\mathbf{q}}\left(\omega_n-\omega_l\right)\psi^{\dagger>}_{\mathbf{k}_2-\mathbf{q}}\left(\omega_m+\omega_l\right)V\left(\left|\mathbf{q}\right|\right)\psi^{<}_{\mathbf{k}_1}\left(\omega_n\right)\psi^{>}_{\mathbf{k}_2}\left(\omega_m\right) \\ &+\frac{1}{2}\int_{k_1,n}\int_{k_2,m}\int_{q,l}\psi^{\dagger>}_{\mathbf{k}_1+\mathbf{q}}\left(\omega_n-\omega_l\right)\psi^{\dagger<}_{\mathbf{k}_2-\mathbf{q}}\left(\omega_m+\omega_l\right)V\left(\left|\mathbf{q}\right|\right)\psi^{>}_{\mathbf{k}_1}\left(\omega_n\right)\psi^{<}_{\mathbf{k}_2}\left(\omega_m\right). \end{aligned}$$

To first order in the coupling constant, the effective action is given by $e^{-S_{\text{eff}}} = e^{-S^<} \left\langle e^{-S^{><}} \right\rangle_> \approx e^{-S^< - \langle S^{><} \rangle_>}$. Integrating over fast modes and carrying out the momentum integration, the first two terms reduce to

$$\int_{k_1,n} \psi^{\dagger <}_{\mathbf{k}_1} (\omega_n) \, \Sigma \left(\mathbf{k}_1 \right) \psi^<_{\mathbf{k}_2} (\omega_m) \, , \tag{1.4}$$

where $\Sigma \left(\mathbf{q} \right) = \int_{k_1,n}^{\Lambda/b<k<\Lambda} G_{\mathbf{k}_1+\mathbf{q}} \left(i\omega_n \right) V \left(\left| \mathbf{k}_1 \right| \right)$, with the momentum integration ranging from Λ/b to Λ is the Fock contribution to the self energy. The last to terms correspond to Hartree self-energy contributions. They can be neglected, since they are constants and therefore amount to a renormalization of the chemical potential which is fixed to zero due to the assumption of charge neutrality. For the same reason, only the Fock self energy to lowest order in $\mathbf{q}$ and at $T = 0$ contributes to the renormalization. Higher orders in $\mathbf{q}$ and T in the expansion of $\Sigma \left(\mathbf{q} \right)$ are rendered irrelevant by the scaling behavior given in Eqs. (1.2) and (1.3).

The self energy at $T = 0$ is given by [82]

$$\begin{aligned} \Sigma \left(\mathbf{q} \right) &= \frac{2\pi e^2}{\epsilon} \int \frac{d^2 k}{(2\pi)^2} \int \frac{d\omega}{2\pi} \frac{\omega + v_0 \boldsymbol{\sigma} \cdot \left(\mathbf{k} + \mathbf{q} \right)}{\omega^2 + v_0^2 \left(\mathbf{k} + \mathbf{q} \right)^2} \frac{1}{|\mathbf{k}|} \\ &= \frac{1}{4} \frac{e^2}{\epsilon} \left(\boldsymbol{\sigma} \cdot \mathbf{q} \right) \log \left(b \right) + \mathcal{O} \left(q^2 \right) . \end{aligned} \tag{1.5}$$

Thus, the non-interacting part of the action renormalizes according to

$$S_0 = \int_{k,n}^{\Lambda/b<k<\Lambda} \psi^{\dagger <}_{\mathbf{k}} (\omega_n) \left(-i\omega_n + v_0 \left(1 + \frac{\alpha}{4} \log \left(b \right) \right) \mathbf{k} \cdot \boldsymbol{\sigma} \right) \psi^<_{\mathbf{k},n} (\omega_n) \, .$$

Since at lowest order the self energy (1.5) is frequency independent, only the group velocity is renormalized:

$$v = v_0 \left(1 + \frac{\alpha_0}{4} \log \left(b \right) \right) . \tag{1.6}$$

Here $\alpha_0 = e^2 / \left(\epsilon v_0 \hbar \right)$ is the bare fine structure constant, which is renormalized according to (1.6):

$$\alpha = \frac{\alpha_0}{1 + \frac{\alpha_0}{4} \log \left(b \right)} . \tag{1.7}$$

Whenever the group velocity v, or the fine structure constant α appear in the text without a subscript zero, the renormalized quantities are meant. The fine structure constant quantifies the ratio of Coulomb interaction energy and kinetic energy. With increasing b, i.e. at small energies α is renormalized to small values, as is evident from Eq. (1.7). This is an essential feature of Coulomb interactions in charge neutral graphene. It demonstrates that at low temperatures graphene electrons and holes behave as independent, well defined, interacting quasi-particles - a picture that motivates and justifies the quantum-Boltzmann approach to transport in charge neutral graphene presented in Sec 5. Interaction effects can be treated in terms of particle collisions and by replacing the bare quantities by their renormalized versions.

1.2.3 Temperature dependence and scaling

It has already been anticipated that the lower cut-off Λ/b can be set by the temperature T. Due to the thermal broadening of the Fermi-Dirac distribution electrons and holes populate an area of $\sim k_B T$ around the Dirac point. This scenario is relevant when dealing with the hydrodynamic regime. Alternatively the cut-off can be set by a different scale, such as e.g. a frequency. Focusing on the first case, the cut-off variable b can be expressed in terms of the band structure cut-off Λ and the physical temperature T. Due to the renormalization of the group velocity v in (1.6), the scaling behavior of the temperature (1.3) is modified, too:

$$T \;=\; Z_T\left(b\right) T\left(b\right), \tag{1.8}$$

where $Z_T\left(b\right) = b^{-1}\left(1+\frac{\alpha_0}{4}\log b\right)$. The upper cut-off is given by Λ, which corresponds to a temperature $T_\Lambda = v\Lambda/k_B$. Fixing b such that the lower cut-off is given by the physical temperature T, Eq. (1.8) yields $T/T_\Lambda = Z_T\left(b\right)$, which is solved by

$$b = \frac{T_\Lambda}{T}\left(1+\alpha_0 \log\left(\frac{T_\Lambda}{T}\right)\right) \tag{1.9}$$

for $b \gg 1$. Using relation (1.9) together with the renormalized group velocity (1.6) and fine structure constant (1.7), the temperature dependence of different physical quantities can be deduced. The compressibility $\kappa = \partial n/\partial\mu$ is an example [47]. Replacing the bare velocity v_0 by v in the free fermion result gives

$$\kappa = \frac{\pi\left(\hbar v_0\right)^2}{4k_B T \log 2}\left(1+\frac{\alpha_0}{4}\log\left(b\right)\right)^2.$$

This result is in reasonable agreement with experiment [47, 83]. Further insights can be won by exploiting the scale invariance of the linear graphene dispersion. E.g. the dimensionless (in 2D), interaction induced electrical conductivity at zero frequency is a function of temperature and the fine structure constant: $\sigma\left(T,\alpha_0\right)$. Due to scale invariance, the conductivity at the physical temperature T should be equal to the conductivity at the cut-off temperature T_Λ and a renormalized fine structure constant:

$$\sigma\left(T,\alpha_0\right) = \sigma\left(T_\Lambda, \alpha\left(T\right)\right).$$

It is immediately clear that the temperature dependece is entering $\sigma\left(T_\Lambda,\alpha\left(T\right)\right)$ through the fine structure constant $\alpha\left(T\right)$. On the other hand, according to Fermi's golden rule, the scattering rate of quasiparticles has to be proportional to the squared modulus of the transition matrix element, i.e. to $\alpha^2\left(t\right)$. The conclusion is that at zero frequency $\sigma \sim \alpha^{-2}\left(T\right)$, i.e. the temperature dependence of electric conductivity is due to the renormalization of v and α.

1.3 Summary

Some fundamental aspects of graphene physics were introduced in this chapter. The band structure of graphene was studied in section 1.1. It was shown, that at low energies the nearest neighbor tight binding model hamiltonian reduces to a massless Dirac hamiltonian

$$H_0 = v_0 \sum_{\mathbf{k}} \psi^\dagger_{\mathbf{k}}\left(\boldsymbol{\sigma}\cdot\mathbf{k}\right)\psi_{\mathbf{k}}$$

with a fourfould spin-valley degeneracy $N = 4$. Here, $\boldsymbol{\sigma}$ is the vector of Pauli matrices and $v_0 \approx 10^6 m/s$ is the electron group velocity.

It was shown in section 1.2, that thermally excited electrons and holes in graphene at the charge neutrality point, which form a so called Dirac liquid, behave as sharply defined quasiparticles. This is because the graphene fine structure constant

$$\alpha = \frac{e^2}{\epsilon v \hbar},$$

which quantifies the interaction strength, is renormalized to small values for excitations that are confined to the narrow region $\sim k_B T$ around the Dirac point. This behavior of α is mediated by the renormalization of the electron group velocity $v_0 \to v$ appearing in the denominator, where

$$v = v_0 \left(1 + \frac{\alpha_0}{4} \log\left(\frac{\Lambda}{k_B T}\right)\right)$$

[47, 74]. The weakening of interactions with the renormalization group flow allows for the use of perturbation theory with the renormalized fine structure constant α as a small parameter. Thus, the quantum Boltzmann equation (see sections 2.4 and 5.1.1) can be used to study the transport properties of the system.

Chapter 2

2 Fundamentals: Electron hydrodynamics

The analogy between electronic systems in solids and gases goes back to the celebrated Drude model of 1900 [5, 6]. It was successful in explaining some fundamental properties of electron transport in systems dominated by impurity scattering. In the 1960s, Gurzhi proposed [9, 10], that the interacting electrons can behave similar to a classical liquid. For example, they should follow the same scaling with the sample width, as a classical liquid in the regime of Poisuille flow (see section 2.1.3). This, however, is only possible, if the crystal hosting the electrons is exceedingly free of any impurities, dislocations and other mechanisms of momentum dissipation, as is a pipe through which flows a classical liquid. This condition is fulfilled, if the mean free path of momentum conserving electron-electron interactions is shorter than the mean free paths of the momentum dissipating scattering mechanisms: impurity scattering, boundary scattering, phonon scattering. If $l_{\mathrm{ee}} \ll l_{\mathrm{imp}}, l_{\mathrm{geo}}, l_{\mathrm{phonon}}$, a hydrodynamic description is appropriate. Another condition on hydrodnymic flow is that there is a scale separation between the time scales of external perturbations and the (shorter) internal time scales of electron-electron interactions. If this is the case, and the above condition on the scattering lengths holds, the electron liquid is in a state of local equilibrium, i.e. its behavior at any point can be characterized by a few parameters such as flow velocity, pressure and density, whereas the intricate details of electron-electron interactions average out. Speaking loosely, the hydrodynamic regime in this sense can be defined as the regime of slow excitations on long scales.

Hydrodynamic equations can be deduced from very simple considerations of symmetries and conservation laws. Thus, they hold even in the case of strongly interacting electrons, where no coherent quasiparticle picture can be constructed [34]. This universality makes electron hydrodynamics a particularely intriguing subject of study. However, when dealing with a system of pronounced quasiparticles as in the case of the Dirac liquid, hydrodynamics can be derived from the underlying kinetic theory of quasiparticle collisions. The transport coefficients governing the hydrodynamic flow can be calculated and the nature of electron-electron collisions itself can be studied in more detail.

In this chapter, the derivation of the Navier-Stokes equations from macroscopic considerations and from the kinetic equation will be discussed. Basic notions of tranport theory will be interoduced. The quantum Boltzmann method, upon which builds the kinetic equation of chapter 5, will be summerized and some experimental results on electron hydrodynamics reviewed.

2.1 Hydrodynamics from a macroscopic point of view

2.1.1 The Navier-Stokes equations

Here, an elegant and simple derivation of the hydrodynamic equations based on Ref. [14] is presented, which is not based on any microscopic details of the liquid. Imagine a small liquid volume element V that is subject to pressure as an accelerating force. The total force on V is given by the surface integral of pressure over the boundary of V:

$$\mathbf{F}_{\text{int}} = -\oint p d\mathbf{A} = -\int \nabla p \, dV.$$

In the last step a well known integral theorem was used. For a Galilean invariant system, by Newton's second law the change of the fluid element's flow velocity $\mathbf{u}$ is

$$\rho_m \frac{\mathrm{d}\mathbf{u}}{\mathrm{d}t} = -\nabla p. \tag{2.1}$$

ρ_m is the mass density of the fluid. The derivative $\mathrm{d}\mathbf{u}(\mathbf{x})/\mathrm{d}t$ is not the acceleration of the fluid element at a certain point $\mathbf{x}$ in space, rather the fluid element travels a distance $\mathrm{d}\mathbf{x}$ during $\mathrm{d}t$. The total derivative $\mathrm{d}\mathbf{u}(\mathbf{x})/\mathrm{d}t$ is therefore the sum of the acceleration during the time $\mathrm{d}t$ at point $\mathbf{x}$ and the difference of velocities at the two points connected by $d\mathbf{x}$:

$$\frac{\mathrm{d}\mathbf{u}(\mathbf{x})}{\mathrm{d}t} = \frac{\partial \mathbf{u}(\mathbf{x})}{\partial t} + \left(\mathbf{u}(\mathbf{x}) \cdot \frac{\partial}{\partial \mathbf{x}}\right) \mathbf{u}(\mathbf{x}).$$

Inserting the above equation into (2.1) yields

$$\frac{\partial \mathbf{u}}{\partial t} + (\mathbf{u} \cdot \nabla)\,\mathbf{u} = -\frac{1}{\rho_m}\nabla p. \tag{2.2}$$

The expression (2.2) is the so called Euler equation. To derive it, translational invariance and momentum conservation were implicitely assumed. The Euler equation governs the dynamics of an ideal fluid. To describe a real fluid, viscous forces have to be added to Eq. (2.2). For what follows, it is convenient to recast the Euler equation to the form

$$\frac{\partial}{\partial t}(\rho_m u_\alpha) = -\partial_\beta \Pi_{\alpha\beta}. \tag{2.3}$$

Here, $\Pi_{\alpha\beta} = p\delta_{\alpha\beta} + \rho_m u_\alpha u_\beta$ is the momentum current tensor. Obviously, (2.3) is a continuity equation for the momentum density $\rho_m u_\alpha$, which also establishes the interpratation of $\Pi_{\alpha\beta}$ as the momentum current tensor. It is clear from everyday experience that viscous forces transport momentum from the fast moving parts of the fluid to the slower moving parts. The viscous terms should therefore appear in the momentum current tensor. Furthermore, viscous forces act only when there are gradients in the flow velocity; the viscous terms must be poportional to terms $\partial_\alpha u_\beta$. There are no viscous forces acting in a unifromily rotating fluid, where the flow velocity can be written as $u_\alpha = \varepsilon_{\alpha\beta\gamma}\Omega_\beta x_\gamma$. Here Ω_β is the rotation axis. It is clear, that this condition is satisfield, if only the symmetric combinations $\partial_\alpha u_\beta + \partial_\beta u_\alpha$ and $\delta_{\alpha\beta}\partial_\gamma u_\gamma$ enter the viscous terms. Let $\tau'_{\alpha\beta}$ be the viscous contribution to $\Pi_{\alpha\beta}$. In two dimesions, the most general $\tau'_{\alpha\beta}$ satisfying the above conditions is

$$\tau'_{\alpha\beta} = \eta\left(\partial_\alpha u_\beta + \partial_\beta u_\alpha - \delta_{\alpha\beta}\partial_\gamma u_\gamma\right) + \zeta\delta_{\alpha\beta}\partial_\gamma u_\gamma. \tag{2.4}$$

η and ζ are the so calles shear and bulk viscosities. The two terms in Eq. (2.4) are constructed such that the first one is traceless. The equation of motion of the viscous fluid now reads

$$\frac{\partial}{\partial t}\left(\rho_m u_\alpha\right) = -\partial_\beta\left(p\delta_{\alpha\beta} + \rho_m u_\alpha u_\beta + \tau'_{\alpha\beta}\right).$$

This is the Navier-Stokes equation. Usually, it can be assumed that the spatial dependencies of η, ζ are small and these quantities can be interchanged with the derivative ∂_β. The Navier-Stokes equation then can be written in its conventional form:

$$\rho_m\left(\frac{\partial \mathbf{u}}{\partial t} + \left(\mathbf{u}\cdot\nabla\right)\mathbf{u}\right) = -\nabla p + \eta\Delta\mathbf{u} + \left(\zeta + \frac{\eta}{3}\right)\nabla\left(\nabla\cdot\mathbf{u}\right). \tag{2.5}$$

If the fluid is incompressible, i.e. $\nabla\cdot\mathbf{u} = 0$ holds, the last term in Eq. (2.5) can be dopped, and the Navier-Stokes equation reads

$$\frac{\partial \mathbf{u}}{\partial t} + \left(\mathbf{u}\cdot\nabla\right)\mathbf{u} = -\frac{1}{\rho_m}\nabla p + \frac{\eta}{\rho_m}\Delta\mathbf{u}. \tag{2.6}$$

No microscopic details were assumed in this derivation. It is mainly based on the conservation of momentum and general symmetry considerations. Even in the context of strongly coupled materials, this equations provide an adequate description of the behavior of the electronic fluid [34].

2.1.2 Stokes flow

The Navier-Stokes equation of an incompressible liquid, Eq. (2.6), is nonlinear due to the second left hand side term. This term was found from kinematic considerations. Speaking in terms of the free / interacting dichotomy, it appears due to the free particle dynamics of the fluid. It is particularely important for nearly ideal fluids, in which inter-particle collisions are not too important. On the other hand, the viscosity η is a measure for the particle's interaction strength. For strongly interacting systems the last right hand side terms dominates the dynamics of the fluid. If the nonlinear term can be neglected, the equation is significantly simplified. These considerations are quantified by the Raynolds number

$$R = \frac{\rho_m l_{\text{geo}} u}{\eta}.$$

This number can be thought of as the ratio between the terms $\left(\mathbf{u}\cdot\nabla\right)\mathbf{u}$ and $\eta/\rho_m\Delta\mathbf{u}$. The characteristic length scale of the studied geometry l_{geo} enters through the spatial derivativs. Sometimes the quantity

$$\nu = \eta/\rho_m$$

is referred to as kinetmatic viscosity. It is this quantity, rather than η, that is associated with the common sense notion of viscosity is fluids like water and honey. For $R \gg 1$, the full nonlinear dynamics of the fluid has to be considered. Turbulence occurs in this regime. On the other hand, for $R \ll 1$, the nonlinear term can be dropped. This limit is called *Stokes flow*. In the steady state, the linearized Navier-Stokes equation then reads

$$\eta\Delta\mathbf{u} = \nabla p. \tag{2.7}$$

$R \ll 1$	Stokes flow: low velocity, creeping flow
$R \gg 1$	Nonlinear regime, turbulence

Table 2.1: Regimes of fluid flow at different Raynolds numbers R.

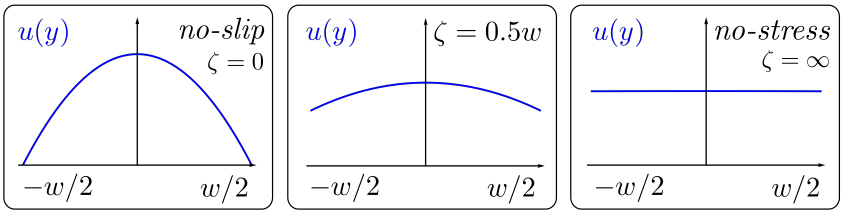

Figure 2.1: Two dimensional Poiseuille flow for different boundary conditions in a channel of width w. The flow velocity is shown as a blue curve. In each of the three pictures, the same current I_0 passes through the sample.

2.1.3 Poiseuille flow, boundary conditions and Gurzhi scaling.

The Poiseuille flow is a paradigmatic example of a hydrodynamic flow, where the fluid is confined to an infinitely long channel (a pipe in 3D or a strip in 2D) of width w. It governs fluid behavior from pipe flows to blood vessels. It is also an ideal example to illustrate the importance of boundary conditions in hydrodynamic flow (see Fig. 2.1). For Poiseuille flow, the Stokes equation (2.7) reduces to an ordinary second order differential equation. If we assume that the channel is oriented parallel to the x-axis, the equation reads

$$\eta \frac{\partial^2 u}{\partial y^2} = \frac{\partial p}{\partial x}. \tag{2.8}$$

The gradient of the pressure is assumed to be constant along the x and y axes. This equation can be easily integrated, after the appropriate boundary conditions at $y = \pm w$ have been applied. The boundary conditions for viscous electron flows were one of the publications on which this theses is based [84] and were shown to be of the form

$$u_\alpha^t\Big|_S = \zeta\, n_\beta \frac{\partial u_\alpha^t}{\partial x_\beta}\Big|_S, \tag{2.9}$$

Where n_β is the normal vector of the sample boundary and u_α^t is the tangential flow velocity of the fluid at the boundary. The velocity component orthogonal to the boundary has to vanish for obvious reasons. ζ is the so called slip length. It quantifies how strongly the fluid sticks to the boundaries. In most classical liquids $\zeta = 0$ and there is no slip: $u_\alpha^t\Big|_S = 0$. However, the slip length is relevant for quantum fluids. In certain extreme cases, even the no-stress conditions $\zeta \to \infty$ can be realized [84].

Solving Eq. (2.8) with the general boundary conditions (2.9) gives.

$$u_x = \frac{1}{8\eta}\left(w^2 + 4\zeta w - 4y^2\right)\frac{\partial p}{\partial x}. \tag{2.10}$$

For $\zeta = 0$ the characteristic classical parabolic Poiseuille profile appears; for $\zeta \to \infty$ the profile becomes flat (see Fig. 2.1).

The shape of the profile is a benchmark of hydrodynamic behavior that is used in experimental studies [30]. It is also connected to the Gurzhi effect, which predicts the hydrodynamic electron current to scale as w^{d+1} in d dimensions:

$$I \propto w^{d+1}.$$

Integrating the flow velocity (2.10) over y to obtain the total current yields

$$I \propto \frac{1}{2\eta}\left(\frac{w^3}{6}+\zeta w^2\right)\frac{\partial p}{\partial x}. \tag{2.11}$$

The Gurzi effect is most pronounced at $\zeta \to 0$. Finding the correct slip length is crucial to most experiments in electron-hydrodynamics and is the subject of chapter 4.

2.2 Quasiparticle picture of electron hydrodynamics.

2.2.1 The kinetic equation

Alternatively to the macroscopic derivation of section 2.1, the hydrodynamic equations can be derived from the kinetic equation. This equation appropriately describes the behavior of a many body systems, if the system consists of sharply defined quasiparticles. Such systems are e.g. the Fermi liquid [13], the superfluid-insulator quantum critical point [53], or the Dirac liquid [49]. The structure of the kinetic equation is very similar to the Boltzmann equation known from statistical physics. In Sec. 2.4 the quantum Boltzmann equation (QBE) will be derived from field theoretical considerations. However, to obtain a general picture the details are unimportant. In the quantum version of the Boltzmann equation, the notion of the particle velocity is slightly generalized to the group velocity of quasiparticles $\mathbf{v}_\mathbf{k} = \partial\varepsilon_\mathbf{k}/\partial\mathbf{k}$, where $\varepsilon_\mathbf{k}$ is the quasiparticle dispersion. The equation reads

$$\left(\partial_t + \mathbf{v}_\mathbf{k}\cdot\nabla_\mathbf{x} + \mathbf{F}\left(\mathbf{x},t\right)\cdot\nabla_\mathbf{k}\right) f_\mathbf{k}\left(\mathbf{x},t\right) \;=\; \mathcal{C}f, \tag{2.12}$$

where $\mathcal{C}$ is the collision operator and $\mathbf{F}\left(\mathbf{x},t\right)$ a force term that can depend on coorinates and time. For electrons the collision term in many cases assumes the form

$$\mathcal{C}f_\mathbf{k} = -\prod_{i=2}^{4}\int\frac{d^dk_i}{(2\pi)^d}W\left(\mathbf{k},\mathbf{k}_2;\mathbf{k}_3,\mathbf{k}_4\right)\left[f_\mathbf{k}f_{\mathbf{k}_2}\left(1-f_{\mathbf{k}_3}\right)\left(1-f_{\mathbf{k}_4}\right)-\left(1-f_\mathbf{k}\right)\left(1-f_{\mathbf{k}_2}\right)f_{\mathbf{k}_3}f_{\mathbf{k}_4}\right], \tag{2.13}$$

where the function $W\left(\mathbf{k},\mathbf{k}_2;\mathbf{k}_3,\mathbf{k}_4\right)$ is essentially given by the modulus squared of the corresponding matrix elements of the interaction potential. Eq. (2.12) is a complicated non-linear equation. The distribution function $f_\mathbf{k}\left(\mathbf{x},t\right)$ gives density of particles in a certain region of phase space at a time t. Physical quantities of interest are found by averaging over $f_\mathbf{k}\left(\mathbf{x},t\right)$, for which it is useful to use the notation $\langle ...\rangle = \int(...)\,f_\mathbf{k}d^dk/\left(2\pi\right)^d$. The particle density ρ, particle current $\mathbf{j}$ and momentum current tensor Π are given by

$$\begin{aligned}\rho\left(\mathbf{x},t\right) &= \langle 1\rangle,\\ j_\alpha\left(\mathbf{x},t\right) &= \left\langle v_{\mathbf{k},\alpha}\right\rangle,\\ \Pi_{\alpha\beta}\left(\mathbf{x},t\right) &= \left\langle v_{\mathbf{k},\alpha}k_\beta\right\rangle.\end{aligned} \tag{2.14}$$

Often additional quantum numbers corresponding to spin or band indeces appear in the kinetic equation. The averages are then extended over these numbers. Later on, the band index $\lambda = \pm 1$ labelling the upper and lower Dirac cones will be important. The Boltzmann equation immediately leads to continuity equations for conserved quantities. Integrating (2.12) over k in the absence of a field $\mathbf{F}\left(\mathbf{x},t\right)$:

$$\partial_t \rho + \nabla_{\mathbf{x}} \mathbf{j} = 0.$$

The conservation of the particle density is expressed through $\int \left(Cf\right) d^d k / \left(2\pi\right)^d = 0$, which is clear from the form of the collision operator (2.13). Finally, multiplying the Boltzmann equation by $\mathbf{k}$ and integrating over $\mathbf{k}$ leads to the continuity equation for the momentum density $\rho_{\mathbf{k},\alpha} = \left\langle \mathbf{k} \right\rangle$ (2.3):

$$\frac{\partial}{\partial t} \rho_{\mathbf{k},\alpha} = -\partial_\beta \Pi_{\alpha\beta}.$$

2.2.2 The Chapman-Enskog method

One way to attack the equation (2.12), is the Chapman-Enskog method [85], where the Boltzmann equation is expanded in terms of the Knudsen number K_n. Roughly speaking K_n is the fraction of the right and left hand side of Eq. (2.12). It is typically expressed in terms of the electron-electron mean free path l_{ee} and the geometrical lengths scale l_{geo}, which is either the scale on which the force $\mathbf{F}\left(\mathbf{x},t\right)$ varies, or the scale of the geometrical confinement due to a given sample size. The Knudsen number then is

$$K_n = \frac{l_{ee}}{l_{\text{geo}}}.$$

The Knudsen number does not appear in the kinetic equation expicitely. It is convenient to introduce the small, dimensionless number ε and write

$$\left(\partial_t + \mathbf{v}_{\mathbf{k}} \cdot \nabla_{\mathbf{x}} + \mathbf{F}\left(\mathbf{x},t\right) \cdot \nabla_{\mathbf{k}}\right) f_{\mathbf{k}}\left(\mathbf{x},t\right) = \frac{1}{\varepsilon} \mathcal{C} f,$$

this expression can be though of as a properly rescaled kinetic equation, where the length units are chosen such that $1/\varepsilon$ appears on the right hand side. Intoducing ε and expanding $f_{\mathbf{k}}\left(\mathbf{x},t\right)$ in powers of ε, then setting $\varepsilon \to 1$ helps to avoid the explicit rescaling of Eq. (2.12). The distribution function then reads

$$f_{\mathbf{k}}\left(\mathbf{x},t\right) = \sum_{i=1}^{\infty} \varepsilon^i f_{\mathbf{k}}^{(i)}\left(\mathbf{x},t\right).$$

To lowest order in ε the expansion yields

$$0 = \mathcal{C} f_{\mathbf{k}}^{(0)}. \tag{2.15}$$

This equation corresponds to the situation where no forces act on the system and the particles are not geometrically confined. It is solved by the *local equilibrium* distribution function. For a system in which particle number and momentum are conserved the local equilibrium distribution function reads

$$f_{\mathbf{k}}^{(0)} = \frac{1}{e^{\beta\left(\varepsilon_{\mathbf{k}} - \mu - \mathbf{u}\left(\mathbf{x},t\right)\cdot\mathbf{k}\right)} + 1}. \tag{2.16}$$

This is simply a general function solving Eq. (2.15), but suggestive symbols are chosen for the quantities μ and $\mathbf{u}$ because they correspond to the chemical potential and the flow velocity. For example in the

case $\varepsilon_{\mathbf{k}} = k^2/2m$, the particle current calculated from Eq. (2.14) is $\mathbf{j} = \rho\mathbf{u}$. Here $\mathbf{u}$ is identical with the flow velocity of the preceeding section.

The approximation (2.16) is sufficient to derive the Euler equation in the form (2.2). To this end $f^{(0)}_{\mathbf{k}}$ is inserted into the Boltzmann equation. Multiplying the Boltzmann equation by $\mathbf{k}$ and averaging over momentum in the absence of external forces ($\mathbf{F}\left(\mathbf{x},t\right)=0$) gives

$$\partial_t \left\langle k_\alpha \right\rangle_0 = \frac{1}{m}\nabla_{\mathbf{x},\beta}\left\langle k_\alpha k_\beta \right\rangle_0, \tag{2.17}$$

if the system is Galilean invariant and therefore the is dispersion $\varepsilon_{\mathbf{k}} = k^2/2m$. $\langle ... \rangle_0$ stands for averaging over $f^{(0)}_{\mathbf{k}}$. The right hand sight can be written as

$$\left\langle k_\alpha k_\beta \right\rangle_0 = \left\langle \left(k_\alpha - u_\alpha\right)\left(k_\beta - u_\beta\right)\right\rangle_0 + \left\langle k_\alpha u_\beta \right\rangle_0 + \left\langle u_\alpha k_\beta \right\rangle_0 - \left\langle u_\alpha u_\beta \right\rangle_0 .$$

Using $\left\langle k_\alpha \right\rangle_0 = m\rho u_\alpha$, which is easily proved by performing a coordinate shift $\mathbf{k} \to \mathbf{k} + m\mathbf{u}$ in the averaging integral, the above expression becomes

$$\left\langle k_\alpha k_\beta \right\rangle_0 = \left\langle \left(k_\alpha - u_\alpha\right)\left(k_\beta - u_\beta\right)\right\rangle_0 + \rho u_\alpha u_\beta .$$

Performing a coordinate shift $\mathbf{k} \to \mathbf{k} + m\mathbf{u}$, it is also easy to see that the first term is proportional to $\delta_{\alpha\beta}$. In fact this term is the pressure tensor $P\delta_{\alpha\beta}$. The zeroth order momentum current tensor is then given by

$$\Pi^{(0)}_{\alpha\beta} = u_\beta \nabla_{\mathbf{x},\beta} u_\alpha + P\delta_{\alpha\beta}. \tag{2.18}$$

Inserting these results into Eq. (2.17) finally yields the Euler equation (compare to (2.2))

$$\partial_t u_\alpha + u_\beta \nabla_{\mathbf{x},\beta} u_\alpha = \frac{1}{m\rho}\nabla_{\mathbf{x},\alpha} P.$$

The next iteration of the Chapman-Enskog procedure gives corrections due to geometrical constraints or external forces. To first order in ε the kinetic equation reads

$$\left(\partial_t + \mathbf{v}_{\mathbf{k}} \cdot \nabla_{\mathbf{x}} + \mathbf{F}\left(\mathbf{x},t\right)\cdot\nabla_{\mathbf{k}}\right) f^{(0)}_{\mathbf{k}}\left(\mathbf{x},t\right) = \mathcal{C}^{(1)} f^{(1)}. \tag{2.19}$$

The operator $\mathcal{C}^1$ is the collision operator linearized in ε, which is a good approximation if the deviations from local equilibrium are small. It is given by

$$\mathcal{C}^{(1)} f^{(1)} = -\prod_{i=2}^{4} \int \frac{d^d k_i}{(2\pi)^d} \tilde{W}\left(\mathbf{k},\mathbf{k}_2;\mathbf{k}_3,\mathbf{k}_4\right)\left(\psi_{\mathbf{k}} + \psi_{\mathbf{k}_1} - \psi_{\mathbf{k}_2} - \psi_{\mathbf{k}_3}\right).$$

Here $\psi_{\mathbf{k}}$ is defined via $f^{(1)} = f^{(0)}_{\mathbf{k}}\left(1 - f^{(0)}_{\mathbf{k}}\right)\psi_{\mathbf{k}}$, with $f^{(0)}_{\mathbf{k}}$ taken at $\mathbf{u}=0$, and $\tilde{W}$ is given by the function W of Eq. (2.13) multiplied by the factor $f^{(0)}_{\mathbf{k}} f^{(0)}_{\mathbf{k}_2}\left(1 - f^{(0)}_{\mathbf{k}_3}\right)\left(1 - f^{(0)}_{\mathbf{k}_4}\right)$ (see Ref. [15] for the details of this calculation). The linearized collision operator for the electrons of a Dirac liquid will have a similar form (see Eq. (5.10)). The left hand side of Eq. (2.19) is known and $\mathcal{C}^{(1)}$ has to be

inverted to find $f_{\mathbf{k}}^{(1)}$. The result will be of first order in the field $\mathbf{F}\left(\mathbf{x},t\right)$, i.e. valid in the regime of linear response. The viscous contribution to the momentum current tensor can be calculated setting $\mathbf{F}\left(\mathbf{x},t\right)=0$. In the static case in 2D, the left fand side of (2.19) can be written as

$$\mathbf{v}_{\mathbf{k}}\cdot\nabla_{\mathbf{x}}f_{\mathbf{k}}^{(0)}\left(\mathbf{x},t\right)=\varepsilon_{\mathbf{k}}I_{\alpha\beta}K_{\alpha\beta}f_{\mathbf{k}}^{(0)}\left(1-f_{\mathbf{k}}^{(0)}\right),$$

with the tensors

$$\begin{aligned}I_{\alpha\beta} &= \left(\frac{k_\alpha k_\beta}{k^2}-\frac{1}{2}\delta_{\alpha\beta}\right)\\ K_{\alpha\beta} &= \left(\partial_\alpha u_\beta+\partial_\beta u_\alpha-\delta_{\alpha\beta}\partial_\gamma u_\gamma\right).\end{aligned}$$

Inverting (2.19) yields the function $f^{(1)}$. To linear order in $\mathbf{u}$, the viscous contribution to $\Pi_{\alpha\beta}$ is then

$$\begin{aligned}\Pi_{\alpha\beta}^{(1)} &= \int\frac{d^2k}{\left(2\pi\right)^2}v_{\mathbf{k},\alpha}k_\beta f^{(1)}\\ &= \eta\left(\partial_\alpha u_\beta+\partial_\beta u_\alpha-\delta_{\alpha\beta}\partial_\gamma u_\gamma\right).\end{aligned}$$

This determines the viscosity η.

2.2.3 Relaxation time and BGK approximations

A simple model for the collision operator is the relaxation time approximation. In its simplest form, this approximation reads

$$\mathcal{C}f=-\frac{f-f^{(0)}\Big|_{\mathbf{u}=0}}{\tau}.$$

Writing such a term in the Boltzmann equations means, that any initial non-equilibrium state $f(t_0)$ will exponentially decay to the equilibrium distribution funtion $f^{(0)}\Big|_{\mathbf{u}=0}$, or, if continuously driven by a field, the system will enter a steady state. The flow velocity $\mathbf{u}$ is purposefully set to zero. Thus the equilibrium state to which the system evolves at $t\to\infty$ does not allow for a finite current. This is appropriate if a system is disordered and momentum is not conserved.

It is possible to incorporate momentum conservation into the relaxation time approximation by allowing a non-vanishing $\mathbf{u}\neq 0$ in $f^{(0)}$:

$$\mathcal{C}f=-\frac{f-f^{(0)}\Big|_{\mathbf{u}\neq 0}}{\tau}. \tag{2.20}$$

The flow velocity itself (for $\varepsilon_{\mathbf{k}}=k^2/2m$) is defined as

$$\mathbf{u}=\frac{1}{\rho m}\left\langle\mathbf{k}\right\rangle$$

The state to which the system relaxes then carries a finite momentum, which has to be determined self-consistently. This usually leads to integral equations for $\mathbf{u}$ that can be complicated in finite geometries

[19, 86, 87]. The collision operator (2.20) is commonly referred to as Bhatnagar-Gross-Krook (BGK) operator. It was proposed by the three authors in Ref [88]. It is easily seen that the BGK collision operator conserves momentum:

$$\begin{aligned}\int \frac{d^dk}{(2\pi)^d}\mathbf{k}\left[\mathcal{C}f\right]_{\mathbf{k}} &= -\frac{1}{\tau}\int \frac{d^dk}{(2\pi)^d}\mathbf{k}\left[f_{\mathbf{k}} - \left(e^{\beta\left(\varepsilon_{\mathbf{k}}-\mathbf{u}\cdot\mathbf{k}\right)}+1\right)^{-1}\right] \\ &= -\frac{1}{\tau}\left[\rho m\mathbf{u} - \int \frac{d^dk}{(2\pi)^d}\mathbf{k}\left(e^{\beta\left(\varepsilon_{\mathbf{k}}-\mathbf{u}\cdot\mathbf{k}\right)}+1\right)^{-1}\right] \\ &= -\frac{1}{\tau}\left[\rho m\mathbf{u} - \rho m\mathbf{u}\right] \\ &= 0.\end{aligned}$$

In the second to last step $\langle k_\alpha \rangle_0 = m\rho u_\alpha$ was used (see Sec. 2.2). The BGK approximation provides a simple but efficient approximation for the collision operator, in situations where momentum conservation is crucial, but the particularities of the relaxation process are not of great importance [19, 86, 87]. It is also the foundation of the celebrated lattice Boltzmann method [89].

2.3 Basic transport theory

2.3.1 Transport coefficients

Chapter 5 of this thesis will be devoted to the non-local transport coefficients of a Dirac liquid. Therefore, in this section, some basics of transport theory shall be reviewed. Transport coefficients such as thermal and electrical conductivity and viscosity quantify the response of a system to applied forces and are defined via constitutive relations of the form

$$\mathcal{J} = \nu\mathcal{F}, \tag{2.21}$$

where $\mathcal{J}$ is a current sourced by the field $\mathcal{F}$ and ν is the corresponding transport coefficient. The relation (2.21) is linear in the field $\mathcal{F}$. Typically, this is only an approximation for small $\mathcal{F}$. The corresponding regime is called the regime of linear response. In this thesis, among other topics, the transport properties of graphene will be studied in linear response. If the field $\mathcal{F}$ is spatially inhomogeneous Eq. (2.21) has to be generalized to a non-local constitutive relation. This case is treated in the following section.

For an electric field, the constitutive relation (2.21) reads

$$\mathbf{j} = \sigma\mathbf{E}.$$

Here, $\mathbf{j}$ is the electric current, $\mathbf{E}$ is the electric field and σ is the electric conductivity. In general, σ is a second rank tensor. However, if the system of interest is isotropic and homogeneous, σ reduces to a number. The most important facts about the electrical conductivity can be derived from the simple Drude-Sommerfeld model [8]. Electrons are assumed to scatter off crystal impurities. The average time that passes between two scattering events is the mean free time τ. In theses collisions the electrons loose all memory of their state prior to the collision. For an oscillating electric field of the form $E = E_0 e^{-i\omega t}$, the Drude expression for σ reads

$$\sigma = \frac{e^2\tau\rho}{m}\left(\frac{1}{1-i\omega\tau}\right) \tag{2.22}$$

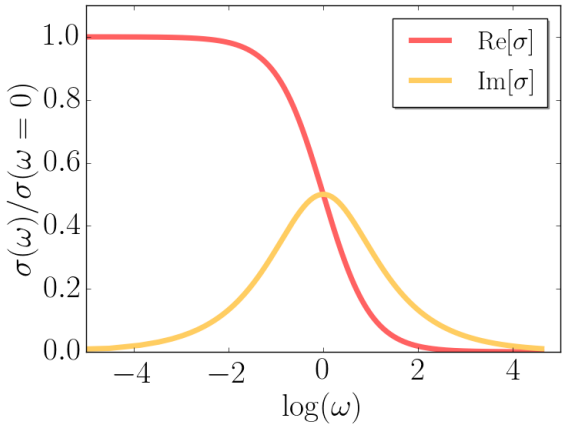

Figure 2.2: Real and imaginary part of the Drude conductivity 2.22.

m is the electron mass and ρ the density of conduction electrons. Other transport coefficients have a very similar ω, τ dependence. The imaginary part describes the phase shift of the current with respect to the applied field. $\mathrm{Im}\,(\sigma)$ is peaked around $\omega \sim 1/\tau$. The real part of the conductivity describes resistive losses in the material. For $\omega \to \infty$, the conductivity vanishes, i.e. the tranport becomes more and more lossy (see Fig. 2.2).

2.3.2 Non-local transport

If the external force depends on the spatial coordinate $\mathbf{r}$, or one is interested in transport in a finite geometry, the constitutive relation (2.21) has to be generalized to its non-local form

$$\mathcal{J}\left(\mathbf{r},\omega\right) = \int d^d r' \, \nu\left(\mathbf{r}-\mathbf{r}',\omega\right) \mathcal{F}\left(\mathbf{r}',\omega\right). \tag{2.23}$$

Again $\mathcal{J}\left(\mathbf{r},\omega\right)$ is a current sourced by the external field $\mathcal{F}\left(\mathbf{r},\omega\right)$ and $\nu\left(\mathbf{r}-\mathbf{r}',\omega\right)$ is a spatially dependent transport coefficient. Being a convolution, the relation (2.23) assumes a much simpler form once it is Fourier transformed:

$$\mathcal{J}\left(\mathbf{q},\omega\right) = \nu\left(\mathbf{q},\omega\right) \mathcal{F}\left(\mathbf{q},\omega\right). \tag{2.24}$$

At this point, some heuristic considerations are helpful. Imagine a crystal with impurities spaced at an average distance l_{mf} - the mean free path. The wave number dependent transport coefficient $\nu\left(\mathbf{q},\omega\right)$ will vary on scales corresponding to the inverse mean free path $q_{\mathrm{mf}} \approx 2\pi/l_{\mathrm{mf}}$. Typically $\nu\left(\mathbf{q},\omega\right)$ will be peaked around $\mathbf{q}=0$ and its width will be of the order of q_{mf}. On the other hand, the scale of relevant wave vectors will be set by the spatial dependence of the external field, or the geometry of the sample - l_{geo}. If $l_{\mathrm{geo}} \gg l_{\mathrm{mf}}$, the approximation $\nu\left(\mathbf{q}_{\mathrm{geo}}\right) \approx \nu\left(\mathbf{q}=0\right)$ can be made. Then it is $\nu\left(\mathbf{r}-\mathbf{r}'\right) \approx \nu\left(\mathbf{q}=0\right)\delta\left(\mathbf{r}-\mathbf{r}'\right)$, and the constitutive relation (2.23) reduces to its local form (2.21): $\mathcal{J}\left(\mathbf{r}\right) = \nu\mathcal{F}\left(\mathbf{r}\right)$. The non-locality of Eq. (2.23) matters if $l_{\mathrm{geo}} \lesssim l_{\mathrm{mf}}$. On scales comparable to the mean free path, transport is intrisically non-local, because particles loose their memory of previous events through collisions with other particles or impurities - a mechanism that ceases to be efficient. This is illustrated in Fig. 2.3 .

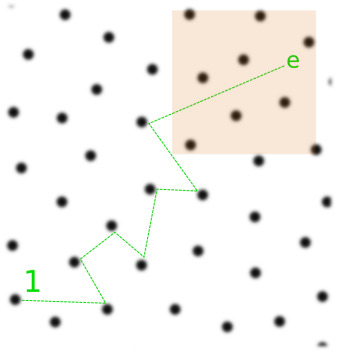

Figure 2.3: Having started at the point marked 1, the electron looses the memory of its initial state at large scales through many scatterings. On scales comparable to the mean free path, e.g. if the electron is confined to the orange rectangle, the electron retains some memory of its earlier states and the transport is non-local. To obtain the current at a given point of the orange rectangle, an average over the whole rectangle has to be performed. This results in formula (2.23).

Further conclusions about the non-local transport coefficients can be drawn from symmetry considerations. The electrical conductivity will be used as an example. In an isotropic system, a reference direction for the non-local conductivity is set by the wavevector $\mathbf{q}$. Thus, the response of the system can be different depending on whether the electric field is parallel or orthogonal to $\mathbf{q}$, i.e. longitudinal or transverse. The projectors on longitudinal and transverse directions are given by

$$\begin{aligned} P_{\parallel,\alpha\beta} &= \frac{q_\alpha q_\beta}{q^2} \\ P_{\perp,\alpha\beta} &= \delta_{\alpha\beta} - P_{\parallel,\alpha\beta}. \end{aligned}$$

The current response ot longitudinal and transverse field must be given by two distinct conductivities. These conductivities are called longitudinal and transverse conductivities. The conductivity tensor can be written as

$$\sigma_{\alpha\beta}\left(\mathbf{q},\omega\right) = \sigma_{\parallel}\left(q,\omega\right)\frac{q_\alpha q_\beta}{q^2} + \sigma_{\perp}\left(q,\omega\right)P_{\perp,\alpha\beta}. \tag{2.25}$$

This expression is constructed such that the longitudinal and transverse components of the electric field are projected out, assigned their corresponding conductivities, and added to give the total current. Here, q is the modulus of $\mathbf{q}$.

In the Kubo formalism (see Ref. [81]), the conductivity can be related to the current-current correlation function $\chi_{J_\alpha J_\beta}\left(\mathbf{q},\omega\right)$:

$$\chi_{J_\alpha J_\beta}\left(\mathbf{q},\omega\right) = -i\omega\sigma_{\alpha\beta}\left(\mathbf{q},\omega\right). \tag{2.26}$$

$\chi_{J_\alpha J_\beta}\left(\mathbf{q},\omega\right)$ in its turn can be related to the charge density-density correlation function with the help of the continuity equation:

$$\chi_{\rho\rho}\left(q,\omega\right) = \frac{q_\alpha q_\beta}{\omega^2}\chi_{J_\alpha J_\beta}\left(\mathbf{q},\omega\right).$$

In follows

$$i\omega\chi_{\rho\rho}\left(q,\omega\right) = q^2\sigma_{\parallel}\left(q,\omega\right).$$

This result implies

$$\sigma_{\parallel}\left(q\neq 0,\omega=0\right) = 0.$$

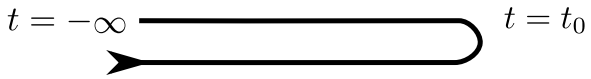

Figure 2.4: The Keldysh contour.

In fact, the violation of this identity would lead to an infinite accumulation of charge at certain points and thus is forbidden by charge conservation.

2.4 Quantum Boltzmann equation

The description of nonlocal transport presented in this thesis relies upon the quantum Boltzmann (quantum kinetic) equation developed in the Refs. [49, 51]. A brief introduction to the quantum Boltzmann formalism is therefore in order. The approach here, as in [49, 51], is based on the simple and efficient equation of motion technique of Refs. [90, 91]. The quantum Boltzmann equation can also be derived within the Keldysh functional integral technique; the interested reader is referred to [92]. The quantum Boltzmann equation derived in this chapter will be related to the kinetic equation of graphene electrons in chapter 5.

2.4.1 Green's functions on the Keldysh contour

Dealing with equilibrium problems in quantum many body physics, it is usually assumed that at $t = -\infty$ the system is in the ground state of the non-interacting problem, then interactions are switched on adiabatically and at $t = \infty$ again turned off. The Green's function is then defined as

$$G\left(t - t', \mathbf{x} - \mathbf{x}'\right) = -i \frac{\left\langle \mathcal{T} \psi_I\left(t, \mathbf{x}\right) \psi_I^\dagger\left(t', \mathbf{x}'\right) S\left(-\infty, \infty\right) \right\rangle}{\left\langle S\left(-\infty, \infty\right) \right\rangle}.$$

λ is a set of quantum numbers, $\psi_I^\dagger\left(t, \mathbf{x}\right)$, $\psi_I\left(t, \mathbf{x}\right)$ are the field operators in the interaction representation. The S matrix, which encorporates all interaction effects, reads

$$S\left(-\infty, \infty\right) = \mathcal{T} \exp\left(-i \int_{-\infty}^{\infty} dt\, H_{\text{int}}\left(t\right)\right)$$

$\mathcal{T}$ is the time ordering operator (see [91], chapter 2 for details). The notion that the system returns to the non-interacting ground state is problematic in the context of non-equilibrium systems, where, roughly speaking, energy and momentum are generated in the system. An alternative is provided by the Keldish contour $\mathcal{C}_K$, where time evolves along a curve starting at $t = -\infty$ running to $t = t_0$ (forward branch) and returning back to $t = -\infty$ (backward branch) (see Fig.). In this way one avoids specifying the state at $t = \infty$ is avoided. The limit $t_0 \to \infty$ is then taken. The S matrix on the Keldysh contour is defined as

$$S = \mathcal{T} \exp\left(-i \int_{\mathcal{C}_K} dt\, H_{\text{int}}\left(t\right)\right),$$

where the time ordering operator $\mathcal{T}$ orders along the Keldysh contour. This calls for a variety of Green's functions, e.g. time ordered Green's functions and anti-time ordered Green's functions (corresponding

to the action of $\mathcal{T}$ on the backwards branch of $\mathcal{C}_K$). Again, the reader is referred to Ref. [91], chapter 2. The most important Green's functions here are

$$\begin{aligned} G^{<}\left(x_1,x_2\right) &= i\left\langle \psi^{\dagger}\left(x_2\right)\psi\left(x_1\right)\right\rangle \\ G^{>}\left(x_1,x_2\right) &= -i\left\langle \psi\left(x_1\right)\psi^{\dagger}\left(x_2\right)\right\rangle \\ G_t\left(x_1,x_2\right) &= \theta\left(t_1-t_2\right)G^{>}\left(x_1,x_2\right)+\theta\left(t_2-t_1\right)G^{<}\left(x_1,x_2\right) \\ G_{\bar{t}}\left(x_1,x_2\right) &= \theta\left(t_1-t_2\right)G^{<}\left(x_1,x_2\right)+\theta\left(t_2-t_1\right)G^{>}\left(x_1,x_2\right) \end{aligned}$$

$\psi_{\lambda}^{\dagger}\left(x\right)$, $\psi_{\lambda}\left(x\right)$ are field operators in the Heisenberg representation. The variable x stands for the coordinate in space and time $\left(t,\mathbf{x}\right)$. For $G^{<}$ the time t_1 is on the forward branch on $\mathcal{C}_K$, while t_2 is on the backward branch. For $G^{>}$ the time t_2 is on the forward branch on $\mathcal{C}_K$, while t_1 is on the backward branch. For the time ordered Green's function $G_t\left(x_1,x_2\right)$ both times are on the forward branch, while for the anti-time-ordered $G_{\bar{t}}\left(x_1,x_2\right)$ both timer are on the backward branch.

2.4.2 Quantum Boltzmann equation

The equations of motion for $G^{\gtrless}$ will ultimatively lead to the Quantum Boltzmann equation. It is convenient to introduce the matrix notation

$$\begin{aligned} \tilde{G} &= \begin{bmatrix} G_t & -G^{<} \\ G^{>} & -G_{\bar{t}} \end{bmatrix} \\ \tilde{\Sigma} &= \begin{bmatrix} \Sigma_t & -\Sigma^{<} \\ \Sigma^{>} & -\Sigma_{\bar{t}} \end{bmatrix}, \end{aligned}$$

where $\tilde{\Sigma}$ is the self energy defined through the Dyson equation

$$\tilde{G}\left(x_1,x_2\right)=\tilde{G}_0\left(x_1-x_2\right)+\int d^dx_3\int d^dx_4\tilde{G}_0\left(x_1-x_3\right)\tilde{\Sigma}\left(x_{3,}x_4\right)\tilde{G}\left(x_4,x_2\right). \tag{2.27}$$

Using the Dyson equation (2.27) and an alternative form, there in the right hand side integral $\tilde{G}_0$ and $\tilde{G}$ shift places and arguments, one can derive two equations of motion for $\tilde{G}$:

$$\begin{aligned} \left(i\frac{\partial}{\partial t_1}-H_0\left(\mathbf{x}_1\right)\right)\tilde{G}\left(x_1,x_2\right) &= \mathbb{1}\delta\left(x_1-x_2\right)+\int d^dx_3\tilde{\Sigma}\left(x_1,x_3\right)\tilde{G}\left(x_3,x_2\right) \\ \tilde{G}\left(x_1,x_2\right)\left(i\frac{\partial}{\partial t_2}-H_0\left(\mathbf{x}_2\right)\right)^{\dagger} &= \mathbb{1}\delta\left(x_1-x_2\right)+\int d^dx_3\tilde{G}\left(x_1,x_3\right)\tilde{\Sigma}\left(x_3,x_2\right). \end{aligned} \tag{2.28}$$

Note, that the time derivative and the Hamiltonain in the second equation acts on the field operator $\psi^{\dagger}\left(x_2\right)$ from the left. The quantity of interest is $G^{<}$. It is related to the distribution function of the quantum Boltzmann equation. First center of mass and relative coordinates in space and time are introduced:

$$\begin{aligned} \mathbf{X} &= \frac{1}{2}\left(\mathbf{x}_1+\mathbf{x}_2\right) \\ T &= \frac{1}{2}\left(t_1+t_2\right) \\ \mathbf{x} &= \mathbf{x}_1-\mathbf{x}_2 \\ t &= t_1-t_2. \end{aligned} \tag{2.29}$$

Now, the Green's function $G^<$ can now be rewritten in terms of the new variables

$$G^< \left(\mathbf{X}, T; \mathbf{x}, t\right) = i \left\langle \psi_\lambda^\dagger \left(\mathbf{X} - \frac{1}{2}\mathbf{x}, T - \frac{1}{2}t\right) \psi_\lambda \left(\mathbf{X} + \frac{1}{2}\mathbf{x}, T + \frac{1}{2}t\right) \right\rangle .$$

The Fourier transform with respect to the relative coordinates

$$G^< \left(\mathbf{X}, T; \mathbf{k}, \omega\right) = \int d^d x e^{i\omega t - i\mathbf{k}\cdot\mathbf{x}} G^< \left(\mathbf{X}, T; \mathbf{x}, t\right) \tag{2.30}$$

gives the distribution function

$$2\pi\delta\left(\omega - \varepsilon_\mathbf{k}\right) f\left(\mathbf{X}, T; \mathbf{k}, \omega\right) = -iG^< \left(\mathbf{X}, T; \mathbf{k}, \omega\right). \tag{2.31}$$

This can be seen as the definition of the distribution function, which is justified by the fact that averages over $f\left(\mathbf{X}, T; \mathbf{k}, \omega\right)$ with respect to $\mathbf{k}$, ω give expectation values for densities, currents, etc. of physical quantities (see Ref. [91], chapter 3). The prefactor $2\pi\delta\left(\omega - \varepsilon_\mathbf{k}\right)$ is due to the fact, that sharp quasiparticles with a well defined dispersion were assumend. This is true because the life time of the quasiparticles is $\tau \sim 1/\left(\alpha^2 k_B T\right)$, where α is small. Thus the energy of a thermally excited quasiparticle is allways much larger than the inverse life time: $k_B T \gg 1/\tau$. A lengthy calculation beginning with subtracting the equations of motion (2.28) and performing a so called gradient expansion leads to the Quantum Boltzmann equation for $f\left(\mathbf{X}, T; \mathbf{k}, \omega\right)$. This procedure is described in chapter 9 of Ref. [90]. It is based on the observation that in thermal equilibrium, in a homogeneous system, the Green's function $G^<\left(\mathbf{k}, \omega\right)$ depends only on the $\mathbf{k}, \omega$ coordinates and has the form

$$G^<\left(\mathbf{k}, \omega\right) = i n_F\left(\omega\right) A\left(\mathbf{k}, \omega\right),$$

where $n_F\left(\omega\right) = \left(e^{\beta\omega} + 1\right)^{-1}$ is the Fermi-Dirac distribution and $A\left(\mathbf{k}, \omega\right)$ is the spectral function (see chapter 3 of Ref. [91]). For well defined quasiparticles $A\left(\mathbf{k}, \omega\right)$ is sharply peaked around $\omega \sim \varepsilon_\mathbf{k}$, where $\varepsilon_\mathbf{k}$ is the electron dispersion. The Fourier transform of the Green's function of a quasiparticle with a decay rate γ is then approximately given by

$$G^<\left(\mathbf{x}, t\right) \sim \int \frac{d^d k}{(2\pi)^d} e^{\beta\varepsilon_\mathbf{k}} e^{-i\varepsilon_\mathbf{k} t + i\mathbf{k}\cdot\mathbf{r}}.$$

Thus, in real space $G^<\left(\mathbf{x}, t\right)$ will decay on length scales of the thermal wavelength $\lambda_T \sim v\hbar\beta$, the same will be true for the decay in time. Here, v is the particles' group velocity. The precise form of the decay will depend on the dispersion relation and the dimensionality. The dependence on $\mathbf{X}$, T, induced by external perturbations, will share the spatio-temporal scales of the perturbations. If these external perturbations, that bring the system out of equilibrium, have frequencies much smaller than the thermal energy $\hbar\omega_\text{ext} \ll \beta^{-1}$ and wave-numbers much smaller that the inverse thermal wavelength $q \ll 2\pi\lambda_T^{-1}$, there will be a clear scale separation between the variables $\mathbf{X}, T$ and x, t. Roughly speaking, the gradient expansion consists of approximating $T + \frac{1}{2}t \approx T$, $\mathbf{X} + \mathbf{x} \approx \mathbf{X}$ in quantities appearing on the right hand side of the subtracted Eqs. (2.28). The resulting expression is transformed according to the Wigner transformation (2.30), giving the quantum Boltzmann equation

$$\left(\frac{\partial}{\partial T} + \mathbf{v}_\mathbf{k} \cdot \nabla_\mathbf{X} + e\mathbf{E} \cdot \nabla_\mathbf{k}\right)\left(-iG^<\right) = -\Sigma^> G^< + \Sigma^< G^>. \tag{2.32}$$

The Green's functions and self energies have arguments $\left(\mathbf{X}, T; \mathbf{k}, \omega\right)$. Eq. (2.32) is equvalent to Eqs. (9-7a) of Ref. [90] and (8.286) of Ref. [91]. Note that as will be seen in the explicit calculation for graphene in chapter 5, the self energies $\Sigma^{\gtrless}$ contain only terms of second order in the coupling constant. This corresponds to the fact that $\Sigma^{\gtrless}$ represent collisional contributions. Mathematically, this follows from the definition (2.27) when the appropriate Feynman rules for the Keldysh formalism are applied [93].

2.5 Some experimental results

As discussed in the introduction to this chapter, the hydrodynamic regime is reached when the electron-electron scattering length becomes the smallest length scale of the system: $l_{ee} \ll l_{\text{imp}}, l_{\text{geo}}, l_{\text{phonon}}$. This is only achieved in the purest materials. Recently a number of such ultra-pure materials has been developed, the most important examples being semiconductor heterostructures [19], graphene [22, 27, 30, 39, 50, 55], delafossite metals [23, 24] and the Weyl semimetal tungsten diphosphide [25].

Many experiments find fingerprints of hydrodynamic behavior in Poiseuille flow geometries. The arguably first observation of a hydrodynamic electron flow is due to Molencamp and de Jong [19] in two dimensional high mobility GaAs heterostructures and dates back to 1995. The fact that more than 30 years passed since the first theoretical works of Gurzhi [10] shows that reaching the hydrodynamical regime experimentally is a highly nontrivial task. The authors used electrostatically induced boundaries, which, together with measuring at different temperatures, allowed them to tune the ratios of l_{ee}, l_{imp} and $l_{\text{geo}} = W$, where W is the channel width. De Jong and Molenkamp were able to demonstrate the crossover between Knudsen and Gurzhi regimes (inlet of Fig. 2.5). In the Knudsen regime, where $l_{ee}/W \gg 1$, the conductivity drops when the ratio l_{ee}/W decreases. Interparticle-collisions disturb the trajectories of individual particles, so that they hit the boundaries more often. Since particles loose their momentum in boundary collisions, the conductivity dops. In the Gurzhi regime $l_{ee}/W \ll 1$, this behavior changes. The particles enter the hydrodynamic regime and begin to act collectively. Particles in the middle of the sample are screened from the boundaries and the conductivity increases when l_{ee}/W is lowered further. Mathematically this can be deduced from the expression (2.11). As will be seen later, but is physically rather clear already at this point, the viscosity behaves as $\eta \propto l_{ee}$. Thus it follows from Eq. (2.11) that the current in the hydrodynamic regime scales as

$$I \propto w^2 \left(\frac{l_{ee}}{w}\right)^{-1}.$$

Similar experiments were performed by Moll et. al. with ultra clean samples cut from the delafossite $PdCoO_2$ [24]. Essentially, the same features were observed, this time in a pure bulk material.

A different experiment designed to observe the hydrodynamic behavior of electrons is the measurement of negative resistances induced by vortices in the fluid flow. Such voritces, also called "electron whirlpools" (see Fig. 2.6), are common to electron fluids and classical fluids. Electron whirlpools were observed in (doped) graphene [27] (see Fig. 2.6). However, the question whether electron whirlpools are indeed a smoking gun evidence for hydrodynamic electorn flow is the subject of an ongoing discussion. Theoretical considerations suggest that similar effects can occur in the balistic regime [28].

Recently it has become possible to directly measure the Poisuille velocity profile in two dimensional samples. Measurements of Poisuille flow profiles through graphene channels have been reported in [30]. Fig. 2.7 showes the measured profiles. Though even in such measurements it is difficult to distinguish

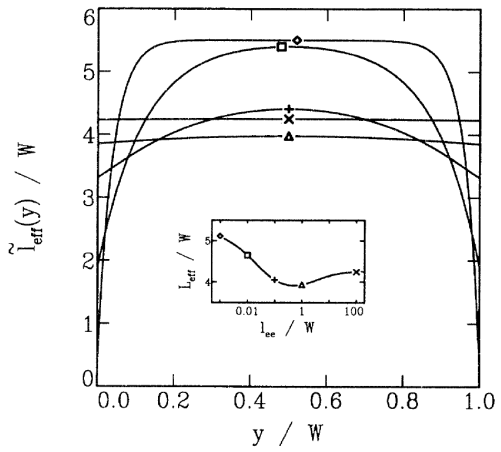

Figure 2.5: The figure is copied from Ref. [19] and shows the results of seminal experiments carried out by de Jong and Molenkamp with 2D high mobility GaAs wires. The inlet shows the conductivity of the high mobility wire in terms of an effective mean free path L_{eff}, which is given in units of the width W. The crossover between Knudsen and Gurzhi regimes (see main text) is observed. The main figure shows the corresponding flow profiles. When the values of l_{ee}/W are lowered, the profiles approach the parabolic shape of the classical Poiseuille flow of Eq. (2.10). However, as W grows, impurity scattering starts to dominate the flow, and the profile turns flatter in the middle of the sample. This is best seen in the flow profile corresponding to the lowest value of l_{ee}/W.

hydrodynamic and ballistic flows, they demonstrate that electron hydrodynamics is becoming more and more intriguing for condensed matter experimentalists.

Most relevantly for the physics of this thesis, hydrodynamic transport has been measured in graphene at the charge neutrality point [50, 55]. While Ref. [50] reports a violation of the Wiedemann-Franz law, as expected for hydrodynamic transport in charge neutral graphene (see Fig. 2.8), Ref. [55] demonstrates that the interaction-induced conductivity due to momentum conserving electron-electron scattering can be disentangled from other contributions to the graphene conductivity.

2.6 Summary

In this chapter the basic notions of electron hydrodynamics were reviewed. The Navier-Stokes equations were derived macroscopically, as well as using kinetic theory. The Chapman-Enskog method was discussed, and the importance of boundary conditions for the hydrodynamic electron flow was pointed out. Momentum conserving (BGK) and non-conserving relaxation time approximations were introduced, and basic tranport theory reviewed. After sketching the derivation of the quantum Boltzmann equation, the chapter was concluded with a brief review of experimental results on electron hydrodynamics. The purpose of this chapter was to introduce the physics of electron hydrodynamics upon which the subsequent chapters will build.

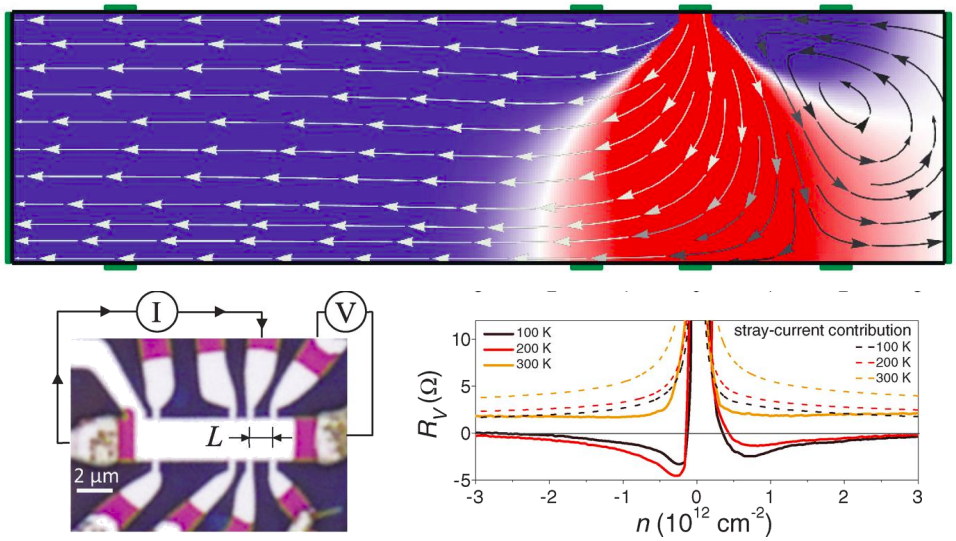

Figure 2.6: Measuring electron whirlpools (vortices) in graphene. The figure is copied from Ref. [27] and edited. The upper panel shows the streamlines of a fluid vortex at the right edge of the sample. The lower left figure shows a photograph of the experimental sample. A vortex at the right edge of the sample leads to a negative voltage betweeen the two indicated spots. The lower right figure shows the measured negative resistance (measured voltage / applied current). The x-axis shows the charge density in the sample. The negative resistance is measured away from charge neutrality.

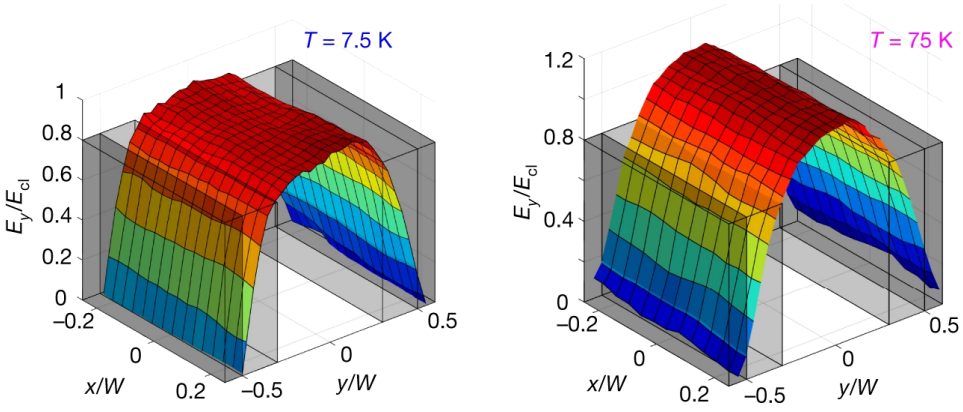

Figure 2.7: The figure is copied from Ref. [30] and edited. Ballistic (left) and hydrodynamic Poiseuille profiles of the electron flow through graphene channels. The hydrodynamic regime is reached by increasing the temperature of the sample to $T = 75\,\mathrm{K}$. Leading to small mean free paths $l_{ee} \sim 1/T$.

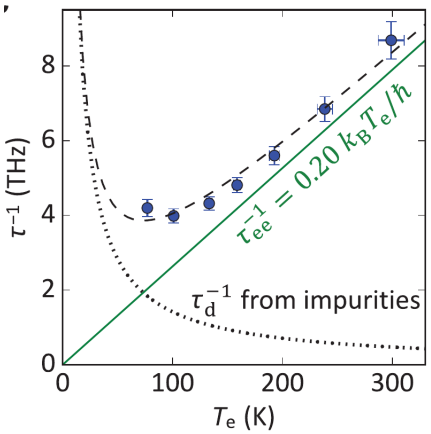

Figure 2.8: Rates of electron-electron and electron-impurity scatterings as extracted from resistivity measurements in charge neutral graphene. The interaction induced and impurity induced conductivities can be disentangled. Electron-electron scattering dominates over the whole temperature range. Figure adapted from [55].

Chapter 3

3 Fundamentals: Lévy flights and anomalous diffusion

The notion of a Lévy flight builds upon the work of Paul Lévy and Alexander Khinchin on stable distributions [94–96]. A Lévy flight can be thought of as a random walk with very specific properties. In Brownian motion a random walker propagates in small steps and the continuous time dynamics of the random walk is determined by the ordinary diffusion equation. The distribution function of step sizes is either Gaussian, or has a well defined second moment, so that Gaussian behavior emerges with an increasing number of steps, as follows from the central limit theorem. During a Lévy flight, the walker occasionally make large leaps, which, in the continuous time description, lead to non-localities. The statistics of Lévy flights does not follow the central limit theorem in its usual form [97], instead the notion of Lévy stable distributions becomes important.

Lévy flights are the subject of many studies concerned with the statistical behavior of biological, ecological and financial systems. Examples are hungry animals in search of food and search strategies in general [98–100], the propagation of earthquake epicenters [101] and prize fluctuations on the stock market [102].

3.1 Gaussian and Lévy-stable random walks

The random walk of a particle is a sequence of steps l_i added up in space. The step sizes are determined by $\rho\left(l\right)$ - the step size distribution function. After N steps the particle travels a distance

$$X_N = \sum_{i=1}^{N} l_i.$$

As an example, consider a one-dimensional walk. Assuming that $\rho\left(l\right)$ is a symmetric function, the expectation value of travelled distances X_N vanishes, $\left\langle X_N \right\rangle = 0$, and its variance is given by $\left\langle X_N^2 \right\rangle = N \left\langle l^2 \right\rangle$, where $\left\langle l^2 \right\rangle$ is the variance of the step size distribution function. Thus if $\left\langle l^2 \right\rangle$ is finite, and each step takes the particle a time Δt, it is

$$\left\langle X_N^2 \right\rangle = \frac{t}{\Delta t} \left\langle l^2 \right\rangle. \tag{3.1}$$

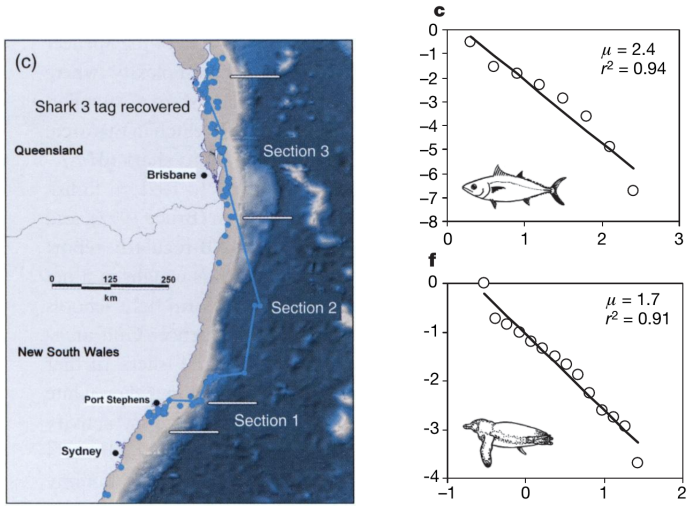

Figure 3.1: Left panel: The trajectory of a foraging shark travelling along the eastern coast of Australia. Large leaps made by the shark indicate Lévy flight behavior. The figure was copied from Ref. [103]. Right panel: Log-log plots of the step size distributions of foraging bigeye tunas (upper image) and magellanic penguins (lower image). The distributions correspond to Lévy-stable random walks (see table 3.1). The figure is due to Ref. [100]. Notice the different conventions for the exponent μ. The μ used in Ref. [100] corresponds to $\mu + 1$ in the rest of this chapter. Remarkably, it can be shown that an exponent $\mu \approx 1$ (in the convention used in the chapter) corresponds to an optimal search pattern [104, 105].

The same dependence on t follows if $\langle l \rangle$ is finite. Conclusions on the distribution of X_N for $N \to \infty$ can be drawn with the help of the central limit theorem even without knowing the precise form of $\rho(l)$. For a one dimensional random walk, the probability that the particle is at a position X_N after N steps, up to a normalization factor, is

$$\begin{aligned} \int \prod_{j=1}^{N} dl_j \rho(l_i)\, \delta\left(\frac{X_N}{\sqrt{N}} - \frac{1}{\sqrt{N}} \sum_{j=1}^{N} l_j\right) &= \int \prod_{j=1}^{N} dl_j \rho(l_i) \int \frac{dk}{(2\pi)} e^{ik\left(\frac{X_N}{\sqrt{N}} - \frac{1}{\sqrt{N}} \sum_{j=1}^{N} l_j\right)} \\ &= \int \frac{dk}{(2\pi)} e^{ik\frac{X_N}{\sqrt{N}}} \left(\int dl \rho(l)\, e^{-i\frac{k}{\sqrt{N}} l}\right)^N . \end{aligned} \tag{3.2}$$

If the condition $\langle l \rangle = 0$ is fulfilled,

$$\int dl \rho(l)\, e^{-i\frac{k}{\sqrt{N}} l} = \left\langle e^{-i\frac{k}{\sqrt{N}} l} \right\rangle = 1 - \frac{1}{N} \frac{k^2 \left\langle l^2 \right\rangle}{2} + \mathcal{O}\left(1/N^{3/2}\right) \tag{3.3}$$

holds. With the identity $\lim_{x\to\infty} (1 + x/N)^N = e^x$, for $N \to \infty$, the probability distribution of the distance X_N the particle travelled after N steps becomes

$$P(X_N) = \frac{1}{\sqrt{N}} \int \frac{dk}{(2\pi)} e^{ik\xi_N} e^{-\frac{1}{2}k^2 \left\langle l^2 \right\rangle} = \frac{1}{\sqrt{2\pi \left\langle l^2 \right\rangle N}} e^{-\frac{X_N^2}{2\left\langle l^2 \right\rangle N}}. \tag{3.4}$$

A glance at Eq. (3.3) shows, that for any step size distribution function $\rho\left(l\right)$ with a finite second moment $\left\langle l^2 \right\rangle$, the random walker behaves according to Eq. (3.4). The simplest example is a Gaussian distribution $\rho\left(l\right) = \sqrt{1/2\pi \left\langle l^2 \right\rangle} e^{-l^2/2\left\langle l^2 \right\rangle}$, which is fully characterized by its second moment $\left\langle l^2 \right\rangle$. Such a distribution function leads to a random walk where the probability distribution of the the travelled distance X_N is, up to a scaling factor $\sqrt{N}$, the same the step size distribution:

$$\sqrt{N} P\left(X_N\right) = \rho\left(X_N/\sqrt{N}\right) \tag{3.5}$$

Now, cases will be examined where the second moment of $\rho\left(l\right)$ can diverge. These cases correspond to anomalous diffusion [97]. $\rho\left(l\right)$ shall be symmetric, such that $\left\langle l \right\rangle = 0$. A central notion is that of Lévy stability. A distribution function F is said to be stable, if the sum $\Sigma = \left(\xi_1 + \xi_2 + ... + \xi_N\right)/c_N$, where ξ_i are random variables all distributed according to F and c_N is a scaling factor, is distributed according to the same function F.

The definition of stability is reminiscent of the above calculation for a Gaussian random walk. Eq. (3.2) is evaluating a sum just like $c_N \Sigma$. It is immediately clear from Eqs. (3.2)-(3.4) that the Gaussian distribution is stable, but it is not the only stable distribution. Stable distrubutions in general can be classified by the behavior of c_N. Roughly speaking, c_N determines the distance a random walker travels in N steps. It is convenient to define the characteristic function of the step size distribution

$$\tilde{\rho}\left(k\right) = \int dl \rho\left(l\right) e^{-ikl}$$

Examining the Eq. (3.2), one sees that a necessary condition for the stability of step size distribution function is

$$\tilde{\rho}\left(k\right)^N = \tilde{\rho}\left(c_N k\right). \tag{3.6}$$

Then, the distribution for the distance travelled in N steps X_N becomes

$$P\left(X_N\right) = \int \frac{dk}{(2\pi)} e^{ikX_N} \tilde{\rho}\left(c_N k\right) = \frac{1}{c_N} \rho\left(X_N/c_N\right),$$

which is in complete analogy to Eq. (3.5) for the Gaussian random walk. The condition (3.6) is fulfilled by the functions

$$\tilde{\rho}_\mu\left(k\right) = e^{-\gamma |k|^\mu}$$

with

$$c_N = N^{\frac{1}{\mu}}. \tag{3.7}$$

where γ is an arbitrary constant.

The characteristic functions of stable distributions must necessarily have this form [106]. The case $\mu = 2$ obviously just gives the Gaussian distribution with its typical $\sqrt{N}$ growth of the travelling distance. For $\mu = 1$ a Cauchy distribution is obtained:

$$\rho_1\left(l\right) = \frac{1}{\pi} \frac{\gamma}{\gamma^2 + l^2}. \tag{3.8}$$

As expected the Cauchy distribution has a divergent second moment. Travelling distances grow $\propto N$. The cases $0 < \mu < 1$ and $1 < \mu < 2$ can be estimated with the help of the expansion ([97], Appendix

B.3)

$$\int_{-\infty}^{\infty} \frac{dk}{(2\pi)} e^{ikx-|k|^{\mu}} = \pi^{-1} \sum_{k=1}^{\infty} (-1)^{k+1} \frac{x^{-(\mu k+1)}}{k!} \Gamma\left(1+k\mu\right) \sin\left(\pi\mu k/2\right).$$

For large arguments the step sizes are distributed according to

$$\rho_{\mu} \approx \frac{1}{\pi} \frac{\gamma \Gamma\left(1+\mu\right) \sin\left(\pi\mu/2\right)}{l^{\mu+1}}, \quad l \to \infty. \tag{3.9}$$

An important property of random walks is that if for $N \to \infty$ the distribution of travelling length approaches a certain distribution $P_{N\to\infty}\left(X_N\right)$, this distribution must be Lévy stable [106]. Hence the importance of stable distributions.

μ	step size distribution	behavior	$\left\langle l^2 \right\rangle$
$0 < \mu < 1$	$\rho_{\mu}\left(l\right) \sim l^{-(\mu+1)}$	Lévy flights	undefined
$\mu = 1$	$\rho_{\mu}\left(l\right) = \frac{1}{\pi}\left(1+l^2\right)^{-1}$	Cauchy flight	undefined
$1 < \mu < 2$	$\rho_{\mu}\left(l\right) \sim l^{-(\mu+1)}$	Lévy flights	undefined
$\mu \geq 2$	$\rho\left(l\right) = \sqrt{1/4\pi} e^{-l^2/4}$	normal (Gaussian) diffusion	finite

Table 3.1: Regimes of random walks governed by Lévy stable step size distributions with characteristic functions $\tilde{\rho}_{\mu}\left(k\right) = e^{-|k|^{\mu}}$. In all cases the particles travel a dictance $\propto N^{1/\mu}$ in N steps. The Cauchy flight is a special case of the Levy flight where the step-size distribution has the simple Cauchy form. Notably, the phase space diffusion of graphene electrons is characterized by a wrapped Cauchy distribution, as will be shown in chapter 6.

Random walks governed by Lévy stable distributions with $\mu \neq 2$ differ very much from Brownian motion. It follows from the definition of Lévy stability that the distance travelled by random walkers in N steps is given by $N^{1/\mu}$. Thinking of the behavior for large N in terms of a continuous process with $N = t/\Delta t$, where Δt is the time corresponding to one step, the travelled distance follows the law $\propto t^{1/\mu}$. Brownian motion ($\mu = 2$) is therefore the slowest process for large times. The reason is the fast decay of the Gaussian step size distribution at large step sizes l. The particle only travels in small steps. In Lévy type motion, the frequent small steps are interrupted by rare large distance jumps, which are extremely improbable for Gaussian random walks. Therefore such random walks are called Lévy flights. Here, the jumps do occur because the distribution function decays as a power-law (see Eqs. (3.8) and (3.9)). The distinct features of a Gaussian random walk and a Lévy flight are demonstrated in Fig. 3.2.

3.2 Fractional diffusion equations

3.2.1 The normal diffusion equation

Differential equations are a useful tool to describe diffusion processes [107]. The well known diffusion equation describes normal diffusion processes, e.g. Brownian motion, in the continuous limit $\Delta t \to 0$. It determines the behavior of the probability distribution function (PDF) $P\left(x,t\right)$ to find the particle

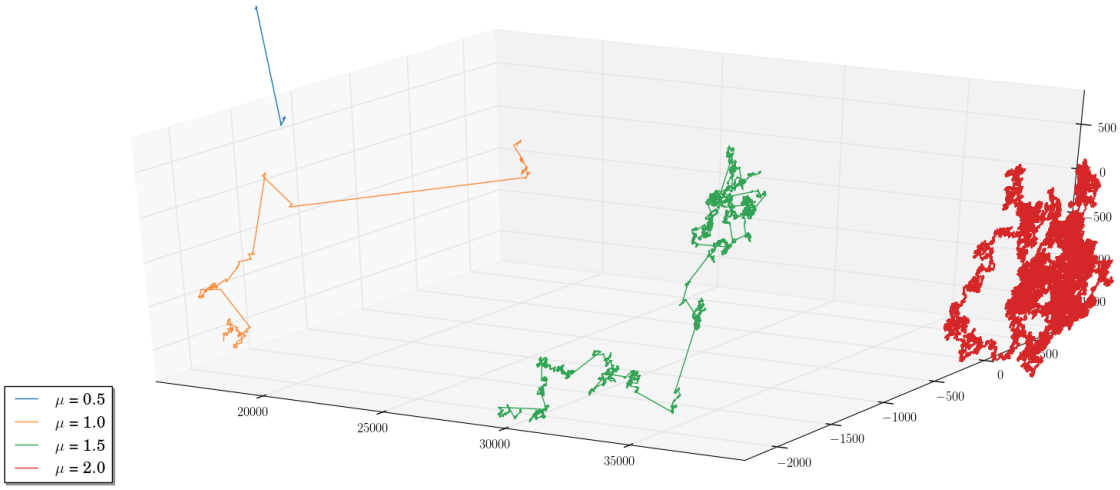

Figure 3.2: The trajectories of four Lévy stable random walks with different exponents μ (see table 3.1) are shown. The number of steps is $N = 1000^{\mu}$ in each case, such that approximately the same volume is covered by each random walk. The red curve shows a Gaussian random walk with one million steps, while the blue curve has a comparable size with only 33 steps. One can clearly see, how the slowly decaying step size distributions for $\mu < 2$ trigger large jumps within the trajectories.

at a given point x at the time t. Assuming that $P\left(x, t + \Delta t\right)$ is determined by the influx of particles to the location x during the time interval Δt, one finds

$$P\left(x, t + \Delta t\right) = \int P\left(x - \Delta x, t\right) \rho\left(\Delta x\right) d\left(\Delta x\right). \tag{3.10}$$

$\rho\left(\Delta x\right)$ is a step size distribution that accumulates the effects of many steps travelled in the period Δt. For a small time interval Δt, and small distances Δx follows

$$\frac{\partial P\left(x,t\right)}{\partial t} \approx D \frac{\partial^2 P\left(x,t\right)}{\partial x^2}, \tag{3.11}$$

with the diffusion constant $D = \left\langle \Delta x^2 \right\rangle / \left(2\Delta t\right)$. It is easy to see, that the diffusion equation describes processes, where the particles spread according to a $\sqrt{t}$ law, as expected for Gaussian processes. A simple solution of Eq. (3.11) for the initial condition $P\left(x, t = 0\right) = \delta\left(x\right)$ is $P\left(x,t\right) = e^{-x^2/4Dt}/\sqrt{4\pi Dt}$. The second moment of this distribution is

$$\left\langle x^2 \right\rangle = 2Dt.$$

3.2.2 Superdiffusive fractional diffusion equations

The situation is more complicated for Lévy-stable step size distributions $\rho_\mu\left(l\right)$ with $\mu < 2$. An expansion as in the Gaussian example (3.11) is not possible because of the divergent second moment of $\rho_\mu\left(l\right)$.

Instead one can use the Fourier representation with regard to the variable x. Eq. (3.10) becomes

$$\tilde{P}\left(k, t+\Delta t\right) = \tilde{P}\left(k, t\right) \tilde{\rho}_{\mu}\left(k, \Delta t\right). \tag{3.12}$$

Here, $\tilde{\rho}_{\mu}\left(k, \Delta t\right) = e^{-\gamma' \Delta t |k|^{\mu}}$ is an effective distribution function of distances travelled during the time interval Δt. This form of $\tilde{\rho}_{\mu}\left(k, \Delta t\right)$ follows immediately from the fact that $\rho_{\mu}\left(l\right)$ is Lévy stable (see Eq. 3.6), and N steps are taken during Δt. Expanding Eq. (3.12) for small Δt and taking the limit $\Delta t \to 0$ yields

$$\frac{\partial P\left(k,t\right)}{\partial t} = -\gamma' \left|k\right|^{\mu} P\left(k,t\right).$$

This equation can be rewritten using the Riesz fractional derivative: $\mathcal{F}\left[\left|k\right|^{\mu} f\left(k\right)\right] = -\Delta^{\mu/2} f\left(x\right)$, where Δ is the laplace operator [108]. Therefore a fractional diffusion equation can be formulated for processes governed by Lévy stable random walks. In the one dimensional case one obtains:

$$\frac{\partial}{\partial t}\rho\left(x,t\right) = \gamma' \left(\frac{\partial^2}{\partial x^2}\right)^{\frac{\mu}{2}} \rho\left(x,t\right), \tag{3.13}$$

where $0 < \mu < 2$ and γ' plays the role of a fractional diffusion constant. Because the mean-squared distance diverges in Lévy flight scenarios, and particles spread faster in space, one often speaks of superdiffusive behavior. This can be illustrated in the following manner. Introduce a fractional mean displacement $\left\langle x\left(t\right)^{\delta}\right\rangle$ [109, 110], where δ is chosen such, that the term is finite. It follows

$$\left\langle x^{\delta}\right\rangle \propto \gamma' t^{\delta/\mu}.$$

A rescaling $\delta \to 2$ shows that the behavior is indeed superdiffusive. This could have been, of course, anticipated from the $N^{1/\mu}$ behavior of travelling distance. The fractional derivative of Eq. (3.13) can be represented as an integral:

$$\left(\frac{\partial^2}{\partial x^2}\right)^{\frac{\mu}{2}} f(x) = \frac{\Gamma\left(1+\mu\right)\sin\left(\pi\mu/2\right)}{\pi} \int \frac{f(x')}{\left|x-x'\right|^{1+\mu}}\, dx'.$$

Note, that the integral is subject to proper regularizations that are incorporated in alternative expressions [108, 110, 111]. This integral representation demonstrates the intrinsic non-locality of the Lévy flight. The evolution of the PDF at a given point as given by (3.13), depends on the PDF at all other points of the domain in question.

3.2.3 Subdiffusive fractional diffusion equations

Another type of anomalous diffusion, that shall be briefly reviewed is subdiffusion. During subdiffusion particles travel slower than in a diffusive process. Their mean squared displacement grows according to

$$\left\langle x^2\right\rangle = 2D_{\zeta} t^{\zeta},$$

where $0 < \zeta < 1$. Such a behavior can stem from a random walk with a Gaussian step size distribution function, where waiting times for the walker are introduced, i.e. there is a chance that the particle

remains on a certain position for a long time [109]. Instead of the simple diffusion equation, the PDF follows a different kind of fractional differential equation. One possible way to write this equation is [109, 110, 112]

$$\frac{\partial}{\partial t}\rho\left(x,t\right) = K_\zeta D_t^{1-\zeta}\frac{\partial^2}{\partial x^2}\rho\left(x,t\right),$$

with the operator

$$D_t^{1-\zeta} f\left(t\right) = \frac{1}{\Gamma\left(\zeta\right)}\frac{\partial}{\partial t}\int_0^t \frac{f\left(t'\right)}{\left(t-t'\right)^{1-\zeta}}.$$

3.3 Summary

In this chapter the notions of normal and anomalous diffusion were introduced. Some properties of Brownian motion were discussed. It was shown that, following the central limit theorem, the tavelled distance of any random walker follows the $\sqrt{N}$ scaling of Brownian motion for large numbers of steps N, if the distribution of step sizes has a well defined second moment. The concept of Lévy stability was then introduced. Lévy stable distributions were classified using their characteristic functions and their behavior at large arguments. It was shown that for random walks whose step size distributions have polynomially decaying tails and divergent second moments (see table 3.1), the travelled distance of a random walker scales as $N^{1/\mu}$ with $0 < \mu < 2$, i.e. the random walker is faster. Such a motion was called superdiffusive.

It was argued, that in the continuous time limit $\Delta t \to 0$, where Δt is the time between successive iterations of the random walk, the dynamics of the distribution function for the position of the random walker can be described by means of diffusion equations. In the case of normal diffusion, the dynamics is follows the ordinary diffusion equation. In the Lévy flight case, a fractional diffusion equation, involving a Riesz-Feller derivative $\Delta^{\mu/2}$ instead of the second derivative of the ordinary diffusion equation, must be used. A similar fractional diffusion equation will be seen to describe the superdiffusive phase space dynamics of graphene electrons in chapter 6.

Chapter 4

4 The boundary conditions of viscous electron flow

As outlined in section 2.1.3, in most effects that are characteristic for hydrodynamic electron flow the behavior of electrons at the sample boundaries is crucial. Often, hydrodynamic electrons are described with the help of Navier-Stokes equations (see e.g. [22, 26, 27, 39, 113]). These equations are second order partial differential equations and need to be supplimented with boundary conditions, when solved on a finite domain. In the simplest case of low Reynolds numbers, the stationary, linearized Stokes flow (see section 2.1.2) can be considered. The Stokes equation reads

$$\eta \Delta \mathbf{u} = \nabla p, \tag{4.1}$$

where $\mathbf{u}$ is the flow velocity, η the shear viscosity and p the pressure. Let S be the boundary of the fluid.

A variety of boundary conditions at S can be formulated. In classical hydrodynamics, in an overwhelming number of cases, the no-slip boundary condition

$$u_\alpha^t \Big|_S = 0 \tag{4.2}$$

applies. Here,$\mathbf{u}^t = \mathbf{u} - (\mathbf{u} \cdot \mathbf{n})\,\mathbf{n}$ is the tangential velocity of a boundary with normal vector $\mathbf{n}$. The fluid is at rest at boundaries. Roughly speaking, it is slowed down at by momentum dissipating collisions of the particles with the rough boundary walls. Contrary to first intuition, even if on average the particles lose all of their momentum in particle-wall collisions, the condition (4.2) does not necessarily apply. This will be discussed later, and it will become clear, why the no-slip condition (4.2) holds in an overwhelming majority of classical hydrodynamic problems.

A different condition applies at the interaface of a liquid and a gas. Here, solutions of the Stokes equation (4.1) have to satisfy

$$n_\beta \frac{\partial u_\alpha^t}{\partial x_\beta}\bigg|_S = 0. \tag{4.3}$$

This is the so-called no-stress boundary condition. Remembering the result of section 2.2 that gradients of the flow velocity $\partial_\alpha u_\beta$ correspond to momentum currents, the no-stress boundary condition prohibits a momentum flow towards the boundary. The physical reason for this is, that no momentum is dissipated at S, and therefore the influx of momentum must vanish.

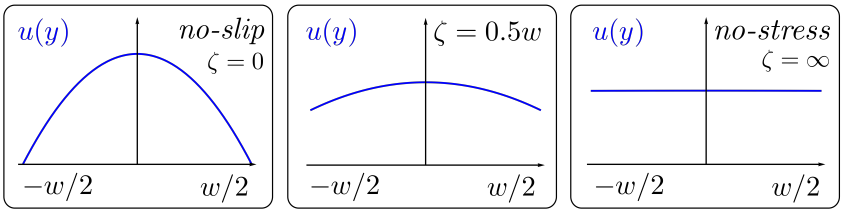

Figure 4.1: Two dimensional Poiseuille flow for different boundary conditions in a channel of width w. The flow velocity is shown as a blue curve. In each of the three pictures, the same current I_0 passes through the sample.

Finally, a mixed boundary condition of the form

$$u^t_\alpha\Big|_S = \zeta\, n_\beta \frac{\partial u^t_\alpha}{\partial x_\beta}\bigg|_S . \tag{4.4}$$

can be imposed. The quantitiy ζ is called the slip length. It is the length at which the flow velocity u^t vanishes, if it is prolonged with a streight line of slope $\partial u^t_\alpha/\partial x_\beta\big|_S$ outside the boundary. This is illustrated in Fig. 4.2. In the limits $\zeta \to 0$ and $\zeta \to \infty$, the no-slip and no-stress conditions are restored.

To clarify the role of ζ, it is useful to take a look at the example of Poiseuille flow, which is the simplest model solution to the Stokes equation (4.1). The formula for the two dimensional Poiseuille flow in x-direction confined to a sample of width w in y-direction reads (see section 2.1.3):

$$u_x = \frac{1}{8\eta}\left(w^2 + 4\zeta w - 4y^2\right)\frac{\partial p}{\partial x}. \tag{4.5}$$

For a large $\zeta \gg w$, the classical parabolic profile, represented by the last term in brakets, is subleading to the slip induced constant term proportional to ζ. For $\zeta \to 0$ the parabolic profile is restored. The flattening of the flow profile with increasing ζ and fixed total current through the sample is demonstrated in Fig. 4.1. From (4.5) follows, that the total current through the sample is $I = \int_{-w/2}^{w/2} u_x dy \propto w^2(6\zeta + w)$. The scaling $I \propto w^3$ that holds in the no-slip case is known as the Gurzhi effect [10]. In experiments with relatively narrow doped graphene samples [27] no clear manifestations of Gurzhi effect were observed. A possible explanation is a large slip length, which serves as a good motivation to take a closer look at ζ. The results presented in this chapter were reported in Ref. [84].

The slip length is an effective quantity that sums up information on the nature of the boundary, and the scattering of fluid particles near the boundary. In the immediate vecinity of the boundary, the fluid is far from local equilibrium, and the hydrodynamic description does not apply. This area is called the Knudsen layer. At distance that is comparable to the momentum conserving mean free path, local equilibrium is restored, and the fluid can be described hydrodynamically. In this chapter the slip length ζ will be derived for Dirac and Fermi liquids. To this end, first a kinetic theory of particle-boundary scattering has to be developed. The boundary conditions for the quantum Boltzmann equation have to be derived microscopically. Solving the kinetic equation in the vicinity of the boundary and averaging over the resulting distribution function will give a boundary condition of the form of Eq. (4.4), and an explicit expression for ζ. This chapter is based on Ref. [84].

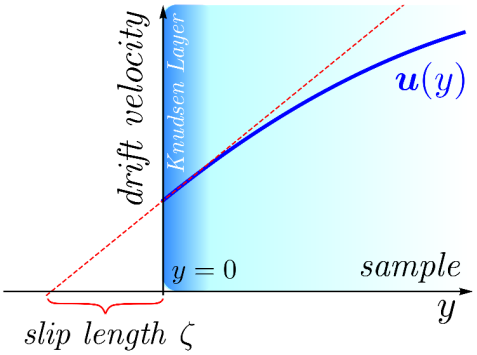

Figure 4.2: The slip length ζ is the length at which the flow velocity u^t vanishes, if it keeps dropping with a slope $\partial u^t_\alpha/\partial x_\beta\Big|_S$ outside the boundary. ζ characterizes the behavior of the liquid at the boundary and thus sums up all information about the microscopic properties of the boundary and the physics of the Knudsen layer, where the particle behavior is dominated by collisions with the wall, rather than by particle-particle collisions. The width of the Knudsen layer is comparable to the momentum conserving mean free path.

4.1 Boundary conditions for the kinetic distribution function.

Here a microscopic theory of boundary scattering will be developed. The case of charge neutral graphene will be examined. The generalization to Fermi liquids requires only minimal changes and will be adressed later. It should be remembered that it is the thermal current $\mathbf{j}_E$ that is proportional to the electron flow velocity $\mathbf{u}$ in charge neutral graphene. This issue has already been adressed in Sec. 4.6. The starting point is the Hamiltonian of massless Dirac electrons in two spatial dimensions

$$H = v\hbar\mathbf{k}\cdot\boldsymbol{\sigma}_{ab}. \tag{4.6}$$

a and b label the two sublattices of graphene. Taking interaction effects into account into account, insofar v is the renormalized group velocity of electrons (see section 1.2)

$$v = v_0\left(1+\alpha\ln\left(\Lambda/k_BT\right)\right), \tag{4.7}$$

where v_0 is the bare group velocity. Here, and in the following the spin and valley indices will be supressed. The spin-valley degeneracy can be easily incorporated at the end of the calculaten giving an overall factor of $N = 4$. The renormalization of the group velocity (4.7) is accompanied by a renormalization of the coupling constant $\alpha_0 \to \alpha = e^2/(4\pi\epsilon\hbar v)$. The massless Dirac Hamiltonian (4.6) is diagonalized by the unitary transform

$$U_{\mathbf{k}} = \frac{1}{\sqrt{2}}\begin{bmatrix} 1 & o^*_{\mathbf{k}} \\ 1 & -o^*_{\mathbf{k}} \end{bmatrix}, \tag{4.8}$$

where $o_{\mathbf{k}} = \left(k_x + ik_y\right)/\sqrt{k_x^2+k_y^2}$, leading to the spectrum $\epsilon_{\lambda\mathbf{k}} = \lambda v\hbar k$. $\lambda = \pm 1$ is the band index, labeling particle and hole bands (upper and lower Dirac cones), respectively.

To derive the boundary conditions consider a semi-infinite graphene sheet that lies in the $y > 0$ half-plane and whose edge aligns with the x-axis (see Fig. 4.3). The flow $\mathbf{u}$ is parallel to the edge

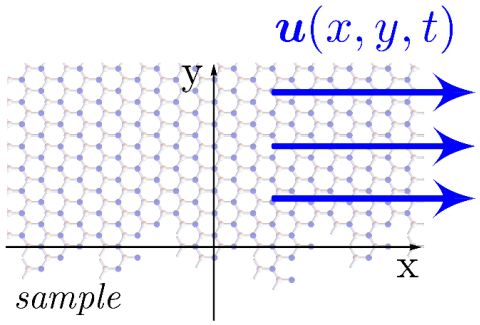

Figure 4.3: A semi-infinite graphene sheet. The sample boundary aligns with the x-axis. The Dirac fluid flows parallel to the boundary. The flow is uniform in x-direction.

everywhere in the half-plane. Formally, the problem of simultaneous scattering of electrons on each other and on the sample edge has to be solved. In principle the quantum Boltzmann equation contains two scattering terms

$$\left(\frac{\partial}{\partial t} - \mathbf{v}_\lambda \cdot \nabla\right) f_{\lambda,\mathbf{k}}(\mathbf{r}) = C_{\mathrm{e.e.}\lambda\mathbf{k}}\left[f\right] + C_{\mathrm{edge}\lambda\mathbf{k}}\left[f\right]. \tag{4.9}$$

$C_{\mathrm{e.e.}\lambda\mathbf{k}}\left[f\right]$ describes electron-electron scattering and has the form of Eq. (2.13). $C_{\mathrm{edge}\lambda\mathbf{k}}\left[f\right]$ describes electron-edge collisions. However, here a different approach based on Ref. [114] is chosen. The edge contribution to the scattering part in the quantum Boltzmann equation can be reduced to boundary conditions for the distribution function at the edge $f_{\lambda,\mathbf{k}}\left(y=0\right)$. Let $f^{>}_{\lambda,\mathbf{k}}\left(y=0\right)$ be the distribution function of electrons (holes) reflected from the wall, i.e. those having a velocity $v^y_{\lambda,\mathbf{k}} > 0$. Let $f^{<}_{\lambda,\mathbf{k}}\left(y=0\right)$ be the distribution function of electrons travelling towards the wall with $v^y_{\lambda,\mathbf{k}} < 0$. The boundary condition will relate $f^{>}_{\lambda,\mathbf{k}}\left(y=0\right)$ to $f^{<}_{\lambda,\mathbf{k}}\left(y=0\right)$. Once $f^{>}_{\lambda,\mathbf{k}}\left(y=0\right)$ and $f^{<}_{\lambda,\mathbf{k}}\left(y=0\right)$ have been found, a hydrodynamic boundary condition in the form of Eq. (4.4) can be derived from the assumption, that no momentum current can flow across the sample edge: i.e. the momentum current transverse to the edge has to vanish at $y=0$:

$$\begin{aligned} 0 \;=\; & 2N\int_{<}\frac{d^dk}{(2\pi)}v^y_{+,\mathbf{k}}k_x f^{<}_{+,\mathbf{k}}\left(y=0\right) \\ & +2N\int_{>}\frac{d^dk}{(2\pi)}v^y_{+,\mathbf{k}}k_x f^{>}_{+,\mathbf{k}}\left(y=0\right). \end{aligned} \tag{4.10}$$

Only the distribution function of electrons ($\lambda = +1$) appears in the above formula, the factor of 2 accounts for the identical hole contribution. The factor $N=4$ accounts for the spin valley gegeneracy. The superscripts $\gtrless$ denote that the integrals have to be taken over the regions in momentum space where $v^y_{\lambda,\mathbf{k}} > 0$, or $v^y_{\lambda,\mathbf{k}} < 0$, respectively. Clearly, $f^{\gtrless}_{\lambda,\mathbf{k}}$ depends on $\mathbf{u}$ and its gradients, the Chapman-Enskog method of Sec. 2.2 therefore seems a good way to attack the problem.

4.1.1 Two limiting cases of boundary scattering

There exist two distinct limiting cases of boundary scattering that result in very different flow behavior at the boundaries. First there is specular scattering, i.e. perfect reflection at the boundary. In this case the velocity component $v^y_{\lambda,\mathbf{k}}$ of scattered particles is inverted, while $v^x_{\lambda,\mathbf{k}}$ remains unchanged. For

the setting of Fig. 4.3 this boundary condition corresponds to mirroring the graphene half-plane on the x-axis and considering an infinite sheet of graphene. The fluid will behave as if there is no boundary. This limit will be called the specular limit.

In the second limit, the momentum component parallel to the edge is fully absorbed in particle-wall collisions. It is enough to assume that the distribution function of reflected electrons $f^{>}_{\lambda,\mathbf{k}}$ is isotropic[61, 115]. Then, on average, reflected electrons do not carry any tangential momentum. Following [61] this limit will be called the diffuse limit.

More complicated scenarios necessarily lie between these two limiting cases. Early phenomenological theories introduce a scattering parameter that describes the fractions of mean particle momenta before and after the collision with the wall. Here, a more microscopic approach that models the reflection on an uneven boundary will be followed [63]. The boundary roughness will be treated as a small parameter. This nearly specular limit will be considered first

Nearly specular limit

Let the rough edge be oriented along the x-axis, and its precise shape given by the function $\xi(x)$. This setting is shown in Fig. 4.4. Before adressing the question of how the edge roughness influences

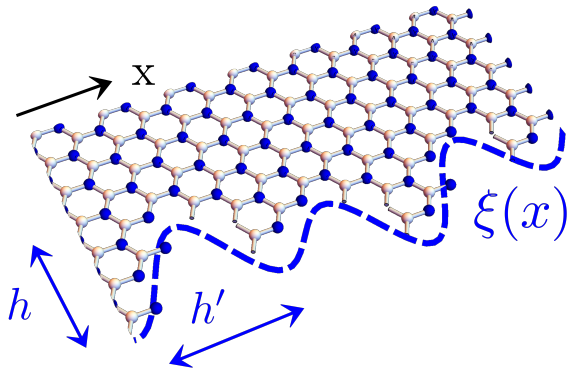

Figure 4.4: A disordered graphene edge. The edge is described by the function $\xi(x)$. Two length scales characterize the disorder: the mean roughness amplitude h, and the correlation length h'. Both lengths are much smaller than the thermal wavelength of electrons $\lambda_T \sim \hbar v/k_B T$. On average, the edge is described by the correlation function $\overline{\xi(x_1)\,\xi(0)} = h^2 \exp\left(-\frac{x_1^2}{h'^2}\right)$.

the kinetic theory, one needs to establish the quantum mechanical boundary conditions for the wave functions of Dirac electrons on the sample edge. This issue was adressed by Akhmerov and Beenakker in Ref. [116]. Here, boundary conditions for clean cuts through the graphene plane for different cutting angles with respect to the lattice basis vectors were considered. Two well known cases are the zigzag and armchair boundaries (see Fig. 4.5). It was shown in Ref. [116] that the boundary conditions for the wave function can be approximated by zigzag boundary conditions, if the sheet is cut at an angle $|\delta| \geq 0.1$ rad with respect to the armchair axis. In the case of a disorderd edge, the cutting angle is disordered, too. It is very improbable that a large portion of the edge will remain within the range $|\delta| \leq 0.1$ rad. To a good approximation, the zigzag boundary condition can be used here. As shown in Fig. 4.5, the zigzag boundary consists of atoms on one of the two sublattices. The boundary condition

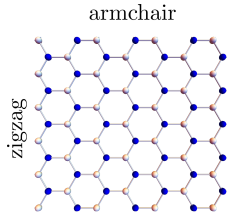

Figure 4.5: Zigzag and armchair boundaries of a graphene sheet. There are significant differences between the two boundary forms (e.g. between the spectra of graphene nano-ribbons) [41]. However the boundary conditions for an arbitrary streight cut through the graphene plane will resemble the boundary conditions for the zigzag boundary, except if the cutting angle is in a narrow range (0.1 rad) [116].

for the wave function ψ_a, where $a \in \{1,2\}$ lables the sublattice, is

$$\psi_{a=1}\left(x, y=\xi\left(x\right)\right)=0. \tag{4.11}$$

The edge function $\xi\left(x\right)$ is characterized by two lengths. The amplitude of the roughness h and the correlation length along the edge h' (see Fig. 4.4). In the nearly specular case, it can be safely assumed that h and h' are are much larger than the interatomic distances, but much smaller than the characteristic wavelength of the electrons, which in our case is the thermal wavelength $\lambda_T \sim \hbar v/k_B T$:

$$h, h' \ll \lambda_T.$$

This means that the wave function can be expanded in the small variation $\xi\left(x\right)$ along $y=0$:

$$\psi_1\left(x,0\right)+\xi\left(x\right)\left.\frac{\partial\psi_1\left(x,y\right)}{\partial y}\right|_{y=0}=0. \tag{4.12}$$

The boundary scattering is static and therefore elastic. It is therefore useful to introduce the projection of the wave function ψ_1 onto quasifree plane waves with a given energy ϵ:

$$\psi_{1,\varepsilon}\left(\mathbf{x}\right)=\sum_{\lambda}\int\frac{d^2k}{\left(2\pi\right)^2}\delta\left(\varepsilon-\varepsilon_{\lambda,k}\right)\gamma_{\mathbf{k},\lambda}U^{-1}_{1,\lambda}\left(\mathbf{k}\right)e^{i\mathbf{k}\cdot\mathbf{r}}. \tag{4.13}$$

Here, $\varepsilon_{\lambda,k}=\lambda v\hbar k$ is the electron dispersion and $U^{-1}_{a,\lambda}\left(\mathbf{k}\right)$ transforms the wavefunctions $\gamma_{\mathbf{k},\lambda}$ from the band basis into the sublattice basis. $\psi_{\mathbf{k},a}=\sum_\lambda\gamma_{\mathbf{k},\lambda}U^{-1}_{a,\lambda}\left(\mathbf{k}\right)$ is the Bloch function projected onto the sublattice. The boundary conditions for the kinetic distribution function can now be derived as follows: Insert $\psi_{1,\epsilon}\left(\mathbf{x}\right)$ into (4.12), carry out the k_x integration, and perform a Fourier transform. Then, to second order in $\xi\left(x\right)$ a relation between the wavefunctions $\gamma_{k_x,|k_y|,\lambda}$ and $\gamma_{k_x,-|k_y|,\lambda}$ on the boundary is obtained. This relation holds for $\lambda=\pm1$ separately, because the scattering process is elastic. Then, an average over the edge functions $\overline{\xi\left(x_1\right)\xi\left(x_2\right)}$ must be taken. Upon averaging, one has:

$$\overline{\xi\left(k_1\right)\xi\left(k_2\right)}=2\pi\delta\left(k_1+k_2\right)W\left(k_1\right). \tag{4.14}$$

The function $W\left(k\right)$ describes the correlations of the surface roughness. The kinetic distribution function is given by the modulus squared of the wave functions $\gamma_{\mathbf{k},\lambda}$

$$f_{\mathbf{k},\lambda}=\left(2\pi v^y_{k_x,\lambda}\right)^{-1}\overline{\left|\gamma_{k_x,k_y\left(\epsilon,k_x\right),\lambda}\right|^2}, \tag{4.15}$$

where the prefactor $\left(2\pi v^y_{k_x,\lambda}\right)^{-1}$ stems from a variable change $k_x, \epsilon \to \mathbf{k}$. In this fashion one arrives at the boundary condition

$$\begin{aligned} f^{>}\left(k_x, k_y\right) &= f^{<}\left(k_x, -k_y\right) \\ &\quad -4f^{<}\left(k_x, -k_y\right) k_y \int \frac{dk'_x}{2\pi} k'_y W\left(k_x - {k'}_x\right) \\ &\quad +4k_y \int \frac{dk'_x}{2\pi} k'_y W\left(k_x - {k'}_x\right) f^{<}\left(k'_x, -k'_y\right). \end{aligned} \tag{4.16}$$

The above equation is this section's main result. Except for the matrix elements $U_{a,\lambda}\left(\mathbf{k}\right)$, which ultimately cancel out due to the unitarity of the transformation, and the fact that two bands $\lambda = \pm 1$ have to be kept track of, the calculation is completely analogous to the one presented by Falkovsky in [63]. The details are summerized in Appendix A.1. The domain of integration in (4.16) ranges from $k'_x = -\epsilon/v$ to $k'_x = \epsilon/v$ where $k_y = \sqrt{\left(\epsilon/v\right)^2 - k_x^2}$. The result of Eq. (4.16) remains unaltered if the sublattice indices in Eq. (4.11) are interchanged.

The precise form of the edge correlation function $\overline{\xi\left(x_1\right)\xi\left(0\right)}$ is not known. It depends on the microscopic details of the edge, which, in their turn, depend on the fabrication process. Two things are clear: the edge correlation function is proportional to h^2, and it has to decay on a scale h' with increasing distance between x_1 and $x = 0$. However, it is clear from Eq. (4.16), that the boundary condition will not strongly depend on the precise form of the edge correlation function, as long as the two above conditions are satisfied. A Gaussian distribution is a good choice

$$\overline{\xi\left(x_1\right)\xi\left(0\right)} = h^2 e^{-\frac{x_1^2}{h'^2}}.$$

The Fourier transform is then given by

$$W\left(k_x\right) = \sqrt{\pi} h^2 h' e^{-\frac{1}{4}k_x^2 h'^2}.$$

Since the wavelengths of electrons are given by λ_T and the condition

$$h' \ll \lambda_T$$

holds, it is $k_x^2 h'^2 \ll 1$ and $W\left(k_x\right)$ can be safely approximeted by a flat function:

$$W\left(k_x\right) = \sqrt{\pi} h^2 h'.$$

The presence of the small parameter

$$\kappa = h^2 h' / \lambda_T^3$$

in the nearly specular limit does not only simplify the boundary conditions but also allows a controlled calculation of the slip length. Integrating Eq. (4.16) over k_x, one easily sees that the boundary condition conserves the particle number.

Diffuse limit

In the diffuse limit, electrons and holes loose all tangential momentum upon reflection on the boundary. The distribution function of the reflected electrons then is isotropic:

$$f^{>}_{\lambda,k} = f^{>}_{\lambda}\left(\left|\mathbf{k}\right|\right). \tag{4.17}$$

The diffuse limit is appropriate when the boundary if very rough, or other momentum sinks, such as for example phonons, dissipate momentum at very fast rates. The boundary condition (4.17) obviosly makes no assumtions on the microscopic mechanism of momentum dissipation.

4.2 The slip length of a Dirac liquid

To derive the hydrodynamic slip length, first the kinetic theory of momentum flow near the boundary has to be adressed. A Chapman-Enskog-like ansatz can be used. The Chapman-Enskog method was summerized in Sec. 2.2. The bulk (subscript b) kinetic distribution function can be written in the form

$$f\Big|_b = f^{l.e.} - f^{(0)}\left(1 - f^{(0)}\right)\Psi, \tag{4.18}$$

where the function Ψ, characterizing the deviations from local equilibrium, should not be confused with the notation for the electron wave function used above. To avoir confusion we will refer to the local equilibrium function of Sec. 2.2 as $f^{l.e.}$ and $f^{(0)}$ will stand for the Fermi-Dirac distribution: $f^{(0)} = f^{l.e.}\Big|_{\mathbf{u}=0}$. For charge neutral graphene the local equilibrium distribution function reads

$$f^{l.e.}_{\lambda,\mathbf{k}} = \frac{1}{e^{\beta\left(\varepsilon_{\lambda,\mathbf{k}} - \mathbf{u}\left(\mathbf{r},t\right)\cdot\mathbf{k} - \mu\right)} + 1}.$$

The reponse of the Coulomb interacting Dirac liquid to stresses caused by gradients of $\mathbf{u}$ will be examined in chapter 5. Here, some results will be used to calculate the slip length [51]. The non-equilibrium contribution Ψ of Eq. (4.18) is given by

$$\begin{aligned} \Psi &= \frac{1}{2}\lambda\left(a_0 + a_1\beta v k\right) I_{\alpha\beta}X_{\alpha\beta} \\ X_{\alpha\beta} &= \frac{\partial u_\alpha}{\partial x_\beta} + \frac{\partial u_\beta}{\partial x_\alpha} - \delta_{\alpha\beta}\nabla\cdot\mathbf{u} \\ I_{\alpha\beta} &= \left(\frac{k_\alpha k_\beta}{k^2} - \frac{1}{2}\delta_{\alpha\beta}\right). \end{aligned} \tag{4.19}$$

Here, a_0 and a_1 are numerical coefficients that will be calculated in chapter 5. They correspond to zero modes of the collinear part of the collision operator of the quantum Boltzmann equation for graphene electrons. These modes are dominant at small values of the fine structure constant α. As shown in Sec. 1.2, the behavior of thermally excited electrons and holes is governed by small α physics. Formally, Eq. (4.19) is very similar to the Chapman-Enskog expressions of Sec. 2.2.

4.2.1 The nearly specular limit

Eq. (4.19) describes the response to stresses in the bulk. Here, the contribution of the boundary is of interest. In the nearly specular scenario, corrections on the order of $\kappa = h^2h'/\lambda_T^3$ due to the edge roughness can be exprected. A good ansatz for the distribution function $f^{<}_{\lambda,\mathbf{k}}\left(y=0\right)$ of impinging particles therefore is

$$f^{<}_{\lambda,\mathbf{k}}\left(y=0\right) = f_{\lambda,\mathbf{k}}\Big|_b + \mathcal{O}\left(\kappa\right) A\left(I_{\alpha\beta}X_{\alpha\beta}\right). \tag{4.20}$$

Here $A\left(I_{\alpha\beta}X_{\alpha\beta}\right)$ is an unknown function of spatial gradients of $\mathbf{u}$ and of momenta $\mathbf{k}$. Later on, it will be shown that the function $A\left(I_{\alpha\beta}X_{\alpha\beta}\right)$ contributes to the slip length only to second order in κ and can be ignored. It is sufficient to use the bulk distribution function for impinging electrons. The loss of tangential momentum is therefore described by Eq. (4.16) and the influence of the boundary on momentum currents does not need to be considered. Inserting Eq. (4.20) into (4.16), an expression for the full distribution function $f_{\lambda,\mathbf{k}}\left(y=0\right)$ at the edge is obtained.

A hydrodynamic boundary condition of the form of Eq. (4.4) can now be obtained with the help of Eq. (4.10). Performing the integrations, only those parts of the distribution function contribute, which are proportional to $\cos\left(\varphi_{\mathbf{k}}\right)$, where $\varphi_{\mathbf{k}}$ is the angle of $\mathbf{k}$. The last right hand side term of (4.16) does therefore not contribute to the momentum current average (4.10) for a flat $W\left(k_x\right)$. The result is

$$0 = -\kappa A u_x + \left(\eta - \kappa B\right)\frac{\partial u_x}{\partial y},$$

with $A = \frac{N31\pi^{11/2}}{672\beta^3 v^3\hbar^2}$. The term with coefficient B that is unimportant in the limit of small κ (showing that the boundary correction for impiging particles in Eq. (4.20) is irrelevant). η is the viscosity of the Dirac liquid [51]

$$\eta = N\frac{\left(\pi^3 a_0 + 27\zeta(3)\pi a_1\right)}{48\pi^2\beta^2 v^2\hbar} \approx \frac{0.449N}{4\alpha^2 v^2\hbar}\left(k_B T\right)^2, \tag{4.21}$$

In the limit $\kappa \to 0$, the boundary condition reduces to the no-stress condition (4.3). This shows, that if the edge is sufficiently smooth on the scale of the electron wavelength, the liquid will not be slowed down at the boundary. With the above expressions, the slip length is

$$\zeta = \left(\frac{\lambda_T^3}{h^2 h'}\right)\chi \approx 0.008\kappa^{-1} l_{ee}, \tag{4.22}$$

where $\chi = \frac{672\beta^3 v^3\hbar^2}{N31\pi^{11/2}}\eta$. For the mean free path due to electron-electron scattering $l_{ee} = v\hbar/\left(C_1\alpha^2 k_B T\right)$, with numerical coefficient $C_1 = 1.950$, was used. This result is only cited here. The electron-electron scattering scattering length will be examined in detail in chapter 5.

4.2.2 The diffuse limit

The diffuse limit can be treated similarely to the nearly specular limit, however, there is no small parameter. A natural first assumption is that the bulk distribution function describes the behavior of particles right up to the boundary. Similar assumptions have been made in the theory of classical gas flow. They lead to the famous Maxwell boundary condition for rarified gas flow [115, 117, 118].

In view of Eq. (4.17) it is clear, that only the impinging particles contribute to the momentum current average (4.10). Eq. (4.10) then gives

$$\zeta = \frac{\pi^2\beta^3 v^3\hbar^2}{3N\zeta(3)}\eta \approx 0.6 l_{ee}. \tag{4.23}$$

Again, the result is written in terms of the electron-electron mean free path $l_{ee} = v\hbar/\left(C_1\nu\alpha^2 k_B T\right)$, $C_1 = 1.950$.

4.2.3 Discussion

For $T \to 0$ the slip length in both, the nearly specular, and the diffuse limits diverge. In the diffuse case it is $\zeta \sim T^{-1} \ln^3 \left(T_\Lambda/T\right)$ with $T_\Lambda = \Lambda/k_B$. The logarithmic factor stems from the renormalization of the electron velocity at low temperatures (see Sec. 1.2). Λ is a band structure dependent cut-off on the order of 1 eV. In the nearly specular limit holds $\zeta \sim T^{-4} \ln^6 \left(T_\Lambda/T\right)$. The reasons for this behavior are twofold. The slowing down of the liquid at the boundary depends on how effective the boundary absorbs momentum (roughness), but also on how efficient the momentum tranport towards the boundary is. Both mechanisms fail at low temperatures. The momentum tranport becomes less efficient because it is caused by electron-electron collisions and the corresponding scattering length diverges as $1/T$. This fact is responsible for the $1/T$ divergence of the slip length in the diffuse limit. On the other hand, the boundary scattering becomes less efficient as the thermal wavelength $\lambda_T = \hbar v/k_B T$ of electrons grows compared to the edge roughness. This mechanism is responsible for the additional factor of $1/T^3$ in the expression for the nearly specular limit. The temperature dependencies of the slip lengths in both limits are shown in Fig. 4.6.

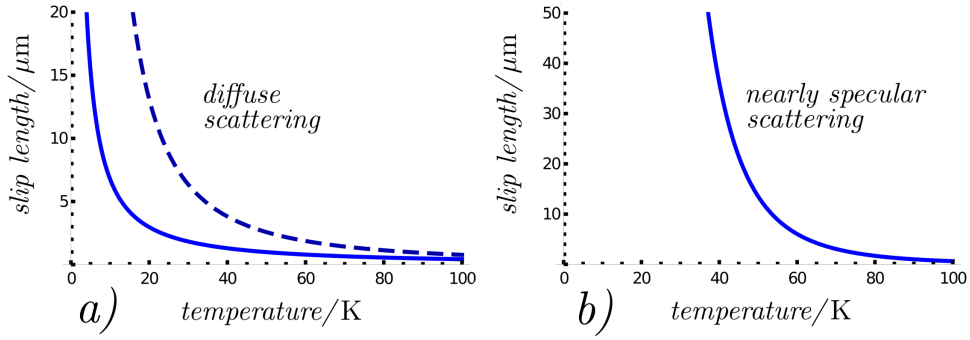

Figure 4.6: The temperature dependence of the slip length ζ for (a) diffuse scattering at the boundary of graphene at the charge neutrality point (continuous line) and at a finite chemical potential $\mu = 0.25\,\text{eV}$ (dashed line) and (b) scattering at a microscopically rough edge with a typical roughness amplitude $h = h' = 250\,\text{Å}$ at charge neutrality. At charge neutrality the slip length grows as $T^{-4} \ln^6 \left(T_\Lambda/T\right)$ in the nearly specular and as $T^{-1} \ln \left(T_\Lambda/T\right)$ in the diffuse limits. $T_\Lambda = \Lambda/k_B$ is the cut-off temperature. $\Lambda = 1\,\text{eV}$ was used here. At a finite chemical potential, the slip length behaves as $\zeta \sim T^{-2}/\ln \left(\epsilon_F/T\right)$ in both limits, but is parametrically larger in the nearly specular case.

In the renormalization of velocity $v_0 \to v = v_0 \left(1 + \alpha \ln \left(\Lambda/k_B T\right)\right)$ and coupling constant $\alpha \to \alpha_r = e^2/(4\pi\epsilon\hbar v)$ a cut-off of $\Lambda = 1\,\text{eV}$ was used. A permittivity of $\varepsilon = 5\varepsilon_0$ was assumed. The small parameter κ for the nearly specular limit remains reasonably small up to $h = h' \approx 250\,\text{Å}$ at temperatures below 100 K.

In the diffusive limit, for the above parameter values, ζ ranges from 100 μm at 1K to 0.4 μm at 100K. In the nearly specular limit, for a small roughness of the order of $h = h' = 10\,\text{Å}$, ζ can compete with the length of the Trans-Siberian Railway at $T = 1\,\text{K}$ and ranges to 1 mm at $T = 100\,\text{K}$. For a fairly rough edge of $h = h' = 250\,\text{Å}$ it is $\zeta = 3.5\,\text{km}$ at 1 K, and at $T = 100\,\text{K}$ the slip length shrinks to $\zeta \approx 0.6\,\mu\text{m}$ and approaches the diffuse limit.

The value of ζ has to be compared to the width of the sample. If ζ is comparable to, or smaller than the width, the mixed boundary condition of Eq. (4.4) should be applied, in certain situations even the

no-stress boundary conditions (4.3) can be appropriate.

4.3 The slip length of Fermi liquids

Now, the calculation of the slip length for a Fermi liquid, which includes graphene at finite charge densities ($\epsilon_F \gg k_B T$) will be adressed. The above results can be easily generalized to this case. In two dimensions, the same set-up with a semi-infinite current carrying sheet at $y > 0$ will be considered. Again, the flow shall be tangential to the sample boundary. In three dimensions, the flow is in x-direction and shall not depend on the z coordinate.

The bulk distribution function has the form of Eq. (4.18), where following Ref. [13], the non-equilibrium contribution Ψ, which describes the response to gradients of the flow velocity $\mathbf{u}$, is written in the from of

$$\Psi = +q\left(k\right) k_x \frac{\partial \varepsilon}{\partial k_y} \frac{\partial u_x}{\partial y}. \tag{4.24}$$

The dispersion relation is given by $\varepsilon = v_F \hbar \left(k - k_F\right) + \varepsilon_F$. The physical content is hidden in the function $q\left(k\right)$, which determines the electron-electron scattering time

$$\tau = \int_{-\infty}^{\infty} dx \frac{q\left(x\right)}{\left(2\cosh\left(\frac{x}{2}\right)\right)^2}. \tag{4.25}$$

Here, $x = \left(\varepsilon - \varepsilon_F\right) / \left(k_B T\right)$ is a dimensionless variable. Quantities of interest can be written in terms of τ. For example the viscosity in $d = 3$ dimensions equals

$$\eta = \frac{2}{15} v_F^2 \rho_F \varepsilon_F m^* \tau \tag{4.26}$$

and for $d = 2$

$$\eta = \frac{1}{4} v_F^2 \rho_F \varepsilon_F m^* \tau. \tag{4.27}$$

Here ρ_F is the density of states at the Fermi surface, m^* is the effective mass of the electrons ($m^* = \hbar k_F / v$ for graphene).

It was shown in Ref. [13] that in $d = 3$, $q\left(x\right)$ can be approximated by a constant. The leading temperature dependece at $\varepsilon_F \gg k_B T$ then is $\eta \propto q \propto T^{-2}$. The only change in the boundary condition for the kinetic equation (4.16) is that the integrations have to be extended over the two dimensions of the xz-surface. Only the $\lambda = +1$ part is relevant for a finite Fermi-energy and a spin degeneracy of $N = 2$ is assumed (for graphene $N = 4$ due do the 2×2 spin valley degeneracy).

The characteristic wavelength of electrons is now given by the Fermi wavelength $\lambda_F = 2\pi / k_F$. This is important for the nearly specular limit. Since $\lambda_F \ll \lambda_T$, Fermi liquids are more susceptible to edge roughness; the roughness parameter $\kappa = h^2 h'^2 / \lambda_F^4$ is larger. The slip length can be derived from Eq. (4.10), and it holds

$$\zeta = \left(\frac{1}{h^2 h'^2 k_F^4}\right) \chi \approx \left(\frac{1}{h^2 h'^2 k_F^4}\right) 3 l_{ee}, \tag{4.28}$$

where $\chi = \frac{45\pi^2}{k_F^4 \hbar} \eta$. In the limit of diffuse scattering the slip length is given by

$$\zeta = \frac{8\pi^2}{k_F^4 \hbar} \eta \approx 0.5 l_{ee}. \tag{4.29}$$

Here $l_{ee} = v_F\tau$ and $\rho_F = m^* k_F / \left(\hbar\pi\right)^2$ were used. The temperature dependence of the slip length in the diffuse scattering limit as well as in the nearly specular limit is $\zeta \sim 1/T^2$. Since the wavelength of Fermi liquid electrons does not depend on the temperature, the behavior in both limits is governed by the efficiency of momentum transport towards the boundary; the limiting factor is the $1/T^2$ divergence of the electron-electron scattering length.

The situation is slightly different for $d = 2$. Here, the scattering time τ can be crudely approximated by the quasiparticle lifetime, which is suppressed by a logarithmic factor compared to the $d = 3$ case [119]. The lifetime of Fermi liquid quasiparticles in $d = 2$ is the subject of a number of publications [120–122]. It can be estimated as

$$\tau_{qp} = A\frac{\varepsilon_F\hbar}{\left(k_B T\right)^2}\frac{1}{\ln\left(\frac{\varepsilon_F}{k_B T}\right)}, \tag{4.30}$$

where A is a coefficient of the order of one. The momentum current balance equation (4.10) gives, in the nearly specular limit,

$$\zeta = \left(\frac{\hbar^3 v_F^3/\varepsilon_F^3}{h^2 h'}\right)\chi \approx \left(\frac{1}{h^2 h' k_F^3}\right) 1.1 l_{ee}, \tag{4.31}$$

with $\chi = \frac{2}{\sqrt{\pi}} v_F\tau$, and in the diffuse limit $\zeta = \frac{3\pi}{8} v_F\tau$, so that

$$\zeta \approx 1.2 l_{ee}. \tag{4.32}$$

These results also apply to graphene at a finite chemical potential. The viscosity of graphene away from the Dirac point is given by $\eta = \frac{1}{8}\rho_F^G \mu^2\tau$, where ρ_F^G is the graphene density of states at the Fermi surface, and $\mu \gg k_B T$ the chemical potential. Due to the $1/T^2$ divergence of the scattering length, the slip lengths of Fermi liquid graphene are larger than those of the Dirac liquid (see Fig. 4.6). For $\mu = 0.25\,\mathrm{eV}$, they can range from $0.8\,\mu\mathrm{m}$ at $100\,\mathrm{K}$ to 3mm at $1\,\mathrm{K}$. The due to the short wavelength λ_F of Fermi liquid excitations, the boundary scattering can be expected to saturate in the diffusive limit for smaller roughnesses then at charge neutrality.

4.4 Comparison to known theoretical results

The importance of the slip length was brought to the attention of the quantum fluid community in the 1980s, in the context of measurements of the viscosity of Fermi liquid He^3 [87]. Ref. [87] calculates the slip length using the Bhatnagar-Gross-Krook theory (see Sec. 2.2.3). Here, the beautiful approach of Ref. [87] will be outlined. In particular, it is demonstrated in Ref. [87] that Maxwell's idea to use the bulk distribution function to approximate the behavior of particles impinging the wall, which was also used here to derive the slip length in the diffuse limit, gives a good lower bound on the slip-length. In general, however, the physics of the Knudsen layer - an approximately one mean free path wide layer at the boundary of the liquid - has to be considered. Here the fluid dynamics is dominated by particle-wall collisions and the distribution function strongly deviates from the local equilibrium (see Fig. 4.7).

The collision integral is modelled by the BGK ansatz of Eq. (2.20). The deviation of the distribution function f from the local equilibrium is called g:

$$g = f - f^{l.e.}.$$

Let the two or three dimensional liquid be contained in the volume $y > 0$ and the y axis be orthogonal to the sample boundary. For the moment the dispersion relation ε doesn't have to be specified, and

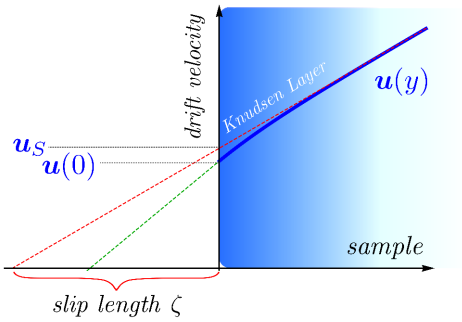

Figure 4.7: The Knudsen layer is a thin fluid layer located at the sample boundary. Here, physics is dominated by particle-wall collisions and the distribution funcion largely deviates from local equilibrium. The Knudsen layer is not described by hydrodynamics. Instead, the slip lenght provides an effective quantity encompassing all information on the edge-fluid bondary.

the kinetic equation reads

$$v_y \frac{\partial g}{\partial y} - v_y p_x \frac{\partial f^0}{\partial \varepsilon} \frac{\partial u_x}{\partial y} = -\frac{g}{\tau}. \tag{4.33}$$

It is $\partial f^0/\partial\varepsilon = \beta f^{(0)}\left(1 - f^{(0)}\right)$ with $\beta = 1/\left(k_B T\right)$. One solution to this first order differential equation for g is given by

$$\begin{aligned} g_{v_y>0} &= p_x u\left(0\right) \frac{\partial f^0}{\partial \varepsilon} e^{-\frac{y}{\tau v_y}} + \int_0^y dy' p_x u'\left(y'\right) \frac{\partial f^0}{\partial \varepsilon} e^{-\frac{|y'-y|}{\tau v_y}} \\ g_{v_y<0} &= -\int_y^\infty dy' p_x u'\left(y'\right) \frac{\partial f^0}{\partial \varepsilon} e^{\frac{|y'-y|}{\tau v_y}}. \end{aligned} \tag{4.34}$$

This solution has several important features. At an infinite distance from the wall it is

$$g\left(\infty\right) = \tau v_y p_x \frac{\partial f^0}{\partial \varepsilon} u'\left(\infty\right). \tag{4.35}$$

This corresponds to a finite gradient of the flow velocity $\mathbf{u}$; at $y \to \infty$ the deviation from local equilibrium is small and is governed by the law of hydrodynamics. Here, the fluid particles have lost all memory of collisions with the wall. On the other hand, diffuse scattering at the wall can be modelled by assuming that the distribution of reflected particles ($v_y > 0$) at the edge is $f^{>}\left(0\right) = f^{(0)}$, which is equivalent to

$$g\left(0\right) = p_x u\left(0\right) \frac{\partial f^0}{\partial \varepsilon},$$

holding for $v_y > 0$. The influx of tangential momentum into the Knudsen layer is given by $-\eta u'(\infty)$. The authors of Ref. [87] assume that this current is constant in the whole Knudsen layer, and is only converted into a tangential flow at the boundary, giving rise to a velocity slip. In our treatment of the kinetic distribution in the nearly specular case (Sec. 4.2.1), we showed that the variation of the tangential momentum current gives a contribution subleading in the small parameter $h^2 L/\lambda_T^3$. Thus,

we explicitly saw that the assumption holds. If it holds in the totally diffuse case as well, we can write

$$\begin{aligned}-\eta u'(\infty) = &\int_> \frac{d^dk}{(2\pi)^d} v_y p_x^2 u(0) \frac{\partial f^0}{\partial \varepsilon} e^{-\frac{y}{\tau v_y}} \\ &+ \int_> \frac{d^dk}{(2\pi)^d} v_y p_x^2 \int_0^y dy' u'\left(y'\right) \frac{\partial f^0}{\partial \varepsilon} e^{-\frac{\left|y'-y\right|}{\tau v_y}} \\ &- \int_< \frac{d^dk}{(2\pi)^d} \int_y^\infty dy' v_y p_x^2 u'\left(y'\right) \frac{\partial f^0}{\partial \varepsilon} e^{\frac{\left|y'-y\right|}{\tau v_y}}. \end{aligned} \tag{4.36}$$

This is an integral equation for $u'\left(y\right)$. Ref. [87] presents an elegent way to derive the slip length without solving this equation explicitely. To this end, an auxilary function $L_n\left(y\right)$ is introduced:

$$L_n\left(y\right) = g_N \int_> \frac{d^dk}{(2\pi)^d} v_y p_x^2 \left(\tau v_y\right)^{n-1} \left(-\frac{\partial f^0}{\partial \varepsilon}\right) e^{-\frac{y}{\tau v_y}}. \tag{4.37}$$

The factor g_N accounts for degeneracies. In the case of graphene $g_N = 2N = 8$ due to the spin-valley degeneracy and the equal contributions of electrons and holes. Physical quantities can be expressed with the help of $L_n\left(y\right)$. For the viscosity holds

$$\eta = \tau \int \frac{d^dk}{(2\pi)^d} v_y^2 p_x^2 \left(-\frac{\partial f^0}{\partial \varepsilon}\right) = 2L_2(0). \tag{4.38}$$

Defining the function $\Phi(z)$ via the equation $u'(z) = u'(\infty)\left(1 + \Phi(z)\right)$ and abbreviating $y_0 = u(0)/u'(\infty)$, Eq. (4.36) can be written as

$$z_0 L_1(z) - L_2(z) = -\int_0^\infty dz' \Phi\left(z'\right) L_1\left(\left|z - z'\right|\right). \tag{4.39}$$

The function $\Phi(z)$ is positive everywhere, since the flow velocity in the Knudsen layer is smaller than the hydrodynamic flow velocity $u_S = \zeta u'(\infty)$ at $y = \infty$. Additionally $\Phi(z)$ vanishes for $y \to \infty$. A look at Fig. 4.7 shows, that for the slip length ζ holds

$$u_S = u'(\infty)\,\zeta = u(0) + \int_0^\infty u'\left(z'\right) - u'(\infty)\, dy', \tag{4.40}$$

or, using the function $\Phi(z)$

$$\zeta = y_0 + \int_0^\infty \Phi\left(y'\right) dy'. \tag{4.41}$$

Combining the Eqs. (4.41) and (4.39) one obtains

$$\zeta L_1\left(y\right) - L_2\left(y\right) = -\int_0^\infty dy' \Phi\left(y'\right) \left(L_2\left(\left|y - y'\right|\right) - L_1\left(y\right)\right). \tag{4.42}$$

Using the fact that $dL_n\left(y\right)/dy = -L_{n-1}\left(y\right)$, the above equation can be integrated over the region $y > 0$. This leads to another identity for the slip-length

$$\zeta L_2(0) - L_3(0) = \int_0^\infty dy' \Phi\left(y'\right) \left(L_2\left(y'\right) - L_2(0)\right). \tag{4.43}$$

The identities (4.42) and (4.43) lead to lower and upper bounds on the slip length. It is $L_n\left(y>0\right) < L_n\left(0\right)$, and on the other hand $\Phi\left(z\right)>0$ holds, therefore from Eq. (4.42) follows

$$\zeta > \frac{L_2\left(0\right)}{L_1\left(0\right)}. \tag{4.44}$$

Similarly, (4.43) yields

$$\zeta < \frac{L_3\left(0\right)}{L_2\left(0\right)}. \tag{4.45}$$

The lower bound can be improved [87]:

$$\zeta > \frac{1}{2}\left(\frac{L_2\left(0\right)}{L_1\left(0\right)} + \frac{L_3\left(0\right)}{L_2\left(0\right)}\right). \tag{4.46}$$

The bounds are typically very close, giving a good estimate on ζ. For graphene, the upper bound and the lower bound are very close: $\zeta_{upper} \approx 1.15\zeta_{lower}$. The result of the Maxwell approach (using the bulk distribution for the impinging particles) as used in Sec. 4.2.2, is in fact equivalent to the lower bound (4.44). Remembering the parametrization (4.18), the momentum current balance equation (4.10) can be written as

$$0 = -\frac{1}{2}\eta\frac{\partial u_x}{\partial y} + \int \frac{d^dk}{(2\pi)} v_y p_x^2 u\left(0\right)\left(-\frac{\partial f^0}{\partial \varepsilon}\right), \tag{4.47}$$

where the degeneracies have been omitted. Approximating $\zeta_{lower} = u\left(0\right)/\left(\partial u_x/\partial y\right)$ (for the exact slip length we need to replace $u\left(0\right)$ by u_S), one obtains

$$\zeta_{lower} = \frac{\eta/2}{\int \frac{d^dk}{(2\pi)} v_y p_x^2 \left(-\frac{\partial f^0}{\partial \varepsilon}\right)} = \frac{L_2\left(0\right)}{L_1\left(0\right)}. \tag{4.48}$$

This result is exactly the lower bound (4.44). It is also identical to the slip lengths of (4.23), (4.29).

4.5 Experimental results

There exists a great number of works studying the specularity of edges of different materials using transverse magnetic focusing [123]. A focused electron beam is injected into the material. Due to a transverse magnetic field the trajectory of the beam is circular. Starting at the edge, the electron beam is again deflected towards the edge by the magnetic field, reflected on the boundary, and send onto a new (semi-)circular trajectory (see Fig. 4.8). The specularity is measured in terms of a coefficient q - the fraction of specularely reflected electrons. For the edges of oxygen-plasma-etched graphene a q between 0.2 and 0.5 was reported [124]. In this case the slip length ζ can be expected to lie between the nearly specular and the diffuse limits.

Several recent experiments allow to draw conclusions on the slip lengths of electron liquids in graphene and delafossite metals. Signatures of hydrodynamic transport in the ultrapure delafossite metal $PdCoO_2$ were reported in Ref. [24]. The estimated viscosity of the electron liquid is $6\times10^{-3}\,\mathrm{kg/ms}$. Eq. (4.29) predicts a slip length of $\zeta = 0.45$, which is consistent with the reported observation of Poiseuille flow (Gurzhi effect) considering the sample sizes of up to $60\,\mu\mathrm{m}$. Similar values were reported in Ref. [25] for the Weyl semimetal WP_2. The reported viscosity seem, however, very small considering the low

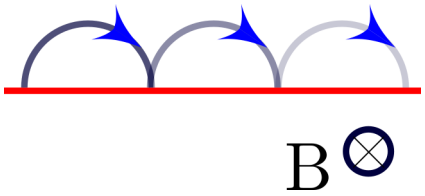

Figure 4.8: A magnetic focusing experiment measuring the specularity of the edge of a solid material (red). A focused electron beam is moving on a circular trajectory due to the out of plane magnetic field B. In each reflection from the edge, a fraction q of electrons is specularely reflected. q is called the specularity coefficient.

temperature at which the experiments were carried out. Much higher viscosities are expected for a typical Fermi liquid due to the $\eta \sim E_F^2/\left(k_B T\right)^2$ scaling [13].

The results of Eqs. (4.22) and (4.23) explain the findings of Ref. [27] for relatively narrow (doped) graphene sheets. Here, no Gurzhi effect in samples of up to 4 µm width could be measured, up to temperatures of 100 K. A small signature of the Gurzhi effect as been reported at temperatures around 100 K. This is in fact consistent with the results presented here. At a temperature of 100 K the slip length indeed drops below 1 µm (see Fig. 4.6).

The most up to date measurements of Poiseuille flow in (doped) graphene are those made by Sulpizio et. al. [30] (see also Sec. 2.5) shown in Fig 4.9. Here an experimental estimate for the slip-length was given: 0.5 µm at 75 K, which is close to the value predicted by Eq. (4.23) (see Fig. 4.6). Considering the large sample witdh used in this experiment, Poseuille flow, indeed, should be observed.

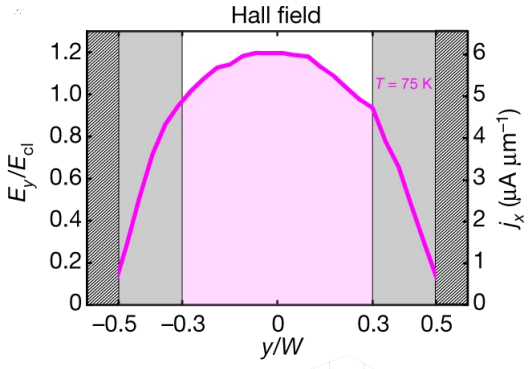

Figure 4.9: Poiseuille profile of the electron liquid of graphene as measured in the experiment of Sulpizio et. al. [30]. The nonzero velocity at the boundary implies finite slip. The extrapolated slip length of 0.5 µm at 75 K agrees with the value predicted by Eq. (4.23) (see Fig. 4.6). The figure was copied from Ref. [30].

4.6 Flow through a strip with a circular defect: an example for the no-stress flow of a Dirac liquid.

Materials in electron hydrodynamics often have sizes in the µm range. At low temperatures, and/or for specular boundaries, slip lengths can be of the same order of magnitude or larger and the no-

stress conditions of Eq. 4.3 describe the behavior of the electron fluid at the sample edges. If so, the conductivity of a Poiseuille sample is infinite, or limited by non-hydrodynamic parameters such as e.g. impurity concetrations. The Gurzhi effect seases to be an accurate indicator of hydrodynamic flow [27].

However, in more complicated geometries, e.g. if the fluid has to pass an obstacle, viscous shear forces dominate the conductivity. This can be used to indentify hydrodynamic behavior, even if the Gurzhi effect is not observable due to a large slip length.

As an example the flow of a Dirac fluid confined to a long strip, past a circular defect (see Fig. 4.10) will be examined. The hydrodynamics of a Dirac liquid has several distinct features setting it apart from classical and Fermi liquids. These include that the hydrodynamic flow velocity $\mathbf{u}$ is connected to the heat current $\mathbf{j}_E$. In Galilei invariant systems the charge current density $\mathbf{j}$ is proportional to the flow velocity $\mathbf{u}$

$$\mathbf{j} = ne\mathbf{u}. \tag{4.49}$$

Here n is the charge density and e the electron charge. Therefore, in a clean material where no momentum is dissipated, the hydrodynamic equations describe the flow of charge and the flow patterns can be inferred from measurements of the charge current density $\mathbf{j}$.

Charge neutral graphene, however, shows a very different behavior. Here, due to the linear dispersion relation (see Sec 1.1), the flow velocity is related to the thermal current $\mathbf{j}_E$ [39]:

$$\mathbf{j}_E = \frac{3n_E\mathbf{u}}{2 + u^2/v^2}. \tag{4.50}$$

$n_E =$ is the energy density of the Dirac liauid. The graphene dispersion is $\varepsilon_{\mathbf{k}} = \lambda v k$ and the group velocity $\mathbf{v}_\lambda = \lambda v\mathbf{k}/k$, where $\lambda = \pm 1$. The heat current $\mathbf{v}_\lambda\varepsilon_{\mathbf{k}} = v\mathbf{k}$ is proportional to momentum. On the other hand, the charge current $e\mathbf{v}_\lambda = \lambda ev\mathbf{k}/k$ is not. Charge neutral graphene possesses an electron-hole symmetry. Electrons ($\lambda = 1$) and holes ($\lambda = -1$) equally contribute to charge and thermal currents. However, under the influence of an electric field electrons and holes move in opposite direction (sign of $\mathbf{v}_\lambda$), and the sum of their momenta averages out. This means that charge currents are not protected by momentum conservation and can decay, leading to a finite interaction induced conductivity in perfectly clean graphen samples [49]. The transport of heat, on the other hand, is protected by momentum conservation and clean graphene samples at the charge neutrality point have an infinite heat conductivity. This is the reason for the violation of the Wiedemann-Franz law observed in [50] (see Sec. 2.5). A temperature gradient has to be applied to excite a finite momentum density. This can be seen from the Gibbs-Duhem relation $\Omega = -pV$. With the differential of the grand potential $\nabla\Omega = S\nabla T + N\nabla\mu - p\nabla V$, and assuming charge neutrality ($n = 0$ see Appendix A.3 for details) one finds

$$\nabla p = s\nabla T. \tag{4.51}$$

Inserting this into the Stokes equation (2.7) gives

$$s\nabla T = \eta\Delta\mathbf{u}. \tag{4.52}$$

Thus hydrodynamics in charge neutral graphene can be probed by measuring thermal currents stemming from applied temperature gradients.

To illustrate these features, the flow and pressure profiles in a graphene strip of width w will be calculated. The strip extands from $y = -w/2$ to $y = w/2$ and is infinitely long. At $y = 0$ an

impenetrable disk of radius a hinders the flow. One quantity of interest is the pressure difference between the opposite ends of the strip at $x = -\infty$ and $x = \infty$, which translates to a temperature difference according to Eq. (4.51)

4.6.1 Stokes' paradox and Oseen's equation

An interesting effect in two dimensional hydrodynamics is the Stokes paradox. It can be statet as "the velocity $\mathbf{u}$ of the flow past an impenetrable object in two dimensions is not a linear function of the pressure gradient ∇p for small ∇p". Imagine an object being dragged through the fluid. A natural assumption would be that the fluid is at rest at infinity $\mathbf{u}(\mathbf{x}) \to 0$ as $|\mathbf{x}| \to \infty$. The paradox here is, that Stokes' equation (4.1), which is linear in $\mathbf{u}$, has no non-trivial solution with vanishing flow at infinity. This problem does not appear in three dimensions, where the object is a less significant perturbation due to the higher dimensionality. The solution was found by swedish physicist Oseen [125, 126] in terms of what is now known as Oseen's equation.

The full Navier-Stokes equation for graphene electrons reads [51, 113]

$$\frac{\tilde{w}}{v^2}\left(\partial_t \mathbf{u} + \left(\mathbf{u}\cdot\nabla\right)\mathbf{u}\right) + \nabla p + \frac{\partial_t p}{v^2}\mathbf{u} - \eta\nabla^2\mathbf{u} = 0. \tag{4.53}$$

$\tilde{w}$ is the enthalpy density $\tilde{w} = \frac{3n_E/2}{2+|\mathbf{u}|/v} \approx \tilde{w}_0 = \frac{3}{2}n_E$, where n_E is the energy density. The idea behind Oseen's equation is to linearize around a constant uniform flow $\mathbf{U}$ instead of linearizing around $\mathbf{u} = 0$. Writing

$$\mathbf{u} = \mathbf{U} + \mathbf{q},$$

the linearized Navier-Stokes equation reads

$$\frac{\tilde{w}_0}{v^2}\left(\mathbf{U}\cdot\nabla\right)\mathbf{q} + \nabla p - \eta\nabla^2\mathbf{q} = 0. \tag{4.54}$$

For the strip geometry to be studied here $\mathbf{U} = U\hat{\mathbf{e}}_x$ is an obvious choise.

4.6.2 Solution with the method of image charges

In Appendix A.2 the general solution to Eq. (4.54) is given. The analysis of Ref. [127] was generalized to arbitrary boundary conditions in the form of Eq. (4.4), and the flow around the obstacle for an arbitrary ζ on an infinite domain was calculated. If the flow is not confined to the strip, the pressure induced by the obstacle vanishes at infinity, where it behaves as $p \sim 1/r$. If, however, the flow is bounded to the region $y = \pm w/2$, the obstacle induces a pressure difference along the strip. The boundary conditions imposed on the electron flow by the two walls at $y = \pm w/2$ are

$$\begin{aligned} q_y\left(y = \pm w/2\right) &= 0 \\ \frac{\partial q_x\left(y = \pm w/2\right)}{\partial y} &= 0. \end{aligned} \tag{4.55}$$

These are no-stress boundary conditions, appropriate for a large slip length. The boundary conditions can be implemented using the method of images, known from electrostatics. The expression

$$\mathbf{q}_{tot} = \sum_{j=-\infty}^{\infty} \mathbf{q}\left(x, y + jw\right), \tag{4.56}$$

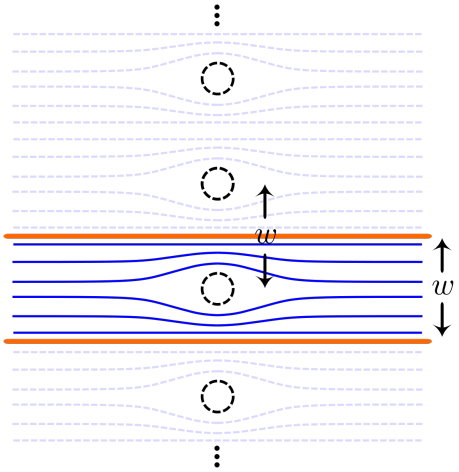

Figure 4.10: The method of images can be used to solve Eq. (4.54) for a strip-like sample geometry with a circular obstacle. The sample and the electron flow are drawn in color, the image fields are shown in light grey. Infinitely many image solutions must be placed symmetrically around the obstacle in the middle of the sample.

where $\mathbf{q}\left(x,y\right)$ is the infinite domain solution obtained in the Eqs. (A.12)-(A.20), does satisfy Eq. (4.54) everywhere inside the strip and matches the conditions of Eq. (4.55). It corresponds to infinitely many image fields placed along the y-axis, symmetrically to the original obstacle at $y=0$ (see Fig. 4.10). The solution $\mathbf{q}_{tot}$ is only approximate, because the boundary condition at the surface of the obstacle is not matched exactly. It is matched, however, at $r=a$ and $y=0$. Therefore, the error is of order $\sim \frac{a}{w}$, i. e. small, if the obstacle is small compared to the width of the strip. The pressure distribution along the sample can then be calculated from the function

$$\phi_j = \phi\left(x, y+jw\right). \tag{4.57}$$

ϕ solves the Laplace equation and is defined in Eq. (A.14). The pressure generated by every single image field is

$$p\left(x,y+jm\right) = U\frac{\tilde{w}_0}{v^2}\partial\phi_j/\partial x$$

(for details see appendix A.2 and Ref [127]). The total pressure at $y=0$ is

$$\begin{aligned} p_{tot} &= \sum_{j=-\infty}^{j=\infty} p\left(x,jm\right) \\ &= \frac{\pi A_0 U^2}{w}\frac{\tilde{w_0}}{v^2}\coth\left(\frac{\pi x}{w}\right) \\ &\quad +\mathrm{sgn}(x)\frac{\pi^2 A_1 U^2}{w^2}\frac{\tilde{w_0}}{v^2}\sinh\left(\frac{\pi x}{w}\right)^{-2}. \end{aligned} \tag{4.58}$$

The constants A_0 and A_1 are given in Eqs. (A.18) and (A.19). While the pressure of any single image field $p\left(x,jm\right)$ vanishes for $x\to\pm\infty$, the sum over all image fields remains finite. The pressure difference across the sample then is

$$\Delta p = p_{tot}\left(x\to\infty\right) - p_{tot}\left(x\to-\infty\right) = 2\frac{\pi A_0 U^2}{w}\frac{\tilde{w_0}}{v^2}. \tag{4.59}$$

Using Eqs. (A.18), (A.20) and expanding the coefficient B_0 for small Reynolds $R = 2Ua/\nu$, as well as taking the limit $\zeta \to \infty$ for the slip length at the obstacle, one obtains

$$\Delta p = -\frac{8\pi U}{3 - 2\left(\log\left(\frac{aU}{4\nu}\right) + \gamma\right)} \frac{\tilde{w_0}}{v^2} \frac{\nu}{w}. \tag{4.60}$$

ν is the kinematic viscosity $\nu = \left(v^2/\tilde{w_0}\right)\eta$. As expected, the pressure arising due to a small flow velocity U cannot be linearized, which is a manifestation of Stoke's paradox. This result can be linked to an experimental setup in which a heat flow through the sample will induce a temperature difference. With the help of Eq. (4.51) the pressure difference is written as a temperature difference. The relation between the flow velocity U and the heat current density is given by the formula [113]

$$\mathbf{j}_E = \frac{3n_E\mathbf{U}}{2 + U^2/v^2} \approx \frac{3}{2} n_E \mathbf{U}. \tag{4.61}$$

With the total energy current being $I_E = j_E w$, Eq. (4.60) becomes

$$\left|\Delta T\right| = \frac{16\pi I_E \eta / \left(n_E w^2 s\right)}{9 - 6\left(\log\left(\frac{1}{9}\frac{I_E a}{v^2 \eta w}\right) + \gamma\right)}. \tag{4.62}$$

$\gamma \approx 0.58$ is the Euler constant. Formula (4.62) can be used to determine the viscosity η. The entropy density is given by [51]

$$s = N \frac{9\zeta(3)}{\pi} k_B \frac{\left(k_B T\right)^2}{\hbar^2 v^2}.$$

Fig. 4.11 shows the dependece of the induced temperature difference on the heat current through a 10 µm wide graphene sample at 50 K for an obstacle of radius $a = 1\,\mu$m. The dependence of the temperature difference $\left|\Delta T\right|$ on the radius a is shown on right panel of Fig. 4.11. The scaling behavior of the current with a and w is non-trivial due to the presence of a third length scale ν/U. Since no momentum is dissipated at the sample boundaries the temperature difference along the sample, far enough from the disc, does not depend on the length of the sample. The temperature difference is induced in the region near the disc only.

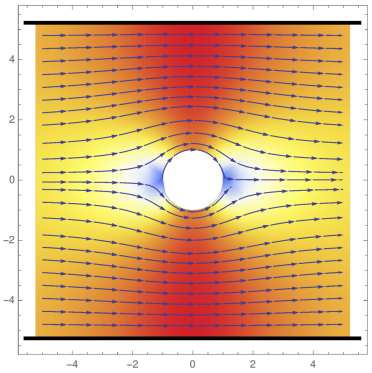

Figure 4.12: Flow velocity **u** for graphene electrons confined to a 10 µm wide strip with a circular defect of radius $a = 1\,\mu$m. For small Reynolds numbers the flow is nearly symmetric with respect to the defect. No-stress conditions were applied at the defect and at the edges of the graphene sample.

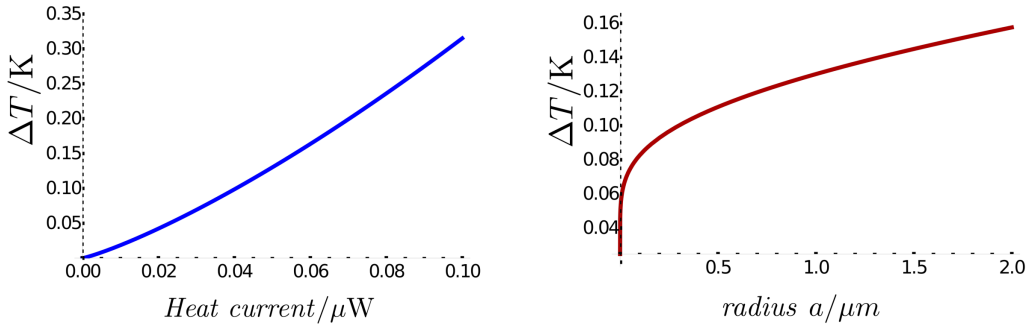

Figure 4.11: Left panel: Temperature difference induced by a heat current I_E through a 10 µm wide strip of charge neutral graphene at 50 K with a circular obstace of radius 1 µm at the center of the strip (see Fig. 4.10). At a heat current of 0.1µm the Reynolds number is ~ 0.74, approaching unity. The temperature difference is induced by viscous shear forces and can be used to measure the viscosity of Dirac liquid (4.62). Right panel: Temperature difference for a fixed heat current of $I_E = 0.5\mu$W through a 10 µm wide graphene channel at $50K$ as a function of the obstacle radius a. Notice the logarithmic divergence at small a - a feature that can be traced back to the Stokes paradox.

4.7 Summary

Hydrodynamic electron flow sensitively depends on the nature of the boundary conditions for the velocity flow field. These boundary conditions can be efficiently characterized by the slip length ζ, which is defined through the equation

$$u_\alpha^t\Big|_S = \zeta\, n_\beta \frac{\partial u_\alpha^t}{\partial x_\beta}\Big|_S , \tag{4.63}$$

where $\mathbf{u}^t\Big|_S$ is the flow velocity tangential to the sample boundary S, $\mathbf{n}$ is the normal vector on S, and x_α are the spatial coordinates. ζ quantifies the ability of the boundary to absorb the fluid's momentum. In the no-stress case $\zeta \to \infty$, the flow profile at the boundary is perfectly flat, meaning that no momentum is transported towards the boundary by viscous forces, and none is absorbed. For $\zeta \to 0$ the flow velocity at the boundary vanishes. The condition $u_\alpha^t\Big|_S = 0$ is thus referred to as no-slip boundary condition.

In order to obtain a quantitative understanding of the slip length in electron fluids, slip lengths at different kinds of edges for Dirac and Fermi liquids were derived. It was found, that for viscous electronic flow the slip length can always be written in the form

$$\zeta = f(\kappa)\, l_{\mathrm{ee,mc}} \tag{4.64}$$

with the dimensionless ratio $\kappa = h^2 h'^{d-1}/\lambda^{d+1}$ and the scattering length of momentum conserving electron-electron collisions $l_{\mathrm{ee,mc}}$. κ depends on the roughness amplitude h and the correlation length h' of the scattering edge, as well as on the electron wavelength λ. For graphene at the neutrality point, the latter is strongly temperature dependent ($\lambda = \hbar v/(k_\mathrm{B}T)$), while it corresponds to the Fermi wave length in the case of Fermi liquids ($\lambda = 2\pi/k_\mathrm{F}$). The scattering length $l_{\mathrm{ee,mc}}$ determins how effective

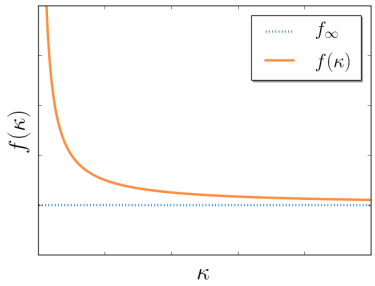

Figure 4.13: The slip length can be written in the form $\zeta = f(\kappa)\, l_{\mathrm{ee,mc}}$, where $l_{\mathrm{ee,mc}}$ is the scattering length of momentum conserving electron-electron collisions, and $f(\kappa)$ is a dimensionless function of the parameter $\kappa = h^2 h'^{d-1}/\lambda^{d+1}$, characterizing the nature of boundary scattering. For large κ (strong scattering), $f(\kappa)$ saturates, whereas for small κ it diverges according to $f(\kappa \ll 1) = f_0/\kappa$.

momentum transport towards the boundary is. The dimensionless function $f(\kappa)$ diverges for small κ: $f(\kappa \ll 1) = f_0/\kappa$, while it approaches a constant for strong interface scattering: $f(\kappa \to \infty) \to f_\infty$. We determined f_∞ using the assumption of diffuse scattering. The numerical values for the coefficients f_0 and f_∞ depend sensitively on the electronic dispersion relation and dimensionality of the system. They are given in Eqs. (4.23), (4.22) for the Dirac liquid, in Eqs. (4.29), (4.28) for the three-dimensional Fermi liquid and in Eqs. (4.32), (4.31) for the two dimensional Fermi liquid.

Since for all quantum fluids the mean free path diverges as the temperature approaches zero, the ultimate behavior of the slip length at low temperatures is $\zeta \to \infty$ and the no-stress boundary conditions are appropriate. For Dirac fluids in samples with weakly disordered edges even the ratio ζ/l_{ee} diverges as $T \to 0$. At intermediate temperatures the slip lengths are such that no-slip boundary conditions are justified for large sample sizes. In particular, it was shown that the electron viscosity of $PdCoO_2$ [24] and WP_2 [25] is small enough, such that Poiseuille type flow can manifest itself, as seen experimentally. The same applies to recent experiments with large graphene samples [30].

The fact that for a range of parameters no-stress boundary conditions hold is a characteristic feature of electron hydrodynamics, which sets it apart from its classical counterpart. Therefore, the flow of a Dirac liquid through a strip geometry with a disc-like obstacle was studied. No-stress boundary conditions were assumed to hold at the boundaries of the strip, as well as at the circumference of the disc. This is a realistic scenario for smooth boundaries at low temperatures. By solving Oseen's equation with the method of images, the pressure drop across the sample was calculated. Unlike with no-slip boundary conditions, here the pressure drop occurs exclusively due to viscous forces. The temperature difference that arises due to the pressure drop according to the formula $\nabla p = s\nabla T$ (see section 4.6 and appendix A.3) can be used to measure the shear viscosity of the Dirac liquid. Another interesting feature of such a flow is Stokes' paradox. Whereas for boundaries with a small slip length, Stokes' paradox is regularized by the loss of momentum at the boundaries [128], for no-stress conditions

$$\left|\Delta T\right| \propto \frac{I_E \eta}{\log\left(I_E\right)} \tag{4.65}$$

holds for a small energy current I_E through the sample. There is no well defined linear response regime, which is a manifestation of Stokes' paradox.

Chapter 5

5 Non-local hydrodynamic transport and collective excitations in Dirac fluids

The transport in a Dirac liquid is in many respects different from the archetypical example of the Fermi liquid. One important difference is that electric currents in a Dirac liquid are not protected by momentum conservation, and therefore decay even in a perfectly clean system. Negatively charged electrons and positive holes flowing in opposite directions sum up to a finite electric current with zero momentum. Thus, even in the absence of impurities, graphene at the charge neutrality point has a finite conductivity due to selectron-electron interactions [49, 54]. On the other hand, the energy current is proportional to the momentum density, and therefore propagates ballistically (see section 5.2.1 and the Refs. [51, 129]). Both phenomena, the interaction induced resistivity and the ballistic transport of energy, are relevant in the broader context of quantum criticality [53, 130]. Several experiments addressed the unique transport properties of the Dirac liquid. A violation of the Wiedemann-Franz law was observed in Ref. [50], indicating the ballistic transport of energy. The interaction induced resistivity was recently measured at finite frequencies [55] and showed to be comparable to theoretical predictions [49, 54].

In this chapter, the non-local hydrodynamic transport properties of the Dirac liquid will be studied. The analysis is based on the quantum Boltzmann equation approach of Ref. [49]. The distribution function will be expanded in terms of so-called collinear zero modes. These modes dominate the transport in the hydrodynamic regime (see section 5.1.2). The electrical and thermal conductivities, as well as the viscosity will be callculated at finite wavenumbers and frequencies. It will be shown, how these transport coefficients determine the hydrodynamics of the Dirac liquid.

In a clean system, hydrodynamics prevails when the electron-electron scattering rate l_{ee} is much smaller than the system size l_{geo}. The ratio between the two lengths is the Knudsen number

$$Kn = \frac{l_{ee}}{l_{\mathrm{geo}}}.$$

In the abscence of strongly inhomogeneous external fields, the characteristic wavenumber is set by the geometry of the sample $q \sim 2\pi/l_{\mathrm{geo}}$. Therefore, for finite Knudsen numbers, the wave-vector dependence of tranport coefficients determines the behavior of the fluid. Thinking in real space, this means that higher order spatial derivatives have to be included into the equations of motion of the fluid, and the flow becomes highly non-local. From a physical point of view, this is due to the fact that electrons loose memory of previous scattering events (e.g. collisions with the boundaries of the sample)

through electron-electron collisions on scales comparable to l_{ee}. In the case $l_{ee} > l_{\text{geo}}$, the trajetory of an electron at a given point depends on much of its history, which gives rise to a significant non-locality. This phenomenon is discussed and illustrated in Sec. 5.4 using the Poiseuille flow as an example.

The kinetic theory presented here also gives access to the collective excitations of the Dirac liquid. The dispersion relations of collective modes can be derived from the poles of transport coefficients, or found from the solutions of the homogeneous quantum Boltzmann equation. Focusing on the charge neutrality point, the work presented here goes beyond the phenomenological treatment of electron-electron interactions of Refs. [131, 132]. It is demonstrated that charge neutral graphene exhibits a plasmon mode that is damped due to the interaction induced resistivity and a second sound mode that describes the ballistic propagation of energy waves. Furthermore, a detailed analysis reveals a complex structure of damped collective excitations. These excitations are similar to the so-called "non-hydrodynamic" modes that were shown to be relevant for the equilibration of unitary fermi gases [133] and the hydrodynamization of quantum chromodynamics [134–136]. In fact, the term non-hydrodynamic is somewhat misleading. It is meant that these modes correspond to excitations of high angular momentum components of the kinetic distribution function, which are not described by the Navier-Stokes equations.

Remarkably, the calculations presented in this chapter are essentially exact in the limit of a small graphene fine structure constant α, which is the experimentally relevant case, because at experimental temperatures α is renormalized to small values (see Sec. 1.2). To calculate the non-local transport coefficients, relaxation rates of non-equilibrium excitations of high angular harmonics m have to be calculated. Surprisingly, the relaxation rates grow linearly with increasing m. This unexpected behavior allows to solve the Boltzmann equation exactly. The presentation here closely follows Ref. [137].

5.1 Theoretical framework

5.1.1 Kinetic equation

The basic methodological framework of this chapter builds upon the quantum Boltzmann equation. In its rudimentary form the quantum Boltzmann equation was derived in Sec. 2.4. Here, the specifics massless Dirac particles will be added. The analysis follows the derrivation presented in Ref. [49]. The Hamiltonian describing the interactions of electrons in graphene at charge neutrality is

$$H = H_0 + H_{\text{int}}, \tag{5.1}$$

where the free part is given by

$$H_0 = v\hbar \int_{\mathbf{k}} \sum_{a,b,i} \psi^{\dagger}_{a,i}\left(\mathbf{k}\right) \left(\mathbf{k}\cdot\sigma\right)_{ab} \psi_{b,i}\left(\mathbf{k}\right), \tag{5.2}$$

and the interaction part reads

$$H_{\text{int}} = \frac{1}{2}\int_{\mathbf{k},\mathbf{k}',\mathbf{q}} \sum_{a,b,i,j} V\left(\mathbf{q}\right) \psi^{\dagger}_{\mathbf{k}+\mathbf{q},a,i}\psi^{\dagger}_{\mathbf{k}'-\mathbf{q},b,j}\psi_{\mathbf{k}',b,j}\psi_{\mathbf{k},a,i}. \tag{5.3}$$

$V\left(\mathbf{q}\right) = \frac{2\pi e^2}{\varepsilon|\mathbf{q}|}$ is the 2D Coulomb potential. The indices $i, j = 1, 2 ..., N = 4$ refer to the spin and valley quantum numbers of an electron, whereas the two sublattices are labelled by the indices a, b. The free particle Hamiltonian H_0 is diagonalized by the unitary transformation

$$U_{\mathbf{k}} = \frac{1}{\sqrt{2}}\begin{bmatrix} 1 & o^*_{\mathbf{k}} \\ 1 & -o^*_{\mathbf{k}} \end{bmatrix}, \tag{5.4}$$

where $o_{\mathbf{k}} = \left(k_x + ik_y\right)/\sqrt{k_x^2 + k_y^2}$. The central quantity of interest is the kinetic distribution function of Eq. (2.31). For the derivation of the quantum Boltzmann equation, it is convenient to use the band representation of Dirac spinors $\psi_{\lambda,\mathbf{k}} = U_{\mathbf{k},\lambda a}\psi_{\mathbf{k},a}$ with $\lambda = \pm 1$ labeling the upper and lower dirac cones. In this way, one can easily distinguish between processes that involve the creation of particle hole pairs and those that do not. The thermally excited electron-hole pairs occupy states in a window of k_BT around the Dirac point. Thus, if the applied fields have frequencies $\omega < 2k_BT/\hbar$, which is true in the hydrodynamic regime, processes that create electron-hole pairs are unlikely and can be neglected. This translates to neglecting the off-diagonal components of the distribution function. Transforming the Green's function from the sublattice basis to the band basis,

$$g^{<}\left(\mathbf{X}, T; \mathbf{k}, \omega\right) = U_{\mathbf{k}}^{\dagger} G^{<}\left(\mathbf{X}, T; \mathbf{k}, \omega\right) U_{\mathbf{k}},$$

the distribution function is defined as

$$2\pi\delta\left(\omega - \varepsilon_{\mathbf{k}}\right) f_{\lambda}\left(\mathbf{X}, T; \mathbf{k}, \omega\right) \delta_{\lambda\lambda'} = -ig^{<}_{\lambda\lambda'}\left(\mathbf{X}, T; \mathbf{k}, \omega\right).$$

In the following, there will be no need to distinguish between center of mass and relative coordinates. $\mathbf{X}$ and T describe the space and time dependencies of the distribution function and will be relabeled $\mathbf{X} \to \mathbf{x}$, $T \to t$. The separation of scales discussed in Sec. 2.4 holds true in the hydrodynamic regime, where the characteristic scales of interactions and external fields are smaller than the characteristic wavelength of thermally excited electrons and holes $\lambda_T \sim \hbar v/k_BT$. The quantum Boltzmann equation then reads

$$\left(\partial_t + \mathbf{v}_{\mathbf{k}\lambda} \cdot \nabla_{\mathbf{x}} + \left(\mathbf{F}\left(\mathbf{x}, t\right) + e\mathbf{E}_V\right) \cdot \nabla_{\mathbf{k}} - \mathcal{C}\right) f_{\mathbf{k}\lambda}\left(\mathbf{x}, t\right) = 0. \tag{5.5}$$

Here, $\mathbf{v}_{\mathbf{k}\lambda} = \partial\varepsilon_{\mathbf{k}\lambda}/\partial\mathbf{k}$ is the group velocity and $\mathbf{F}\left(\mathbf{x}, t\right)$ an external force, in our case due to an electric field, or a thermal gradient. $\mathbf{E}_V$ is a self consistent electrich field produced by an inhomogeneous distribution of charges - the so called Vlasov field. It will be dealt with at the end of this section. $\mathcal{C}$ represents the Boltzmann collision operator describing short range electron-electron interactions. Details on the derivation of $\mathcal{C}$ are summerized in Appendix B.1, based on Refs. [49, 138].

Studying the linear response to $\mathbf{F}\left(\mathbf{x}, t\right)$, we expand the distribution function around the local equilibrium distribution $f^{(0)}_{k\lambda}$

$$f_{\mathbf{k}\lambda}\left(\mathbf{x}, t\right) = f^{(0)}_{k\lambda} + f^{(0)}_{k}\left(1 - f^{(0)}_{k}\right)\psi_{\mathbf{k}\lambda}\left(\mathbf{x}, t\right). \tag{5.6}$$

where $f^0_{k,\lambda}$ is given by

$$f^{(0)}_{k\lambda} = \frac{1}{e^{\beta\left(\varepsilon_{\mathbf{k}\lambda} - \mathbf{u}\cdot\mathbf{k}\right)} + 1}. \tag{5.7}$$

The product $f^{(0)}_{k}\left(1 - f^{(0)}_{k}\right)$ does not depend on λ, and the corresponding index is dropped in Eq. (5.6) and in the following. Linearized in the external force, the Boltzmann equation (5.5) reads

$$\left(\mathcal{L} + \mathcal{V} - \mathcal{C}\right)\psi = S. \tag{5.8}$$

$\mathcal{L}$ is the Liouville operator (without the linearized terms due to external forces and the without the Vlasov term) and is given by

$$\left(\mathcal{L}\psi\right)_{\mathbf{k},\lambda} = \left(\frac{\partial}{\partial t} + \mathbf{v}_{\lambda\mathbf{k}} \cdot \nabla_{\mathbf{x}}\right) f^{(0)}_{k}\left(1 - f^{(0)}_{k}\right)\psi_{\mathbf{k},\lambda}. \tag{5.9}$$

$\mathcal{V}$ represents the Vlasov term. This linearization scheme is equivalent to the Chapman-Enskog method carried out to first order in Sec. 2.2. The collision operator takes the form

$$\begin{aligned}\left(\mathcal{C}\psi\right)_{\mathbf{k}\lambda} &= \frac{2\pi}{\hbar}\int_{k'q}\delta\left(k+k'-\left|\mathbf{k}+\mathbf{q}\right|-\left|\mathbf{k}'-\mathbf{q}\right|\right) \\ &\times \left(1-f_k^{(0)}\right)\left(1-f_{k'}^{(0)}\right)f_{|\mathbf{k}+\mathbf{q}|}^{(0)}f_{|\mathbf{k}'-\mathbf{q}|}^{(0)} \\ &\times \left\{\gamma_{\mathbf{k},\mathbf{k}',\mathbf{q}}^{(1)}\left(\psi_{\mathbf{k}+\mathbf{q},\lambda}+\psi_{\mathbf{k}'-\mathbf{q},\lambda}-\psi_{\mathbf{k}',\lambda}-\psi_{\mathbf{k},\lambda}\right)\right. \\ &+ \left.\gamma_{\mathbf{k},\mathbf{k}',\mathbf{q}}^{(2)}\left(\psi_{\mathbf{k}+\mathbf{q},\lambda}-\psi_{-\mathbf{k}'+\mathbf{q},\bar{\lambda}}+\psi_{-\mathbf{k}',\bar{\lambda}}-\psi_{\mathbf{k},\lambda}\right)\right\}. \end{aligned} \tag{5.10}$$

The matrix elements $\gamma_{\mathbf{k},\mathbf{k}',\mathbf{q}}^{(1)}$, $\gamma_{\mathbf{k},\mathbf{k}',\mathbf{q}}^{(2)}$ are given in Appendix B.1. The right hand side of Eq. (5.8) is determined by the forces acting on the system $S = \mathbf{F}\left(\mathbf{x},t\right)\cdot\nabla_{\mathbf{k}}f_{k\lambda}^{(0)}$. The three forces studied here are the electric fields, thermal gradients and viscous forces. For an electric field E_0 oriented along the x-axis, $\mathbf{E}_0 = E_0\hat{\mathbf{e}}_x$, it reads

$$S_E = -eE_0\cos\theta\left(\lambda v\beta\right)f_k^{(0)}\left(1-f_k^{(0)}\right), \tag{5.11}$$

where θ is the polar angle of the momentum $\mathbf{k}$. The corresponding term for a thermal gradient ∇T is given by

$$S_T = -k\left|\nabla T\right|\cos\theta k_B\left(v\beta\right)^2 f_k^{(0)}\left(1-f_k^{(0)}\right). \tag{5.12}$$

A viscous force is present if the drift velocity $\mathbf{u}$ in the local equilibrium distribution function (5.7) is a function of the coordinate $\mathbf{x}$. Then the drift term of the Boltzmann equation (5.5) can be thought of as a force term:

$$\begin{aligned} S_S &= -\mathbf{v}_{\mathbf{k}\lambda}\cdot\nabla_{\mathbf{x}}f_{k\lambda}^{(0)} \\ &= -vkX_{0,\alpha\beta}\left(\frac{k_\alpha k_\beta}{k^2}-\frac{1}{2}\delta_{\alpha\beta}\right)\lambda\beta f_k^{(0)}\left(1-f_k^{(0)}\right), \\ &= -\frac{1}{2}kX_0\sin\left(2\theta\right)\left(\lambda v\beta\right)f_k^{(0)}\left(1-f_k^{(0)}\right), \end{aligned} \tag{5.13}$$

where the stress tensor is given by

$$X_{0,\alpha\beta} = \frac{1}{2}\left(\frac{\partial u_\alpha}{\partial x_\beta}+\frac{\partial u_\beta}{\partial x_\alpha}-2\delta_{\alpha\beta}\nabla\cdot\mathbf{u}\right).$$

In the following, we consider a flow with $\mathbf{u}\left(y\right) = u\left(y\right)\hat{\mathbf{e}}_x$ and therefore only include the component $X_{0,xy}$, which is relevant for the calculation of the shear viscosity.

Another important term in the kinetic equation describes the electrostatic forces that arise due to an inhomogeneous distribution of charges. These forces are mediated by a self consistent electric field $\mathbf{E}_V$, first introduced by Vlasov [139]. It reads

$$e\mathbf{E}_V = -\alpha vN\nabla_{\mathbf{x}}\int d^2x_1\sum_\lambda\int\frac{d^2k}{\left(2\pi\right)^2}\frac{f_k^{(0)}\left(1-f_k^{(0)}\right)\psi_{\mathbf{k},\lambda}\left(\mathbf{x}_1\right)}{\left|\mathbf{x}-\mathbf{x}_1\right|}. \tag{5.14}$$

A rigorous derivation of the term can be found in Ref. [90] (Eqs. (7-3) and (9-16)). Applying a Fourier transform to Eq. (5.14) one findse

$$e\mathbf{E}_V = -\alpha v N\left(i\mathbf{q}\right)\sum_\lambda \int \frac{d^2k}{\left(2\pi\right)^2}\frac{2\pi f_k^{(0)}\left(1-f_k^{(0)}\right)\psi_{\mathbf{k},\lambda}\left(\mathbf{x}_1\right)}{q}.$$

The corresponding term in the Boltzmann equation, linearized in $\psi_{\mathbf{k},\lambda}$, reads

$$\mathcal{V} = e\mathbf{E}_V\cdot\nabla_{\mathbf{k}} f^0_{k\lambda}. \tag{5.15}$$

5.1.2 Collinear zero modes

This section summerizes how Eq. (5.8) is solved in the limit of a small fine structure constant. A standard way to deal with an integral equation like (5.8) is to expand the function $\psi_{\mathbf{k},\lambda}$ into a set of suitable basis functions. The choice of this basis is facilitated by the fact that for small values of the graphene fine structure constant α, the collision operator (5.10) logarithmically diverges, if the velocities of involved particles are parallel to each other. This is a consequence of the linear single particle spectrum and the resulting momentum independent velocity of massless Dirac particles. Intuitively speaking, the scattering is enhanced, because particles travelling in the same direction interact with each other during a particularely long period of time. A more mathematical picture of this so-called collinear scattering is presented in Appendix (B.2). It is convenient to write the collision operator as a sum of the so-called collinear part $\mathcal{C}_c$ and the non-collinear part $\mathcal{C}_{nc}$:

$$\mathcal{C} = \log\left(1/\alpha\right)\mathcal{C}_c + \mathcal{C}_{nc}. \tag{5.16}$$

The factor $\log\left(1/\alpha\right)$ is large at small α. Both operators, $\mathcal{C}$ and $\mathcal{C}_c$, are hermitian with respect to the scalar product

$$\left\langle \phi \,\middle|\, \chi\right\rangle = \sum_\lambda \int \frac{d^2k}{\left(2\pi\right)^2}\phi_{\mathbf{k},\lambda}\chi_{\mathbf{k},\lambda}. \tag{5.17}$$

Let $\varphi^n_{\mathbf{k},\lambda}$ be the orthogonal eigenfunctions of $\mathcal{C}_c$ such that

$$\left(\mathcal{C}_c\varphi^n\right)_{\mathbf{k},\lambda} = b_n\varphi^n_{\mathbf{k},\lambda}. \tag{5.18}$$

$\psi_{\mathbf{k},\lambda}$ is expanded in terms of these functions:

$$\psi_{\mathbf{k},\lambda} = \sum_n \gamma_n\varphi^n_{\mathbf{k},\lambda}. \tag{5.19}$$

Suppose, some of the orthogonal basis functions φ^n, namely those with $n < n_0$, set the collinear part of the collision operator to zero, i.e.

$$\mathcal{C}_c\varphi^{n<n_0} = 0. \tag{5.20}$$

Then, inserting the expansion (5.19) into Eq. (5.8) and projecting it onto the basis functions $\varphi^{n'}$, one finds

$$\gamma_{n'>n_0} = \frac{\left\langle \varphi^{n'}\,\middle|\, S\right\rangle - \left\langle \varphi^{n'}\,\middle|\, \left(\mathcal{L}-\mathcal{C}_{nc}\right)\psi\right\rangle}{b_{n'}\log\left(1/\alpha\right)}. \tag{5.21}$$

This means that if there exist zero eigenfunctions of $\mathcal{C}_c$, they are dominant by the large factor $\log\left(1/\alpha\right)$. In fact, such eigenfunctions do exist. The functions

$$\chi_{\mathbf{k},\lambda}^{(m,s)} = \lambda^m e^{im\theta}\left\{1, \lambda, \lambda\beta v\hbar k\right\}, \tag{5.22}$$

where m labels the angular momentum, $s \in \left\{1,2,3\right\}$ the modes $\left\{1, \lambda, \lambda\beta vk\right\}$, and θ is the polar angle of the momentum vector $\mathbf{k}$, set the integral (5.10) to zero for collinear processes (see Appendix B.2). The modes of Eq. (5.19) are commonly referred to as collinear zero modes [49].

From Eq. (5.21) follows that for small values of α, only the collinear zero modes have to be retained in the expansion of Eq. (5.19), i.e. the kinetic equation (5.5) can be solved using the restricted subspace of basis functions of Eq. (5.22). To proceed, the matrix elements of Eq. (5.8) in this basis must be calculated. The matrix elements of the Liouville operator $\mathcal{L}$ are given by

$$\left\langle \chi_{\mathbf{k},\lambda}^{(m,s)} \left| \mathcal{L} \right| \chi_{\mathbf{k},\lambda}^{(m',s')} \right\rangle = \left(-i\omega\delta_{m,m'} + \frac{1}{2}ivq\left(e^{-i\vartheta_{\mathbf{q}}}\delta_{m,m'+1} + e^{i\vartheta_{\mathbf{q}}}\delta_{m,m'-1}\right)\right)\left(v\beta\hbar\right)^{-2} L_{s,s'}, \tag{5.23}$$

where $\vartheta_{\mathbf{q}}$ is the polar angle of the wavevector $\mathbf{q}$

$$L = \begin{bmatrix} \frac{\log(2)}{\pi} & 0 & 0 \\ 0 & \frac{\log(2)}{\pi} & \frac{\pi}{6} \\ 0 & \frac{\pi}{6} & \frac{9\zeta(3)}{2\pi} \end{bmatrix}. \tag{5.24}$$

The rows and columns of the matrix notation refer to the mode index s of Eq. (5.22). The matrix elements of the collision operator $\mathcal{C}$ are calculated numerically (some values are given in Appendix B.3). Due to the rotational invariance of the low-energy Dirac Hamiltonian (5.1), they are diagonal in the angular momentum representation. That the matrix elements asymptotically approach a linear behavior for large $|m|$:

$$\left\langle \chi_{\mathbf{k},\lambda}^{(m,s)} \left| \mathcal{C} \right| \chi_{\mathbf{k},\lambda}^{(m',s')} \right\rangle = \frac{\delta_{m,m'}}{v^2\beta^3\hbar^3}\left(|m|\,\gamma_{s,s'} - \eta_{s,s'}\right) \tag{5.25}$$

as $|m| \to \infty$. $\gamma_{s,s'}$ and $\eta_{s,s'}$ are numerical coefficients that will be defined below Eqs. (5.35) and (5.37). This surprising result allows to solve the Boltzmann equation exactly, as will be seen later. The linear behavior of the scattering rates is shown in Fig. 5.1. To find closed expressions for the non-local transport coefficients, the scattering rates are approximated by Eq. (5.25) for $m > 2$. In principle, the numerically exact scattering rates up to an arbitrary m can be included. Here, rates for $m > 2$ will be approximated to keep the algebraic effords at a minimum. The projections of the force terms (5.11)-(5.13) onto collinear zero modes read

$$\left\langle S_E \,\middle|\, \chi_{\mathbf{k},\lambda} \right\rangle = -\frac{eE_0}{2\hbar^2\beta v}\delta_{|m|,1}\begin{bmatrix} \frac{\log(2)}{\pi} \\ 0 \\ 0 \end{bmatrix}, \tag{5.26}$$

$$\left\langle S_T \,\middle|\, \chi_{\mathbf{k},\lambda} \right\rangle = \frac{\left|\nabla T\right| k_B\pi^4}{v\beta\hbar^2}\delta_{|m|,1}\begin{bmatrix} 0 \\ \frac{\pi}{6} \\ \frac{9\zeta(3)}{2\pi} \end{bmatrix}, \tag{5.27}$$

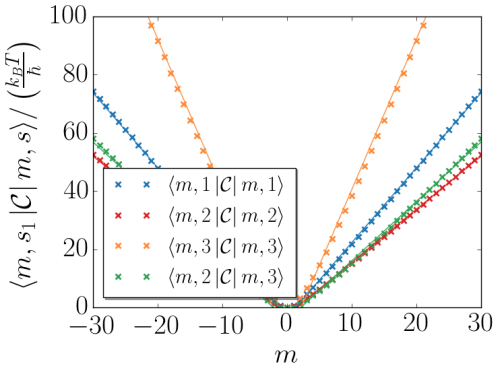

Figure 5.1: The matrix elements of the collision operator (5.10) with respect to the collinear zero modes (5.22) grow linearly with increasing angular harmonic numbers m. The linear fits of Eqs (5.35), (5.37) are plotted as solid blue and orange lines. The linear behavior of the matrix elements and scattering rates allows to solve the quantum Boltzmann equation exactly.

$$\left\langle S_S \middle| \chi_{\mathbf{k},\lambda} \right\rangle = -\frac{iX_0}{4\left(v\beta\hbar\right)^2} \mathrm{sign}\,(m)\, \delta_{|m|,2} \begin{bmatrix} 0 \\ \frac{\pi}{6} \\ \frac{9\zeta(3)}{2\pi} \end{bmatrix}. \tag{5.28}$$

For the Vlasov term (5.15) on finds

$$\begin{aligned} \left\langle \psi^{(m,s)}_{\mathbf{k},\lambda} | \mathcal{V} | \psi^{(m',s')}_{\mathbf{k},\lambda} \right\rangle &= i\alpha N \left(e^{-i\vartheta_{\mathbf{q}}} \delta_{m,1} + e^{i\vartheta_{\mathbf{q}}} \delta_{m,-1} \right) \\ &\quad \times \frac{\delta_{1,s}\delta_{1,s'}\delta_{m',0}}{2v^2\beta^3\hbar^3} \begin{bmatrix} \frac{\log(2)^2}{\pi^2} \\ 0 \\ 0 \end{bmatrix} \end{aligned} \tag{5.29}$$

The non-equilibrium part of the distribution function expanded in the subset of colinear zero modes becomes

$$\psi_{\mathbf{k},\lambda} = \sum_{m=-\infty}^{\infty} \sum_{s=1}^{3} a_{m,s}\left(\omega, \mathbf{q}\right) \chi^{(m,s)}_{\mathbf{k},\lambda}. \tag{5.30}$$

Together, the expressions (5.8), (5.23), (5.25), (5.26)-(5.28), (5.29) and (5.30) provide a linearized kinetic equation restricted to the basis of collinear zero modes that becomes exact for small values of the fine structure constant α. Since no assumptions on the spatial dependencies were made, except that they are be within the limits of the applicability of the kinetic equation, this expansion can be used to derive the non-local transport coefficients in the linear-response regime, as well as the dispersion relations of collective excitations.

5.2 Non-local Transport

5.2.1 Effects of electron-hole symmetry, momentum conservation and thermal transport

Within the kinetic approach, the charge current $\mathbf{j}_c$ and the heat current $\mathbf{j}_\varepsilon$ are given by

$$\mathbf{j}_c = e\sum_\lambda \int_{\mathbf{k}} \lambda v \frac{\mathbf{k}}{k} f_{\mathbf{k},\lambda}, \tag{5.31}$$

$$\mathbf{j}_\varepsilon = \sum_\lambda \int_{\mathbf{k}} v^2 \hbar \mathbf{k} f_{\mathbf{k},\lambda}. \tag{5.32}$$

In these expressions intraband processes that create particle-hole pairs are neglected (see Appendix B.1). Thus the even in λ part of the distribution function $f_{\mathbf{k},\lambda}$ contains information about thermal transport, whereas the odd part governs the transport of charge. Since the electric field contribution to the kinetic equation (5.11) is odd in λ, and the thermal gradient leads to a term that is even in λ (Eq. (5.12)), the phenomena of thermal and charge transport are decoupled to linear order in the external fields. This can be traced back to particle-hole symmetry. The distribution function has a similar structure for higher m: The collinear modes of Eq. (5.22) are proportional to λ^m for $s = 1$ and to λ^{m+1} for $s = 2, 3$. Consequently the kinetic equation in the subspace of collinear zero modes is block diagonal in the $s = 1$ and $s = 2, 3$ modes, as can be seen from Eqs. (5.10), (5.23), (5.11)-(5.29). In the following this will further simplify the calculation of transport coefficients.

Another important consequence of the linear graphene spectrum is that the heat current $\mathbf{j}_\varepsilon$ is proportional to the momentum density $n_{\mathbf{p}} = \sum_\lambda \int_k \hbar \mathbf{k} f_{\mathbf{k},\lambda}$ and therefore conserved. The charge current, unlike in Galileian invariant systems, is not conserved, and decays due to interactions, giving rise to a finite restistvity in the clean system.

5.2.2 Scattering times

The matrix elements of the collision operator determine the scattering rates of the three collinear zero modes in different angular harmonic channels. In the absence of spatial inhomogeneities and external forces, the kinetic equation in the basis of collinear zero modes (5.22) reads

$$\sum_{s'} \left(\partial_t \delta_{s,s'} + \Gamma_m^{s,s'} \right) a_{m,s'} = 0, \tag{5.33}$$

where the $a_{m,s}$ are the coefficients of the expansion (5.30). Posed as an initial value problem, this equation describes the exponential decay of collinear zero modes. This decay governs the behavior of the system at long time scales, because modes that do not set the collinear part of the collision integral to zero decay faster by a factor $\log\left(1/\alpha\right)$ (see Eq. (5.16)).

The scattering rates $\Gamma_m^{s,s'}$ are given by

$$\Gamma_m^{s,s'} = \left(v\beta\hbar\right)^2 L^{-1}_{s,s'} \left\langle \chi^{(m,s)}_{\mathbf{k},\lambda} \left| \mathcal{C} \right| \chi^{(m',s')}_{\mathbf{k},\lambda} \right\rangle. \tag{5.34}$$

Because of the definition of the scalar product in Eq. (5.17), the matrix elements have dimension length^2/time. Vanishing scattering rates indicate conservation laws, and the corresponding modes are

zero modes of the full collision operator as well as its collinear part. These modes reflect the conservation of particle density, imbalance density, energy density and momentum density:

$$\chi_{\mathbf{k},\lambda}^{(s=1,m=0)} = 1, \qquad \chi_{\mathbf{k},\lambda}^{(s=2,m=0)} = \lambda,$$

$$\chi_{\mathbf{k},\lambda}^{(s=3,m=0)} = \lambda\beta v\hbar k, \qquad \chi_{\mathbf{k},\lambda}^{(s=3,m=1)} = \lambda e^{i\theta}\beta v\hbar k.$$

The imbalance density is conserved only to order α^2, as it decays due to higher order interaction processes. An important simplification stems from the fact that all scattering rates, for large $|m|$, share the asymptotic behavior $\Gamma_m \sim |m|$. This becomes a reasonable approximation for the scattering rates with $m \geq 2$. In the next section it is shown, how this behavior allows us to obtain closed form expressions for the non-local transport coefficients. As discussed in the previous section, the matrix of scattering rates $\Gamma_m^{s,s'}$ is block diagonal in the modes describing charge ($s = 1$) and thermal excitations ($s = 2, 3$), i.e. $\Gamma_m^{1,2} = \Gamma_m^{2,1} = \Gamma_m^{1,3} = \Gamma_m^{3,1} = 0$. Therefore, the scattering times determining the non-local electric conductivity are given by $\tau_{c,m} = 1/\Gamma_m^{1,1}$: $\tau_{c,0} \to \infty$, $\tau_{c,1} = \frac{1}{\alpha^2}\frac{\hbar}{k_BT}\frac{\log 2}{0.804\pi}$, $\tau_{c,2} = \frac{1}{\alpha^2}\frac{\hbar}{k_BT}\frac{\log 2}{2.617\pi}$ as well as

$$\tau_{c,m} \approx \frac{1}{\alpha^2}\frac{\hbar}{k_BT}\frac{\log 2}{\pi}\left(\gamma_c \cdot |m| - \eta_c\right)^{-1} \text{ if } m > 2, \tag{5.35}$$

where $\gamma_c = 2.57$ and $\eta_c = 3.45$ (see Appendix B.3 for more numerical values). It is also convenient to define an effective scattering time for the Vlasov term:

$$\tau_V = \frac{2\pi^2\beta\hbar}{\alpha N \log(2)}. \tag{5.36}$$

Notice, that $\tau_V/\tau_{c,m} \sim 1/\alpha$ is large for small α.

In the thermal sector, there are two relevant modes. However, the $s = 3$ mode is physically more important, because the vanishing of the corresponding scattering rates for the $m = 0$ and $m = 1$ channels indicate the conservation of energy and momentum. In the following, it is shown that the neglecting of the $s = 2$ imbalance mode in the calculation of the thermal conductivity and viscosity, while significantly simplifying the analysis, does only result in a small numerical error. Therefore, for the purpose of calculating the transport coefficients, only the $s = 3$ energy mode will be considered. The scattering times are then given by $\tau_{\varepsilon,m} = 1/\Gamma_m^{3,3}$. Because of energy and momentum conservation, we have $\tau_{\varepsilon,m=0,1} \to \infty$, and for $m = 2$, it is $\tau_{\varepsilon,2} = \frac{1}{\alpha^2}\frac{\hbar}{k_BT}\frac{9\zeta(3)}{3.341\cdot 2\pi}$. For $m > 2$ the linear approximation can be used:

$$\tau_{\varepsilon,m} \approx \frac{1}{\alpha^2}\frac{\hbar}{k_BT}\frac{9\zeta(3)}{2\pi}\left(\gamma_\varepsilon \cdot |m| - \eta_\varepsilon\right)^{-1} \; m > 2, \tag{5.37}$$

with $\gamma_\varepsilon = 5.18$ and $\eta_\varepsilon = 11.3$.

5.2.3 Non-local transport coefficients

Non-local transport coefficients have been discussed in section 2.3.2 using impurity scattering as an example. Here, a clean system is studied and electron-electron collisions take the role of impurity scattering. Neverthesess, much of what was discussed in Sec. 2.3.2 applies here. The consitutive relations in Fourier space have the form

$$\mathcal{J}(\mathbf{q},\omega) = \nu(\mathbf{q},\omega)\,\mathcal{F}(\mathbf{q},\omega), \tag{5.38}$$

where $\mathcal{J}\left(\mathbf{q},\omega\right)$ is a current sourced by the external field $\mathcal{F}\left(\mathbf{q},\omega\right)$. The $\mathbf{q}$-dependence of the conductivity $\nu\left(\mathbf{q},\omega\right)$ matters when the sample size is comparable to the mean free path of electron-electron collisions $l_{\text{geo}} \lesssim l_{ee}$, or the applied field varies on scales comparable to l_{ee}. In the following, the electric conductivity, thermal conductivity and viscosity of graphene at charge neutrality are calculated using the kinetic equation (5.5) and the collinear zero mode expansion summerized in the previous section 5.1.2.

Electric conductivity

As mentioned in Sec. 5.2.2, only the first collinear mode $s = 1$ is involved in the calculation of the electric conductivity. Inserting the expansion of the distribution function in terms of collinear zero modes (5.30) into the kinetic equation (5.8) using its matrix representation of Eqs. (5.23), (5.25), (5.26)-(5.28) and (5.29), the left hand side of (5.8) can be transformed into a recurrence relation for the coefficients $a_{1,m}$, where, for the rest of this section, the $s = 1$ index is dropped. A similar analysis for electrons in a random magnetic field was performed in Ref.[140]. For $m > 2$, Eq. (5.35) can be used, and the recurrence relation reads

$$a_{m+1} = \frac{2ie^{-i\vartheta_{\mathbf{q}}}}{vq}\left(i\omega - \tau_{c,m}^{-1}\right)a_m - e^{-2i\vartheta_{\mathbf{q}}}a_{m-1}. \tag{5.39}$$

This recurrence relation has the form

$$a_{m+1} = \left(\alpha' m + \beta'\right)a_m - e^{i\delta}a_{m-1} \tag{5.40}$$

with $\alpha' = -\frac{2ie^{-i\vartheta_{\mathbf{q}}}}{vq}\frac{k_B T}{\hbar}\frac{\pi}{\log 2}\gamma_c$, $\beta' = \frac{2ie^{-i\vartheta_{\mathbf{q}}}}{vq}\left(i\omega - \eta_c\frac{k_B T}{\hbar}\frac{\pi}{\log 2}\right)$ and $\delta = -2\vartheta_{\mathbf{q}}$. It has two solutions that can be given in terms of modified Bessel functions. The physically interesting solution is

$$a_m = c\cdot e^{i\frac{\delta}{2}\left(m+\frac{\beta'}{\alpha'}\right)}\mathrm{I}_{m+\frac{\beta'}{\alpha'}}\left(-\frac{2e^{i\delta/2}}{\alpha'}\right), \tag{5.41}$$

where $\mathrm{I}_\nu\left(z\right)$ is the modified Bessel function of the first kind. Another solution that diverges for $m \to \infty$ is given by

$$c_m = c\cdot e^{i\frac{\delta}{2}\left(m+\frac{\beta'}{\alpha'}\right)}\mathrm{K}_{m+\frac{\beta'}{\alpha'}}\left(\frac{2e^{i\delta/2}}{\alpha'}\right).$$

K_ν is the modified Bessel function of the second kind. Making use of the coefficients a_m for $m > 2$ as given by Eq. (5.41), the kinetic equation can be reduced to a 5×5 component matrix equation:

$$\begin{bmatrix} -i\omega + M_c\left(q,\omega\right) & \frac{1}{2}ivqe^{i\vartheta_{\mathbf{q}}} & 0 & 0 & 0 \\ \frac{1}{2}ivqe^{-i\vartheta_{\mathbf{q}}} & -i\omega + \tau_{c,1}^{-1} & \frac{1}{2}ivqe^{i\vartheta_{\mathbf{q}}} & 0 & 0 \\ 0 & \frac{1}{2}ivqe^{-i\vartheta_{\mathbf{q}}} & -i\omega & \frac{1}{2}ivqe^{i\vartheta_{\mathbf{q}}} & 0 \\ 0 & 0 & \frac{1}{2}ivqe^{-i\vartheta_{\mathbf{q}}} & -i\omega + \tau_{c,1}^{-1} & \frac{1}{2}ivqe^{i\vartheta_{\mathbf{q}}} \\ 0 & 0 & 0 & \frac{1}{2}ivqe^{-i\vartheta_{\mathbf{q}}} & -i\omega + M_c\left(q,\omega\right) \end{bmatrix}\begin{bmatrix} a_{-2} \\ a_{-1} \\ a_0 \\ a_1 \\ a_2 \end{bmatrix} = \begin{bmatrix} 0 \\ \frac{eE_0\beta v}{2} \\ 0 \\ \frac{eE_0\beta v}{2} \\ 0 \end{bmatrix}, \tag{5.42}$$

where $M_c\left(q,\omega\right) = \tau_{c,2}^{-1} + a_3\left(q,\omega\right)/a_2\left(q,\omega\right)$ is a memory function containing information on scattering channels with higher angular momentum numbers. Using the Eqs. (5.40) and (5.41), the memory function is written

$$M_c\left(q,\omega\right) = \tau_{c,2}^{-1} + \frac{1}{2}vq\frac{\mathrm{I}_{3+\frac{\eta_c}{\gamma_c}-i\omega\tau_c}\left(\tau_c vq\right)}{\mathrm{I}_{2+\frac{\eta_c}{\gamma_c}-i\omega\tau_c}\left(\tau_c vq\right)}, \tag{5.43}$$

with the abbreviation $\tau_c = \frac{\hbar}{k_B T}\frac{\log 2}{\pi}\gamma_c^{-1}$. Notice, that the Vlasov term of Eqs. (5.14), (5.15) does not enter the matrix Boltzmann equation (5.42) explicitely. By definition, the electric conductivity characterizes the response to $\mathbf{E}$ - the total electric field in the system. In Eq. (5.5), the total electric field is $\mathbf{E} = \mathbf{F}\left(\mathbf{x}, t\right) + e\mathbf{E}_V$. Thus, only a forcing according to Eq. (5.26) is included. It is now straightforward to calculate the electric conductivity from the relation

$$j_{c,x}\left(\mathbf{q}, \omega\right) = \sigma_{xx}\left(\mathbf{q}, \omega\right) E_x\left(\mathbf{q}, \omega\right). \tag{5.44}$$

The non-local conductivity can be decomposed into a longitudinal part $\sigma_{\parallel}\left(\omega, q\right)$ and a transverse part $\sigma_{\perp}\left(\omega, q\right)$, both depending on the modulus of $\mathbf{q}$. The longitudinal and transverse parts describe currents that flow in the direction of $\mathbf{q}$, or orthogonal to $\mathbf{q}$, respectively:

$$\sigma_{\alpha\beta} = \frac{q_\alpha q_\beta}{q^2}\sigma_{\parallel}\left(q, \omega\right) + \left(\delta_{\alpha\beta} - \frac{q_\alpha q_\beta}{q^2}\right)\sigma_{\perp}\left(q, \omega\right). \tag{5.45}$$

We assumed that the electric field is parallel to the x-axis. According to Eq. (5.45), $\sigma_{\parallel}\left(q, \omega\right)$ can be read off from the x-component of the current density $j_{c,x}$ by letting $\mathbf{q}$ be parallel to $\mathbf{e}_x$, and $\sigma_{\perp}\left(q, \omega\right)$ by considering the case $\mathbf{q} \parallel \mathbf{e}_y$. The conductivities are then given by

$$\begin{aligned} \sigma_{\parallel} &= \frac{\sigma_0}{1 - i\tau_{1,c}\omega + \frac{1}{4}v^2\tau_{c,1}q^2\left(\frac{2i}{\omega} + \frac{1}{M_c\left(q,\omega\right) - i\omega}\right)}, \\ \sigma_{\perp} &= \frac{\sigma_0}{1 - i\tau_{c,1}\omega + \frac{\frac{1}{4}v^2\tau_{c,1}q^2}{M_c\left(q,\omega\right) - i\omega}}, \end{aligned} \tag{5.46}$$

where $\sigma_0 = N\frac{e^2\log\left(2\right)\tau_{c,1}}{2\pi\beta\hbar^2}$ is the quantum critical conductivity calculated in Ref. [49]. Note that $\sigma_{\parallel}\left(q \neq 0, \omega = 0\right) = 0$ holds, which also follows from formula (5.48). If this was not the case, static currents with a finite wave-vector $\mathbf{q}$ would lead to an infinite accumulation of charge at certain points, which is forbidden by the conservation of charge. In Fig. 5.2 the charge conductivities are plotted as functions of ω for different values of q.

The electric conductivity tensor $\sigma_{\alpha\beta}\left(\mathbf{q}, \omega\right)$ of Eq. 5.46 gives access to different electric response functions. The current-current correlation function is given by

$$\chi_{J_\alpha J_\beta}\left(\mathbf{q}, \omega\right) = -i\omega\sigma_{\alpha\beta}\left(\mathbf{q}, \omega\right), \tag{5.47}$$

where α, β denote the components of the current vector (see e.g. Ref. [141]). With the help of the continuity equation, the charge density-density correlation function is obtained from Eq. (5.47):

$$\begin{aligned} \chi_{\rho\rho}\left(q, \omega\right) &= \frac{q_\alpha q_\beta}{\omega^2}\chi_{J_\alpha J_\beta}\left(\mathbf{q}, \omega\right). \\ &= \frac{q^2}{i\omega}\sigma_{\parallel}\left(q, \omega\right). \end{aligned} \tag{5.48}$$

Finally, the charge compressibility $K = \partial\rho/\partial\mu$ is given by

$$K\left(q\right) = \chi_{\rho\rho}\left(\omega = 0\right). \tag{5.49}$$

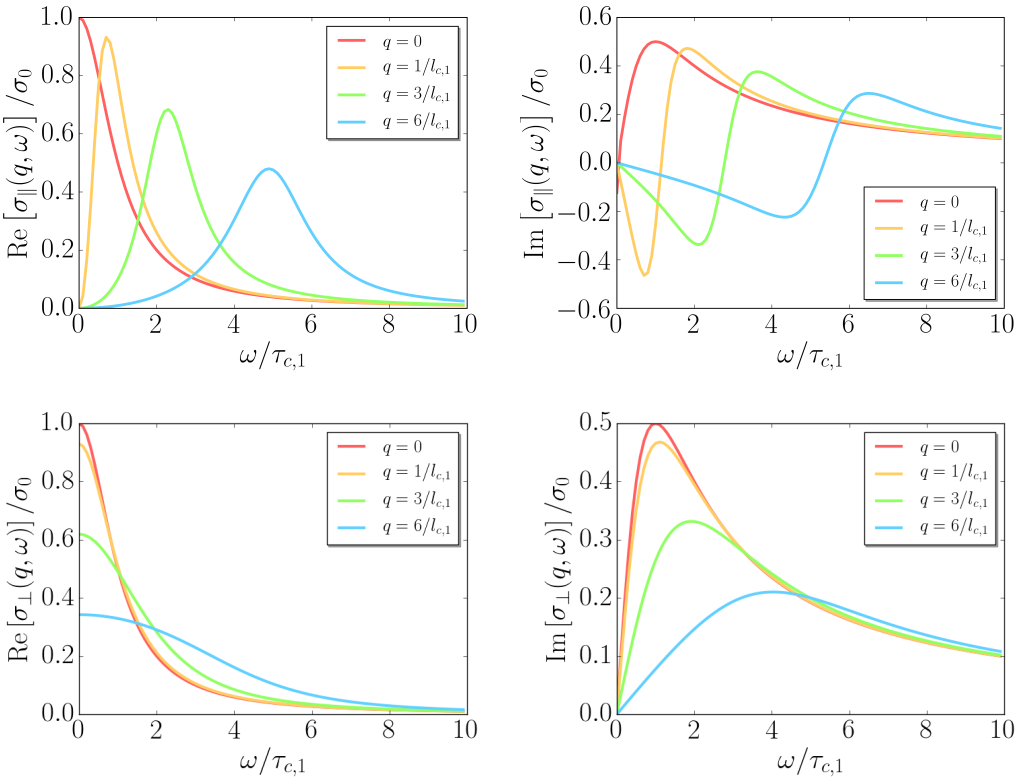

Figure 5.2: Longitudinal (upper row) and transverse (lower row) electric conductivities of charge neutral graphene as functions of the electric field frequency ω as given by Eqs (5.46). Different colors indicate different values of the wavenumber q. Frequencies and wavenumbers are normalized to the characteristic scattering times and lengths $\tau_{c,1}$, $l_{c,1} = v\tau_{c,1}$. σ_0 is the interaction induced conductivity at the neutrality point [49, 54]. The graphs show distinct resonant features at frequencies $\omega \sim q/v$, where v is the electron group velocity. Whereas the real part of the longitudinal and the imaginary part of the transverse conductivities are peaked around $\omega \sim q/v$, the imaginary part of the longitudinal conductivity exhibits a sign change indicating an abrubt phase change of the current response. The real parts approach σ_0 for $q \to 0$, $\omega \to 0$. For $q \neq 0$, $\omega = 0$ the longitudinal conductivity vanishes. This general property of the charge conductivity follows from the conservation of charge (see Eq. (5.48)).

Thermal conductivity

Next we presemt our analysis for the non-local thermal conductivity. Since momentum conservation implies for a Dirac liquid the conservation of the heat current, thermal transport is expected to display classical hydrodynamic behavior, i.e. one expects non-local effects to be even more important than for charge transport.[129, 141].

As pointed out in Sec. 5.2.2, the $s = 3$ energy mode must be kept in the calculation of the thermal conductivity, whereas the $s = 2$ imbalance mode can be neglected, contributing only a small correction to the overall result. With only a single mode involved, the calculation is formally analogous to the calculation of the electrical conductivity in Sec. 5.2.3, even though there are crucial differences in the actual result, given the distinct role of momentum conservation. The relaxation time $\tau_{c,m}$ must be replaced by $\tau_{\varepsilon,m}$ as given by Eq. (5.37). The conservation of momentum is incorporated via $\tau_{\varepsilon,1} \to \infty$, whivch follows from the Boltzmann approach. The resulting longitudinal and transverse thermal conductivities read

$$\begin{aligned} \kappa_{\parallel}\left(q,\omega\right) &= \frac{\kappa_0}{i\omega\tau_{\varepsilon,2} - \frac{1}{4}v^2q^2\tau_{\varepsilon,2}\left(\frac{2i}{\omega} - \frac{1}{M_\varepsilon\left(q,\omega\right)+i\omega}\right)} \\ \kappa_{\perp}\left(q,\omega\right) &= \frac{\kappa_0}{i\omega\tau_{\varepsilon,2} + \frac{\frac{1}{4}v^2q^2\tau_{\varepsilon,2}}{M_{\varepsilon,2}\left(q,\omega\right)+i\omega}}, \end{aligned} \tag{5.50}$$

with the memory function

$$M_\varepsilon\left(q,\omega\right) = \tau_{\varepsilon,2}^{-1} + \frac{1}{2}vq\frac{\mathrm{I}_{3+\frac{\eta_\varepsilon}{\gamma_\varepsilon}+i\omega\tau_\varepsilon}\left(\tau_\varepsilon vq\right)}{\mathrm{I}_{2+\frac{\eta_\varepsilon}{\gamma_\varepsilon}+i\omega\tau_\varepsilon}\left(\tau_\varepsilon vq\right)}.$$

The abbreviation $\tau_{\varepsilon,2} = \frac{1}{\alpha^2}\frac{\hbar}{k_BT}\frac{9\zeta(3)}{3.341\cdot 2\pi}$ is used. For convenience $\kappa_{\parallel/\perp}$ is given in units of a thermal conductivity $\kappa_0 = 9N\pi^3k_B\zeta(3)\tau_{\varepsilon,2}/2\beta^2\hbar^2$, however, $\tau_{\varepsilon,2}$ is the relaxation time in the $|m| = 2$ channel, and should not be confused with an alleged relaxation time of the energy current, which is infinite due to the conservation of momentum.

In Fig. 5.2 the thermal conductivities are plotted as functions of ω for different values of q. The fact that thermal currents are protected by momentum conservation leads to a divergence of the thermal conductivity at small frequencies: for $q = 0$, κ is purely imaginary and shows the characteristic $1/\omega$ Drude behavior.

Non-local shear viscosity

The non-local viscosity is defined through a constitutive relation of the form of Eq. (5.38), linking the shear force $X_{0,\alpha\beta}\left(\mathbf{r}'\right)$ to the momentum-current tensor $\tau_{\alpha\beta}$:

$$\tau_{\alpha\beta}\left(\mathbf{r},t\right) = \int d^2r' \int dt'\, \eta_{\alpha\beta\gamma\delta}\left(\mathbf{r}-\mathbf{r}',t-t'\right) X_{0,\gamma\delta}\left(\mathbf{r}',t'\right). \tag{5.51}$$

Since the system is isotropic, the shear force can be chosen such that the flow velocity is aligned with the x-axis, and its gradient shows in the y direction. It is assumed that the shear force is wavelike: $X_{0,xy}\left(\mathbf{r}\right) = X_{0,xy}e^{i\mathbf{q}\cdot\mathbf{r}-i\omega t}$. The wave-vector $\mathbf{q}$ can have an arbitrary direction in the xy-plane, introducing a preference direction to the system's response. In addition to τ_{xy}, this gives rise to

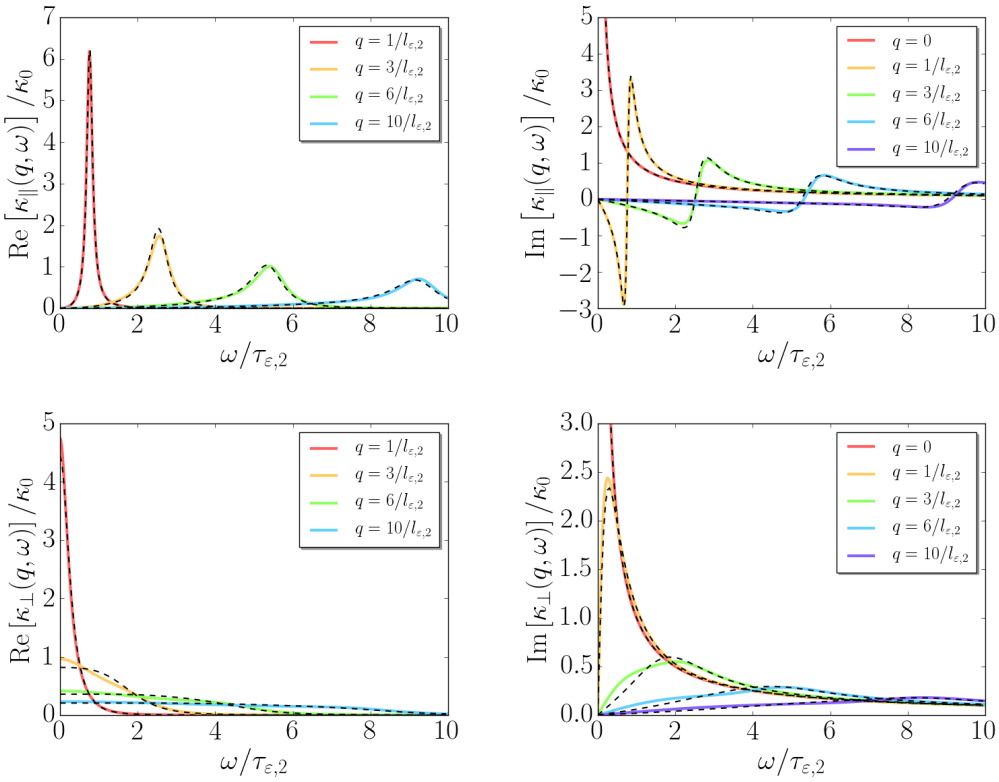

Figure 5.3: The figure shows the longitudinal (upper row) and transverse (lower row) thermal conductivities (5.46) as functions of the electric field frequency ω. Different colors indicate different values of the wavenumber q. The conductivities are normalized to $\kappa_0 = 9N\pi^3 k_B \zeta(3)\tau_{\varepsilon,2}/2\beta^2\hbar^2$. For small ω and vanishing q, the imaginaty part of $\kappa_{\parallel/\perp}$ diverges as $1/\omega$, whereas the real part vanishes - a behavior indicating that thermal transport in the system is ballistic. The solid lines show the analytical result of Eq. (5.50), the dashed lines show the full numerical result including all modes and the exact scattering times.

nonzero components τ_{xx}, τ_{yy}, if $\mathbf{q}$ does not align with the x or the y-axes. The viscosity tensor $\eta_{\alpha\beta xy}$ can be decomposed into transverse and longitudinal parts (see Eq. (5.45)) analogously to the electric and charge conductivities. Because $\eta_{\alpha\beta xy}$ is a fourth rank tensor the decomposition is slightly more involved and the reader is referred to Appendix B.4 for details. The general $\mathbf{q}$-dependent viscosity tensor can be constructed with the help of three rank two tensors:

$$\begin{aligned} e^{(1)}_{\alpha\beta} &= \frac{q_\alpha q_\beta}{q^2} \\ e^{(2)}_{\alpha\beta} &= \delta_{\alpha\beta} - \frac{q_\alpha q_\beta}{q^2} \\ e^{(3)}_{\alpha\beta} &= \frac{1}{\sqrt{2}} \left(q_\alpha p_\beta + p_\alpha q_\beta \right) / \left(pq \right), \end{aligned} \tag{5.52}$$

where

$$p_\alpha = q_\gamma \varepsilon_{\gamma\alpha}. \tag{5.53}$$

The viscosity tensor is parameterized by two frequency and momentum dependent functions, $\eta_\parallel \left(\mathbf{q},\omega\right)$ and $\eta_\perp \left(\mathbf{q},\omega\right)$, which we will call longitudinal and transverse viscosities:

$$\begin{aligned} \eta_{\alpha\beta\gamma\delta} \left(\mathbf{q},\omega\right) = \eta_1 \left(\mathbf{q},\omega\right) \left(e^{(1)}_{\alpha\beta} e^{(1)}_{\gamma\delta} + e^{(2)}_{\alpha\beta} e^{(2)}_{\gamma\delta} \right) \\ + \eta_2 \left(\mathbf{q},\omega\right) e^{(3)}_{\alpha\beta} e^{(3)}_{\gamma\delta}. \end{aligned}$$

Let the flow be in x-direction: $\mathbf{u}\left(y\right) = u\left(y\right)\hat{\mathbf{e}}_x$, and let the wave-vector be parameterized by $\mathbf{q} = q\left(\cos\left(\vartheta_\mathbf{q}\right), \sin\left(\vartheta_\mathbf{q}\right)\right)^T$, where θ is measured with respect to the x-axis. For $\vartheta_\mathbf{q} = 0$ or $\vartheta_\mathbf{q} = \pi/2$ follows $e^{(1,2)}_{\alpha\beta} = 0$, $\eta_{xxxy} = \eta_{xxyx} = 0$ and $\eta_{xyxy} = \eta_2/2$. This corresponds to the familiar shear flow in e.g. a Poiseuille geometry where $\tau_{xx} = \tau_{yy} = 0$. The momentum current flows orthogonal to the direction of the momentum density. For $\vartheta_\mathbf{q} = \pi/4$, the viscosity is determined by η_1: $\eta_{xyxy} = \eta_1/2$.

As in the case of thermal conductivity, dropping the $s = 2$ imbalance mode produces only a small numerical correction in the final result for the viscosity. With an external shear force of the form of Eqs. (5.13), (5.28) applied to the system, the kinetic equation can be written as 5×5 component matrix equation, similar to the case of an applied electric field (see Eq. (5.42)). The force acts in the $|m| = 2$ channels, and the equation reads

$$\begin{bmatrix} -i\omega + M_\varepsilon\left(q,\omega\right) & \frac{1}{2}ivqe^{i\theta} & 0 & 0 & 0 \\ \frac{1}{2}ivqe^{-i\theta} & -i\omega & \frac{1}{2}ivqe^{i\theta} & 0 & 0 \\ 0 & \frac{1}{2}ivqe^{-i\theta} & -i\omega & \frac{1}{2}ivqe^{i\theta} & 0 \\ 0 & 0 & \frac{1}{2}ivqe^{-i\theta} & -i\omega & \frac{1}{2}ivqe^{i\theta} \\ 0 & 0 & 0 & \frac{1}{2}ivqe^{-i\theta} & -i\omega + M_\varepsilon\left(q,\omega\right) \end{bmatrix} \begin{bmatrix} a_{-2} \\ a_{-1} \\ a_0 \\ a_1 \\ a_2 \end{bmatrix} = \begin{bmatrix} -\frac{iX_0}{4} \\ 0 \\ 0 \\ 0 \\ \frac{iX_0}{4} \end{bmatrix}. \tag{5.54}$$

Solving the matrix equation (5.54) for $a_{\pm 2}$, the viscosity is calculated with the help of Eq. (5.51) which takes the form $\tau_{xy} = N\sum_\lambda \int_k v_x k_y f_{\mathbf{k},\lambda} = \eta_{xyxy} X_{0,xy}$. As explained above, the viscosity components η_1 and η_2 can be read off from the general result $\eta_{xyxy}\left(\mathbf{q} = q\left(\cos\left(\vartheta_\mathbf{q}\right), \sin\left(\vartheta_\mathbf{q}\right)\right)^T, \omega\right)$ by setting

$\vartheta_{\mathbf{q}} = 0$ and $\vartheta_{\mathbf{q}} = \pi/2$:

$$\begin{aligned} \eta_1\left(q,\omega\right) &= \frac{2\eta_0}{-i\tau_{\varepsilon,2}\omega - q^2v^2\frac{i\tau_{\varepsilon,2}\omega}{2q^2v^2-4\omega^2} + \tau_{\varepsilon,2}M_\varepsilon\left(q,\omega\right)}, \\ \eta_2\left(q,\omega\right) &= \frac{2\eta_0}{-i\tau_{\varepsilon,2}\omega - \frac{q^2v^2\tau_{\varepsilon,2}}{4i\omega} + \tau_{\varepsilon,2}M_\varepsilon\left(q,\omega\right)}. \end{aligned} \tag{5.55}$$

Here, η_0 is the viscosity at $q = 0$, $\omega = 0$, $\eta_0 = N\left(k_BT\right)^3\tau_{\varepsilon,2}/\left(8\hbar^2v^2\right)$, as it was first calculated in Ref. [51] including both modes, $s = 2$ and $s = 3$.

5.3 Collective modes

Collective modes are solutions to the homogeneous part of the kinetic equation (5.5), (5.8) (see e.g. [22]). Consider Eq. (5.8). With the force terms set to zero it holds

$$\left(\mathcal{L} + \mathcal{V} + \mathcal{C}\right)\psi = 0.$$

Here, $\mathcal{L}$ and $\mathcal{C}$ have are the matrix operators of Eqs. (5.23) and (5.25). Solutions to this equation exist only if

$$\det\left(\mathcal{L} + \mathcal{V} + \mathcal{C}\right) = 0 \tag{5.56}$$

holds. This is only the case for certain values of the variable pairs ω, q. Eq. (5.56) is an eigenvalue problem where the eigenvalues $\omega\left(q\right)$ determine the dispersion relations of the collective modes. On the other hand, collective modes can be found from poles of response functions for an external force S. The two methods are equivalent. Within the kinetic equation formalism, response functions are calculated as averages over the distribution function $\psi = \left(\mathcal{L} + \mathcal{V} + \mathcal{C}\right)^{-1}S$. If the condition (5.56) is fulfilled, the operator $\left(\mathcal{L} + \mathcal{V} + \mathcal{C}\right)^{-1}$ is singular and thus singularities in the response to S appear. We will use Eq. (5.56) to study the collective modes in charge neutral graphene.

As in the previous sections, the kinetic equation will be expanded in terms of collinear zero modes (5.22): $\chi_{\mathbf{k},\lambda}^{(m,s)} = \lambda^m e^{im\theta}\left\{1, \lambda, \lambda\beta v\hbar k\right\}$. For $m = 0$ these modes correspond to excitations of the charge, imbalance and energy densities; for $|m| = 1$ they correspond to the associated currents. At the end of this section it will be shown that including non-collinear zero modes in the calculation does not change the result as long as the fine structure constant α is kept small.

To get a feeling for the structure of collective modes in the system, it is useful to begin with the case $q = 0$. In the subspace of collinear zero modes, the kinetic equation reduces to Eq. (5.33) and the condition (5.56) reads

$$\det\left(-i\omega\delta_{s,s'} + \Gamma_m^{s,s'}\right) = 0. \tag{5.57}$$

This is an eigenvalue equation for the frequencies of collective modes that can be solved independently for any m. Since, as pointed out in Sec. 5.2.1, $\Gamma_m^{s,s'}$ is block-diagonal in the subspaces of electric ($s = 1$) and imbalance/energy ($s = 2, 3$) excitations, the above equation, as well as its extension to $q \neq 0$, can be solved independently in these two sectors. For $s = 1$, the eigenfrequencies are $\omega_m\left(q = 0\right) = -i/\tau_{c,m}$. Since in this scenario the time evolution of the modes is given by the factor $e^{-i\omega_m t}$, all but the $m = 0$ mode, which is protected by charge conservation, exponentially decay at a rate inversely proportional

to their scattering time. The $m = 0$ zero mode corresponds to the charge density, which is conserved, and therefore does not decay. In the following two sections, the collective charge, as well as energy and imbalance excitations will be described at finite $\mathbf{q}$. Figs. 5.4, 5.5, 5.6, 5.7, 5.8 show the dispersion relations of these modes.

5.3.1 Collective charge excitations

In general, conserved modes do not decay at $q = 0$, and therefore their dispersion relations must vanish in a spatially homogeneous system. The only conserved mode in the charge sector is the charge density mode $\chi_{\mathbf{k},\lambda}^{(m=0,s=1)} = 1$. In the limit $q \ll v\tau_{c,1}$, the memory matrix (5.43) reduces to $M_c\left(q,\omega\right) \approx \tau_{c,2}^{-1}$ and Eq. (5.56) can be solved analytically. The dispersions of the two lowest modes are

$$\omega_{\text{charge diff.}} \approx \omega_{\pm} = -\frac{i}{2\tau_{c,1}} \pm \sqrt{\frac{vq}{\tau_V} - \frac{1}{4\tau_{c,1}^2}}. \tag{5.58}$$

The conserved charge density mode is described by ω_-. The dispersion relations of Eq. (5.58) have a non-vanishing real part for

$$q > q_{pl}^* = \frac{\tau_V}{4v\tau_{c,1}^2}. \tag{5.59}$$

For wave-vectors below q_{pl}^*, the plasmon is over-damped (see Fig. 5.4). However, we have $vq_{pl}^* \sim \alpha^3 k_B T/\hbar$ such that the plasmon mode becomes more and more pronounced at low temperatures.

The plasmon mode is gapped out due to the intrinsic interaction induced resistivity. At $q = 0$ it has a vanishing real part and its decay rate is given by the scattering rate in the $m = 1$ channel:

$$\omega_{pl}\left(q \to 0\right) = -i/\tau_{c,1} \tag{5.60}$$

(see also [113]). It is the most weakly damped of an infinite set of modes corresponding to higher angular harmonics (see Fig. 5.4). It is clearly seen, that the modes relate to different angular harmonic channels m. For $q = 0$ their dispersions approach $\omega_m\left(q = 0\right) = -i/\tau_{c,m}$. Such modes play a crucial role in the relaxation mechanism of focused current beams in graphene [138]. Similar collective modes have been argued to influence the relaxation behavior of unitary fermi gases [133] and QCD plasmas [134–136].

5.3.2 Collective energy and imbalance excitations

In the energy sector spanned by the modes $s = 2, 3$, the Eqs. (5.56) and (5.57) give rise three zero eigenvalues. These correspond to the conserved energy ($\chi_{\mathbf{k},\lambda}^{(m=0,s=3)} = \lambda\beta v\hbar k$) and quasiparticle (imbalance) densities ($\chi_{\mathbf{k},\lambda}^{(m=0,s=2)} = \lambda$), as well as momentum ($\chi_{\mathbf{k},\lambda}^{(m=1,s=3)} + (-)\,\chi_{\mathbf{k},\lambda}^{(m=-1,s=3)} = 2\left(i\right)\beta v\hbar k_{x(y)}$). The first two conservation laws lead to two diffusive modes. The conservation of momentum gives rise to second sound - ballistic thermal waves propagating through the two dimensional graphene plane [52]. This mode is the analogue of the density modes of a clean neutral Galilean invariant system.

Truncating the mode expansion of Eq. (5.56) at $m = 2$, which is a good approximation for low wave-numbers, yields the dispersions

$$\begin{aligned} \omega_{\text{heat diff.}} &\approx \frac{1}{4}v^2q^2\tau_{\varepsilon,2}, \\ \omega_{\text{qp diff.}} &\approx \frac{1}{8}v^2q^2\tau_{\varepsilon,2}, \end{aligned} \tag{5.61}$$

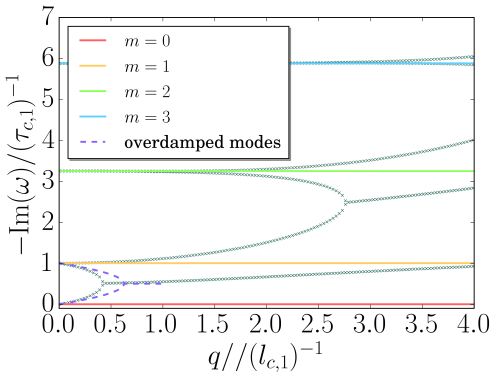

Figure 5.4: The imaginary parts of the dispersion relations of collective charge excitations in different angular harmonic channels m are shown. The wave-vector q is given in units of the inverse scattering length $v\tau_{c,1}^{-1}$. The grey symbols correspond to the numerical solution of Eq. (5.56). The purely imaginary $m = 0$ diffusive mode is the only mode approaching zero for small q - a behavior necessitated by charge conservation. Modes with a higher m are damped and approach the values $-i/\tau_{c,m}$ for $q \to 0$. The corresponding excitations decay even in the absence of spatial inhomogeneities. At a value $q = q_{pl}^*$ (Eq. 5.59), the dispersions of the diffusive mode and the $m = 1$ excitation merge, giving rise to a plasmon mode, which has a finite real part (see Fig 5.5). This value is slightly overestimated by the simplified expression of Eq. (5.59).

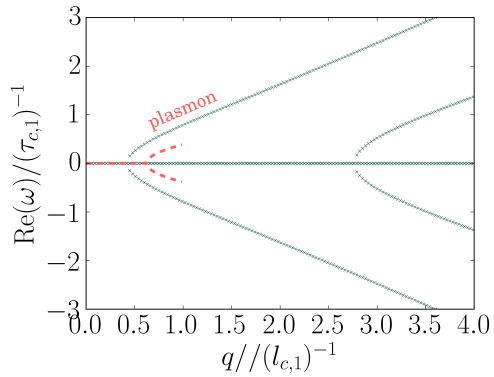

Figure 5.5: The figure shows the real parts of the dispersion relations of collective charge excitations in different angular harmonic channels m. The wave-vector q is given in units of the inverse scattering length $v\tau_{c,1}^{-1}$. The grey symbols correspond to the numerical solution of Eq. (5.56). The plasmon mode is gapped out by the interaction induced conductivity and only obtains a finite real part around $q = q_{pl}^*$ (the simplified value of q_{pl}^* given in Eq. (5.59) (red dashed line) overestimates the branching point). At higher q, other, strongly damped modes corresponding to higher angular harmonics appear. The dampings of these modes are given by the $m > 1$ modes of Fig. 5.4.

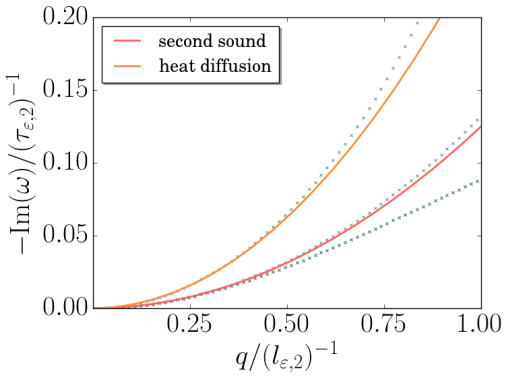

Figure 5.6: The figure shows the imaginary part of the dispersion relations of second sound, heat diffusion, and quasiparticle (imbalance) diffusion excitations. The wavevector q is given in units of the inverse scattering length $v\tau_{c,2}^{-1}$. The grey symbols correspond to the numerical solution of Eq. (5.56). The damping of second sound is due to scattering in the $m = 2$ channel and follows the dispersion $\mathrm{Im}\left(\omega_{\text{sec. sound}}\right) \approx \frac{1}{8}v^2q^2\tau_{\varepsilon,2}$ (red curve). For small q the imaginary part of the second sound dispersion and the dispersion of the quasiparticle diffusion mode merge. A third diffusive mode corresponds to the diffusion of heat (orange curve).

for the heat and quasiparticle (imbalance) diffusion modes, respectively. The second sound dispersion is given by

$$\omega_{\text{sec. sound}} \approx \frac{vq}{\sqrt{2}} + i\tau_{\varepsilon,2}\frac{v^2q^2}{8}. \tag{5.62}$$

Second sound mediated by phonons has been previously observed in solids [142] and had a velocity comparable to the velocity of sound. Here, the second sound is carried by electrons and propagates with a velocity $v_0/\sqrt{2}$. The above dispersion relations are shown in Figs. 5.6 and 5.8. The dispersion of the quasiparticle diffusion mode and the imaginary part of the second sound dispersion merge at low wavenumbers. As in the case of charge excitations, there exists an infinite number of damped modes associated with scattering in higher angular harmonic channels. These modes are depicted in Figs. 5.7 and 5.8. Note, that modes associated with imbalance excitations ($s = 2$) are damped stronger by an order of magnitude as compared to energy excitations ($s = 3$).

5.3.3 Validity of the collinear zero mode approximation for collective modes

The discussion so far was carried out in the restricted subspace of collinear zero modes. In this section it is shown that the results for collective excitations obtained within the restricted subspace remain valid, if this restriction is lifted, and non-collinear zero modes are added. These modes introduce large corrections to the matrix of scattering rates $\Gamma_m^{s,s'}$, and it is not obvious that they can be neglected. It is sufficient to consider the $\mathbf{q} = 0$ case. The extension to finite wavenumbers is straightforward.

The scattering rate matrix $\Gamma_m^{s,s'}$ of Eq. (5.34) is extended to include modes that are not collinear

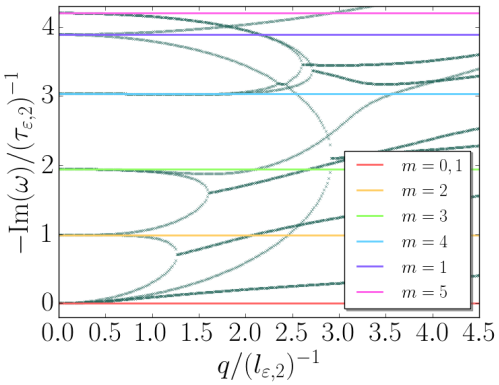

Figure 5.7: The imaginary part of the dispersion relations of collective charge excitations in different angular harmonic channels m are shown. The wave-vector q is given in units of the inverse scattering length $v\tau_{c,2}^{-1}$. The grey symbols correspond to the numerical solution of Eq. (5.56). For small q, the modes approach values given by the scattering rates $-i/\tau_{c,m}$ and are thus strongly damped. At larger values of q, the dispersions tend to merge in a complex fashion. Fig. 5.6 shows the weakly damped modes (second sound and diffusive modes) for small values of q.

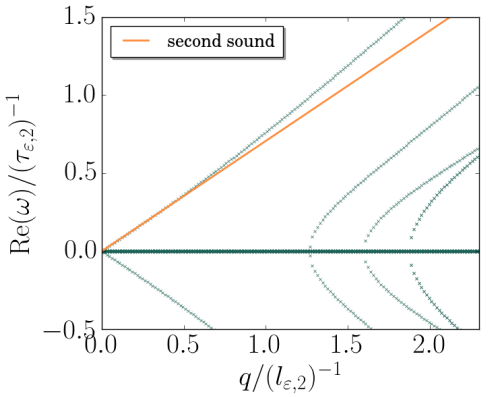

Figure 5.8: The real parts of the dispersion relations of collective energy and imbalance excitations are depicted. The grey symbols correspond to the numerical solution of Eq. (5.56). The linear dispersion of the second sound mode given by $vq/\sqrt{2}$ for small q is shown in orange color. The wave-vector q is given in units of the inverse scattering length $v\tau_{c,2}^{-1}$.

zero modes, which are labeled with indices $s > 3$. It is useful to define the following matrices

$$\begin{aligned} S &= \left(v\beta\hbar\right)^2 \left\langle \chi_{\mathbf{k},\lambda}^{(s<3)} \left|\mathcal{C}\right| \chi_{\mathbf{k},\lambda}^{(s'<3)} \right\rangle \\ P &= \left(v\beta\hbar\right)^2 \left\langle \chi_{\mathbf{k},\lambda}^{(s>3)} \left|\mathcal{C}\right| \chi_{\mathbf{k},\lambda}^{(s'<3)} \right\rangle \\ Q &= \left(v\beta\hbar\right)^2 \left\langle \chi_{\mathbf{k},\lambda}^{(s<3)} \left|\mathcal{C}\right| \chi_{\mathbf{k},\lambda}^{(s'>3)} \right\rangle \\ R &= \left(v\beta\hbar\right)^2 \left\langle \chi_{\mathbf{k},\lambda}^{(s>3)} \left|\mathcal{C}\right| \chi_{\mathbf{k},\lambda}^{(s'>3)} \right\rangle . \end{aligned}$$

Here, $\chi_{\mathbf{k},\lambda}^{(s<3)}$ are the familiar collinear zero modes (5.22). $\chi_{\mathbf{k},\lambda}^{(s>3)}$ are modes with a different $\left|\mathbf{k}\right|$-dependence, such that the full set of modes forms a complete basis. Since $\mathcal{C}$ is Hermitian, we have $Q = P^T$. The mode expansion of the Liouville operator $L_{s,s'}$ of Eq. (5.23) also has to be enlarged by the $s > 3$ modes. However, we do not need to know the precise values of the correponding elements of L. The eigenvalue equation (5.57) reads

$$\det\left(-i\omega L - F\right) = 0, \tag{5.63}$$

where F is the composite matrix

$$F = \begin{bmatrix} S & P \\ P^T & R \end{bmatrix}.$$

In the following, the Liouville matrix L will also be separated into blocks corresponding the same subspaces: $L = \Big(\left(L_S, L_P\right), \left(L_P^T, L_S\right)\Big)$. It follows from Eq. (5.16) and the Hermiticity of the collinear part of the collision operator $\mathcal{C}_c$ that

$$\begin{aligned} S &\sim P \sim 1 \\ R &\sim \log\left(1/\alpha\right), \end{aligned}$$

meaning that non collinear zero modes are scattered faster by a factor of $\log\left(1/\alpha\right)$. The determinant can be found using the block matrix identity[1]

$$\det\begin{bmatrix} A & B \\ C & D \end{bmatrix} = \det\left(D\right)\det\left(A - BD^{-1}C\right). \tag{5.64}$$

Applying this identity to Eq. (5.63) and noticing that for $\alpha \to 0$ the inverse matrix in the last determinant vanishes, one has

$$\det\left(i\omega L + F\right) \approx \det\left(i\omega L_R + R\right)\det\left(i\omega L_S + S\right).$$

Eq. (5.63) therefore separates into two independent parts: $\det\left(i\omega L_R + R\right) = 0$ and $\det\left(i\omega L_S + S\right) = 0$. The second equation is equivalent to the eigenvalue equation (5.57). In the limit of a small fine structure constant, the weakly damped collective modes can therefore be found by solving the kinetic equation in the restricted subspace of collinear zero modes, even if there is significant coupling between all modes.

[1] I'm greatful to B. Jeevanesan for bringing this identity to my attention.

5.4 Poiseuille profiles

The wavevector-dependence of transport coefficients is of importance when the currents in a system are spatially inhomogeneous, either because the applied fields are inhomogeneous, or because the inhomogeneity is imposed by the geometry of the system. The simplest example for the latter case is the Poiseuille flow. In undoped graphene, the energy current is conserved due to the conservation of momentum, however it is dissipated by the uneven boundaries of the sample [138]. In a Poiseuille geometry, which consists of an infinitely long, streight sample of width w, the boundaries slow down the current flow. The current profile becomes parabolic across the sample. On the other hand, charge currents decay in the bulk of undoped graphene due to the interaction induced resistivity. In this case, there exists a crossover from an almost flat current profile if $w \gg v\tau_{1,c}$ to a more parabola-like shape at $w < v\tau_{1,c}$. However, as shown in Ref. [138], the slowing down of the flow by the boundaries becomes inefficient when $w \lesssim v\tau_{2,c}$, again changing the profile. In this section we investigate the Poiseuille profiles of charge currents in undoped graphene using the full non-local conductivity (5.46).

5.4.1 Flow equations and boundary conditions

The thermal and charge flow is governed by the constitutive relations $\kappa^{-1}\left(\mathbf{q},\omega\right)_{\alpha\beta} j_{\varepsilon,\beta} = -\partial_\alpha T$ and $\sigma^{-1}\left(\mathbf{q},\omega\right)_{\alpha\beta} j_{c,\beta} = E_\alpha$, where $j_{\varepsilon,\beta}$ is the thermal current and $j_{c,\beta}$ the electric current. With the thermal and electric conductivities κ and σ depending on the wave vector $\mathbf{q}$, these equations can be seen as Fourier transforms of differential equations. Similar equations have been studied to describe non-localities induced by vortices in type II superconductors [143]. The temeprature gradient $-\partial_\alpha T$ and the electric field E_α act as source terms. In a Poiseuille geometry, the force fields act perpendicular to the gradient of the flow velocity, i.e. it is $\mathbf{E} \perp \mathbf{q}$, $\nabla T \perp \mathbf{q}$. Therefore, the currents are determined by the transverse conductivities. Let the sample be oriented in y-direction and centered around $x = 0$. The equations then read

$$\kappa_T^{-1}\left(q_x,\omega\right) j_{\varepsilon,y}\left(q_x,\omega\right) = -\partial_y T, \tag{5.65}$$

$$\sigma_T^{-1}\left(q_x,\omega\right) j_{c,y}\left(q_x,\omega\right) = E_y. \tag{5.66}$$

To solve the above equations, boundary conditions at the sample boundaries at $\pm w/2$ are needed. As discussed in the previous chapter, the partial slip boundary conditions of Eq. (4.4) are appropriate:

$$j_{\varepsilon/c,y}\left(x = \pm w/2,\omega\right) = \mp\zeta \left.\frac{\partial j_{\varepsilon/c,y}}{\partial x}\right|_{x=\pm w/2}. \tag{5.67}$$

It was shown in chapter 4, that if the boundaries are sufficiently rough, the so-called slip length ζ is of the order as the mean free path associated with the $m = 2$ scattering time: $\zeta \sim v\tau_{\varepsilon/c,2}$. In principle, the Eqs. (5.65), (5.66) represent infinite order differential equations and require infinitely many boundary conditions. However, this problem does not appear explicitely in the calculation. The finite width of the sample w sets a natural cut-off for the wavenumbers q and therefore only the low powers of q are relevant on the right hand side of Eqs. (5.65), (5.66). For simplicity, the boundary condition (5.67) is used, which is reasonable for not too small widths.

The Eqs. (5.65), (5.66) now can be solved by performing a Fourier transform. To fix the boundary conditions two pointlike delta-function inhomogneities are positioned at $\pm w$. In real space the equations

take the form

$$\kappa_T^{-1}\left(\partial_x,\omega\right) j_{\varepsilon,y}\left(x,\omega\right) = -\partial_y T - \alpha\delta\left(x-w\right) - \beta\delta\left(x+w\right) \tag{5.68}$$

$$\sigma_T^{-1}\left(\partial_x,\omega\right) j_{c,y}\left(x,\omega\right) = E_y - \alpha\delta\left(x-w\right) - \beta\delta\left(x+w\right). \tag{5.69}$$

If the constants α, β are chosen such that Eq. (5.67) is satisfied, the solution inside the sample will be identical to the solution of the homogeneous equations with the matching boundary conditions.

Here, the profiles of electric current flows through samples of different widths will be calculated. Solving the Eq. (5.68) in Fourier space one obtains

$$j_{c,y}\left(q_x,\omega\right) = \left(2\pi E_y \delta\left(q_x\right) - \alpha e^{-iwq_x} - \beta e^{iwq_x}\right)\sigma_T\left(q_x,\omega\right). \tag{5.70}$$

Inserting this result into Eq. (5.67) gives two algebraic equations, from which α and β can be determined:

$$\begin{aligned}\zeta\int\frac{dq_x}{2\pi}\left(iq_x\right)\left(\alpha e^{-iq_x\frac{3w}{2}} + \beta e^{iq_x\frac{w}{2}}\right)\sigma_T\left(q_x,\omega\right) = \\ \int\frac{dq_x}{2\pi}\left(\alpha e^{-iq_x\frac{3w}{2}} + \beta e^{iq_x\frac{w}{2}}\right)\sigma_T\left(q_x,\omega\right) - \\ E_y\sigma_T\left(0,\omega\right)\end{aligned}$$

$$\begin{aligned}\zeta\int\frac{dq_x}{2\pi}\left(iq_x\right)\left(\alpha e^{-iq_x\frac{w}{2}} + \beta e^{iq_x\frac{3w}{2}}\right)\sigma_T\left(q_x,\omega\right) = \\ -\int\frac{dq_x}{2\pi}\left(\alpha e^{-iq_x\frac{w}{2}} + \beta e^{iq_x\frac{3w}{2}}\right)\sigma_T\left(q_x,\omega\right) + \\ E_y\sigma_T\left(0,\omega\right).\end{aligned}$$

The above integrals are calculated with the FFT algorithm. Once α, β are found, a Fourier transform the of the solution (5.70) gives the desired flow profiles.

Figs. 5.9 and 5.10 show the results for different widths w. For demonstrational purposes no-slip boundary conditions ($\zeta = 0$) were assumed in Fig. 5.9. Here, for $w > v\tau_{c,1}$ the flow profile turns flat in the middle of the sample and steeply descends to zero at the boundaries (as necessitated by the boundary conditions). This is behavior is due to the interaction induced conductivity that dissipates momentum uniformily across the sample - at a distance $d > v\tau_{c,1}$ away from the boundary a uniform flow is restored. On the other hand, for $w < v\tau_{c,1}$ the current relaxing scattering in the $m = 1$ channel becomes less and less important. The scattering in the $m = 2$ channel dominates. It acts in the same way viscous forces act when flows with finite momentum are considered. Current is transported from the middle of the sample, where it is maximal, to the sample edges, where current is dissipated. A finite sliplength (as discussed, $\zeta = vl_{c,2}$ was chosen for simplicity) alters these results (see Fig. 5.10): Whereas for widths $w > v\tau_{c,1}$ the finite slip gives the current a non-negligable velocity at the sample boundary, for small widths $w < v\tau_{c,2}$, the flow profiles are rendered flatter, and the boundary effects become negligable. In the crossover region $w \sim v\tau_{c,1}$, the profiles are curved and resemble a parabola. This takes place around $w \sim 0.5v\tau_{c,2}$ and is in accordance with the general expectations [84]: for $w < v\tau_{c,2}$ the quasi-viscous transport of currents from the middle of the sample towards the boundaries becomes inefficient, and the boundary does efficiently dissipate the current.

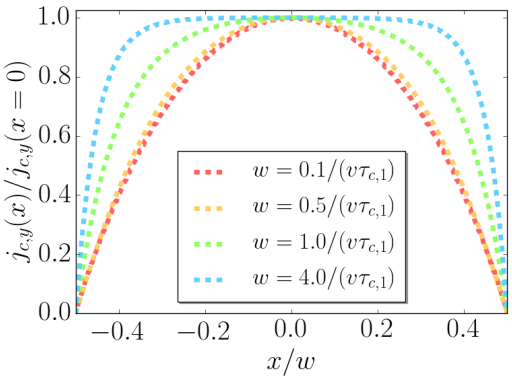

Figure 5.9: Poiseuille profiles of charge currents in undoped graphene samples of different widths w. Although physically incorrect, no-slip boundary conditions were assumed for clarity. The profiles are normalized to the current at $x = 0$. At large widths $w > v\tau_{c,1}$, the flow profiles turn flat. In the bulk they resemble Ohmic flow. For small widths $w < v\tau_{c,1}$, the momentum non-conserving scattering becomes inefficient. The electrons travel a distance corresponding to several width before loosing their momentum. Consequently, the profiles take a parabolic form, resembling classical Poiseuille flow. The profiles were calculated from Eq. (5.70).

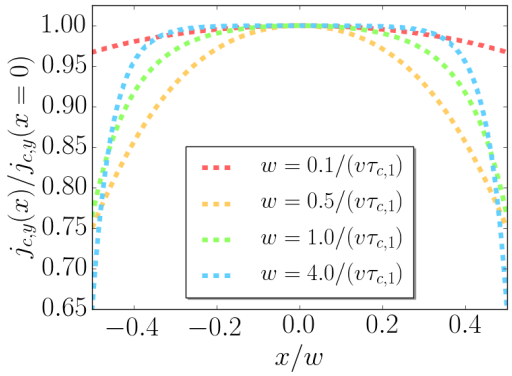

Figure 5.10: Poiseuille profiles of charge currents in undoped graphene samples of different widths w, normalized to the current at $x = 0$. Partial slip boundary conditions with a slip length $\zeta = v\tau_{c,2}$ were applied. At very small widths $w \ll \zeta$, boundary scattering ceases to be an efficient mechanism for the dissipation of electric current. The profiles turn flat, as they do in the nearly Ohmic regime $w > v\tau_{c,1}$. In the crossover regime at widths $w \sim 0.5v\tau_{c,1}$, profile curvature is most pronounced. The profiles were calculated from Eq. (5.70).

5.5 Summary

This chapter focussed on the non-local tranport properties and collective excitations of graphene electrons at the charge neutrality point. The quantum Boltzmann method developed in Ref. [49] was used. This method relies on the fact that at experimental temperatures the graphene fine structure constant α is renormalized to small values. Thermally excited electrons and holes therefore appear as sharply defined quasiparticles, whose transport properties can be studied by means of a kinetic equation. The solution of this equation is facilitated by the presence of so-called collinear modes, whose scattering rates are enhanced by a large factor of $\log\left(1/\alpha\right)$. Here, the velocities of the interacting particles are parallel to each other. Due to the linear graphene spectrum, all particles travel at the same speed, regardless of their momentum. Particles traveling in parallel have a particularely long time to interact with each other, hence the strong enhancement. Transport in the hydrodynamic regime, however, is dominated by processes, which have the smallest scattering rates (for details see Eq. (5.16) and below). Such "slow" processes are represented by collinear zero modes – functions that set the collinear part of the collision operator to zero [49, 54].

In this chapter, the kinetic equation was solved by reducing it to a matrix equation in the space of collinear zero modes $\chi_{\mathbf{k},\lambda}^{(m,s)} = \lambda^m e^{im\theta}\left\{1, \lambda, \lambda\beta v\hbar k\right\}$. Here, θ is the polar angle and k the modulus of the momentum variable $\mathbf{k}$, $\lambda = \pm 1$ is the band index, m labels the angular harmonics and $s \in \left\{1, 2, 3\right\}$ labels the three basis functions written in curly brakets.

It was found that, to an excellent approximation, it is sufficient to retain only the $s = 1$ and $s = 3$ modes. These modes describe charge (c) and energy (ε) excitations, respectively. A numerical evaluation of the collision integral showed, that the relaxation rates of these modes grow linearly with increaling m:

$$\tau_{\varepsilon/c,m}^{-1} \sim |m|\,, \tag{5.71}$$

for large m (see sections 5.1.2 and 5.2.2). It is an important feature of charge neutral graphene, that the hydrodynamic modes excited by electric and thermal fields decouple in linear response and in the abscence of magnetic fields [51, 144]. They are characterized by the distinct scattering rates of Eq. (5.71). Due to the surprising linear behavior of the relaxation rates, an exact solution to the linearized Boltzmann equation could be found, which is valid to first order in the Knudsen number. The Boltznann equation could be rewritten into a recurrence relation, which has solutions in terms of modified Bessel functions (see Eq. 5.39 and below). Using this result, the non-local, i.e. wavevector-dependent, charge and thermal conducitivities as well as the non-local viscosity were calculated. The results are given in Eqs. (5.46), (5.50), and (5.55), respectively. The transport coefficients show pronounced resonance features at $vq \approx \omega$ where q and ω are the wavenumber and frequency of the applied electric field or thermal gradient (see Figs. 5.2, 5.3). The non-local charge conductivity is of possible relevance to experiments with surface acoustic waves [145–147].

Non-local transport coefficients determine the transport behavior in spacially inhomogeneous fields or in confined geometries. The latter case was illustrated for the electric conductivity, using the Poiseuille geometry as an example. The constitutive relation linking the electric current to the electric field along the channel was interpreted as a differential equation (Eq. (5.66)) and solved with the appropriate boundary conditions (Eq. (5.67)). These boundary conditions were the subject of the preceding chapter 4. It was found, that the flow profiles strongly depend on the channel width w as compared to the electron-electron scattering lengths in the $m = 1$ and $m = 2$ channels: $l_{c,1} = v\tau_{c,1}$, $l_{c,2} = v\tau_{c,2}$. While $l_{c,1}$ governs the decay of charge currents, $l_{c,2}$ determines the effectiveness of current transfer from regions with high current density to regions with low current density. This latter mechanism is

analogous to viscous momentum transfer. The flow profiles in dependence on w can be separated into three regimes. For $w \gg l_{c,1} > l_{c,2}$, the samples are in the Ohmic regime, where the current is dissipated uniformily across the sample. The flow profile is flat. For $l_{c,1} < w < l_{c,2}$, the profile curvature is maximal, since on the one hand the current decay due to electron-electron scattering in the $m = 1$ channel becomes inefficient, on the other hand the current transfer to the boundaries of the sample, where the flow is slowed down, is sufficiently strong. For even smaller widths $w < l_{c,2}$, the profile turns flat again, because the current transfer mechanism associated with $l_{c,2}$ ceases to be efficient. This characteristic pattern is shown in Fig. 5.10. Current profiles are accessible experimentaly, e.g. through the scanning single electron transistor technique of Refs. [29, 30].

Finally, the collective modes of a Dirac liquid were studied. As do the transport coefficients, the collective modes separate into a sector of charge excitations and a sector of energy and imbalance excitations ($s = 2$). These two sectors are decoupled and can be studied separately. It was found, that while the plasmon mode is gapped out at small wavenumbers due to the interaction induced resistivity (see Fig. 5.5), a so-called second sound mode, corresponding to the wavelike propagation of energy, appears (Fig. 5.8). Diffusive modes, corresponding to the diffusion of charge, heat and quasiparticles were found (see Figs. 5.4, 5.6). Their dispersion relations were calculated and showed to agree with known results [52, 113, 132]. Besides these well studied modes, an infinite set of damped modes connected to excitations in higher angular harmonic channels was found (see Figs. 5.4, 5.7). The dispersions of these modes are purely imaginary at vanishing wavenumbers and approach the values $\omega_m\left(q = 0\right) = -i/\tau_{\varepsilon/c,m}$ for the m-th angular harmonic in the energy (ε) or the charge (c) channels. At finite wavenumbers, these modes show a complex structure of merging branches. Similar modes play an important role in the equilibration of unitary fermi gases [133]. They also determine the unusual phase space dynamics of graphene electrons presented in the next chapter.

Chapter 6

6 Lévy flights and superdiffusion in phase space

In this chapter it is shown, that the phase space dynamics of the electron-hole plasma in charge neutral graphene is described by a Fokker-Planck equation involving a fractional derivative. Such equations are known from the theory of anomalous diffusion and were reviewed in section 3. In the case of graphene, the dynamics is superdiffusive, and the underlying trajectories of single particles (viewed as classical objects) are Lévy flights.

The description of interacting gases and plasmas by means of Fokker-Planck equations is well developed [64–68]. Applications range from the computational physics of plasma confinenment [69] to the study of galaxy clusters [70]. In these cases, the single particle tajectories are Gaussian random walks through phase space. The kinetic equation can be reduced to a Fokker-Planck equation describing diffusion in phase space. The kinetic equation of graphene electrons, however, cannot be handled in the same way. Graphene electrons can make huge leaps through phase space – a behavior known from the theory of Lévy flights. As a consequence, the equations governing the behavior of the kinetic distribution functions become highly non-local, necessitating the use of integral operators or fractional derivetives. The connection between Lévy flights and fractional Fokker-Planck equations was established in sec. 3. In the following, the fractional Fokker-Planck equation for graphene will be derived and applied to study the relaxation behavior of a focussed current beam. The results presented here have been published in Ref. [138].

6.1 Relaxation behavior of collinear zero modes

The problem of deriving a Fokker-Planck-type equation for graphene at charge neutrality can be attacked by the quantum Boltzmann methods of chapter 5. Again the notions of collinear and non-collinear scattering processes are crucial. In collinear scattering the velocities of scattered particles point in the same direction, whereas they can point in different directions for non-collinear scattering. The expansion of the quantum Boltzmann equation in terms of collinear zero modes, introduced in chapter 5, again proves a useful tool. In chapter 5 it was shown, following Ref. [49], that the scattering rates of collinear processes are enhanced by a large factor of

$$\log\left(1/\alpha\right)$$

Here, α is the small graphene fine structure constant. Intuitively, this enhancement is due to the fact that because of the linear spectrum of graphene, all particles are travelling at the same speed, regardless of their momentum. Therefore, particles whose velocities point in the same direction, interact with each other for a particularly long period of time. so-called collinear zero modes, which set the collinear part of the collision integral to zero, i.e. describe only non-collinear processes, prevail in the hydrodynamic limit of long times and slow excitations. In the preceding chapter 5, it was shown that an effective kinetic equation can be constructed by projecting the full quantum Boltzmann equation onto collinear zero modes. This projection was used, to calculate the transport coefficients of charge neutral graphene in the hydrodynamic limit. Here, relaxation processes will be studied, and therefore a slightly different perspective will be taken.

Imagine that at $t = 0$ the system is in a state of strong non-equilibrium. At $t > 0$ this state begins to relax. The equilibration is caused by electron-electron collisions and takes place on two separate time scales. First there are the collinear processes that are enhanced by the factor $\log\left(1/\alpha\right)$. These processes will very soon relax the system to a near-equilibrium state where the distribution function can be expanded in the usual form:

$$f_{\mathbf{k}\lambda}\left(\mathbf{x},t\right) = f_{k\lambda}^{(0)} + f_{k}^{(0)}\left(1 - f_{k}^{(0)}\right)\psi_{\mathbf{k}\lambda}.$$

The deviation from local equilibrium $\psi_{\mathbf{k}\lambda}$ can be expanded in terms of the not yet decayed collinear zero modes

$$\chi_{\mathbf{k},\lambda}^{(m,s)} = \lambda^{m} e^{im\theta}\left\{1, \lambda, \lambda\beta v\hbar k\right\}. \tag{6.1}$$

It is

$$\psi_{\mathbf{k},\lambda} = \sum_{m=-\infty}^{\infty}\sum_{s=1}^{3} a_{m,s}\left(\omega,\mathbf{q}\right)\chi_{\mathbf{k},\lambda}^{(m,s)}. \tag{6.2}$$

Here m labels the angular harmonics and s the collinear zero modes. Considering, for simplicity, excitations connected to charge currents and electric fields, only the $s = 1$ modes of Eq. (6.1) are relevant (see the discussion of Sec. 5.2). They are given by

$$\chi_{\mathbf{k},\lambda}^{(m,1)} = \lambda^{m} e^{im\theta_{\mathbf{k}}}. \tag{6.3}$$

These modes depend on the polar angle of the momentum vector, $\theta_{\mathbf{k}}$, but not its modulus k. There is therefore a fast relaxation in k, and a slower hydrodynamic relaxation in the angular variable $\theta_{\mathbf{k}}$. The latter is slower by the factor $\log\left(1/\alpha\right)$. As a result, for times $t \to \infty$ the overall evolution of the system is governed by the collinear zero mode hydrodynamic theory introduced in chapter 5. This long-term behavior is studied here. Fig. 6.1 illustrates the relaxation process and its time scales.

It has already been discussed in chapter section 5.1.2 that the scattering rates of collinear zero modes grow like $|m|$ with increasing angular harmonic numbers m. This behavior is demonstrated in Fig. 5.1 and for the $s = 1$ mode, that is of interest here, on the log-log plot of Fig. 6.2. It is the non-analytic dependence on the absolute value of m, that leads to the unusal superdiffusive behavior. To simplify the analysis, the scattering times of Eq. 5.35 can be approximated by

$$\tau_{m}^{-1} = \tau_{L}^{-1}\left|m\right| \tag{6.4}$$

with

$$\tau_{L}^{-1} = \kappa\tau_{c,1}^{-1}$$

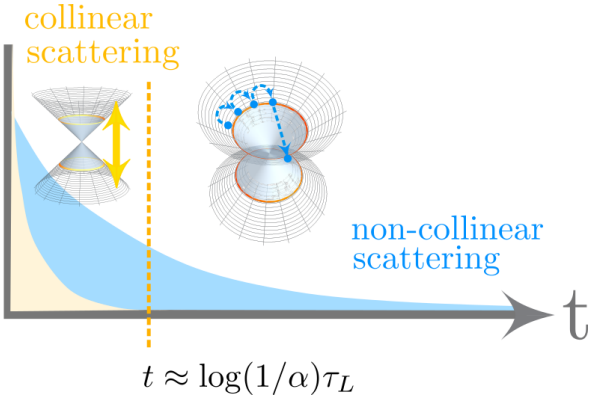

Figure 6.1: The time scales of a typical relaxation process. At short times $t < \log\left(1/\alpha\right)\tau_L$ the relaxation is dominanted by collinear scattering processes. Due to their suppressed scattering rate, the collinear zero modes dominate the long time behavior $t > \log\left(1/\alpha\right)\tau_L$ (blue curve). This regime is characterized by Lévy flights and hydrodynamic superdiffusion. τ_L is the characteristic time scale of the hydrodynamic Lévy process. Whereas in the fast regime the system equilibrates along the energy axis, in the slow regime an equilibration in the angular coordinate $\theta_{\mathbf{k}}$ takes place.

where $\kappa = 3.2$ is a constant stemming from the numerical evaluation of the collision integral. $\tau_{c,1}^{-1}$ is the relaxation rate of a homogeneous charge current defined above Eq. (5.35). It appears in the expression for the interaction induced conductivity [49]

$$\sigma_0 = \frac{2e^2 \log\left(2\right)\tau_{c,1}}{\pi k_B T \hbar^2}.$$

While the approximation (6.4) is not too good at low $|m|$, it captures the essential features of the Lévy flight dynamics, for which the linear behavior at large $|m|$ is relevant. The location of the crossover between the fast relaxation and the slow Lévy flight regime can be estimated by $\tau_L/\log\left(1/\alpha\right)$. By that time, the collinear modes have decayed and only collinear zero modes remain.

6.2 Fractional Fokker-Planck equation

In this section the quantum Boltzmann equation of chapter 5 will be reduced to a fractional Fokker-Planck equation, where the appearance of the fractional derivative will be necessitated by the non-analytic m-dependence of the scattering rates. The linearized kinetic equation for graphene electrons of section 5.1) reads

$$\left(\partial_t + \mathbf{v}_{\mathbf{k}\lambda}\cdot\nabla_{\mathbf{x}} - \mathcal{C}\right)\psi_{\mathbf{k},\lambda}\left(\mathbf{x},t\right) = S_{\mathbf{k}\lambda}. \tag{6.5}$$

Here and in the following, it is tacitly assumed, that the system is in the hydrodynamic regime, and that only the charge mode $\chi_{\mathbf{k},\lambda}^{(m,1)} = \lambda^m e^{im\theta_{\mathbf{k}}}$ is excited, so that the expansion (6.2) reads $\psi_{\mathbf{k},\lambda} = \sum_{m=-\infty}^{\infty}\lambda^m a_m\left(\omega,\mathbf{q}\right)e^{im\theta_{\mathbf{k}}}$. The collision operator $\mathcal{C}$ is characterized by its matrix elements with respect to the modes $\chi_{\mathbf{k},\lambda}^{(m,1)}$, which in their turn give the scattering rates τ_m^{-1}. The action of $\mathcal{C}$ on an

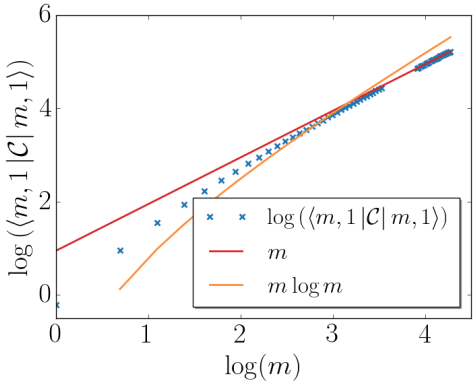

Figure 6.2: Log-log plot of the matrix elemets of the collision operator given in Eq. (5.10). m is labels the angular harmonics $e^{im\theta_{\mathbf{k}}}$. It is demonstrated that the linear in m behavior can be destiguished from e.g. an $|m|\log|m|$ dependence.

arbitrary θ-dependent function can be examined by performing a Fourier transformation:

$$\sum_m e^{im(\theta-\theta')}\tau_m^{-1} = -\frac{\tau_L^{-1}}{2}\frac{1}{\sin^2\left(\frac{\theta-\theta'}{2}\right)} = \tau_L^{-1}\frac{\partial}{\partial\theta}\frac{1}{\tanh\left(\frac{\theta-\theta'}{2}\right)}. \tag{6.6}$$

With the convolution theorem, for a function $g\left(\theta\right)$ follows

$$\sum_m e^{im(\theta-\theta')}\tau_m^{-1}g_m = \tau_L^{-1}\frac{\partial}{\partial\theta}\int_0^{2\pi}\frac{g\left(\theta'\right)}{\tanh\left(\frac{\theta-\theta'}{2}\right)}d\theta'.$$

This result can be written using the Riesz-Feller derivative $\Delta^{\mu/2}$ [108, 148] with $\mu = 1$:

$$\left(\frac{\partial^2}{\partial\theta^2}\right)^{1/2} g\left(\theta\right) = \frac{\partial}{\partial\theta}\int_0^{2\pi}\frac{g\left(\theta'\right)}{\tanh\left(\frac{\theta-\theta'}{2}\right)}d\theta'.$$

This generalization of the a derivative builds upon its Fourier representation: for the second derivative holds $\partial^2/\partial\theta^2 \to m^2$, for the fractional derivative one has $\partial^{\mu/2}/\partial\theta^{\mu/2} \to |m|^{\mu/2}$. Using the fractional derivative, the Boltzmann equation (6.5) can be written as

$$\left(\partial_t + \mathbf{v}_{\mathbf{k}\lambda}\cdot\nabla_{\mathbf{x}} - \tau_L^{-1}\left(\frac{\partial^2}{\partial\theta_{\mathbf{k}}^2}\right)^{1/2}\right)\psi_{\mathbf{k},\lambda}\left(\mathbf{x},t\right) = S_{\mathbf{k}\lambda}. \tag{6.7}$$

This equation is a fractional Fokker-Planck equation type of the of Eq. (3.13). The second term in brackets is a drift term, and vanishes if the system is homogeneous. The discussion of section 3.2 showed that the dynamics of Eq. (6.7) corresponds to Lévy flights of particles on horizontal cuts through the Dirac cone.

6.3 Lévy flight interpretation

The scattering rates for different angular harmonic channels are determined by the matrix elements of the collision operator:

$$\left\langle m \left| \mathcal{C} \right| m \right\rangle \propto \tau_m^{-1}.$$

(see section 5.2.2). A Fourier transformation of Eq. (6.6) gives

$$\left\langle \theta \left| \mathcal{C} \right| \theta' \right\rangle \propto \frac{1}{\sin^2\left(\frac{\theta-\theta'}{2}\right)}, \tag{6.8}$$

where the index $\mathbf{k}$ of $\theta_{\mathbf{k}}$ was dropped. Eq (6.8) shows that most collisions will be of forward scattering type due to the divergence at $\theta = \theta'$, scattering events away from forward scattering are only weakly suppressed by the power law $\sim \left(\theta - \theta'\right)^{-2}$. Therefore large angle scattering events are relatively probable. Taking up the discussion of section 3.1, where the Lévy flight was defined as a random walk whose step size distribution decays as a power law, a random walk governed by the scattering behavior (6.8) is expected to be a Lévy flight.

According to section 3.2, the step size distribution function is given by the solution of the fractional Fokker-Planck equation (6.7). In a spatially homogeneous scenario, the drift term vanishes. Focussing on states on the upper Dirac cone $\lambda = +1$, let the initial condition at $t = 0$ be $\psi_+\left(t = 0, \theta\right) = \delta\left(\theta\right)$, $\psi_-\left(t = 0, \theta\right) = 0$. The solution in Fourier space is easily found: $\psi_{+,m}\left(t\right) = e^{-\tau_L^{-1}|m|t}$. A Fourier transform gives the solution in phase space. Inserting $t = \Delta t$, where Δt is the small time interval during which a step of the random walk takes place, the step size distribution reads

$$\psi_{+,m}\left(\Delta t\right) = \frac{\sinh\left(\Delta t/\tau_L\right)}{\cosh\left(\Delta t/\tau_L\right) - \cos\left(\theta\right)}. \tag{6.9}$$

This is a so-called wrapped Cauchy distribution. It determinines the random walk of a particle on a horizontal cut through the Dirac cone. Like the matrix elements (6.8), it is characterized by the power law decay of step sizes $\sim \theta^2$. It is useful to compare Eq. (6.9) to the solution that one would have obtained for ordinary diffusion. Here, the fractional dericative in Eq. (6.7) has to be replaced by the second derivative $\partial^2/\partial\theta^2$. The solution reads $\psi_{\lambda,m}\left(t\right) = \delta h \Theta\left(t\right) \sum_m \lambda^m e^{im\theta - \tau_L^{-1} m^2 t}$. The sum gives an expression involving the Jacobi theta function, however the von Mises distribution $\psi_\lambda^{\text{Gauss}}\left(\theta, t\right) = \delta h \Theta\left(t\right) e^{\cos(\theta)\tau_L/\Delta t} / \left(2\pi I_0\left(\tau_L/\Delta t\right)\right)$ is a good approximation [149]. Clearly, large angle scattering is much stronger suppressed in the Gaussian case. A random walk for the step size distribution (6.9) is shown in Fig. 6.3 in comparison to a Gaussian random walk, which would correspond to normal diffusion. Finally, it must be stressed, that the notion of an electronic random walk sustained by electron-electron collisions is problematic, because electrons are indistiguishable particles. However, it is appropriate on a semi-classical level, and provides a good illustration of the physics behind electron-electron scattering in charge neutral graphene.

6.4 Decay of injected current beams and anomalous heating

An immediate consequence of the fact that graphene electrons perform Lévy flights through phase space, is the superdiffusive decay of focused current beams and the unconventional heating of the system. The

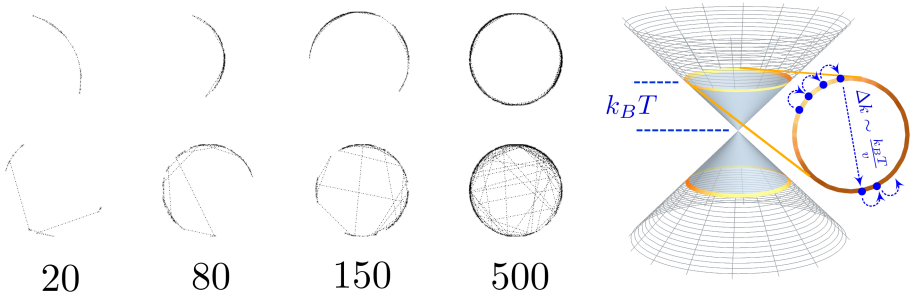

Figure 6.3: Comparison between Gaussian random walks (upper row) and Lévy flights (lower row) on the Dirac cone. Due to their long tail step size distribution, Lévy flights cover the available phase space more quickly. They dominate the dynamics in the slow hydrodynamic regime, where they are confined to horizontal sections through the Dirac cone with typical energies on the scale of k_BT (right side).

injection of focused electron beams as a tool to investigate electron-electron scattering in hydrodynamic electron systems was first applied to two dimensional electron gases in semiconductor heterostructures [59]. In the following, the behavior of a focussed electron beam in graphene is examined.

The injection such a beam can be modelled by inserting the term

$$S_{\mathbf{k}\lambda}(t) = \delta(t) f_k^{(0)} \left(1 - f_k^{(0)}\right) \sum_m \delta h_{\lambda m} e^{im\theta} \tag{6.10}$$

into Eq. (6.7). The beam consists of electrons and holes in a window $\pm k_BT$ around the Dirac point, which is ensured by the factor $f_k^{(0)}\left(1 - f_k^{(0)}\right)$. The linearized Boltzmann equation can be used if $\left|\delta h_{\lambda m}\right| \ll 1$ holds for the coefficients in the expansion in angular harmonics. Choosing $\delta h_{\lambda m} = \delta h \lambda^m$, the $s = 1$ collinear zero mode of Eq. (6.3) is excited, which corresponds to a charge current. Intuitively, one can think of identical beams of electrons and holes flowing in opposite directions. Because electrons and holes have opposite charge, the total current is twice the contribution of one species. The solution of the Fokker-Planck equation is

$$\psi_\lambda(\theta, t) = \delta h \Theta(t) \frac{\sinh\left(t/\tau_L\right)}{\cosh\left(t/\tau_L\right) - \lambda\cos\left(\theta\right)}, \tag{6.11}$$

where $\Theta(t)$ is the step function. $\psi_+(\theta, t)$ is shown on the left hand side of Fig. 6.4.

For $t = 0$, $\psi_\lambda(\theta, t)$ corresponds to two delta functions due to particle and hole flows in opposite directions. In the following, it is sufficient to concentrate on the particle channel $\lambda = +1$. For short times $t \ll \tau_L$, the peak in the initial current direction decays as

$$\psi_+(t, \theta = 0) \approx \delta h \frac{\tau_L}{\pi t}, \tag{6.12}$$

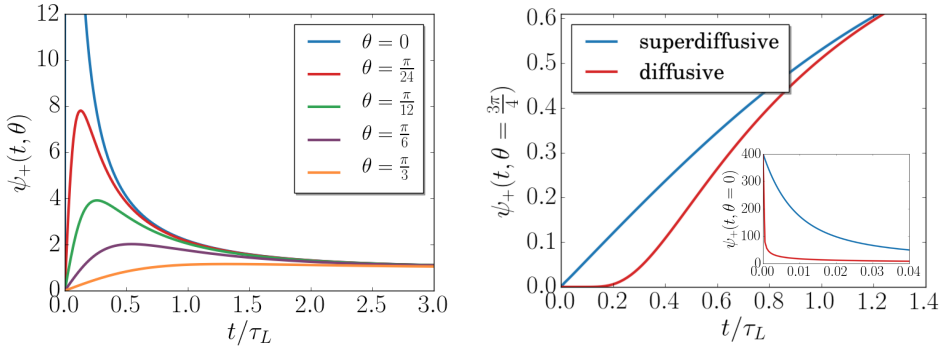

Figure 6.4: Left hand side: Post-injection dynamics of the distribution function calculated from the fractional Fokker-Planck equation, Eq. 6.7, with the external perturbation of Eq.6.10. Right hand side: Comparison of superdiffusive and diffusive dynamics at short times. The initial peak at $\theta = 0$ decays and broadens. At angles away from the peak, superdiffusion leads to a faster growth of the distribution function. Inset: the initial peak at $\theta = 0$ decays as $1/t$ for superdiffusion and $1/\sqrt{t}$ for ordinary diffusion. This behavior dominates the heating of the system, as is shown in the main text.

while the distribution function grows linearly for all non-zero angles:

$$\psi_+\left(t, \theta \neq 0\right) \approx \frac{\delta h}{4\pi \sin^2\left(\theta/2\right)} \frac{t}{\tau_L}. \tag{6.13}$$

The same behavior occurs for $\lambda = -1$ with the shift $\theta \to \theta + \pi$. This is in contrast to what follows from usual Fokker-Planck diffusion, where one has $\tau_m^{-1} \sim m^2$. The spreading due to Gaussian diffusion occurs with $\psi_+\left(t, \theta = 0\right) \propto t^{-1/2}$ and $\psi_+\left(t, \theta \neq 0\right) \propto t^2$ (right hand side of Fig. 6.4). While in the forward direction the beam decays slower for Levy flights than for normal diffusion, the growth at larger angles is much faster, hence the name superdiffusion.

One observable manifestation of this superdiffusive charge motion is the heating of the system after the injection. The heating rate can be calculated from the rate of entropy growth. Using the standard expression for the entropy of a fermionic system [15] $s = -k_B \sum_\lambda \int dk \left(f_{\mathbf{k}\lambda} \log f_{\mathbf{k}\lambda} + \left(1 - f_{\mathbf{k}\lambda}\right) \log\left(1 - f_{\mathbf{k}\lambda}\right)\right)$ one obtains for the entropy production rate

$$\dot{s} = 4k_B \sum_\lambda \int_k \log\left(\frac{1 - f_{\mathbf{k}\lambda}}{f_{\mathbf{k}\lambda}}\right) \frac{\partial f_{\mathbf{k}\lambda}}{\partial t}. \tag{6.14}$$

Inserting the distribution function of Eq. (6.11) gives th

$$\dot{s} = \frac{4\log 2}{9\zeta\left(3\right)} \frac{s_{\text{eq}}}{\tau_L} \frac{\left(\delta h\right)^2}{\sinh^2\left(t/\tau_L\right)}, \tag{6.15}$$

where $s_{\text{eq}} = 4\frac{9\zeta(3)}{\pi} k_B \frac{\left(k_B T\right)^2}{\hbar^2 v^2}$ is the equilibrium entropy density [51]. This formula can be used to estimate the heating rates after the injection of the current beam: $\dot{q} = T\dot{s}$. For the Lévy flight process governing the electron behavior in graphene one finds $\dot{q} \propto 1/t^2$ for small t. For the Gaussian process it is $\dot{q} \propto 1/t^{3/2}$. For small t, the heating rate of the Lévy process is larger, reflecting its

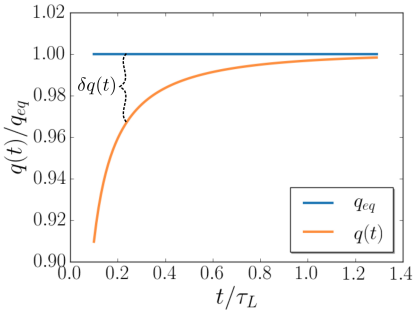

Figure 6.5: Heating after the injection of a focussed current beam. The time dependent heat density of the system is given by $q(t) = Ts(t)$. The quantity $\delta q(t)$ corresponds to the heat produced by the injected beam.

superdiffusive nature. For $t \to \infty$ the entropy approaches its equilibrium values $s \to s_{\text{eq}}$, and thus $s(t) = s_{\text{eq}}\left(1 - (\delta h)^2 \frac{4\log(2)}{9\zeta(3)}\left(\coth\left(\frac{t}{\tau_L}\right) - 1\right)\right)$. As illustrated in Fig. 6.5 the heat density caused by the injection is given by $\delta q(t) = T\left(s_{\text{eq}} - s(t)\right)$. The initial heating occurs according to the law

$$\delta q(t) \propto T s_{\text{eq}} \delta h^2 \frac{\tau_L}{t}. \tag{6.16}$$

In order to stay within the regime of linear response, the condition $t > \delta h \tau_L$ must hold. This result is a direct consequence of the superdiffusive behavior, in particular of the slow decay along the forward direction (see Eq. (6.12)). In the case of ordinary diffusion follows $\delta q(t) \propto t^{-1/2}$ which is a faster power-law (see Fig. 6.4). It is important to note, that the total amounts of heat released by the superdiffusive and the diffusive processes is different. Adjusting δh such that the same amount of heat is produced for Lévy and diffusive behavior, the initial heating of the Lévy flight is faster.

Finally, it should be said that there exist many other systems in which anomalous phase space diffusion can be found. One example are electrons in a random magnetic fields, as they occur in the description of composite fermions in the fractional quantum Hall regime [140]. The scattering rates were predicted to behave as $\tau_m^{-1} \propto |m|$ and thus the system should show similar Lévy flight behavior. Two dimensional Fermi liquids are another example. Here the scattering rates are given by $\tau_m^{-1} \propto \left(T^2/T_F\right)\log|m|$ for even m and $\tau_m^{-1} \propto \left(T^4/T_F^3\right) m^4 \log|m|$ for odd m, in the regime $1 < |m| < \sqrt{T_F/T}$, where T_F is the Fermi temperature, whereas for $|m| > M$ it is $\tau_m^{-1} \propto T^2/T_F$. This corresponds to an anomalous behavior in a broad regime of temperatures [57, 58].

6.5 Summary

The phase space evolution of many interacting gases and plasmas is governed by normal diffusive behavior [64–68]. These systems can be described in terms of Fokker-Planck equations in phase space. Graphene electrons at the charge neutrality point behave differently. In this chapter, starting from the quantum Boltzmann equation (6.5), it was shown, that in the hydrodynamic regime the electron-hole plasma of graphene undergoes Lévy flights on the Dirac cone [138]. This results in a superdiffusive

dynamics, which can be captured by the fractional Fokker-Planck equation

$$\left(\partial_t + \mathbf{v}_{\mathbf{k}\lambda} \cdot \nabla_{\mathbf{x}} - \tau_L^{-1} \left(\frac{\partial^2}{\partial \theta^2} \right)^{1/2} \right) \psi_{\mathbf{k},\lambda} \left(\mathbf{x}, t \right) = S_{\mathbf{k}\lambda}. \tag{6.17}$$

here, $\psi_{\mathbf{k},\lambda}$ is the non-equilibrium contribution to the kinetic distribution function, $\mathbf{v}_{\mathbf{k}\lambda} = \lambda v \mathbf{k}/k$ is the group velocity of electrons $\left(\lambda = -1\right)$ and holes $\left(\lambda = +1\right)$, θ is the polar angle of the momentum variable $\mathbf{k}$, $S_{\mathbf{k}\lambda}$ represents forces acting on the system and τ_L is the characteristic time scale of the underlying Lévy process. The fractional derivative is of the Riesz-Feller type [108, 148].

As in chapter 5, use has been made of the fact, that collinear electron-electron scattering is enhanced by the large factor $\log\left(1/\alpha\right)$. Here, α is graphene's fine structure constant, which is renormalized to small values at low temperatures (see section 1.2). In the long time limit, only so-called collinear zero modes (see Eq. 6.1) survive. These modes do not decay due to collinear processes. Correspondingly, their decay is slower by the factor $\log\left(1/\alpha\right)$ and governs the long term evolution of the system. The phase space dynamics of the collinear zero mode associated with charge excitations (see Eq. 6.3) is confined to the polar angle θ of the momentum variable $\mathbf{k}$. The Lévy flight nature of this dynamics is due to the non-analytic behavior of the scattering rates of collinear zero modes in different angular harmonic channels m:

$$\tau_m^{-1} = \tau_L^{-1} \left| m \right|. \tag{6.18}$$

The anomalous phase space dynamics has deep consequences for the relaxational behavior of charge neutral graphene, for example on the decay of an injected focussed charge current beam. Here, the evolution of an initial perturbation consisting of an electron beam and an oppositely directed hole beam was calculated. The directional spreading of the current beam (see Eq. 6.11 and Fig. 6.4) was shown to be faster than in ordinary diffusion. It was found, that the heating of the system after the injection is characterized by laws that reflect the superdiffusive nature of the relaxation process. In particular, the heating rate is determined by $\dot{q} = 1/t^2$. This is in contrast to the much slower normal diffusive heating $\dot{q} \propto 1/t^{3/2}$.

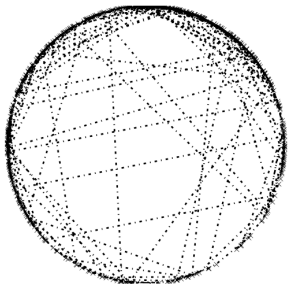

Figure 6.6: Lévy flight of a particle on a horizontal section through the Dirac cone, as described by equation (6.17). Small angle scattering events are separated by large jumps. The step size distribution governing the particle's random walk is a long-tailed wrapped Cauchy distribution.

List of publications

[1] E. I. Kiselev, M. S. Scheurer, P. Wölfle, and J. Schmalian, *Limits on dynamically generated spin-orbit coupling: Absence of $l = 1$ Pomeranchuk instabilities in metals*, Phys. Rev. B **95**, 125122 (2017)

[2] I. Kiselev, E. I. Kiselev, M. Drexel and M. Hauptmannl, *Noise robustness of interferometric surface topography evaluation methods. Correlogram correlation*, Surf. Topogr.: Metrol. Prop. **5**, 045008 (2017)

[3] J. M. Link, B. N. Narozhny, E. I. Kiselev, and J. Schmalian, *Out-of-Bounds Hydrodynamics in Anisotropic Dirac Fluids*, Phys. Rev. Lett. **120**, 196801 (2018).

[4] I. Kiselev, E. I. Kiselev, M. Drexel and M. Hauptmannl, *Precision of evaluation methods in white light interferometry. Correlogram correlation method*, Measurement **123**, 125 (2018).

[5] E. I. Kiselev, A. S. Averkin, M. V. Fistul, V. P. Koshelets, A. V. Ustinov, *Two-tone spectroscopy of a SQUID metamaterial in the nonlinear regime*, Phys. Rev. Research **1**, 033096 (2019).

[6] E. I. Kiselev and J. Schmalian, *Boundary conditions of viscous electron flow*, Phys. Rev. B **99**, 035430 (2019).

[7] E. I. Kiselev and J. Schmalian, *Lévy flights and hydrodynamic superdiffusion on the Dirac cone of Graphene*, Phys. Rev. Lett. **123**, 195302 (2019).

Acknowledgements

I would like to thank Prof. Jörg Schmalian for the opportunity to pursue my PhD in his group. I appreciated his insightful supervision and his great intuition for promising research subjects as much, as I did appreciate his openness towards my own ideas and his willingness to discuss anything at any time. I am also thankful to Prof. Alexander Mirlin for co-refereeing this thesis.

During the years at TKM, I appreciated the support from Sonja König and Fabienne Flatter in all formal and bureaucratic matters. I would also like to thank the Karlsruhe House of Young Scientists for its generous support during my three month stay in Cambridge, Massachusetts, as well as my host Prof. Leonid Levitov.

Furthermore, I am grateful for many valuable discussions (on science and beyond) to my fellow physicists Ali Fahimniya, Mareike Hoyer, Mathias Hecker, Billa Jeevanesan, Jonas Karcher, Markus Klug, Cyprian Lewandowski, Julia Link, Tim Ludwig, Mathias Scheurer and Piotr Witkowski, as well as all current and former members of TKM. “The institute” was a great place to be. I am especially indebted to Jonas, Billa and Markus, who helped me to improve this manuscript.

Special thanks go to my parents for their support during my entire life.

Appendix A

A The boundary conditions of viscous electron flow

A.1 Boundary condition for the kinetic equation

Falkovsky [62, 63] gave a microscopic derivation of the boundary conditions for the kinetic distribution function at a rough surface. The resulting boundary conditions are similar to those of earlier phenomenological approaches [61, 115], however, the effective parameters are expressed in terms of the surface roughness. Consider a sample oriented in the x-direction with a disordered edge $\xi(x)$ centered around $y = 0$. Important information is contained in the edge autocorrelation function

$$\overline{\xi(x_1)\,\xi(x_2)} = W(x_1 - x_2).$$

The overline in $\overline{\xi(x_1)\,\xi(x_2)}$ indicates an average over disorder realizations. If the edge is uniform on average, the autocorrelation will only depend on the distance between the two correlated points. For the Fourier transformation then holds

$$\overline{\xi(k_1)\,\xi(k_2)} = 2\pi\delta(k_1 + k_2)\,W(k_1). \tag{A.1}$$

As pointed out in the main text (section 4.1.1) the boundary condition for the wavefunctions of Dirac electrons is

$$\psi_a\big(x, y = \xi(x)\big) = 0, \tag{A.2}$$

where a is *one* of the two sublattice indices. Since the scattering at the boundary is elastic, the derived boundary conditions will be diagonal in the energy ε. It is therefore usefull to introduce the projection of the wave function ψ_a onto quasifree plane waves with a given energy ε:

$$\psi_{a,\epsilon}(\mathbf{x}) = \sum_\lambda \int \frac{d^2k}{(2\pi)^2}\delta\left(\epsilon - \varepsilon_{\lambda,k}\right)\psi_{\mathbf{k},\lambda}U_{a,\lambda}(\mathbf{k})\,e^{i\mathbf{k}\cdot\mathbf{r}}. \tag{A.3}$$

Here, $\varepsilon_{\lambda,k} = \lambda v\hbar k$ is the electron dispersion and $U_{a,\lambda}(\mathbf{k})$ transforms the wavefunctions $\psi_{\mathbf{k},\lambda}$ from the band basis into the sublattice basis: $\psi_{\mathbf{k},a} = \sum_\lambda \psi_{\mathbf{k},\lambda}U_{a,\lambda}(\mathbf{k})$. Note, that in this appendix the notation $\psi_{\mathbf{k},\lambda}$ is used for the wavefunctions $\gamma_{\mathbf{k},\lambda}$ of chapter 4. Assuming that the length scale on which the wavefunction varies near the boundary is large compared to the typical disorder scale of the edge h, i.e. the for the wavelength of electrons holds

$$\lambda_T \gg h,$$

one can expand the boundary condition (A.2) to first order in ξ around $y = 0$ giving

$$\psi_a\left(x, y=0\right) + \xi\left(x\right) \left.\frac{\partial \psi_a\left(x,y\right)}{\partial y}\right|_{y=0} = 0. \tag{A.4}$$

Carrying out the integration over k_y in equation (A.3), one has to differentiate between the two bands with negative and positive energies $\lambda = \pm 1$:

$$\underline{\varepsilon > 0:}$$

$$\begin{aligned}
\psi_{a,\varepsilon}\left(\mathbf{x}\right) &= \sum_{\lambda} \int \frac{d^2k}{(2\pi)} \delta\left(\varepsilon - \lambda v \sqrt{k_x^2 + k_y^2}\right) \psi_{\mathbf{k},\lambda} U_{a,\lambda}\left(\mathbf{k}\right) e^{i\mathbf{k}\cdot\mathbf{r}} \\
&= \int \frac{d^2k}{(2\pi)} \left(v_g^2 \sqrt{\frac{\varepsilon^2}{\lambda^2 v_g^2} - k_x^2}/\varepsilon\right)^{-1} \left[\delta\left(k_y - \sqrt{\frac{\varepsilon^2}{v_g^2} - k_x^2}\right) + \delta\left(k_y + \sqrt{\frac{\varepsilon^2}{v_g^2} - k_x^2}\right)\right] \\
&\quad \times \psi_{\mathbf{k},+} U_{a,+}\left(\mathbf{k}\right) e^{ik_x x + ik_y y} \\
&= \int \frac{dk_x}{(2\pi)} \frac{1}{\left|v^y\left(\varepsilon, k_x\right)\right|} \Big[\psi_+\left(k_x, k_y\right) U_{a,+}\left(k_x, k_y\right) e^{ik_y(\varepsilon, k_x) y} \\
&\quad + e^{-ik_y(\varepsilon,k_x)y} \psi_+\left(k_x, -k_y\right) U_{a,+}\left(k_x, -k_y\right) e^{ik_x x}\Big]
\end{aligned} \tag{A.5}$$

and

$$\underline{\varepsilon < 0:}$$

$$\begin{aligned}
\psi_{a,\varepsilon}\left(\mathbf{x}\right) &= \sum_{\lambda} \int \frac{d^2k}{(2\pi)} \delta\left(\varepsilon - \lambda v \sqrt{k_x^2 + k_y^2}\right) \psi_{\mathbf{k},\lambda} U_{a,\lambda}\left(\mathbf{k}\right) e^{i\mathbf{k}\cdot\mathbf{r}} \\
&= \int \frac{d^2k}{(2\pi)} \left(v_g^2 \sqrt{\frac{\varepsilon^2}{\lambda^2 v_g^2} - k_x^2}/\varepsilon\right)^{-1} \left[\delta\left(k_y - \sqrt{\frac{\varepsilon^2}{v_g^2} - k_x^2}\right) + \delta\left(k_y + \sqrt{\frac{\varepsilon^2}{v_g^2} - k_x^2}\right)\right] \\
&\quad \times \psi_{\mathbf{k},-} U_{a,-}\left(\mathbf{k}\right) e^{ik_x x + ik_y y} \\
&= \int \frac{dk_x}{(2\pi)} \frac{1}{\left|v^y\left(\varepsilon, k_x\right)\right|} \Big[\psi_-\left(k_x, k_y\right) U_{a,-}\left(k_x, k_y\right) e^{ik_y(\varepsilon, k_x) y} \\
&\quad + e^{-ik_y(\epsilon,k_x)y} \psi_-\left(k_x, -k_y\right) U_{a,-}\left(k_x, -k_y\right) e^{ik_x x}\Big].
\end{aligned} \tag{A.6}$$

Remember, that $k_y = k_y\left(k_x, \varepsilon\right)$ is not an independent component. Inserting into the wavefunction boundary condition

$$\psi_{a=1,\varepsilon}\left(x, y=0\right) + \xi\left(x\right) \left.\frac{\partial \psi_{a=1,\varepsilon}\left(x,y\right)}{\partial y}\right|_{y=0} = 0,$$

one gets

$$\begin{aligned} 0 &= \int \frac{dk_x}{2\pi} \frac{1}{\left|v^y\left(\varepsilon,k_x\right)\right|} \left[\psi_\lambda\left(k_x,k_y\right) U_{a,\lambda}\left(k_x,k_y\right) + \psi_\lambda\left(k_x,-k_y\right) U_{a,\lambda}\left(k_x,-k_y\right)\right] e^{ik_x x} \\ &+ \int \frac{dq_x}{2\pi} \xi\left(q_x\right) e^{iq_x x} \int \frac{dk_x}{2\pi} \frac{ik_y\left(\varepsilon,k_x\right)}{\left|v^y\left(\varepsilon,k_x\right)\right|} \\ &\times \left[\psi_\lambda\left(k_x,k_y\right) U_{a,\lambda}\left(k_x,k_y\right) - \psi_\lambda\left(k_x,-k_y\right) U_{a,\lambda}\left(k_x,-k_y\right)\right] e^{ik_x x}. \end{aligned}$$

Here, no summation over the indicex λ is impled. A Fourier transform $\int dx\, e^{-ik'_x x}$ yields

$$\begin{aligned} 0 &= \psi_\lambda\left(k'_x,k'_y\right) U_{a,\lambda}\left(k_x,k_y\right) + \psi_\lambda\left(k'_x,-k'_y\right) U_{a,\lambda}\left(k_x,-k_y\right) \\ &+ \left|v^y\left(\varepsilon,k'_x\right)\right| \int \frac{dk_x}{2\pi} \xi\left(k'_x-k_x\right) \frac{ik_y\left(\varepsilon,k_x\right)}{\left|v^y\left(\varepsilon,k_x\right)\right|} \left[\psi_\lambda\left(k_x,k_y\right) U_{a,\lambda}\left(k_x,k_y\right)\right. \\ &\left. -\psi_\lambda\left(k_x,-k_y\right) U_{a,\lambda}\left(k_x,-k_y\right)\right] \\ \psi_\lambda\left(k'_x,k'_y\right) &= -\psi_\lambda\left(k'_x,-k'_y\right) \frac{U_{a,\lambda}\left(k'_x,-k'_y\right)}{U_{a,\lambda}\left(k'_x,k'_y\right)} \\ &-i\frac{\left|v^y\left(\varepsilon,k'_x\right)\right|}{U_{a,\lambda}\left(k'_x,k'_y\right)} \int \frac{dk_x}{2\pi} \xi\left(k'_x-k_x\right) \frac{k_y\left(\varepsilon,k_x\right)}{\left|v^y\left(\varepsilon,k_x\right)\right|} \left[\psi_\lambda\left(k_x,k_y\right) U_{a,\lambda}\left(k_x,k_y\right)\right. \quad \text{(A.7)} \\ &\left. -\psi_\lambda\left(k_x,-k_y\right) U_{a,\lambda}\left(k_x,-k_y\right)\right]. \quad \text{(A.8)} \end{aligned}$$

Four separate equations are obtained, since (A.4) devides into four independet parts for $a = 1, 2$ and $\varepsilon \lessgtr 0$. Now, an expression for the wavefunction of the reflected electrons in terms of the wavefunction of incident electrons can be derived. Incident electrons with $\lambda = +1$ carry momentum $k_y < 0$, while incident holes with $\lambda = -1$ carry momentum $k_y > 0$. First, the case

$$\underline{\lambda = +1}$$

will be considered. Starting with $a = 1$ one has:

$$\begin{aligned} \psi_+\left(k'_x,k'_y\right) &= -\psi_+\left(k'_x,-k'_y\right) \frac{\frac{\varepsilon_{\mathbf{k}'}}{k'_x-ik'_y}}{\frac{\varepsilon_{\mathbf{k}'}}{k'_x+ik'_y}} \\ &-i\left|v^y\left(\epsilon,k'_x\right)\right| \frac{1}{\frac{\varepsilon_{\mathbf{k}'}}{k'_x+ik'_y}} \int \frac{dk_x}{2\pi} \xi\left(k'_x-k_x\right) \frac{k_y\left(\varepsilon,k_x\right)}{\left|v^y\left(\varepsilon,k_x\right)\right|} \\ &\times \left[\psi_+\left(k_x,k_y\right) \frac{\varepsilon_{\mathbf{k}}}{k_x+ik_y} - \psi_+\left(k_x,-k_y\right) \frac{\varepsilon_{\mathbf{k}}}{k_x-ik_y}\right]. \end{aligned}$$

The above formula is an integral equation for $\psi_+\left(k'_x, k_y\left(\varepsilon, k'_x\right)\right)$. Iterating it for $\psi_+\left(k'_x, k_y\left(\varepsilon, k'_x\right)\right)$ gives to second order in ξ

$$\begin{aligned}
\psi_+\left(k'_x, k'_y\right) &= -\psi_+\left(k'_x, -k'_y\right)\frac{k'_x + ik'_y}{k'_x - ik'_y} + 2i\left|v^y\left(\varepsilon, k'_x\right)\right|\left(k'_x + ik'_y\right) \\
&\quad \times \int \frac{dk_x}{2\pi}\xi\left(k'_x - k_x\right)\frac{k_y\left(\varepsilon, k_x\right)}{\left|v^y\left(\varepsilon, k_x\right)\right|}\psi_+\left(k_x, -k_y\right)\frac{1}{k_x - ik_y} \\
&\quad +2\left|v^y\left(\varepsilon, k'_x\right)\right|\left(k'_x + ik'_y\right) \\
&\quad \times \int \frac{dk_x}{2\pi}\left|v^y\left(\varepsilon, k_x\right)\right|\left(k_x + ik_y\right)\int \frac{dk''_x}{2\pi}\xi\left(k'_x - k_x\right)\xi\left(k_x - k''_x\right) \\
&\quad \times \frac{k_y\left(\varepsilon, k_x\right)}{\left|v^y\left(\varepsilon, k_x\right)\right|}\frac{k_y\left(\varepsilon, k''_x\right)}{\left|v^y\left(\varepsilon, k''_x\right)\right|}\psi_+\left(k''_x, -k''_y\right)\frac{1}{k_x + ik_y}\frac{1}{k''_x - ik''_y}.
\end{aligned}$$

Abbreviating $\left|v^y\left(\varepsilon, k'_x\right)\right| = \left|v^y\right|'$, etc:

$$\begin{aligned}
\psi_+\left(k'_x, k'_y\right) &= -\psi_+\left(k'_x, -k'_y\right)\frac{k'_x + ik'_y}{k'_x - ik'_y} \\
&\quad +2i\left|v^y\right|'\left(k'_x + ik'_y\right)\int \frac{dk_x}{2\pi}\xi\left(k'_x - k_x\right)\frac{k_y}{\left|v^y\right|}\psi_+\left(k_x, -k_y\right)\frac{1}{k_x - ik_y} \\
&\quad +2\left|v^y\right|'\left(k'_x + ik'_y\right) \\
&\quad \times \int \frac{dk_x}{2\pi}\int \frac{dk''_x}{2\pi}\xi\left(k'_x - k_x\right)\xi\left(k_x - k''_x\right)k_y\frac{k''_y}{\left|v^y\right|''}\psi_+\left(k''_x, -k''_y\right)\frac{1}{k''_x - ik''_y}
\end{aligned} \tag{A.9}$$

Factors of the form $k_y\left(\varepsilon, k_x\right) / \left|v^y\right|$ do not depend on momentum and can be taken outside the integrals:

$$\begin{aligned}
\psi_+\left(k'_x, k'_y\right) &= -\psi_+\left(k'_x, -k'_y\right)\frac{k'_x + ik'_y}{k'_x - ik'_y} \\
&\quad +2ik'_y\left(k'_x + ik'_y\right)\int \frac{dk_x}{2\pi}\xi\left(k'_x - k_x\right)\psi_+\left(k_x, -k_y\right)\frac{1}{k_x - ik_y} \\
&\quad +2k'_y\left(k'_x + ik'_y\right) \\
&\quad \times \int \frac{dk_x}{2\pi}\int \frac{dk''_x}{2\pi}\xi\left(k'_x - k_x\right)\xi\left(k_x - k''_x\right)k_y\left(\epsilon, k_x\right)\psi_+\left(k''_x, -k''_y\right)\frac{1}{k''_x - ik''_y}.
\end{aligned}$$

Finally, $\left|\psi_+\left(k'_x,k'_y\right)\right|^2$ is calculated to second order in ξ. Anticipating that upon taking the average over disorder terms linear in ξ must vanish, they are dropped:

$$\begin{aligned}
\left|\psi_+\left(k_x,k_y\right)\right|^2 &= \left|\psi_+\left(k_x,-k_y\right)\right|^2 \\
&\quad -2k_y\left(k_x-ik_y\right)\psi_+^*\left(k_x,-k_y\right) \\
&\qquad \times\int\frac{dk'_x}{2\pi}\int\frac{dk''_x}{2\pi}\xi^*\left(k_x-k'_x\right)\xi^*\left(k'_x-k''_x\right)k_y\left(\epsilon,k'_x\right)\psi_+\left(k''_x,-k''_y\right)\frac{1}{k''_x-ik''_y} \\
&\quad -2k_y\left(k_x+ik_y\right)\psi_+\left(k_x,-k_y\right) \\
&\qquad \times\int\frac{dk'_x}{2\pi}\int\frac{dk''_x}{2\pi}\xi\left(k_x-k'_x\right)\xi\left(k'_x-k''_x\right)k_y\left(\epsilon,k'_x\right)\psi_+^*\left(k''_x,-k''_y\right)\frac{1}{k''_x+ik''_y} \\
&\quad +4k_y^2\left(k_x^2+ik_y^2\right) \\
&\qquad \times\int\frac{dk'_x}{2\pi}\int\frac{dk''_x}{2\pi}\xi\left(k_x-k'_x\right)\xi^*\left(k_x-k''_x\right)\psi_+\left(k'_x,-k'_y\right)\psi_+^*\left(k''_x,-k''_y\right)\frac{1}{k'_x-ik'_y}\frac{1}{k''_x+ik''_y}.
\end{aligned}$$

Averaging over disorder with the help of (A.1) and using $\xi^*\left(k\right)=\xi\left(-k\right)$ results in

$$\begin{aligned}
\left|\psi_+\left(k_x,k_y\right)\right|^2 &= \left|\psi_+\left(k_x,-k_y\right)\right|^2 \\
&\quad -2k_y\left(k_x-ik_y\right)\psi_+^*\left(k_x,-k_y\right)\int\frac{dk'_x}{2\pi}W\left(k_x-k'_x\right)k_y\left(\epsilon,k'_x\right)\psi_+\left(k_x,-k_y\right)\frac{1}{k_x-ik_y} \\
&\quad -2k_y\left(k_x+ik_y\right)\psi_+\left(k_x,-k_y\right)\int\frac{dk'_x}{2\pi}W\left(k_x-k'_x\right)k_y\left(\epsilon,k'_x\right)\psi_+^*\left(k_x,-k_y\right)\frac{1}{k_x+ik_y} \\
&\quad +4k_y^2\left(k_x^2+ik_y^2\right)\int\frac{dk'_x}{2\pi}W\left(k_x-k'_x\right)\psi_+\left(k'_x,-k'_y\right)\psi_+^*\left(k'_x,-k'_y\right)\frac{1}{k'_x-ik'_y}\frac{1}{k'_x+ik'_y},
\end{aligned}$$

which reduces to

$$\begin{aligned}
\left|\psi_+\left(k_x,k_y\right)\right|^2 &= \left|\psi_+\left(k_x,-k_y\right)\right|^2 \\
&\quad -4k_y\left|\psi_+\left(k_x,-k_y\right)\right|^2\int\frac{dk'_x}{2\pi}W\left(k_x-k'_x\right)k_y\left(\varepsilon,k'_x\right) \\
&\quad +4k_y^2\int\frac{dk'_x}{2\pi}W\left(k_x-k'_x\right)\left|\psi_+\left(k'_x,-k'_y\right)\right|^2. \qquad \text{(A.10)}
\end{aligned}$$

The same relation for $\left|\psi_+\left(k_x,k_y\right)\right|^2$ follows, if the calculation is carried out for the other sublattice.

Since for negative energies,

$$\underline{\lambda=-},$$

the reflected particles have momentum $k_y < 0$, Eq. (A.7) is rewritten for $\psi_\lambda\left(k'_x, -k'_y\right)$:

$$\begin{aligned}\psi_\lambda\left(k'_x,-k'_y\right) &= -\psi_\lambda\left(k'_x,k'_y\right)\frac{u_{a,\lambda}\left(k'_x,k'_y\right)}{u_{a,\lambda}\left(k'_x,-k'_y\right)}\\ &\quad -i\frac{\left|v^y\left(\varepsilon,k'_x\right)\right|}{u_{a,\lambda}\left(k'_x,-k'_y\right)}\int\frac{dk_x}{2\pi}\xi\left(k'_x-k_x\right)\frac{k_y\left(\varepsilon,k_x\right)}{\left|v^y\left(\varepsilon,k_x\right)\right|}\\ &\quad\times\left[\psi_\lambda\left(k_x,k_y\right)U_{a,\lambda}\left(k_x,k_y\right)-\psi_\lambda\left(k_x,-k_y\right)U_{a,\lambda}\left(k_x,-k_y\right)\right].\end{aligned}$$

Iterating in $\psi_\lambda\left(k'_x,-k'_y\right)$ gives

$$\begin{aligned}\psi_-\left(k'_x,-k'_y\right) &= -\psi_-\left(k'_x,k'_y\right)\frac{U_{a,\lambda}\left(k'_x,k'_y\right)}{U_{a,\lambda}\left(k'_x,-k'_y\right)}\\ &\quad -2i\frac{\left|v^y\left(\varepsilon,k'_x\right)\right|}{u_{a,-}\left(k'_x,-k'_y\right)}\int\frac{dk_x}{2\pi}\xi\left(k'_x-k_x\right)\frac{k_y\left(\varepsilon,k_x\right)}{\left|v^y\left(\varepsilon,k_x\right)\right|}\psi_-\left(k_x,k_y\right)U_{a,-}\left(k_x,k_y\right)\\ &\quad +2\frac{\left|v^y\left(\varepsilon,k'_x\right)\right|}{u_{a,-}\left(k'_x,-k'_y\right)}\int\frac{dk_x}{2\pi}\int\frac{dk''_x}{2\pi}\\ &\quad\times\xi\left(k'_x-k_x\right)\xi\left(k_x-k''_x\right)k_y\left(\varepsilon,k_x\right)\frac{k_y\left(\varepsilon,k''_x\right)}{\left|v^y\left(\varepsilon,k''_x\right)\right|}\psi_-\left(k''_x,k''_y\right)U_{a,-}\left(k''_x,k''_y\right),\end{aligned}$$

or explicitly for $a = 1$:

$$\begin{aligned}\psi_-\left(k'_x,-k'_y\right) &= -\psi_-\left(k'_x,k'_y\right)\frac{k'_x-ik'_y}{k'_x+ik'_y}\\ &\quad -2i\left|v^y\left(\varepsilon,k'_x\right)\right|\left(k'_x-ik'_y\right)\int\frac{dk_x}{2\pi}\xi\left(k'_x-k_x\right)\frac{k_y\left(\varepsilon,k_x\right)}{\left|v^y\left(\varepsilon,k_x\right)\right|}\psi_-\left(k_x,k_y\right)\frac{1}{k_x+ik_y}\\ &\quad +2\left|v^y\left(\varepsilon,k'_x\right)\right|\left(k'_x-ik'_y\right)\int\frac{dk_x}{2\pi}\int\frac{dk''_x}{2\pi}\\ &\quad\times\xi\left(k'_x-k_x\right)\xi\left(k_x-k''_x\right)k_y\left(\epsilon,k_x\right)\frac{k_y\left(\varepsilon,k''_x\right)}{\left|v^y\left(\varepsilon,k''_x\right)\right|}\psi_-\left(k''_x,k''_y\right)\frac{1}{k''_x+ik''_y}.\end{aligned}$$

Comparting to the analogous expression for positive energies (A.9), one sees that the modulus squared

of $\psi_-\left(k'_x,-k'_y\right)$ is given by the expression (A.10), with k_y and $-k_y$ interchanged:

$$\begin{aligned}\left|\psi_-\left(k_x,-k_y\right)\right|^2 &= \left|\psi_-\left(k_x,k_y\right)\right|^2 \\ &\quad -4k_y\left|\psi_-\left(k_x,k_y\right)\right|^2\int\frac{dk'_x}{2\pi}W\left(k_x-k'_x\right)k_y\left(\epsilon,k'_x\right) \\ &\quad +4k_y^2\int\frac{dk'_x}{2\pi}W\left(k_x-k'_x\right)\left|\psi_-\left(k'_x,k'_y\right)\right|^2. \end{aligned} \tag{A.11}$$

Bearing in mind that the calculated probability density $\left|\psi_{\lambda,\epsilon}\left(k_x,k_y\left(\epsilon,k_x\right)\right)\right|^2$ is a function of ε and k_x as is clear from (A.5), (A.6), one needs to change variables to find the Boltzmann distribution function $f_{\mathbf{k},\lambda}$. The distribution function is obtained by equating the probabilities of each phase space element:

$$\frac{dk_x}{(2\pi)}\frac{dk_y}{(2\pi)}f_{\mathbf{k},\lambda}=d\varepsilon\frac{dk_x}{2\pi}\frac{1}{2\pi v^y_{k_x,k_y\left(k_x,\varepsilon\right),\lambda}}f_{k_x,k_y\left(k_x,\varepsilon\right),\lambda}=d\varepsilon\frac{dk_x}{2\pi}\frac{1}{2\pi v^y_{k_x,k_y\left(k_x,\varepsilon\right),\lambda}}\left|\psi_{\lambda,\varepsilon}\left(k_x,k_y\left(\varepsilon,k_x\right)\right)\right|^2.$$

Thus, one can identify (again in shorthand notation)

$$f_{\mathbf{k},\lambda}=\left(2\pi v^y_{k_x,\lambda}\right)^{-1}\left|\psi_{\lambda,\varepsilon}\left(k_x,k_y\right)\right|^2.$$

Eqs. (A.10), (A.11) then take the form

$$\begin{aligned}f_+\left(k_x,\left|k_y\right|\right) &= f_+\left(k_x,-\left|k_y\right|\right) \\ &\quad -4f_+\left(k_x,-\left|k_y\right|\right)\left|k_y\right|\int\frac{dk'_x}{2\pi}\left|k'_y\right|W\left(k_x-k'_x\right) \\ &\quad +4\left|k_y\right|\int\frac{dk'_x}{2\pi}\left|k'_y\right|W\left(k_x-k'_x\right)f_+\left(k'_x,-\left|k'_y\right|\right),\end{aligned}$$

$$\begin{aligned}f_-\left(k_x,-\left|k_y\right|\right) &= f_-\left(k_x,\left|k_y\right|\right) \\ &\quad -4f_-\left(k_x,\left|k_y\right|\right)\left|k_y\right|\int\frac{dk'_x}{2\pi}\left|k'_y\right|W\left(k_x-k'_x\right) \\ &\quad +4\left|k_y\right|\int\frac{dk'_x}{2\pi}\left|k'_y\right|W\left(k_x-k'_x\right)f_-\left(k'_x,\left|k'_y\right|\right),\end{aligned}$$

It is important to remember, that the function $k_y\left(\varepsilon,k_x\right)=\sqrt{\varepsilon^2/v_g^2-k_x^2}$ is always positive.

A.2 Flow around a circular obstacle: Solution on an infinite domain

The general solution in polar coordinates (r, θ) to Eq. (4.54) can be given in terms of modified Bessel functions of the first and second kind, I_m and K_m:

$$\begin{aligned} q_r &= -U\sum_{n=1}^{\infty} A_n \frac{\cos\left(n\theta\right)}{r^{n+1}} - \frac{1}{4}U\sum_{m=0}^{\infty} B_m \left(\frac{2}{kr} + \sum_{n=1}^{\infty}\Phi_{m,n}\left(kr\right)\cos\left(n\theta\right)\right) \\ q_\theta &= -U\sum_{n=1}^{\infty} A_n \frac{\sin\left(n\theta\right)}{r^{n+1}} - \frac{1}{4}U\sum_{m=0}^{\infty}\sum_{n=1}^{\infty} B_m \Psi_{m,n}\left(kr\right)\sin\left(n\theta\right), \end{aligned} \tag{A.12}$$

$$\begin{aligned} \Phi_{m,n}\left(kr\right) &= \left(K_{m+1}+K_{m-1}\right)\left(I_{m-n}+I_{m+n}\right) + K_m\left(I_{m-n-1}+I_{m-n+1}+I_{m+n-1}+I_{m+n+1}\right), \\ \Psi_{m,n}\left(kr\right) &= \left(K_{m+1}-K_{m-1}\right)\left(I_{m-n}-I_{m+n}\right) + K_m\left(I_{m-n-1}-I_{m-n+1}-I_{m+n-1}+I_{m+n+1}\right), \end{aligned} \tag{A.13}$$

with $k = U/\left(2\nu\right)$, where ν is the kinematic viscosity $\nu = \left(v^2/\tilde{w}_0\right)\eta$ [127]. The Bessel functions in the above equations have the argument $\left(kr\right)$. The pressure is given by

$$p = U\frac{\tilde{w}_0}{v^2}\frac{\partial\phi}{\partial x}, \tag{A.14}$$

with

$$\phi = UA_0\log\left(r\right) - U\sum_{n=1}^{\infty}\frac{A_n}{n}\frac{\cos\left(n\theta\right)}{r^n}. \tag{A.15}$$

For details of the calculation, we refer to Ref. [127]. The Reynolds number of the problem is

$$R = \frac{Ud}{\nu} = 4ka. \tag{A.16}$$

In our case, the general boundary condition of Eq. (4.4) reads

$$\begin{aligned} q_r &= -U\cos\left(\theta\right) \\ q_\theta &= U\sin\left(\theta\right) + \zeta\frac{\partial q_\theta}{\partial r}. \end{aligned} \tag{A.17}$$

Inserting the general solution (A.12) into the boundary conditions (A.17) we derive an infinite set of coupled equations for A_n, B_m. If the set is truncated at some m_{max} and $n_{max} = m_{max} + 1$ the coefficients $A_{n\leq n_{max}}$, $B_{m\leq m_{max}}$ are uniquely determined. The higher the Reynolds number, the larger m, n have to be considered. Here, we restrict ourselves to $m = 0$. While it might be important to include terms with higher m, n to describe the behavior near the obstacle, the pressure far away is gouverned by the $m = 0$ term, which decays slowest (see Eqs. (A.14) and (A.15)). For completeness, we give the coefficients A_0, A_1 and B_0:

$$A_0 = -\frac{B_0}{2k} \tag{A.18}$$

$$A_1 = a^2 - \frac{1}{2}a^2 B_0\left(\left(I_0(ak) + I_2(ak)K_0(ak) + 2I_1(ak)K_1(ak)\right)\right) \tag{A.19}$$

$$B_0 = \frac{2(a+\zeta)}{(a+\zeta)I_0(ak)K_0(ak) + (a+3\zeta)I_1(ak)K_1(ak)}. \tag{A.20}$$

A.3 Pressure and temperature gradients in charge neutral graphene

In this appendix, it is shown how pressure gradients can be related to temperature gradients in graphene at charge neutrality. From the Gibbs-Duhem relation follows, that the pressure of a system is equal to minus the grand potential density

$$\frac{\Omega}{V} = -p.$$

The standard expression for Ω/V can be integrated by parts to give

$$\begin{aligned}\frac{\Omega}{V} &= -\beta^{-1}\sum_{\lambda}\int\frac{d^2k}{(2\pi)^2}\ln\left(1+e^{-\beta\left(\epsilon_{\lambda,\mathbf{k}}-\mu\right)}\right)\\ &= \beta^{-1}\sum_{\lambda}\int\frac{d^2k}{(2\pi)^2}k_i\frac{\partial}{\partial k_i}\ln\left(1+e^{-\beta\left(\epsilon_{\lambda,\mathbf{k}}-\mu\right)}\right)\\ &\quad -\frac{1}{4\pi}\Lambda^2\left(v\Lambda-\mu\right).\end{aligned}$$

An upper cut-off Λ for the momentum integration over the $\lambda=-1$ band was introduced. Therefore it is

$$\begin{aligned}p &= \sum_{\lambda}\int\frac{d^2k}{(2\pi)^2}\frac{\lambda v_i k_i}{1+e^{\beta\left(\epsilon_{\lambda,\mathbf{k}}-\mu\right)}}\\ &\quad +\frac{1}{4\pi}\Lambda^2\left(v\Lambda-\mu\right).\end{aligned}$$

The first right hand side term is the expression for pressure p_{kin} as it enters the kinetic theory. The second term is the Fermi pressure p_Λ of the occupied lower Dirac cone:

$$p = p_{kin} + p_\Lambda.$$

The pressure gradient can be written

$$\nabla p_{kin} = \frac{\partial p_{kin}}{\partial T}\nabla T + \frac{\partial p_{int}}{\partial \mu}\nabla\mu.$$

Since p_Λ does not depend on temperature, the relation

$$s = -\frac{\partial\left(\Omega/V\right)}{\partial T} = \frac{\partial p_{kin}}{\partial T}$$

holds, where s is the entropy density. On the other hand, at charge neutrality ($\mu=0$) one has

$$\begin{aligned}\left.\frac{\partial p_{kin}}{\partial\mu}\right|_{\mu=0} &= -\sum_{\lambda}\int\frac{d^2k}{(2\pi)^2}\left(\lambda v_i k_i\right)\frac{\partial}{\partial\epsilon_{\lambda,\mathbf{k}}}\frac{1}{e^{\beta\epsilon_{\lambda,\mathbf{k}}}+1}\\ &= \sum_{\lambda}\int\frac{d^2k}{(2\pi)^2}\frac{1}{e^{\beta\epsilon_{\lambda,\mathbf{k}}}+1}-\frac{1}{4\pi}\Lambda^2,\end{aligned}$$

where again the last term stems from the integration limit $\lambda=-1$, $k\to\infty$. Keeping in mind that

$$\sum_{\lambda}\int\frac{d^2k}{(2\pi)^2}\frac{1}{e^{\beta\epsilon_{\lambda,\mathbf{k}}}+1} = \int_0^{2\pi}\frac{d\varphi}{(2\pi)^2}\int^{\Lambda}kdk\,1,$$

one finds

$$\left.\frac{\partial p_{kin}}{\partial \mu}\right|_{\mu=0} = 0,$$

and therefore

$$\nabla p_{kin} = s\nabla T.$$

For simplicity, in the main text p_{kin} is referred to as p.

B Appendix B

Non-local hydrodynamic transport and collective excitations in Dirac fluids

The calculations of this Appendix are adopted from Ref. [138].

B.1 Collision operator

Transformed to the band basis, the interaction part of the Hamilton operator (5.1) reads

$$H_{\text{int}} = \frac{1}{2}\int_{k,k',q}\sum_{\alpha\beta} T_{\lambda\mu\mu'\lambda'}\left(\mathbf{k},\mathbf{k}',\mathbf{q}\right)\gamma^{\dagger}_{\lambda'}\left(\mathbf{k}+\mathbf{q},t\right)\gamma^{\dagger}_{\mu}\left(\mathbf{k}'-\mathbf{q},t\right)\gamma_{\mu'}\left(\mathbf{k}',t\right)\gamma_{\lambda}\left(\mathbf{k},t\right) \tag{B.1}$$

where the matrix elements $T_{\lambda\mu\mu'\lambda'}\left(\mathbf{k},\mathbf{k}',\mathbf{q}\right)$

$$T_{\lambda\mu\mu'\lambda'}\left(\mathbf{k},\mathbf{k}',\mathbf{q}\right) = V\left(q\right)\left(U_{\mathbf{k}+\mathbf{q}}U^{-1}_{\mathbf{k}}\right)_{\lambda'\lambda}\left(U_{\mathbf{k}'-\mathbf{q}}U^{-1}_{\mathbf{k}'}\right)_{\mu\mu'}. \tag{B.2}$$

U is the usual transformation from sublattice space to the band space (see Eq. 5.4). For the quantum Boltzmann equation. the self energies $\Sigma^{\gtrless}_{\lambda}\left(\mathbf{k},\omega\right)$ and the Green's functions $g^{\gtrless}_{\lambda'}\left(\mathbf{X},T;\mathbf{k}\right)$ are of interest (the small g is used for the Green's function transformed to the band basis $g^{\gtrless}\left(\mathbf{X},T;\mathbf{k},\omega\right) = U_{\mathbf{k}}G^{\gtrless}\left(\mathbf{X},T;\mathbf{k},\omega\right)U^{\dagger}_{\mathbf{k}}$). The off diagonal elements of greens functions in band space can be neglected if the frequencies of interest are smaller than the energies of thermally excited particles: $\omega \ll k_B T$ (see main text). In the following, only the weak space and time dependencies induced by external forces and represented by the center of mass coordinates will be of interest. For simplicity, the notation will be changed: $\mathbf{X} \to \mathbf{x}$, $T \to t$. The Green's functions $g^{\gtrless}_{\lambda'}\left(\mathbf{x},t;\mathbf{k}\right)$ can be related to the distribution function:

$$\begin{aligned} g^{>}_{\lambda}\left(\mathbf{x},t,\mathbf{k}\right) &= -i2\pi\delta\left(\omega-\varepsilon_{\lambda}\left(\mathbf{k}\right)-U_{\text{pot}}\left(\mathbf{x}\right)\right)\left(1-f_{\lambda,\mathbf{k}}\left(\mathbf{x},t\right)\right) \\ g^{<}_{\lambda}\left(\mathbf{x},t,\mathbf{k}\right) &= i2\pi\delta\left(\omega-\varepsilon_{\lambda}\left(\mathbf{k}\right)-U_{\text{pot}}\left(\mathbf{x}\right)\right)f_{\lambda,\mathbf{k}}\left(\mathbf{x},t\right) \end{aligned} \tag{B.3}$$

To second order in perturbation theory, for the self-energies

$$\begin{aligned}\Sigma_{\lambda}^{\gtrless}\left(\mathbf{k},\omega\right) &= N\sum_{\mu\mu'\lambda'}\int\frac{d^2qd^2k'd\omega_1d\omega_2}{\left(2\pi\right)^6}\left|T_{\lambda\mu\mu'\lambda'}\left(\mathbf{k},\mathbf{k}',\mathbf{q}\right)\right|^2\\ &\times\ g_{\lambda'}^{\gtrless}\left(\mathbf{k}+\mathbf{q},\omega_1\right)g_{\mu}^{\gtrless}\left(\mathbf{k}'-\mathbf{q},\omega_2\right)g_{\mu'}^{\lessgtr}\left(\mathbf{k}',\omega_1+\omega_2-\omega\right)\\ &-\ \sum_{\mu\mu'\lambda'}\int\frac{d^2qd^2k'}{\left(2\pi\right)^4}\int\frac{d\omega_1d\omega_2}{\left(2\pi\right)^2}T_{\lambda\lambda'\mu'\mu}\left(\mathbf{k},\mathbf{k}',\mathbf{k}'-\mathbf{q}-\mathbf{k}\right)T_{\lambda\mu\mu'\lambda'}\left(\mathbf{k},\mathbf{k}',\mathbf{q}\right)^*\\ &\times\ g_{\lambda'}^{\gtrless}\left(\mathbf{k}+\mathbf{q},\omega_1\right)g_{\mu}^{\gtrless}\left(\mathbf{k}'-\mathbf{q},\omega_2\right)g_{\mu'}^{\lessgtr}\left(\mathbf{k}',\omega_1+\omega_2-\omega\right)\end{aligned}\tag{B.4}$$

holds. $N=4$ accounts for the spin-valley degeneracy.

The collision operator, as it appears on the right hand side of Eq. (2.32), can now be determined from the self energies $\Sigma^<$ and $\Sigma^>$. The delta function $\delta\left(\omega-\varepsilon_\lambda\left(\mathbf{k}\right)-U_{\text{pot}}\left(\mathbf{x}\right)\right)$ sets the left hand side of Eq. (2.32) to zero and therefore cancels out. The collision operator can then be written in terms of the distribution function $f_\lambda\left(\mathbf{k}\right)$:

$$\mathcal{C}_\lambda\left(\mathbf{k}\right)=-i\Sigma_\lambda^<\left(\mathbf{k},\varepsilon_\lambda\left(\mathbf{k}\right)\right)\left(1-f_\lambda\left(\mathbf{k}\right)\right)-i\Sigma_\lambda^>\left(\mathbf{k},\varepsilon_\lambda\left(\mathbf{k}\right)\right)f_\lambda\left(\mathbf{k}\right).\tag{B.5}$$

Inserting Eqs. (B.3) into the self energies, parametrizing the deviations of $f_\lambda\left(\mathbf{k}\right)$ from the equilibrium distribution function as shown in Eq. (5.6), and linearizing in $\psi_{\mathbf{k}\lambda}\left(\mathbf{x},t\right)$ leads to the collision operator of Eq. (5.10). The matrix elements $\gamma^{(1,2)}_{\mathbf{k},\mathbf{k}',\mathbf{q}}$ of Eq. (5.10) are given by:

$$\begin{aligned}\gamma_1\left(\mathbf{k},\mathbf{k}',\mathbf{q}\right) &= \left(N-1\right)\left|T_A\left(\mathbf{k},\mathbf{k}',\mathbf{q}\right)\right|^2+\frac{1}{2}\left|T_A\left(\mathbf{k},\mathbf{k}',\mathbf{k}'-\mathbf{q}-\mathbf{k}\right)-T_A\left(\mathbf{k},\mathbf{k}',\mathbf{q}\right)\right|^2\\ &\quad-\left|T_A\left(\mathbf{k},\mathbf{k}',\mathbf{k}'-\mathbf{q}-\mathbf{k}\right)\right|^2\\ \gamma_2\left(\mathbf{k},\mathbf{k}',\mathbf{q}\right) &= \left(N-1\right)\left|T_B\left(\mathbf{k},\mathbf{k}',\mathbf{k}'-\mathbf{k}-\mathbf{q}\right)\right|^2+\left(N-1\right)\left|T_A\left(\mathbf{k},\mathbf{k}',\mathbf{q}\right)\right|^2\\ &\quad+\left|T_A\left(\mathbf{k},\mathbf{k}',\mathbf{q}\right)-T_B\left(\mathbf{k},\mathbf{k}',\mathbf{k}'-\mathbf{q}-\mathbf{k}\right)\right|^2,\end{aligned}\tag{B.6}$$

with

$$\begin{aligned}T_A\left(\mathbf{k},\mathbf{k}',\mathbf{q}\right) &= T_{++++}\left(\mathbf{k},\mathbf{k}',\mathbf{q}\right)=T_{----}\left(\mathbf{k},\mathbf{k}',\mathbf{q}\right)\\ &= T_{+--+}\left(\mathbf{k},\mathbf{k}',\mathbf{q}\right)=T_{-++-}\left(\mathbf{k},\mathbf{k}',\mathbf{q}\right)\\ &= \frac{V\left(q\right)}{4}\left(1+\frac{\left(K+Q\right)K^*}{\left|\mathbf{k}+\mathbf{q}\right|k}\right)\left(1+\frac{\left(K'-Q\right)K'^*}{\left|\mathbf{k}'-\mathbf{q}\right|k'}\right)\end{aligned}$$

and

$$\begin{aligned} T_B\left(\mathbf{k},\mathbf{k}',\mathbf{q}\right) &= T_{++--}\left(\mathbf{k},\mathbf{k}',\mathbf{q}\right) = T_{--++}\left(\mathbf{k},\mathbf{k}',\mathbf{q}\right) \\ &= \frac{V\left(q\right)}{4}\left(1-\frac{\left(K+Q\right)K^*}{\left|\mathbf{k}+\mathbf{q}\right|k}\right)\left(1-\frac{\left(K'-Q\right)K'^*}{\left|\mathbf{k}'-\mathbf{q}\right|k'}\right) \end{aligned} \tag{B.7}$$

Upper-case letters like $K = k_x + ik_y$ etc. combine the two components of the momentum vector onto a complex variable.

Since the quantum Boltzmann equation only accounts for the diagonal in λ components of the distribution function, the currents also have to be decomposed into contributions that involve particle-hole pair creation $\left(\mathbf{j}_{\text{inter}}\right)$ and those who do not $\left(\mathbf{j}_{\text{intra}}\right)$. Here, the identity

$$U_{\mathbf{k}}\sigma U_{\mathbf{k}}^{-1} = \frac{\mathbf{k}}{k}\sigma_z - \frac{\mathbf{k}\times\mathbf{e}_z}{k}\sigma_y \tag{B.8}$$

is usefull. The charge current

$$\mathbf{j}_c = ev\int_{\mathbf{k}}\psi^\dagger\left(\mathbf{k}\right)\sigma\psi\left(\mathbf{k}\right) \tag{B.9}$$

can be written as

$$\mathbf{j}_c = \mathbf{j}_{c,\text{intra}} + \mathbf{j}_{c,\text{inter}}, \tag{B.10}$$

where the two contributions are given by

$$\begin{aligned} \mathbf{j}_{c,\text{intra}} &= ev\int_{\mathbf{k}}\sum_{\lambda=\pm}\frac{\lambda\mathbf{k}}{k}\gamma^\dagger_{\mathbf{k},\lambda}\gamma_{\mathbf{k},\lambda} \\ \mathbf{j}_{c,\text{inter}} &= iev\int_{\mathbf{k}}\frac{\mathbf{k}\times\mathbf{e}_z}{k}\left(\gamma^\dagger_{\mathbf{k},+}\gamma_{\mathbf{k},-} - \gamma^\dagger_{\mathbf{k},-}\gamma_{\mathbf{k},+}\right). \end{aligned} \tag{B.11}$$

The energy current $\mathbf{j}_\varepsilon$ and the momentum current tensor τ_{xy} can be decomposed in a similar manner. This leads to the expressions (5.31) and (5.32) of the main text and the expression that is used for τ_{xy} in Sec. 5.2.3. As discussed above, in the hydrodynamic regime, it is legitimate to focus on the intra-band contributions, which dominate the transport behavior of the system.

B.2 Collinear scattering and collinear zero modes

Here, the logarithmic divergence of the collision operator for collinear processes is demonstrated following Ref. [49]. The essential mathematics behind the divergence is contained in phase space density available for two particle collisions. The phase space is restricted by the delta function ensuring energy conservation: $\delta\left(k+k_1-\left|\mathbf{k}+\mathbf{q}\right|-\left|\mathbf{k}_1-\mathbf{q}\right|\right)$. This can be seen from power counting in Eq. (5.10) using Eqs. (B.6), (B.7).

Choosing $\mathbf{k} = \left(k,0\right)$ with $k>0$, and writing $\mathbf{k}_1 = \left(k_1,k_\perp\right)$, $\mathbf{q} = \left(q,q_\perp\right)$, collinear scattering occurs when $k_1>0$, $k+q>0$, $k_1-q>0$ and $q_\perp\approx 0$, $k_\perp\approx 0$. For small $q_\perp$, $k_\perp$ the argument of the delta function can be approximated as

$$k+k_1-\left|\mathbf{k}+\mathbf{q}\right|-\left|\mathbf{k}_1-\mathbf{q}\right| \approx \frac{k_\perp^2}{2k_1} - \frac{q_\perp^2}{2\left(k+q\right)} - \frac{\left(k_\perp-q_\perp\right)^2}{2\left(k_1-q\right)}. \tag{B.12}$$

The right hand side of this equation is a polynomial in $q_\perp$, and can be written in terms of linear factors as

$$\frac{k_\perp^2}{2k_1} - \frac{q_\perp^2}{2\left(k+q\right)} - \frac{\left(k_\perp - q_\perp\right)^2}{2\left(k_1-q\right)} = -\frac{k_1+k}{2\left(k+q\right)\left(k_1-q\right)}\left(q_\perp - \zeta_1 k_\perp\right)\left(q_\perp - \zeta_2 k_\perp\right).$$

It is then easy to see by performing the $q_\perp$ integration that

$$\int dk_\perp dq_\perp \delta\left(-\frac{k_1+k}{2\left(k+q\right)\left(k_1-q\right)}\left(q_\perp - \zeta_1 k_\perp\right)\left(q_\perp - \zeta_2 k_\perp\right)\right) \propto \int \frac{dk_\perp}{k_\perp}.$$

This behavior leads to a logarithmic divergence. The divergence is however cut off by the screening of the Coulomb potential [144]

$$V\left(\left|\mathbf{q}\right|\right) \to V\left(\left|\mathbf{q}\right| + q_{TF}\right),$$

where q_{TF} is the Thomas Fermi screening length. In the case of charge neutral graphene $q_{FT} = \alpha k_B T/v$. If the screening is included, the integrad of (5.10) vanishes in the infrared. Thus, the contribution of collinear processes to the scattering rates is enhanced by the large factor

$$\log\left(1/\alpha\right).$$

It was demonstrated in sec. 5.1.2 of the main text, that relaxation processes in the hydrodynamic regime are dominated by collinear zero modes. As demonstrated above, these modes describe scattering events in which all particle velocities show in the same direction. Examining the delta function responsible for energy conservation $\delta\left(k + k_1 - \left|\mathbf{k}+\mathbf{q}\right| - \left|\mathbf{k}_1 - \mathbf{q}\right|\right)$, it is easy to see that, if all momenta are parallel to each other, energy is only conserved, if the above conditions $k > 0$, $k_1 > 0$, $k+q > 0$, $k_1 - q > 0$ apply (except for unimportant isolated points in phase space). The exchange momentum q, however, can be positive or negative. To find those $\psi_{\mathbf{k}\lambda}$ that correspond to collinear zero modes, two terms in the collision operator Eq. (5.10) have to be considered:

$$\begin{aligned} A^{(1)}_{\mathbf{k},\mathbf{k}_1,\mathbf{q},\lambda} &= \psi_{\mathbf{k}+\mathbf{q}\lambda} + \psi_{\mathbf{k}_1-\mathbf{q}\lambda} - \psi_{\mathbf{k}_1\lambda} - \psi_{\mathbf{k}\lambda} \\ A^{(2)}_{\mathbf{k},\mathbf{k}_1,\mathbf{q},\lambda} &= \psi_{\mathbf{k}+\mathbf{q}\lambda} - \psi_{-\mathbf{k}_1+\mathbf{q}\bar{\lambda}} + \psi_{-\mathbf{k}_1\bar{\lambda}} - \psi_{\mathbf{k}\lambda}. \end{aligned} \tag{B.13}$$

Using the parametrization

$$\psi_{\mathbf{k},\lambda} = a_{\lambda,m}\left(k\right) e^{im\theta_{\mathbf{k}}} \tag{B.14}$$

yields

$$\begin{aligned} A^{(1)}_{\mathbf{k},\mathbf{k}',\mathbf{q},\lambda} &= \left(a_{\lambda,m}\left(k+q\right) + a_{\lambda,m}\left(k_1-q\right) - a_{\lambda,m}\left(k_1\right) - a_{\lambda,m}\left(k\right)\right) e^{im\theta_{\mathbf{k}}} \\ A^{(2)}_{\mathbf{k},\mathbf{k}',\mathbf{q},\lambda} &= \left(a_{\lambda,m}\left(k+q\right) - (-1)^m a_{\bar{\lambda},m}\left(k_1-q\right) + (-1)^m a_{\bar{\lambda},m}\left(k_1\right) - a_{\lambda,m}\left(k\right)\right) e^{im\theta_{\mathbf{k}}}. \end{aligned} \tag{B.15}$$

For collinear zero modes

$$\begin{aligned} A^{(1)}_{\mathbf{k},\mathbf{k}',\mathbf{q},\lambda} &= 0 \\ A^{(2)}_{\mathbf{k},\mathbf{k}',\mathbf{q},\lambda} &= 0 \end{aligned}$$

has to hold. $A^{(1)}_{\mathbf{k},\mathbf{k}',\mathbf{q},\lambda}$ is set to zero by $a_{\lambda,m}\left(k\right) = \left\{1, \lambda, \beta v\hbar k, \lambda\beta v\hbar k\right\}$. $A^{(2)}_{\mathbf{k},\mathbf{k}',\mathbf{q},\lambda}$ is more restrictive. For even m its zero modes are given by $a_{\lambda,m}\left(k\right) = \left\{1, \lambda, \lambda\beta v\hbar k\right\}$, for odd m the zero modes are $a_{\lambda,m}\left(k\right) = \left\{1, \lambda, \beta v\hbar k\right\}$. Summing up the collinear zero modes are given by

$$a_{\lambda,m} = \lambda^m \left\{1, \lambda, \lambda\beta v\hbar k\right\} e^{im\theta_{\mathbf{k}}}.$$

B.3 Matrix elements of the collision operator

The values of some matrix elements are shown in Table B.1. For $m \geq 2$ the values can be approximated by

$$\begin{aligned}
\left\langle \chi_{\mathbf{k},\lambda}^{(m,s=1)} \left| \mathcal{C} \right| \chi_{\mathbf{k},\lambda}^{(m,s=1)} \right\rangle &= 2.574 \cdot |m| - 3.456 \\
\left\langle \chi_{\mathbf{k},\lambda}^{(m,s=2)} \left| \mathcal{C} \right| \chi_{\mathbf{k},\lambda}^{(m,s=2)} \right\rangle &= 1.825 \cdot |m| - 2.741 \\
\left\langle \chi_{\mathbf{k},\lambda}^{(m,s=3)} \left| \mathcal{C} \right| \chi_{\mathbf{k},\lambda}^{(m,s=3)} \right\rangle &= 5.184 \cdot |m| - 11.37 \\
\left\langle \chi_{\mathbf{k},\lambda}^{(m,s=2)} \left| \mathcal{C} \right| \chi_{\mathbf{k},\lambda}^{(m,s=3)} \right\rangle &= 2.042 \cdot |m| - 4.398.
\end{aligned} \tag{B.16}$$

All values are given in units of $\frac{1}{v^2\beta^3\hbar^3}$.

B.4 Decomposition of the viscosity tensor into longitudinal and transverse parts

Consider a system in which a preference direction is introduced by the wavevector $\mathbf{q}$. It is useful to define the orthogonal tensor basis

$$\begin{aligned}
e_{\alpha\beta}^{(1)} &= \frac{q_\alpha q_\beta}{q^2} \\
e_{\alpha\beta}^{(2)} &= \delta_{\alpha\beta} - \frac{q_\alpha q_\beta}{q^2} \\
e_{\alpha\beta}^{(3)} &= \frac{1}{\sqrt{2}} \left(q_\alpha p_\beta + p_\alpha q_\beta \right) / \left(pq \right),
\end{aligned} \tag{B.17}$$

which is normalized according according to

$$\sum_{\alpha\beta} e_{\alpha\beta}^{(i)} e_{\alpha\beta}^{(j)} = \delta_{ij}.$$

Here it is

$$p_\alpha = q_\gamma \varepsilon_{\gamma\alpha}.$$

In this basis, the symmetric shear force tensor $X_{0,\alpha\beta}$ can be written

$$X_{0,\alpha\beta} = X^{(1)} e_{\alpha\beta}^{(1)} + X^{(2)} e_{\alpha\beta}^{(2)} + X^{(3)} e_{\alpha\beta}^{(3)}. \tag{B.18}$$

The same holds for the momentum current (stress) tensor

$$\tau_{\alpha\beta} = \tau^{(1)} e_{\alpha\beta}^{(1)} + \tau^{(2)} e_{\alpha\beta}^{(2)} + \tau^{(3)} e_{\alpha\beta}^{(3)}. \tag{B.19}$$

Since the system is fully isotropic, except for the preference direction set by $\mathbf{q}$, the response of the system to different components of $X_{0,\alpha\beta}$ can only be distinct as far as these components relate differently to

m	s	s'	$\left\langle \chi^{(m,s)}_{\mathbf{k},\lambda} \middle\vert \mathcal{C} \middle\vert \chi^{(m,s')}_{\mathbf{k},\lambda} \right\rangle$
0	1	1	0
0	1	2	0
0	1	3	0
0	2	2	0
0	2	3	0
0	3	3	0
1	1	1	0.804
1	1	2	0
1	1	3	0
1	2	2	0.463
1	2	3	0
1	3	3	0
2	1	1	2.617
2	1	2	0
2	1	3	0
2	2	2	1.745
2	2	3	1.243
2	3	3	3.341
3	1	1	4.728
3	1	2	0
3	1	3	0
3	2	2	3.167
3	2	3	2.573
3	3	3	6.647
4	1	1	6.988
4	1	2	0
4	1	3	0
4	2	2	4.722
4	2	3	4.122
4	3	3	10.456
5	1	1	9.345
5	1	2	0
5	1	3	0
5	2	2	6.351
5	2	3	5.800
5	3	3	14.610

Table B.1: Matrix elements of the collision operator (5.10) with respect to the collinear zero modes $\chi^{(m,s)}_{\mathbf{k},\lambda} = \lambda^m e^{im\theta} \left\{1, \lambda, \lambda\beta v\hbar k\right\}$. The index m labels the angular harmonic and s one of the modes in curved brackets.

the direction of $\mathbf{q}$. Eqs (B.18) and (B.19) are decompositions of the shear force and momentum current tensors into such components. The fourth rank viscosity tensor $\eta_{\alpha\beta\gamma\delta}$ is defined through the constitutive relation

$$\tau_{\alpha\beta} = \eta_{\alpha\beta\gamma\delta} X_{0,\gamma\delta}.$$

In general, such a tensor connecting the quantities $\tau_{\alpha\beta}$ and $X_{0,\alpha\beta}$ as given by Eqs. (B.18), (B.19) can be written as $\eta_{\alpha\beta\gamma\delta} = \sum_{ij} e^{(i)}_{\alpha\beta} e^{(j)}_{\gamma\delta} \eta^{(ij)}$. However it follows from an Onsager reciprocity relation that $\eta_{\alpha\beta\gamma\delta}$ has to be symmetric with respect to interchanging the first and last pairs of indices:

$$\eta_{(\alpha\beta)(\gamma\delta)} = \eta_{(\gamma\delta)(\alpha\beta)}.$$

This condition further restricts the form of $\eta_{\alpha\beta\gamma\delta}$ to

$$\eta_{\alpha\beta\gamma\delta} = \sum_i e^{(i)}_{\alpha\beta} e^{(i)}_{\gamma\delta} \eta^{(i)}. \tag{B.20}$$

Calculating the scalars $\eta^{(i)}$ using the quantum Boltzmann equation one finds $\eta^{(1)} = \eta^{(2)} \neq \eta^{(3)}$. For reasons explained in the main text, $\eta^{(1)} = \eta^{(2)} = \eta_\perp$ is called the transverse and $\eta^{(3)} = \eta_\parallel$ the londitudinal viscosity. In the sence that $\eta_{\alpha\beta\gamma\delta}$ is spanned by projection operators onto the tensorial subspaces which span the force and current tensors and are given in Eqs. (B.17), the decomposition (B.20) is completely analogous to the decomposition of a conductivity tensor into transverse and longitudinal parts (see Eq. (5.45)).

Appendix C

C Green's function for the quantum Boltzmann equation

Here, a Green's function for the charge sector of the quantum Boltzmann equation of chapters 6 and 5 will be derived. In the absence the Boltzmann equation for the $s = 1$ collinear zero mode $\chi^{(m,s=1)}_{\mathbf{k},\lambda} = \lambda^m e^{im\theta}$ (see Eq. 5.22) reads

$$\sum_{m'} \left[\left(-i\omega + \tau_m^{-1} \right) \delta_{m,m'} + \frac{i}{2} vqe^{-i\vartheta} \delta_{m,m'+1} + \frac{i}{2} vqe^{i\vartheta} \delta_{m,m'-1} \right] a_{m'} \left(\mathbf{x}, t \right) = 0. \tag{C.1}$$

The scattering rates τ_m^{-1} are those of Eq. (C.2):

$$\tau_m^{-1} = \tau_L^{-1} |m| \tag{C.2}$$

with

$$\tau_L^{-1} = \kappa \tau_{c,1}^{-1} \tag{C.3}$$

where $\kappa = 3.2$ and $\tau_{1,c} = 0.804 \frac{\log 2}{\pi} \frac{\hbar}{k_B T}$ (see Eq. (5.35)). Eq. (C.1) can be written as a recurrence relation for the sequence a_m:

$$a_{m+1} = \frac{2ie^{-i\vartheta_{\mathbf{q}}}}{vq} \left(i\omega - \tau_m^{-1} \right) a_m - e^{-2i\vartheta_{\mathbf{q}}} a_{m-1}. \tag{C.4}$$

This recurrence relation has the form

$$a_{m+1} = \left(\alpha' m + \beta' \right) a_m - e^{i\delta} a_{m-1}, \tag{C.5}$$

with $\alpha' = -\frac{2ie^{-i\vartheta_{\mathbf{q}}}}{vq} \tau_L^{-1}$, $\beta' = -\frac{2e^{-i\vartheta_{\mathbf{q}}}}{vq} \omega$ and $\delta = -2\vartheta_{\mathbf{q}}$, where $\vartheta_{\mathbf{q}}$ is the polar angle of $\mathbf{q}$. The solutions for $m > 0$ are

$$a_m = c \cdot e^{i\frac{\delta}{2}\left(m + \frac{\beta'}{\alpha'}\right)} \mathrm{I}_{m+\frac{\beta'}{\alpha'}} \left(-\frac{2e^{i\delta/2}}{\alpha'} \right) \tag{C.6}$$

$$c_m = c \cdot e^{i\frac{\delta}{2}\left(m + \frac{\beta'}{\alpha'}\right)} \mathrm{K}_{m+\frac{\beta'}{\alpha'}} \left(\frac{2e^{i\delta/2}}{\alpha'} \right) \tag{C.7}$$

I_ν and K_ν are modified Bessel functions of the first and second kind. The solutions for $m < 0$ are obtained by making the replacements $m \to -m$, $\vartheta_{\mathbf{q}} \to -\vartheta_{\mathbf{q}}$.

The Green's function $g_{m',m''}$ is defined as the solution to Eq. (C.1) for a point source. In real space and time coordinates, the equation for $g_{m',m''}$ reads

$$\sum_{m'} \left[\left(\partial_t + \tau_m^{-1} \right) \delta_{m,m'} + \frac{1}{2} v \nabla \cdot \left(\begin{bmatrix} 1 \\ -i \end{bmatrix} \delta_{m,m'+1} + \begin{bmatrix} 1 \\ i \end{bmatrix} \delta_{m,m'-1} \right) \right] g_{m',m''} \left(\mathbf{x}, t \right) = \delta \left(\mathbf{x} \right) \delta \left(t \right) \delta_{m,m''}. \tag{C.8}$$

Performing a Fourier transform and rewriting it in terms of the coefficient α', the equation becomes (compare (C.5)):

$$\left(\alpha' \left| m \right| + \beta' \right) g_{m,m''} - e^{i\delta} g_{m-1,m''} - g_{m+1,m''} = \alpha' \tau_L \delta_{m,m''}. \tag{C.9}$$

To find $g_{m,m''} \left(\mathbf{x}, t \right)$ it is convenient to choose specific indices $m'' = m_1$. Assuming that $m_1 \geq 2$, one has

$$g_{m,m_1} = \begin{cases} s \cdot a_m & m > m_1 \\ u \cdot a_m + w \cdot c_m & 0 \leq m \leq m_1 \\ t \cdot a_{-m} \left(-\delta \right) & m < 0. \end{cases} \tag{C.10}$$

g_{m,m_1} must have this form, since the solution c_m is divergent for $m \to \pm\infty$. The $\left(-\delta\right)$ is a reminder, that for negative m, the replacement $\vartheta_{\mathbf{q}} \to -\vartheta_{\mathbf{q}}$ has to be made. The coefficients s, u, w and t can be found by inserting the ansatz (C.10) into Eq. (C.9). Then, four equations are obtained for $m = m_1 + 1$, $m = m_1$, $m = 0$, $m = -1$, respectively. For example, the equation for $m = m_1$ reads:

$$\begin{aligned} \left(\alpha' m + \beta' \right) \left(u \cdot a_m + w \cdot c_m \right) - e^{i\delta} \left(u \cdot a_{m-1} + w \cdot c_{m-1} \right) - s \cdot a_{m+1} &= \alpha' \tau_L \\ u \cdot a_{m+1} + w \cdot c_{m+1} - s \cdot a_{m+1} &= \alpha' \tau_L. \end{aligned}$$

In the last line the recurrence (C.5) was used. The full set of equations reads

$$-s a_{m_1} + u a_{m_1} + w c_{m_1} = 0 \tag{C.11}$$

$$s a_{m_1+1} - u a_{m_1+1} - w c_{m_1+1} = \alpha' \tau_L \tag{C.12}$$

$$u a_1 + w c_1 - t a_{-1} \left(\vartheta \to -\vartheta \right) = 0 \tag{C.13}$$

$$u a_0 + w c_0 - t a_0 \left(\vartheta \to -\vartheta \right) = 0. \tag{C.14}$$

The solution is

$$u = -\alpha' \tau_L \frac{a_{m_1} \left(c_1 a_0 \left(-\delta \right) - c_1 a_{-1} \left(-\delta \right) \right)}{\left(a_1 a_0 \left(-\delta \right) - a_0 a_{-1} \left(-\delta \right) \right) \left(a_{m_1+1} c_{m_1} - a_{m_1} c_{m_1+1} \right)} \tag{C.15}$$

$$w = \alpha' \tau_L \frac{a_{m_1}}{a_{m_1+1} c_{m_1} - a_{m_1} c_{m_1+1}} \tag{C.16}$$

$$s = -\alpha' \tau_L \frac{\left(c_{m_1} \left(a_0 a_{-1} \left(-\delta \right) - a_1 a_0 \left(-\delta \right) \right) + a_{m_1} \left(c_1 a_0 \left(-\delta \right) - c_0 a_{-1} \left(-\delta \right) \right) \right)}{\left(a_1 a_0 \left(-\delta \right) - a_0 a_{-1} \left(-\delta \right) \right) \left(a_{m_1+1} c_{m_1} - a_{m_1} c_{m_1+1} \right)} \tag{C.17}$$

$$t = -\alpha' \tau_L \frac{a_{m_1} \left(a_1 c_0 - a_0 c_1 \right)}{\left(a_1 a_0 \left(-\delta \right) - a_0 a_{-1} \left(-\delta \right) \right) \left(a_{m_1} c_{m_1+1} - a_{m_1+1} c_{m_1} \right)}. \tag{C.18}$$

The solution for $m_1 \leq 2$, the solution is "mirrored" on $m = 0$:

$$g_{m,m_1} = \begin{cases} s \cdot a_{-m}\left(-\delta\right) & m < m_1 \\ u \cdot a_{-m}\left(-\delta\right) + w \cdot c_{-m}\left(-\delta\right) & 0 \geq m \geq m_1 \\ t \cdot a_m & m > 0. \end{cases} \tag{C.19}$$

Furthermore, the replacement $\delta \to -\delta$ must be made.

The cases $m_1 = \pm 1$ and $m_1 = 0$ have to be treated separately. For $m_1 = 0$ and $m_1 = -1$, one can chose

$$g_{m,m_1} = \begin{cases} s \cdot a_m & m \geq 0 \\ t \cdot a_{-m}\left(-\delta\right) & m < 0. \end{cases} \tag{C.20}$$

For $m_1 = 0$, Eq. (C.9) then gives:

$$\begin{aligned} e^{i\delta} t \cdot a_1\left(-\delta\right) - e^{i\delta} s \cdot a_{-1}\left(+\delta\right) &= \alpha' \tau_L \\ t \cdot a_0\left(-\delta\right) - s \cdot a_0\left(+\delta\right) &= 0. \end{aligned}$$

The solution is

$$\begin{aligned} s &= \frac{\alpha' \tau_L e^{-i\delta} a_0\left(-\delta\right)}{a_0\left(+\delta\right) a_1\left(-\delta\right) - a_0\left(-\delta\right) a_{-1}\left(+\delta\right)} \\ t &= s \frac{a_0\left(+\delta\right)}{a_0\left(-\delta\right)} \end{aligned}$$

For $m_1 = -1$, one has

$$\begin{aligned} e^{i\delta} t \cdot a_1\left(-\delta\right) - e^{i\delta} s \cdot a_{-1}\left(+\delta\right) &= 0 \\ t \cdot a_0\left(-\delta\right) - s \cdot a_0\left(+\delta\right) &= \alpha'\left(-\delta\right) \tau_L. \end{aligned}$$

These equations are solved by

$$\begin{aligned} s &= \frac{\alpha'\left(-\delta\right) \tau_L a_1\left(-\delta\right)}{a_{-1}\left(+\delta\right) \cdot a_0\left(-\delta\right) - a_0\left(+\delta\right) a_1\left(-\delta\right)} \\ t &= s \frac{a_{-1}\left(+\delta\right)}{a_1\left(-\delta\right)} \end{aligned}$$

Finally, for $m_1 = 1$ the ansatz

$$g_{m,m_1} = \begin{cases} s \cdot a_m & m > 0 \\ t \cdot a_{-m}\left(-\delta\right) & m \leq 0 \end{cases} \tag{C.21}$$

must be chosen. The equations for s and t then are

$$\begin{aligned} e^{i\delta} s \cdot a_0\left(+\delta\right) - e^{i\delta} t \cdot a_0\left(-\delta\right) &= \alpha' \tau_L \\ t \cdot a_{-1}\left(-\delta\right) - s \cdot a_1\left(+\delta\right) &= 0, \end{aligned}$$

which is solved by

$$\begin{aligned} s &= \frac{\alpha' \tau_L e^{-i\delta} a_{-1}\left(-\delta\right)}{a_0\left(+\delta\right) a_{-1}\left(-\delta\right) - a_1\left(+\delta\right) \cdot a_0\left(-\delta\right)} \\ t &= s \frac{a_1\left(+\delta\right)}{a_{-1}\left(-\delta\right)}. \end{aligned}$$

Thus, all components of $g_{m',m''}$ are known.

Bibliography

[1] G. Wiedemann and R. Franz, *Über die Wärme–Leitungsfähigkeit der Metalle*, Annalen der Physik **165**, 497 (1853).

[2] L. Lorenz, *Bestimmung der Wärmegrade in absolutem Maaße*, Annalen der Physik **223**, 429 (1872).

[3] L. Lorenz, *Über das Leitungsvermögen der Metalle für Wärme und Electricität*, Annalen der Physik **249**, 422 (1881).

[4] J. J. Thomson, *Cathode Rays*, Philosophical Magazine **5**, 293 (1897).

[5] P. Drude, *Zur Elektronentheorie der Metalle*, Annalen der Physik **306**, 566 (1900).

[6] P. Drude, *Zur elektronentheorie der Metalle; II. Teil. galvanomagnetische und thermomagnetische effecte*, Annalen der Physik **308**, 369 (1900).

[7] F. Bloch, *Über die Quantenmechanik der Elektronen in Kristallgittern*, Zeitschrift für physik **52**, 555 (1929).

[8] A. Sommerfeld, *Zur Elektronentheorie der Metalle auf Grund der Fermi'schen Statistik*, Zeitschrift für Physik **47**, 1 (1928).

[9] R. N. Gurzhi, *Minimum of resistance in impurity-free conductors*, Zh. Eksp. Teor. Fiz. **44**, 771 (1963).

[10] R. Gurhzi, *Hydrodynamic effects in solids at low temperature*, Sov. Phys. Usp. **11**, 255 (1968).

[11] L. D. Landau, *The Theory of a Fermi Liquid*, Sov. Phys. JETP **3**, 920 (1957).

[12] L. D. Landau, *Oscillations in a Fermi Liquid*, Sov. Phys. JETP **5**, 101 (1957).

[13] A. A. Abrikosov and I. M. Khalatnikov, *The theory of a fermi liquid (the properties of liquid 3He at low temperatures)*, Reports on Progress in Physics **22**, 329 (1959).

[14] L. D. Landau and E. M. Lifshits, *Fluid mechanics*, Butterworth-Heinemann (1987). ISBN 978-0750627672.

[15] J. M. Ziman, *Electrons and Phonons*, Oxford University Press (2001). ISBN 978-0198507796.

[16] Z. Z. Yu, M. Haerle, J. W. Zwart, J. Bass, J. W. P. Pratt, and P. A. Schroeder, *Negative Temperature Derivative of Resistivity in Thin Potassium Samples: The Gurzhi Effect?*, Phys. Rev. Lett. **52**, 368 (1984).

[17] M. Kaveh and N. Wiser, *Electron-electron scattering in conducting materials*, Advances in Physics **33**, 257 (1984).

[18] J. Zhao, J. W. P. Pratt, H. Sato, P. A. Schroeder, , and J. Bass, *Electronic transport properties of thin potassium wires below 1 K. I. Derivative of electrical resistivity, $d\rho/dT$*, Phys. Rev. B **37**, 8738 (1988).

[19] M. J. M. de Jong and L. W. Molenkamp, *Hydrodynamic electron flow in high-mobility wires*, Phys. Rev. B **51**, 13389 (1995).

[20] L. Wang, I. Meric, P. Y. Huang, Q. Gao, Y. Gao, H. Tran, T. Taniguchi, K. Watanabe, L. M. Campos, D. A. Muller, J. Guo, P. Kim, J. Hone, K. L. Shepard, and C. R. Dean, *One–dimensional electrical contact to a two-dimensional material*, Science **342**, 614 (2013).

[21] D. K. Efetov and P. Kim, *Controlling Electron-Phonon Interactions in Graphene at Ultrahigh Carrier Densities*, Phys. Rev. Lett. **105**, 256805 (2010).

[22] A. Lucas and K. C. Fong, *Hydrodynamics of electrons in graphene*, Journal of Physics: Condensed Matter **30**, 53001 (2018).

[23] A. P. Mackenzie, *The properties of ultrapure delafossite metals*, Rep. Prog. Phys. **80**, 32501 (2017).

[24] P. J. W. Moll, P. Kushwaha, N. Nandi, B. Schmidt, and A. P. Mackenzie, *Evidence for hydrodynamic electron flow in* $PdCoO_2$, Science **351**, 1061 (2016).

[25] J. Gooth, F. Menges, N. Kumar, V. Süß, C. Shekhar, Y. Sun, U. Drechsler, R. Zierold, C. Felser, and B. Gotsmann, *Thermal and electrical signatures of a hydrodynamic electron fluid in tungsten diphosphide*, Nat. Commun **9**, 4093 (2018).

[26] L. Levitov and G. Falkovich, *Electron viscosity, current vortices and negative nonlocal resistance in graphene*, Nature Physics **12**, 672 (2016).

[27] D. A. Bandurin, I. Torre, R. K. Kumar, M. B. Shalom, A. Tomadin, A. Principi, G. H. Auton, E. Khestanova, K. S. Novoselov, I. V. Grigorieva, L. A. Ponomarenko, A. K. Geim, and M. Polini, *Negative local resistance caused by viscous electron backflow in graphene*, Science **351**, 1055 (2016).

[28] A. Shytov, J. F. Kong, G. Falkovich, and L. Levitov, *Particle Collisions and Negative Nonlocal Response of Ballistic Electrons*, Phys. Rev. Lett. **121**, 176805 (2018).

[29] L. Ella, A. Rozen, J. Birkbeck, M. Ben-Shalom, D. Perello, J. Zultak, T. Taniguchi, K. Watanabe, A. K. Geim, S. Ilani, and J. A. Sulpizio, *Simultaneous voltage and current density imaging of flowing electrons in two dimensions*, Nature Nanotechnology **14**, 480 (2019).

[30] J. A. Sulpizio, L. Ella, A. Rozen, J. Birkbeck, D. J. Perello, D. Dutta, M. Ben-Shalom, T. Taniguchi, K. Watanabe, T. Holder, R. Queiroz, A. Principi, A. Stern, T. Scaffidi, A. K. Geim, and S. Ilani, *Visualizing Poiseuille flow of hydrodynamic electrons*, Nature **576**, 75 (2019).

[31] M. J. Ku, T. X. Zhou, Q. Li, Y. J. Shin, J. K. Shi, C. Burch, H. Zhang, F. Casola, T. Taniguchi, K. Watanabe, P. Kim, A. Yacoby, and R. L. Walsworth, arXiv:1905.10791 (2019).

[32] V. O. A. Hui, S. Lederer and E.-A. Kim, *Quantum aspects of hydrodynamic transport from weak electron-impurity scattering*, Phys. Rev. B **101**, 121107 (2020).

[33] D. Forster, *Hydrodynamic Fluctuations, Broken Symmetry, and Correlation Functions*, CRC Press (2018). ISBN 978-0367091323.

[34] A. V. Andreev, S. A. Kivelson, and B. Spivak, *Hydrodynamic Description of Transport in Strongly Correlated Electron Systems*, Phys. Rev. Lett. **106**, 256804 (2011).

[35] A. Lucas and S. A. Hartnoll, *Resistivity bound for hydrodynamic bad metals*, PNAS **43**, 11344 (2017).

[36] H. van Houten and C. W. J. Beenakker, *Quantum point contacts*, Phys Today **49**, 22 (1996).

[37] H. Guo, E. Ilseven, G. Falkovich, and L. S. Levitov, *Higher-than-ballistic conduction of viscous electron flows*, PNAS **114**, 3068 (2017).

[38] R. K. Kumar, D. A. Bandurin, F. M. D. Pellegrino, Y. Cao, A. Principi, H. Guo, G. H. Auton, M. B. Shalom, L. A. Ponomarenko, G. Falkovich, K. Watanabe, T. Taniguchi, I. V. Grigorieva, L. S. Levitov, M. Polini, and A. K. Geim, *Superballistic flow of viscous electron fluid through graphene constrictions*, Nature Physics **13**, 1182 (2017).

[39] B. N. Narozhny, I. V. Gornyi, and A. D. Mirlin, *Hydrodynamic Approach to Electronic Transport in Graphene*, Ann. d. Phys. **529**, 1700043 (2017).

[40] C. R. Dean, A. F. Young, I. Meric, C. Lee, L. Wang, S. Sorgenfrei, K. Watanabea, T. Taniguchi, P. Kim, K. L. Shepard, and J. Hone, *Boron nitride substrates for high-quality graphene electronics*, Solid State Communications **5**, 722 (2010).

[41] A. H. C. Neto, F. Guinea, N. M. R. Peres, K. S. Novoselov, and A. K. Geim, *The electronic properties of graphene*, Rev. Mod. Phys. **81**, 109 (2009).

[42] P. R. Wallace, *The Band Theory of Graphite*, Phys. Rev. **71**, 622 (1947).

[43] P. Kim, *Graphene and Relativistic Quantum Physics*, Springer (2017). Published in „Dirac Matter“, B. Duplantier, V. Rivasseau, J.-N. Fuchs editors.

[44] M. I. Katsnelson, K. S. Novoselov, and A. K. Geim, *Chiral tunnelling and the Klein paradox in graphene*, Nature Physics **2**, 620 (2006).

[45] N. Stander, B. Huard, and D. Goldhaber-Gordon, *Evidence for Klein Tunneling in Graphene p-n Junctions*, Nature **102**, 26807 (2009).

[46] K. S. Novoselov, A. K. Geim1, S. V. Morozov, D. Jiang, Y. Zhang, S. V. Dubonos, I. V. Grigorieva, and A. A. Firsov, *Electric Field Effect in Atomically Thin Carbon Films*, Science **306**, 666 (2004).

[47] D. E. Sheehy and J. Schmalian, *Quantum Critical Scaling in Graphene*, Phys. Rev. Lett. .

[48] B. N. Narozhny, *Optical conductivity in graphene: Hydrodynamic regime*, Phys. Rev. B **100**, 115434 (2019).

[49] L. Fritz, J. Schmalian, M. Müller, and S. Sachdev, *Quantum critical transport in clean graphene*, Phys. Rev. B **78**, 85416 (2008).

[50] J. Crossno, J. K. Shi1, K. Wang, X. Liu, A. Harzheim, A. Lucas, S. Sachdev, P. Kim, T. Taniguchi, K. Watanabe, T. A. Ohki, and K. C. Fong, *Observation of the Dirac fluid and the breakdown of the Wiedemann-Franz law in graphene*, Science **351**, 1058 (2016).

[51] M. Müller, J. Schmalian, and L. Fritz, *Graphene: A Nearly Perfect Fluid*, Phys. Rev. Lett. **103**, 25301 (2009).

[52] T. V. Phan, J. C. W. Song, and L. S. Levitov, *Ballistic Heat Transfer and Energy Waves in an Electron System*, arXiv:1306.4972 (2016).

[53] K. Damle and S. Sachdev, *Nonzero-temperature transport near quantum critical points*, Phys. Rev. B **56**, 8714 (1997).

[54] A. B. Kashuba, *Conductivity of defectless graphene*, Phys. Rev. B **78**, 85415 (2008).

[55] P. Gallagher, C.-S. Yang, T. Lyu, F. Tian, R. Kou, H. Zhang, K. Watanabe, T. Taniguchi, and F. Wang, *Quantum-critical conductivity of the Dirac fluid in graphene*, Science **364**, 158 (2019).

[56] R. N. Gurzhi, A. N. Kalinenko, and A. I. Kopeliovich, *Electron-Electron Collisions and a New Hydrodynamic Effect in Two-Dimensional Electron Gas*, Phys. Rev. Lett. **74**, 3872 (1995).

[57] R. N. Gurzhi, A. N. Kalinenko, and A. I. Kopeliovich, *Inefficiency of odd relaxation and propagation of electron beams in a two-dimensional electron system*, Surf. Sci. **497**, 361 (1996).

[58] P. J. Ledwith, H. Guo, and L. Levitov, *The hierarchy of excitation lifetimes in two-dimensional Fermi gases*, Ann. Phys. **411**, 167913 (2019).

[59] H. Predel, H. Buhmann, L. W. Molenkamp, R. N. Gurzhi, A. N. Kalinenko, A. I. Kopeliovich, and A. V. Yanovsky, *Effects of electron-electron scattering on electron-beam propagation in a two-dimensional electron gas*, Phys. Rev. B **62**, 2057 (2000).

[60] P. Ledwith, H. Guo, A. Shytov, and L. Levitov, *Tomographic Dynamics and Scale-Dependent Viscosity in 2D Electron Systems*, Phys. Rev. Lett. **123**, 116601 (2019).

[61] K. Fuchs, *The conductivity of thin metallic films according to the electron theory of metals*, Proc. Cambridge Philos. Soc. **34**, 100 (1938).

[62] L. A. Falkovksy, *Conductivity of thin metal slabs with rough surfaces*, Journal of Low Temperature Physics **36**, 713 (1979).

[63] L. A. Falkovsky, *Transport phenomena at metal surfaces*, Advances in Physics **32**, 753 (1983).

[64] H. W. W. Jr. and D. Pines, *Kinetic Equation for Plasma*, Phys. Rev. **127**, 1851 (1962).

[65] R. Balescu, *Irreversible Processes in Ionized Gases*, The Physics of Fluids **3**, 52 (1960).

[66] R. Balescu, *On Bogoliubov's kinetic equation for a spatially homogeneous plasma*, Ann. Phys. **10**, 390 (1960).

[67] N. Rostoker and M. N. Rosenbluth, *Test Particles in a Completely Ionized Plasma*, The Physics of Fluids **3**, 1 (1960).

[68] M. N. Rosenbluth, W. M. MacDonald, and D. L. Judd, *Fokker-Planck Equation for an Inverse-Square Force*, Phys. Rev. **107**, 1 (1957).

[69] A.G.R.Thomas, M.Tzoufras, A.P.L.Robinson, R.J.Kingham, C.P.Ridgers, M.Sherlock, and A.R.Bell, *A review of Vlasov–Fokker–Planck numerical modeling of inertial confinement fusion plasma*, Journal of Computational Physics **231**, 1051 (2012).

[70] D. F. Chernoff and M. D. Weinberg, *Evolution of globular clusters in the Galaxy*, Astrophysical Journal **351**, 121 (1990).

[71] A. K. Geim and K. S. Novoselov, *The rise of graphene*, Nature Materials **6**, 183 (2007).

[72] N. D. Mermin, *Crystalline Order in Two Dimensions*, Phys. Rev. **176**, 250 (1968).

[73] J. C. Meyer, A. K. Geim, M. I. Katsnelson, K. S. Novoselov, T. J. Booth, and S. Roth, *The structure of suspended graphene sheets*, Nature **446**, 60 (2007).

[74] J.Gonzaleza, F. Guinea, and M. A. H. Vozmedianoc, *Non-Fermi liquid behavior of electrons in the half-filled honeycomb lattice (A renormalization group approach)*, Nuclear Physics B **424**, 595 (1994).

[75] K. S. Novoselov, A. K. Geim, S. V. M. D. Jiang, M. I. Katsnelson, I. V. Grigorieva, S. V. Dubonos, and A. A. Firsov, *Two-dimensional gas of massless Dirac fermions in graphene*, Nature **438**, 197 (2005).

[76] Y. Zhang, Y.-W. Tan, H. L. Stormer, and P. Kim, *Experimental observation of the quantum Hall effect and Berry's phase in graphene*, Nature **438**, 201 (2005).

[77] K. S. Novoselov, Z. Jiang, Y. Zhang, S. V. Morozov, H. L. Stormer, U. Zeitler, J. C. Maan, G. S. Boebinger, P. Kim, and A. K. Geim, *Room-Temperature Quantum Hall Effect in Graphene*, Science **315**, 1378 (2007).

[78] J. E. Drut and T. A. Lähde, *Is Graphene in Vacuum an Insulator?*, Phys. Rev. Lett. **102**, 26802 (2009).

[79] D. C. Elias, R. V. Gorbachev, A. S. Mayorov, S. V. Morozov, A. A. Zhukov, P. Blake, L. A. Ponomarenko, I. V. Grigorieva, K. S. Novoselov, F. Guinea, and A. K. Geim, *Dirac cones reshaped by interaction effects in suspended graphene*, Nature Physics **7**, 701 (2011).

[80] M. V. Ulybyshev, P. V. Buividovich, M. I. Katsnelson, and M. I. Polikarpov, *Monte Carlo Study of the Semimetal-Insulator Phase Transition in Monolayer Graphene with a Realistic Interelectron Interaction Potential*, Phys. Rev. Lett. **111**, 56801 (2013).

[81] A. Altland and B. D. Simons, *Condensed matter field theory*, Cambridge university press (2010). ISBN: 978-0521769754.

[82] M. Schütt, P. M. Ostrovsky, I. V. Gornyi, and A. D. Mirlin, *Coulomb interaction in graphene: Relaxation rates and transport*, Phys. Rev. B **83**, 155441 (2011).

[83] J. Martin, N. Akerman, G. Ulbricht, T. Lohmann, J. H. Smet, K. von Klitzing, and A. Yacoby, *Observation of electron-hole puddles in graphene using a scanning single-electron transistor*, Nature **4**, 144 (2008).

[84] E. I. Kiselev and J. Schmalian, *Boundary conditions of viscous electron flow*, Phys. Rev. B **99**, 35430 (2019).

[85] C. Cercignani, *The Boltzmann Equation and its Applications*, Springer (1988). ISBN 978-1461210399.

[86] O. Kashuba, B. Trauzettel, and L. W. Molenkamp, *Relativistic Gurzhi effect in channels of Dirac materials*, Phys. Rev. B **97**, 205129 (2018).

[87] H. H. jgaard Jensen, H. Smith, P. Wölfle, K. Nagai, and T. M. Bisgaard, *Boundary effects in fluid flow. Application to quantum liquids*, J. of Low Temp. Phys. **41**, 473 (1980).

[88] P. L. Bhatnagar, E. P. Gross, and M. Krook, *A Model for Collision Processes in Gases. I. Small Amplitude Processes in Charged and Neutral One-Component Systems*, Physical Review **94**, 511 (1980).

[89] S. Chen and G. D. Doolen, *Lattice Boltzmann Method for Fluid Flows*, Ann. Rev. of Fluid Mech. **30**, 329 (1998).

[90] L. P. Kadanoff and G. Baym, *Quntum Statistical Mechanics*, Addison-Wesley (1994). ISBN: 978-0201410464.

[91] G. D. Mahan, *Many-Particle Physics*, Springer (2000). ISBN: 978-0306463389.

[92] A. Kamenev, *Field Theory of Non-Equilibrium Systems*, Cambridge university press (2011). ISBN: 987-0521760829.

[93] T. Kita, *Introduction to Non-equilibrium Statistical Mechanics with Quantum Field Theory*, Prog. Theor. Phys. **123**, 581 (2010).

[94] P. Lévy, *L'addition des variables aléatoires définies sur une circonférence*, Bulletin de la Societe mathematique de France **67**, 1 (1939).

[95] A. Y. Khinchine and P. Levy, *Sur les lois stables*, C. R. Acad Sci **202**, 374 (1936).

[96] K. V. Mardia and P. E. Jupp, *Directional Statistics*, Wiley (1999). ISBN 978-0471953333.

[97] J.-P. Bouchaud and A. Georges, *Anomalous diffusion in disordered media: Statistical mechanisms, models and physical applications*, Physics Reports **195**, 127 (1990).

[98] F. Bartumeus, M. G. E. D. Luz, G. M. Viswanathan, and J. Catalan, *Animal search strategies: A quantitative random-walk analysis*, Ecology **86**, 3078 (2005).

[99] A. M. Reynolds and C. J. Rhodes, *The Lévy flight paradigm: random search patterns and mechanisms*, Ecology **90**, 877 (2009).

[100] D. W. Sims, E. J. Southall, N. E. Humphries, G. C. Hays, C. J. A. Bradshaw, J. W. Pitchford, A. James, M. Z. Ahmed, A. S. Brierley, M. A. Hindell, D. Morritt, M. K. Musyl, D. Righton, E. L. C. Shepard, V. J. Wearmouth, R. P. Wilson, M. J. Witt, and J. D. Metcalfe, *Scaling laws of marine predator search behaviour*, Nature **451**, 1098 (2008).

[101] A. Corral, *Universal earthquake-occurrence jumps, correlations with time, and anomalous diffusion*, Phys. Rev. Lett. **97**, 178501 (2006).

[102] R. N. Mantegna and H. E. Stanley, *Econophysics: Scaling and its breakdown in finance*, J. of stat. Phys. **89**, 469 (1997).

[103] D. W. Sims, N. E. Humphries, R. W. Bradford, and B. D. Bruce, *Lévy flight and Brownian search patterns of a free-ranging predator reflect different prey field characteristics*, Journal of Animal Ecology **81**, 432 (2012).

[104] G. M. Viswanathan, S. V. Buldyrev, S. Havlin, M. G. E. da Luz, E. P. Raposo, and H. E. Stanley, *Optimizing the success of random searches*, Zh. Eksp. Teor. Fiz. **401**, 911 (1999).

[105] E. P. Raposo1, G. M. V. S. V. Buldyrev, M. G. E. da Luz, and H. E. Stanley, *Optimizing the success of random searches*, Journal of Physics A **42** (2009).

[106] B. V. Gnedenko and A. N. Kolmogorov, *Limit Distributions for Sums of Independent Random Variables*, Adison Wesley (1954).

[107] N. G. van Kampen, *Stochastic Processes in Physics and Chemistry*, North Holland (2007). ISBN: 978-0444529657.

[108] S. G. Samko, A. A. Kilbas, and O. I. Marichev, *Fractional integrals and derivatives*, Taylor & Francis (1993). ISBN: 978-2881248641.

[109] R. Metzler and J. Klafter, *The random walk's guide to anomalous diffusion: a fractional dynamics approach*, Phys. Rep. **339**, 1 (2000).

[110] R. Metzler, A. V. Chechkin, and J. Klafter, *Lévy Statistics and Anomalous Transport in „Computational Complexity„*, Springer (2012). ISBN 978-1461418009.

[111] A. V. Chechkin, V. Y. Gonchar, and J. Klafter, *Lévy Flights in a Steep Potential Well*, Journal of Statistical Physics **115**, 1505 (2004).

[112] R. Metzler, E. Barkai, and J. Klafter, *Anomalous Diffusion and Relaxation Close to Thermal Equilibrium: A Fractional Fokker-Planck Equation Approach*, Phys. Rev. Lett. **82**, 3563 (1999).

[113] U. Briskot, M. Schütt, I. V. Gornyi, M. Titov, B. N. Narozhny, and A. D. Mirlin, *Collision-dominated nonlinear hydrodynamics in graphene*, Phys. Rev. B **92**, 115426 (2015).

[114] V. I. Okulov and V. V. Ustinov, *Boundary condition for the distribution function of conduction electrons scattered by a metal surface*, Zh. Eksp. Teor. Fiz. **67**, 1176 (1974).

[115] J. C. Maxwell, Philos. Trans. Soc. London **170**, 231 (1867).

[116] A. R. Akhmerov and C. W. J. Beenakker, *Boundary conditions for Dirac fermions on a terminated honeycomb lattice*, Phys. Rev. B **77**, 85423 (2008).

[117] H. A. Kramers, *On the behaviour of a gas near a wall*, Il Nuovo Cimento **6**, 297 (1949).

[118] E. H. Kennard, *Kinetic theory of gases, with an introduction to statistical mechanics*, McGraw-Hill (1938). ISBN: none.

[119] C. Hodges, H. Smith, and J. W. Wilkins, *Effect of fermi surface geometry on electron-electron scattering.*, Physical Review B **4**, 302 (1971).

[120] M. Reizer and J. W. Wilkins, *Electron-electron relaxation in heterostructures*, Physical Review B **55**, R7363 (1997).

[121] L. Zheng and S. D. Sarma, *Coulomb scattering lifetime of a two-dimensional electron gas*, Physical Review B **53**, 9964 (1996).

[122] D. Menashe and B. Laikhtman, *Quasiparticle lifetime in a two-dimensional electron system in the limit of low temperature and excitation energy*, Physical Review B **54**, 11561 (1996).

[123] V. S. Tsoi, J. Bass, and P. Wyder, *Studying conduction-electron/interface interactions using transverse electron focusing*, Rev. Mod. Phys. **71**, 1641 (1999).

[124] T. Taychatanapat, K. Watanabe, T. Taniguchi, and P. Jarillo-Herrero, *Electrically tunable transverse magnetic focusing in graphene*, Nat. Phys. **9**, 225 (2013).

[125] C. Oseen, *Über die Stokes'sche formel, und über eine verwandte Aufgabe in der Hydrodynamik*, Arkiv för matematik, astronomi och fysik (29) (1910).

[126] G. Batchelor, *An introduction to fluid dynamics, publisher = Cambridge University Press, year = 2000, note = ISBN 978-0521663960.*

[127] S. Tomotika and T. Aoi, *The steady flow of a viscous fluid past a sphere and circular cylinder at small Reynolds numbers*, The Quarterly Journal of Mechanics and Applied Mathematics **3**, 141 (1950).

[128] A. Lucas, *Stokes paradox in electronic Fermi liquids*, Phys. Rev. B **95**, 115425 (2017).

[129] M. S. Foster and I. L. Aleiner, *Slow imbalance relaxation and thermoelectric transport in graphene*, Phys. Rev. B **79**, 85415 (2009).

[130] S. A. Hartnoll, P. K. Kovtun, M. Müller, and S. Sachdev, *Theory of the Nernst effect near quantum phase transitions in condensed matter and in dyonic black holes*, Phys. Rev. B **76**, 144502 (2007).

[131] D. Svintsov, *Hydrodynamic-to-ballistic crossover in Dirac materials*, Phys. Rev. B **97**, 121405 (2018).

[132] I. Torre, L. V. de Castro, B. V. Duppen, D. B. Ruiz, F. M. Peeters, F. H. L. Koppens, and M. Polini, *Acoustic plasmons at the crossover between the collisionless and hydrodynamic regimes in two-dimensional electron liquids*, Phys. Rev. B **99**, 144307 (2019).

[133] J. Brewer and P. Romatschke, *Nonhydrodynamic Transport in Trapped Unitary Fermi Gases*, Phys. Rev. Lett. **115**, 190404 (2015).

[134] P. Romatschke, *Retarded correlators in kinetic theory: branch cuts, poles and hydrodynamic onset transitions*, Eur. Phys. J. C **76**, 352 (2016).

[135] P. Romatschke, *Relativistic Fluid Dynamics Far From Local Equilibrium*, Phys. Rev. Lett. **120**, 12301 (2018).

[136] M. P. Heller, A. Kurkela, M. Spalinski, and V. Svensson, *Hydrodynamization in kinetic theory: Transient modes and the gradient expansion*, Phys. Rev. D **97**, 91503 (2018).

[137] *Non-local hydrodynamic transport and collective excitations in Dirac fluids* .

[138] E. I. Kiselev and J. Schmalian, *Lévy Flights and Hydrodynamic Superdiffusion on the Dirac Cone of Graphene*, Phys. Rev. Lett. **123**, 195302 (2019).

[139] A. A. Vlasov, *On Vibration Properties of Electron Gas*, J. Exp. Theor. Phys. **8**, 291 (1938).

[140] A. D. Mirlin and P. Wölfle, *Composite Fermions in the Fractional Quantum Hall Effect: Transport at Finite Wave Vector*, Phys. Rev. Lett. .

[141] J. M. Link, P. P. Orth, D. E. Sheehy, and J. Schmalian, *Universal collisionless transport of graphene*, Phys. Rev. B **93**, 235447 (2016).

[142] V. Narayanamurti and R. Dynes, *Observation of Second Sound in Bismuth*, Phys. Rev. Lett. **28**, 1461 (1972).

[143] D. A. Huse and S. N. Majumdar, *Nonlocal resistivity in the vortex liquid regime of type-II superconductors*, Phys. Rev. Lett. **71**, 2473 (1993).

[144] M. Müller, L. Fritz, and S. Sachdev, *Quantum-critical relativistic magnetotransport in graphene*, Phys. Rev. B **78**, 115406 (2008).

[145] K. A. Ingebrigtsen, *Surface waves in piezoelectrics*, J. Appl. Phys. **40**, 2681 (1969).

[146] K. A. Ingebrigtsen, *Linear and nonlinear attenuation of acoustic surface waves in a piezoelectric coated with a semiconducting film*, J. Appl. Phys. **41**, 454 (1970).

[147] A. L. Efros and Y. M. Galperin, *Quantization of the acoustoelectric current in a two-dimensional electron system in a strong magnetic field*, Phys. Rev. Lett. **41**, 1959 (1990).

[148] W. Feller, *An Introduction to Probability Theory and its Applications*, vol. 2, Wiley, 2nd ed. (1971). ISBN 978-0471257097.

[149] G. Kurz, I. Gilitschenski, and U. D. Hanebeck, *Efficient evaluation of the probability density function of a wrapped normal distribution*, 2014 Sensor Data Fusion: Trends, Solutions, Applications (SDF), IEEE (2014).